OPTIMIZED TRANSIENT MODULATION AND CONTROL STRATEGIES FOR BIDIRECTIONAL DUAL-ACTIVE-BRIDGE DC-DC CONVERTERS

CHUAN SUN

PhD

The Hong Kong Polytechnic University

2023

The Hong Kong Polytechnic University

Department of Electrical and Electronic Engineering

Optimized Transient Modulation and Control Strategies for Bidirectional Dual-Active-Bridge DC-DC Converters

Chuan SUN

A thesis submitted in partial fulfilment of the requirements for the degree of Doctor of Philosophy

April 2023

Certificate of Originality

I hereby declare that this thesis is my own work and that, to the best of my knowledge and belief, it reproduces no material previously published or written, nor material that has been accepted for the award of any other degree or diploma, except where due acknowledgement has been made in the text.

__________________(Signed)

Chuan SUN (Name of student)

Dedication

This PhD thesis is dedicated to my late grandparents. It is a great pity that I was not around them during their last moments.
I also would like to dedicate it to my parents for their endless love, and to my supervisor for his guidance.

Abstract

Due to the advantages of simple structure, wide-range soft-switching features, ease of modulation and control, etc., both non-resonant dual-active-bridge converter (NR-DABC) and series-resonant DABC (SR-DABC) are preferred options for isolated bidirectional dc-dc power-conversion applications. As DABC is more frequently employed in power-electronic systems that demand fast dynamics, its optimal transient performance is an active research topic.

It is found that when the control variables, i.e., phase-shift angles, are updated through conventional transient phase-shift modulation, severe transient oscillations and/or dc offsets will be induced in the high-frequency-link currents of DABC. These transient oscillations and dc offsets will lead to high current stresses on power devices, and they can span many switching periods during transient stage, thus introducing excessive time delays between the PWM generator and controller. Consequently, truly optimal dynamic performance cannot be achieved with a high-performance controller alone, and the modulation-induced problems must also be thoroughly investigated.

In this thesis, an optimized transient phase-shift modulation (OTPSM) method, known as symmetric single-sided OTPSM (SS-OTPSM), is proposed for single-phase-shift (SPS) modulated NR-DABC. It can fully eliminate all undesired transient dc offsets, and be easily implemented under closed-loop conditions. Furthermore, an enhanced model-predictive controller (EMPC) is proposed for precisely matching the transient energy-transfer model under SS-OTPSM. By integrating SS-OTPSM with EMPC, ultra-fast dynamics can be realized without any transient dc offsets in NR-DABC.

To suppress transient oscillations in SR-DABC, a novel sensorless trajectory-switching modulation (TSM) strategy is proposed for cost-effectively achieving the function of transient trajectory planning of the resonant waveforms. Besides avoiding complicated computation for its cycle-by-cycle implementation, the proposed

TSM can be compatible with high-gain controllers for demonstrating ultra-fast and oscillation-free transient performance in SPS-modulated SR-DABC.

TSM and the other existing OTPSM strategies are mainly developed for suppressing transient oscillations in SPS-modulated SR-DABC, and they cannot eliminate the transient dc offset in transformer's magnetizing current. Hence, this thesis also proposes a generalized TSM (GTSM) method for improving the dynamic performance of multi-phase-shift modulated SR-DABC. GTSM can achieve fast elimination of transient oscillations and dc offsets simultaneously, and ensure safe transient operation of both NR-DABC and SR-DABC. Furthermore, it can be easily adapted to all single/dual/triple/multi-phase-shift gating schemes regardless of power-flow directions and operation modes.

This thesis focuses on developing sensorless OTPSM methods for DABC and presents detailed theoretical analyses, mathematical derivations, and real-time closed-loop experimental verifications. The reported findings provide insights on the optimization of the dynamics of DABC using advanced and effective transient modulation schemes and controller design.

Keywords: Dual-Active-Bridge converter (DABC), dc offsets, dynamics, high-frequency oscillations, phase-shift modulation, series-resonant converter, transient response.

Publications

The following peer-reviewed journal articles are arising from the research described in this thesis:

[1] **C. Sun**, X. Jiang, J. Liu, L. Cao, Y. Yang and K. H. Loo, "A Unified Design Approach of Optimal Transient Single-Phase-Shift Modulation for Non-resonant Dual-Active-Bridge Converter With Complete Transient DC-Offset Elimination," *IEEE Transactions on Power Electronics*, vol. 37, no. 11, pp. 13217–13237, Nov. 2022, doi: 10.1109/TPEL.2022.3182966.

[2] **C. Sun**, X. Jiang, L. Cao and K. H. Loo, "Total Suppression of High-Frequency Transient Oscillations in Dual-Active-Bridge Series-Resonant Converter by Trajectory-Switching Modulation," *IEEE Transactions on Power Electronics*, vol. 37, no. 6, pp. 6511–6529, June 2022, doi: 10.1109/TPEL.2021.3138150.

[3] **C. Sun**, J. Liu, X. Jiang, L. Cao, Y. Wang, J. Shen, and K. H. Loo, "Generalized Multiphase-Shift Transient Modulation for Dual-Active-Bridge Series-Resonant Converter," *IEEE Transactions on Power Electronics*, vol. 38, no. 7, pp. 8291-8309, July 2023, doi: 10.1109/TPEL.2023.3267297.

Acknowledgements

I would like to express my deep gratitude to my supervisor, Dr. Ka-Hong LOO, for his patient guidance, enthusiastic encouragement, and valuable suggestions over these past four years. He gave me the opportunity to learn more about power electronics at The Hong Kong Polytechnic University (HK PolyU). During the course of my research, he provided me many insightful academic ideas on how to conduct high-impact research and make the work better and better. Dr. Loo is a kind, wise, and excellent supervisor, and he can always open our minds and help us to think more deeply, thus addressing the difficulties successfully. His teaching style and philosophy will forever inspire me to be a better researcher.

My grateful thanks are also extended to Prof. Fei GAO from The University of Technology of Belfort-Montbéliard, Prof. Chunhua LIU from The City University of Hong Kong, and Dr. Yui-Lam CHAN from the HK PolyU, for their time and valuable suggestions on my thesis.

I must thank many former and current members in our Electronics and Telecommunications Research Lab at HK PolyU, including Dr. Ling-Ling CAO, Dr. Jun-Wei LIU, Dr. Chi-Shing WONG, Dr. Xing-Yue JIANG, Dr. Fei XU, Dr. Akif Zia KHAN, Dr. Yiu-Pang CHAN, Dr. Qing-Chao Song, Dr. Xing-Xing Chen, Ms. Jia ZHAN, Mr. Ka-Hei LEUNG, and Mr. Gao-Xiang CHEN for their assistance with my study and daily life.

Finally, special thanks should be given to my family members. Without my parents' endless love, support, and tremendous understanding, it would be impossible for me to continue my education. It was my dear girlfriend, Dr. Jun-Ping Ma, who brought me company, confidence, and inspiration during the most difficult time of my PhD life, and I hope everything goes well for us in the future.

— Chuan Sun @ HK PolyU

Contents

List of Figures

List of Tables

Glossary of Terms

IBDC	Isolated Bidirectional DC-DC Converter
DABC	Dual-Active-Bridge Converter
NR-DABC	Non-Resonant Dual-Active-Bridge Converter
SR-DABC	Series-Resonant Dual-Active-Bridge Converter
HF	High-Frequency
PWM	Pulse-Width-Modulation
CTPSM	Conventional Transient Phase-Shift Modulation
OTPSM	Optimized Transient Phase-Shift Modulation
SS-OTPSM	Symmetric Single-Sided OTPSM
MPC	Model Predictive Controller
EMPC	Enhanced Model Predictive Controller
TSM	Trajectory-Switching Modulation
GTSM	Generalized Trajectory-Switching Modulation
SPS	Single-Phase-Shift
EPS	Extended-Phase-Shift
DPS	Dual-Phase-Shift
TPS	Triple-Phase-Shift
MPS	Multi-Phase-Shift
ZVS	Zero-Voltage Switching
RMS	Root-Mean-Square

List of Symbols

V_1, V_2	Input and output voltages.
M	Voltage gain.
C_o	Output capacitance.
R_L	Load resistance.
L_r	Resonant inductance.
L_p	Primary-side auxiliary inductance.
L_s	Secondary-side leakage inductance.
L_m	Magnetizing inductance.
C_r	Resonant capacitance.
J, ∇J	Cost function and its gradient.
P	Transferred power.
R_s	Lumped resistance.
$N : 1$	Transformer's turns ratio.
i_r	Resonant tank current of SR-DABC.
i_L	Inductor current of NR-DABC.
i_m	Transformer's magnetizing current.
i_2	Terminal current of secondary-side bridge.
I_o	Load current.
v_{Lr}, v_{Cr}	Voltages across L_r and C_r.
v_{LC}	Voltage across the L_r-C_r network.
v_{ab}, v_{cd}	HF-link square-wave or quasi-square-wave voltages.
$W_1 \sim W_6$	Transient modulation variables of SS-OTPSM.
$\alpha_1 \sim \alpha_4$	Transient modulation variables of GTSM.

θ/D	Phase-shift angle/ratio of SPS modulation.
δ, d	Phase-shift increment or decrement.
β	Transient phase-shift angle of TSM.
γ	Transient pulse width of v_{ab} or v_{cd} under TSM.
ω_s	Angular switching frequency.
ω_r	Angular resonant frequency.
f_s	Switching frequency.
T_s	Switching period.
T_{hc}	Half a switching period
f_r	Resonant frequency.
F	Normalized frequency.
Z_r	Characteristic impedance.
X_r	Equivalent impedance.
ϕ	Angular displacement at time t.
$S_1 \sim S_4$	Primary-side power MOSFETs
$Q_1 \sim Q_4$	Secondary-side power MOSFETs

Chapter 1

Introduction

1.1 Research Background

Rapid urbanization and industrialization around the world lead to sustained growth in electricity consumption and demand. Nowadays the majority of scientists believe that the carbon-based electricity generation makes a contribution to climate change [1]; and meanwhile, the issues of environmental degradation and resource limitations are increasingly apparent for human lives. As a result, there is an urgent need to transform the world's energy-generation systems from carbon-based to renewable-based. Many governments, especially in recent years, have scheduled cleaner and more sustainable energy routes. According to the latest forecast released by the International Renewable Energy Agency (IRENA) as depicted in Fig. 1.1 [2], the renewable sources (e.g., solar and wind energy) will account for 86% of the global power generation by 2050, while the use of traditional fossil-fuel sources (e.g., coal and oil) will be significantly reduced, thus securing a model of low-carbon living.

The development of renewable energy resources and improvement in energy conversion efficiency are the twin pillars for next-generation smart grids, and power electronics is a key enabling technology for achieving them both. Specifically, the main objective of a power electronics converter is to convert electricity from one

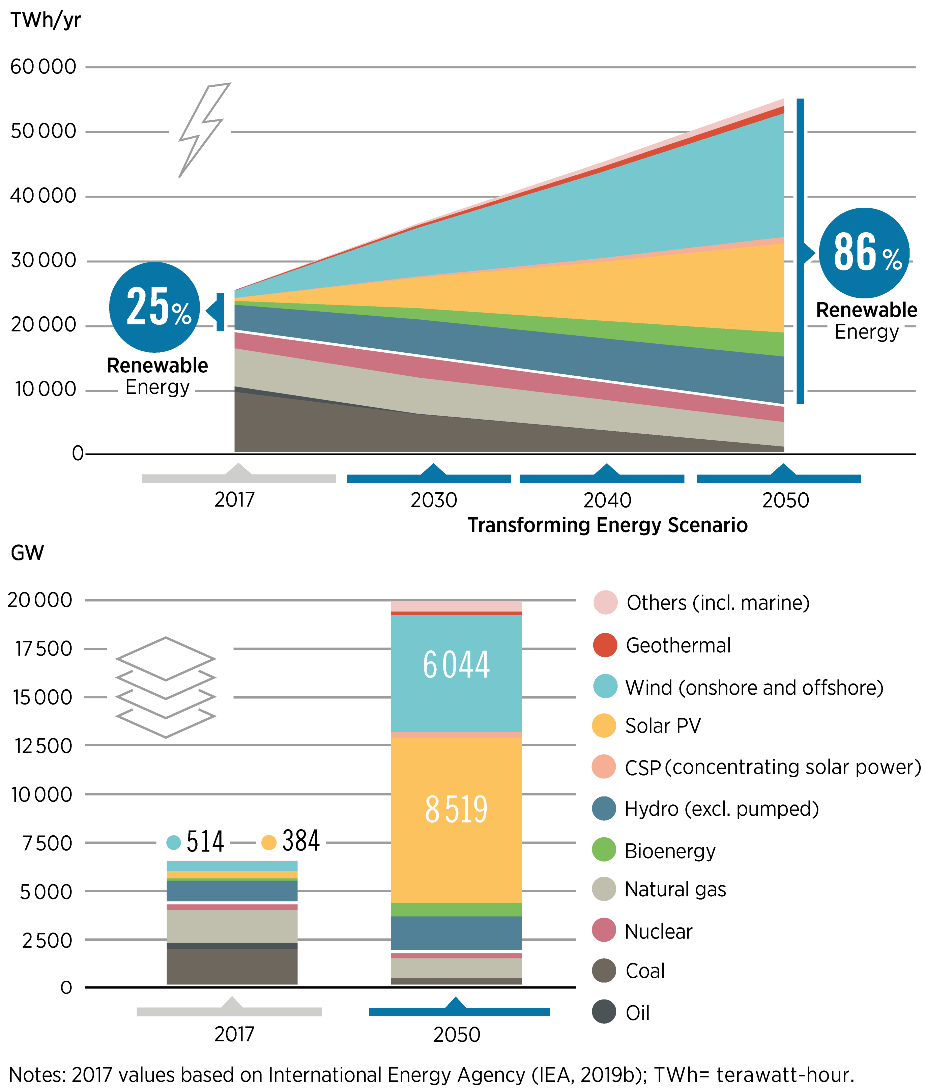

Fig. 1.1. Forecast of global electricity generation and installed capacity by source until 2050. (Source: the report entitled "Global Renewables Outlook: Energy Transformation 2050" was published by IRENA in 2020 [2].)

form to another efficiently by using power semiconductor devices as switches in the circuits, thereby controlling the voltages and currents to meet specific requirements of the sources and loads. With high penetration of renewable energy scenarios, it is expected that power-electronic techniques will play an essential and increasing role in providing sustainable electrical energy to us [3]. For example, Fig. 1.2 depicts a typical power-electronics-based solution for harvesting renewable energy, which is a distributed renewable energy generation and storage system [4]. In general, the wind and solar energy is transformed into electrical energy through

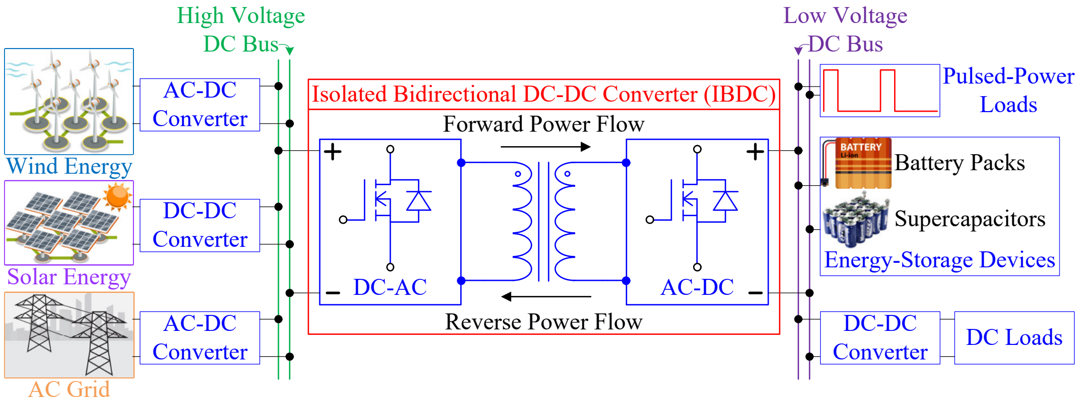

Fig. 1.2. Distributed renewable energy generation and storage system.

renewable generation units (e.g., wind turbines and photovoltaic panels) and then transferred to the dc grid (i.e., high-voltage dc bus) via ac-dc and dc-dc power converters, respectively. As both wind and solar energy sources are intermittent, large-scale energy-storage devices (e.g., battery packs and supercapacitors) are often connected to the low-voltage dc bus through isolated bidirectional dc-dc converters (IBDCs) to store redundant energy when electricity demand is low and discharge it in the scenario of high electricity demand, thus increasing the flexibility of the distributed energy system [5], [6].

However, the large uncertain and unpredictable power-flow fluctuations induced by renewable electricity generation can considerably complicate the dynamics of IBDCs [7], [8]. In addition, except for renewable applications, IBDCs-based energy-storage systems are widely used in many industrial and scientific applications, and they are expected to regulate the output voltage robustly and exhibit fast transient responses under strongly non-linear loads such as radar transmitters, electroplating units, particle accelerators, and electromagnetic weapons [9]–[11]. For example, in a dc shipboard microgrid shown in Fig. 1.3, the advanced electromagnetic weapons in the form of pulsed-power loads need to draw a high peak power from the dc microgrid system within a very short period, and IBDCs have to deal with the rapid and repeated power changes while ensuring that the high-energy pulsed nature of weapons does not cause strong disturbances to the dc bus

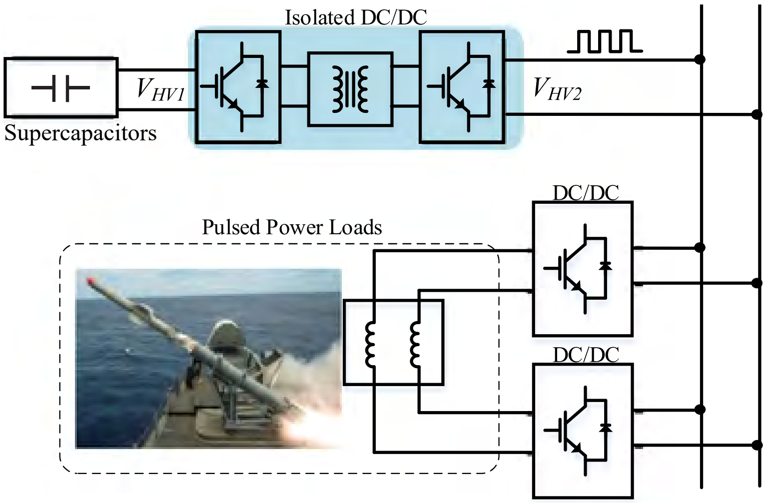

Fig. 1.3. Description of a dc shipboard microgrid [9].

and power system. Since IBDC directly supplies such pulsed-power loads, excellent transient performance is therefore a desirable design specification for IBDC, which largely depends on its control and modulation strategies.

Unfortunately, conventional control methods showing relatively slow dynamic responses are inefficient for reducing the strong power fluctuations, and existing IBDCs still lack sufficiently satisfactory dynamic performance that enable fast and smooth load transitions under extreme operating conditions. In light of the above background and reasons, optimization of the dynamics and control design of IBDCs is an essential research topic, and effective control methodologies for ensuring the reliability, stability, and safety of IBDCs should be developed.

1.2 Bidirectional Dual-Active-Bridge DC-DC Converter for Energy-Storage Applications

There are various isolated dc-dc converter topologies, and some of the most commonly used ones, such as the phase-shifted full-bridge (PSFB) converter [see Fig. 1.4(a)], full-bridge resonant CLLLC converter [see Fig. 1.4(b)], and dual-active-bridge converter (DABC), are systematically compared in Table 1.1. Among

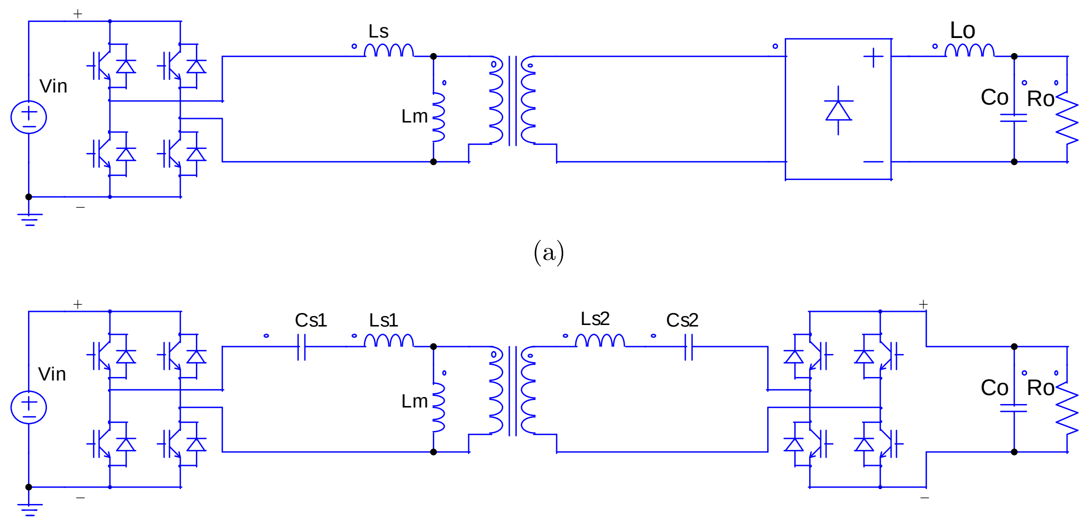

Fig. 1.4. Common isolated dc-dc converter topologies: (a) PSFB converter and (b) CLLLC converter.

Table 1.1 Comparisons of Common Isolated DC-DC Converter Topologies.

Parameter	PSFB	CLLLC	DAB
Isolation	Yes	Yes	Yes
Bidirectional	No	Yes	Yes
No. of Power Devices	4 Switches + Rectifiers	8 Switches	8 Switches
Conversion Ratio	Wide	Narrow	Wide
Modulation Method	Fixed-Frequency Inner-Phase-Shift Modulation	Variable-Frequency Modulation	Fixed-Frequency Multi-Phase-Shift Modulation
Transformer Design	Simple	Difficult	Simple
Synchronous Rectification	Simple	Difficult (Require Current Sensing)	No Need
ZVS Range	Difficult at Light Loads	More Difficult as Frequency Increased	Full-Load ZVS under Multi-Phase-Shift Modulation
Output Capacitance	Small (Low Ripple)	Large (High Ripple)	Small (Low Ripple)

various IBDCs, the DABC has become the most preferred converter topology for connecting energy storages to the dc grid due to an array of practical merit features, such as simple circuit structure, provision of galvanic isolation, high-power density, ease of control, flexibility of phase-shift modulation, and soft-switching capability. From the last decade, with the progress in wide-band-gap semiconductors and magnetic devices, DABC and its variants have attracted considerable attention for high-efficiency power conversion in many emerging applications, including grid-connected energy storage systems [12]–[14], data centers [15], next-generation telecommunication systems (5G/6G, satellite) [16]–[19], vehicle-to-grid (V2G) enabled electric vehicles (cars, trains, ships, aircrafts) [20]–[22], smart/solid-state transformers [23]–[25], and energy routers [26]–[28], and research on DABC is a rapidly growing field in power electronics.

DABCs can generally be categorized into non-resonant DABC (NR-DABC) and resonant DABC. Traditional single-inductor-based NR-DABC was originally invented by Rik W. De Doncker et al. (1991) [29], which consists of two full-bridge converters, a purely inductive (i.e., non-resonant) energy-transfer network, and a high-frequency (HF) transformer. Fig. 1.5(a) illustrates the schematic of a closed-loop controlled NR-DABC. The HF transformer is used for providing electrical isolation between the two dc terminals of NR-DABC, and its turns ratio is $N : 1$. The main energy-transfer components, L_p and L_s, are made up of transformer's leakage inductances and auxiliary inductances, and their inductance values are much lower than the magnetizing inductance L_m referred to primary side, which is generally assumed to be very large. Through the use of transformer's T-equivalent model (T-model), a primary-referred equivalent circuit of NR-DABC can be obtained as shown in Fig. 1.5(b), where the effect of lumped resistance R_s, including the PCB trace resistances, on-state resistances of power switches, winding resistances of magnetic components, etc., is neglected as R_s is generally small.

The most straightforward and widely-used modulation technique for DABC is single-phase-shift (SPS) modulation, and Fig. 1.6 shows the main steady-state voltage and current waveforms of SPS-modulated NR-DABC. To prevent short circuit, the two active power switches on a bridge leg of DABC (i.e., $\{S_1, S_2\}$, $\{S_3, S_4\}$, $\{Q_1, Q_2\}$ and $\{Q_3, Q_4\}$) are switched complementarily with a fixed-frequency 50% duty ratio, while the diagonal switches (i.e., $\{S_1, S_4\}$, $\{S_2, S_3\}$, $\{Q_1, Q_4\}$ and

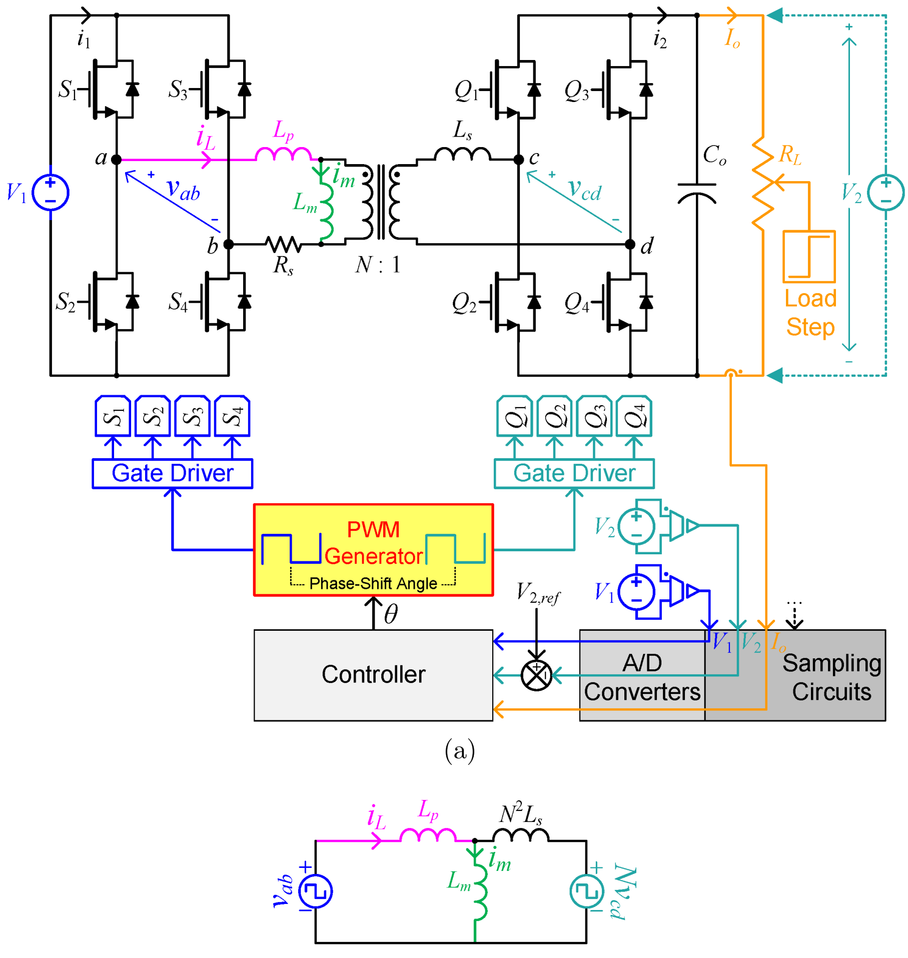

Fig. 1.5. Circuit schematic of NR-DABC. (a) Generic closed-loop control architecture of NR-DABC. (b) Equivalent circuit of NR-DABC.

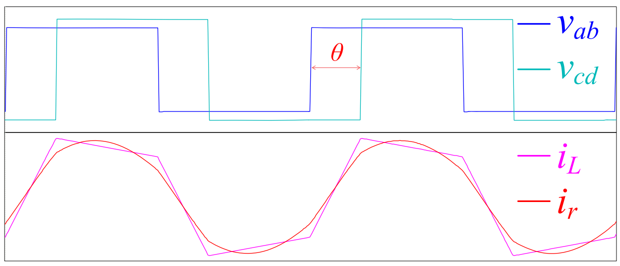

Fig. 1.6. Typical steady-state waveforms of NR-DABC and SR-DABC under SPS modulation.

$\{Q_2, Q_3\}$) are switched concurrently to generate HF square-wave voltages v_{ab} and v_{cd}, across the primary-side and secondary-side full bridges, respectively. The phase-shift angle between v_{ab} and v_{cd} is θ, which can determine both the amount and direction of power flow. When $\theta > 0$, DABC is operated under forward-power

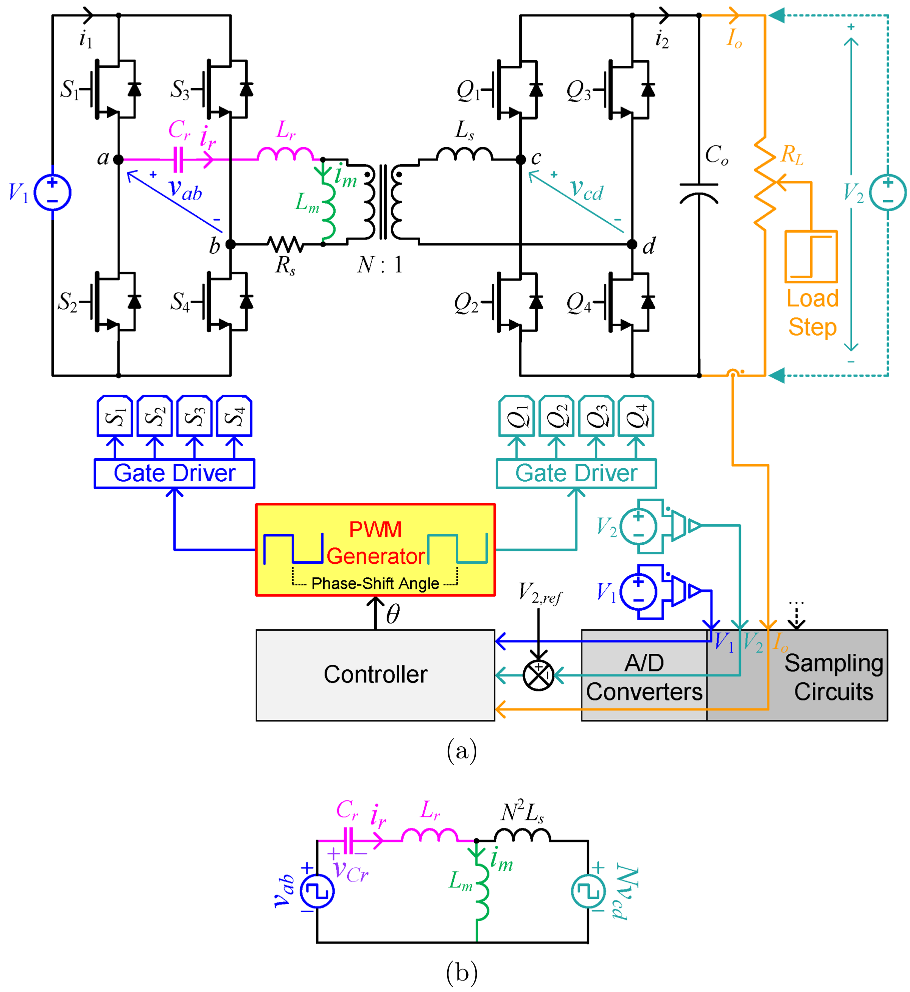

Fig. 1.7. Circuit schematic of SR-DABC. (a) Generic closed-loop control architecture of SR-DABC. (b) Equivalent circuit of SR-DABC.

mode, and the net power is transferred from the input voltage source (V_1) to the load (R_L). The inductor current i_L is rectified to produce i_2 (output terminal current of DABC), which is smoothed by the output filter capacitor C_o to generate a dc load current I_o. In addition, owing to the inductive nature of NR-DABC, i_L and i_m (transformer's magnetizing current) are of triangular/trapezoidal shapes, which makes zero-voltage switching (ZVS) easy to realize [30]. When $\theta < 0$ and the load R_L is replaced by a dc voltage source V_2, reverse power flow, from V_2 to V_1, can also be achieved accordingly.

By connecting a resonant capacitor in series with NR-DABC's power inductor, the simplest resonant version, i.e., single-sided LC-type series-resonant DABC

(SR-DABC), can be constructed as shown in Fig. 1.7(a). The series combination of L_r and C_r can act as a high-Q resonant tank to attenuate the HF harmonics of v_{ab} and v_{cd}, thereby generating an approximately sinusoidal resonant-tank current i_r. A fixed-frequency SPS modulated SR-DABC is systematically investigated in an earlier study [31]. It can be observed from Fig. 1.6, unlike the triangular inductor current (i_L) in NR-DABC, the high-frequency-link resonant current (i_r) of DABSRC is near sinusoidal, which implies lower turn-off and root-mean-square (RMS) currents as well as smaller harmonic current distortion. Thus, compared with NR-DABC, it is easier for SR-DABC to achieve reduced switching and conduction losses in power switches, lower reactive power, and smaller eddy-current loss in transformer's windings [32]–[35], and SR-DABC generally has higher efficiency at the same power level as pointed out by some survey studies [36], [37].

Overall, NR-DABC and SR-DABC are both very popular choices for achieving bidirectional power transmission, and they are the two most widely used topologies of DABC family. SR-DABC inherits most of the features from conventional NR-DABC because of their similar structures, while offering additional advantages such as higher system efficiency. In addition, according to the analysis presented in [32], traditional NR-DABC can be viewed as a subset of SR-DABC with infinite C_r.

1.3 Dynamic Performance of Dual-Active-Bridge Converter and Its Challenges

Given that DABC has a broad variety of applications, besides pursuing higher power conversion efficiency, it is of great interest and importance to understand its optimal dynamics. As shown in Fig. 1.5(a) and Fig. 1.7(a), the roles of controller and pulse-width-modulation (PWM) generator (i.e., modulation) are different in the closed-loop control architecture. The objective of a controller is to

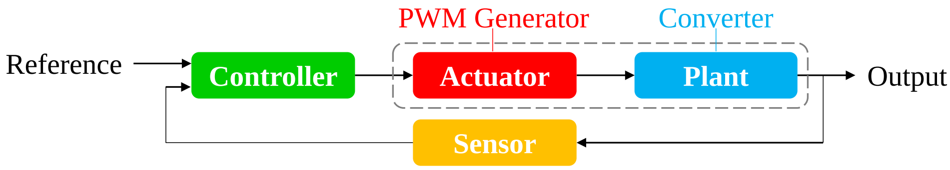

Fig. 1.8. Relationship between actuator and controller.

determine optimal control variables, i.e., phase-shift angles, for the next switching cycle with the assistance of DABC's dynamic model for minimizing output voltage variations. A PWM generator is linked to the controller and utilized to generate gating signals of the power switches. It is clear from Fig. 1.8 that the PWM generator is actually an actuator that performs the specific control action (i.e., the phase-shift adjustment) as commanded by the controller. As a result, both the controller's performance and the transient switching sequences determined by PWM generator can affect the transient performance of a closed-loop controlled DABC.

Specifically, once the controller outputs the signal for power adjustment in response to a load change, the current value of the control variable (i.e., $\theta[n]$) should be changed to the desired value (i.e., $\theta[n+1] = \theta[n] + \Delta\theta$), where $\Delta\theta$ represents the phase increment or decrement. It is the PWM generator's responsibility to indicate how θ should be updated. There is no standard way for updating the value of θ, and it is typically determined by how the PWM generator is implemented in a microprocessor. Conventional transient phase-shift modulation (CTPSM) is the default implementation approach used by the PWM modules of most commercial microprocessors. The operating mechanism of CTPSM is illustrated in the left side of Fig. 1.9. In order to realize a desired new phase-shift angle $\theta[n+1]$, the transient low-level duration of v_{cd} will be increased (when $\theta > 0$) or decreased (when $\theta < 0$) by $|\theta|$ (i.e., the turn-on instants of Q_1 and Q_4 should be advanced or delayed by $|\theta|$), while the other low- and high-level durations of both v_{ab} and v_{cd} will maintain a constant value of π during transient state. The impacts of CTPSM on NR-DABC and SR-DABC are demonstrated by the simulation exam-

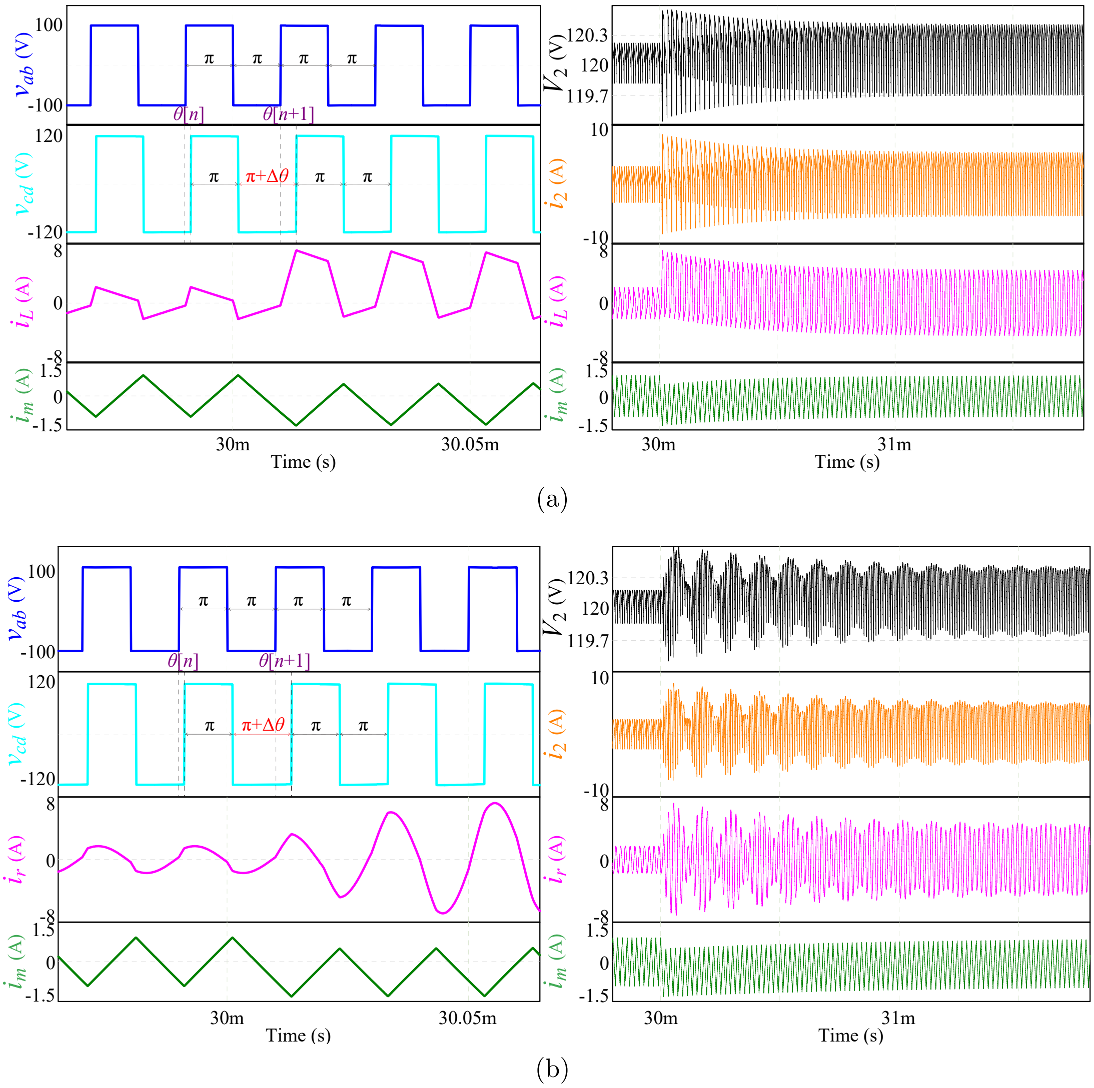

Fig. 1.9. Typical transient waveforms under CTPSM. (a) Transient waveforms of NR-DABC. (b) Transient waveforms of SR-DABC. The simulation parameters are as follows: switching frequency $f_s = 50$ kHz, $V_1 = 100$ V, $V_2 = 120$ V, $L_p = 97$ μH, $L_s = 1.70$ μH, $L_m = 650$ μH, $L_r = 321$ μH, $C_r = 45$ nF, $\theta[n] = 1/9$ rad, $\theta[n+1] = 1/3$ rad, and $\Delta\theta = 2/9$.

ples presented in Figs. 1.9(a) and (b), respectively. It is observed that, during steady state, all the HF-link waveforms are symmetrical and their average values are zero for each period. However, during transient state, CTPSM leads to dc offset in NR-DABC's inductor current, HF oscillations (i.e., beat-frequency oscillation phenomenon [38], [39]) in SR-DABC's resonant waveforms, and dc offset in transformer's magnetizing current in both NR-DABC and SR-DABC. This problem will also arise in the terminal voltages and currents of DABC (e.g., V_2 and

i_2). Typically, the first peaks of the transient waveforms are significantly higher than the new steady-state values, and hence they are accompanied by significant overshoots/undershoots. Since inductors and capacitors cannot dissipate energy, the excess transient energy can only be absorbed by the parasitic resistance R_s of the circuit gradually and slowly, and hence such dc offsets and oscillations will sustain for many switching cycles between the original and new steady states. In addition, they can result in high current and voltage stresses on the power-stage devices, additional power losses, risk of magnetic saturation, poor output voltage quality, and even permanent damage to power devices. Collectively, they have considerable negative influences on the dynamic performance of DABC.

Based on the above analysis, it is well understood that the undesirable transient dc offsets and oscillations are induced by the sudden changes in the turn-on and turn-off durations of some gating signals of DABC, i.e., they are resulted from the inappropriate switching sequence generated by unoptimized PWM generator. In fact, the presence of excessive transient dc offsets and oscillations under CTPSM means that the PWM generator (i.e., the actuator shown in Fig. 1.8) cannot immediately control the HF-link current trajectory of DABC according to controller's commands, thereby resulting in time delays between the actuator and controller. Besides, CTPSM can bring about a severe degradation of the overall dynamics and even instability of the system. For closed-loop controlled DABC, these unwanted transient dc offsets and oscillations are viewed as HF disturbances generated outside the control loop, and can hardly be suppressed by means of controller design, as the disturbance frequencies are generally much higher than the controller's cut-off frequency. To achieve optimum dynamic performance in DABC, more advancements in transient modulation methods, in addition to the use of advanced controllers, are required.

It should be noted that the above-mentioned transient dc offsets and oscillations mainly result from the sudden changes in control variables under CTPSM.

In fact there also exist steady-state dc offsets and oscillations in DABC, which typically result from the inconsistencies in circuit parameters [40], [97], such as different on-state resistance values of power switches, uncertain delays in gating signals, and inaccurate pulse durations. Nevertheless, such steady-state dc offsets should be mitigated by optimized circuit designs and specific elimination methods, which will not be discussed in this thesis.

1.4 Motivation and Objectives of the Thesis

In general, an ultra-fast dynamic response is indispensable to reduce the size of converter's output filter, which enables more compact system integration. Accordingly, in order to speed up the dynamic response of DABC, its controller's gain should be sufficiently high. However, although a fast and high-gain controller such as model-predictive controller (MPC) can result in lower output voltage fluctuation, smaller steady-state tracking error, and reduced response time [9], [41]–[45], it also leads to more abrupt and larger transient variations in the control variable θ, which tends to produce severe transient dc offsets and oscillations when CTPSM is used.

It is clear that the dilemma between the benefits of using high-gain controller and the potential problems posed by CTPSM cannot be compromised unless the HF-link current of DABC can be modulated properly. Unfortunately, a thorough review of the literature on enhancing the transient performance of DABC reveals that earlier efforts have mostly concentrated on the feedback control design, with little attention paid to the dynamic behaviour of DABC and transient modulation schemes. To further optimize the dynamics of DABC and ensure reliable operation under large-amplitude external disturbances (e.g., pulsed-power loads), there is an urgent need to gain a thorough understanding of DABC's transient behaviour and its relation to the transient modulation scheme.

Although some optimized transient phase-shift modulation (OTPSM) strategies have been proposed for both NR-DABC and SR-DABC, they have their own drawbacks. This motivates our research to develop more generalized and high-performance transient phase-shift modulation schemes for achieving ultra-fast, dc-offset-free, and oscillation-free dynamics in DABC.

The main objectives of this thesis are summarized as follows:

(1) To better analyze and explain the causes of transient dc offsets generated in the magnetic elements of NR-DABC and HF transient oscillations generated in the resonant tank of SR-DABC.

(2) To investigate the fundamental relationships between various types of OTPSM schemes, and to attempt to establish a set of unified equations that can govern the existing schemes.

(3) To propose new and more advanced OTPSM strategies for both NR-DABC and SR-DABC, and to examine their effects on fast closed-loop controlled DABCs when they are implemented in a cycle-by-cycle manner.

(4) To compare the simulation and experimental results under different OTPSM strategies, and to find the optimal ones for NR-DABC and SR-DABC.

(5) To offer a systematic approach and design philosophy for developing OTPSM strategies, and to shed light on the general theory of optimizing the dynamics of DABC.

The ultimate goal of this thesis is to develop ideal transient modulation schemes that can realize smooth transition between different operating modes of DABCs. Such efforts can help DABC to achieve faster response and better transient performance, thus making the whole power conversion system more reliable and stable in practice.

1.5 Outline of the Thesis

This rest of this thesis is organized as follows:

In Chapter 2, several popular modulation and control strategies for DABC are reviewed systematically. Through this chapter, the roles of steady-state modulation, transient modulation, control algorithm, and their inner relationships are disclosed. Eventually, the research gaps related to achieving optimal dynamics of DABC are identified.

In Chapter 3, an optimal transient SPS modulation for NR-DABC which is capable of achieving zero transient dc offsets in both inductor current and transformer's magnetizing current is presented to guarantee the safety of circuit elements during transient stage. Moreover, this chapter attempts to demonstrate to the readers that the overall dynamics of NR-DABC can be further optimized by a co-optimization of an enhanced MPC (based on a more accurate transient power model) and OTPSM. In order to assess the effectiveness of the proposed transient modulation and control methods, various cases of open-loop and closed-loop experiments are conducted and the transient performances of different combinations of controllers and transient modulation strategies are effectively compared.

In Chapter 4, the analysis, design, and cycle-by-cycle implementation approach of a novel transient SPS modulation for suppressing transient oscillations in SR-DABC is presented. Accurate and efficient time-domain solution of the proposed modulation strategy is available. Its effectiveness is then confirmed by simulation and experimental tests under different open-loop and closed-loop conditions, and its performance is compared with CTPSM.

In Chapter 5, a generalized MPS transient modulation strategy is presented, which can simultaneously achieve fast, oscillation-free, and dc-offset-free dynamics in SR-DABC and NR-DABC. The design philosophy for developing OTPSM that can eliminate transient oscillations is fully discussed in this chapter. In addition, the design of MPS-modulation-based MPC and an automatic resonant-frequency detection method for SR-DABC are presented. Finally, all the proposed techniques are verified experimentally, and their effectiveness is demonstrated by comparison with the conventional schemes.

In Chapter 6, conclusions are drawn and a few suggestions for future research are provided. The main contributions of this thesis are also summarized.

Chapter 2

Overview of Existing Modulation and Control Strategies for Dual-Active-Bridge Converter

2.1 Introduction

Modulation and control strategies have different effects on the dynamic performance of DABC, and both play important roles in the analysis and design of closed-loop controlled DABC. In this chapter, various commonly used modulation and control strategies for DABC are reviewed, with particular emphasis on the basic concepts of OTPSM and MPC. The objectives of this chapter are to introduce general analysis methods and the core principle for controlling DABC; to illustrate the effectiveness of some advanced modulation and control strategies with a few examples; and to reveal some of the research topics.

2.2 Literature Review of Modulation Strategies

There is only one control variable for SPS modulation, i.e., the outer phase-shift angle between v_{ab} and v_{cd}. By introducing an inner phase-shift angle in the

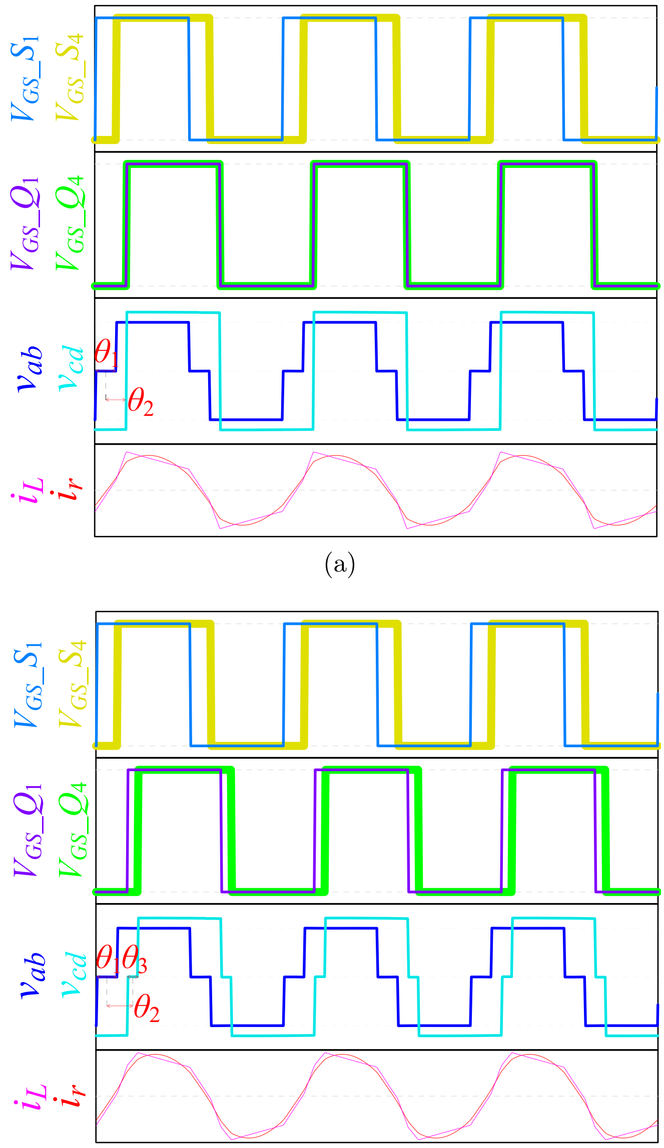

(a)

(b)

Fig. 2.1. Typical steady-state waveforms of NR-DABC and SR-DABC under DPS and TPS modulation schemes. (a) Steady-state waveforms under DPS modulation. (b) Steady-state waveforms under TPS modulation.

full-bridge converter, more degrees of freedom (DOF) can be employed to operate DABC. Hence, in addition to SPS modulation, there exists some multi-phase-shift (MPS) modulation schemes for DABC, including the dual phase-shift (DPS) [46]–[48] modulation and triple phase-shift (TPS) [49]–[54] modulation as shown in Figs. 2.1(a) and (b), respectively. Note that DPS modulation is also referred to as extended phase-shift (EPS) modulation in some literature [55]. In this thesis, DPS modulation employs only one inner phase-shift angle (i.e., either θ_1 or θ_3)

and an outer phase-shift angle (θ_2), while TPS modulation has two inner phase-shift angles (both θ_1 and θ_3) produced by the primary-side and secondary-side full-bridge converters, respectively. Hence, TPS modulation is the most general one among these commonly used phase-shift modulation strategies, as it has three DOF and both SPS modulation and DPS modulation can be regarded as two special cases of TPS modulation.

2.2.1 Optimized Steady-State Modulation Strategies for Improving Conversion Efficiency

Although SPS modulation is simple, the steady-state performance of SPS-modulated DABC is determined solely by one phase-shift angle, and hence it has limitations in current stress, ZVS range, backflow power, etc., at different converter gains and power levels, which cannot be further improved [56]. On the contrary, MPS modulation can provide flexibility to change the HF-link voltage and current waveforms of DABC (e.g., v_{ab} and v_{cd} may become three-level quasi-square waveforms), thus enhancing the steady-state performance and alleviating the limitations posed by SPS modulation. Typically, for a given power level, a variety of combinations of θ_1, θ_2, and θ_3 can be found under MPS modulation, and meanwhile these different combinations yield different steady-state modes and performances. For example, Fig. 2.2 shows six typical operation modes of NR-DABC under TPS modulation. Thus, the optimal phase-shift angles are the solutions for an optimization problem where the objective is generally to minimize the peak or root-mean-square (RMS) value of HF-link current of DABC while ensuring low or zero backflow power, wide-range ZVS operation, etc., thereby maximizing the overall efficiency [57]–[68]. The optimization problem can generally be handled via the method of Lagrange multipliers and Karush–Kuhn–Tucker (KKT) conditions [51], [57], particle swarm optimization (PSO) algorithm [62]–[64], genetic algorithm [65], artificial intelligence (AI) algorithm [66]–[68], etc., and researches

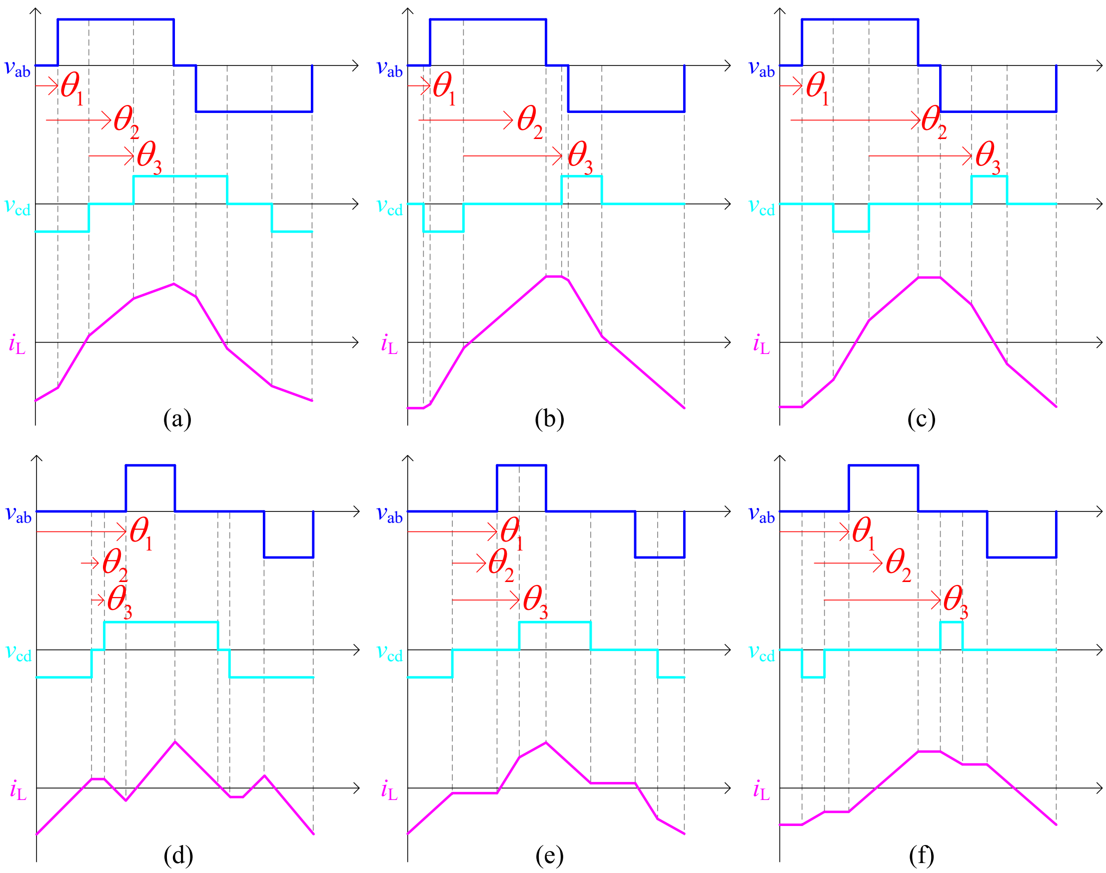

Fig. 2.2. Six operation modes of NR-DABC under TPS modulation.

on this topic are still evolving.

To further improve the steady-state performance of DABC, more recently, researchers have proposed some enhanced modulation schemes, such as asymmetrical pulse-width modulation [69]–[76] and variable-frequency modulation [77]–[82], which utilize the duty ratios and switching frequencies of gating signals as additional control variables to more effectively increase the waveform quality of DABC.

In addition, due to the inherent limitations of conventional DABC, it is still difficult or inconvenient to achieve wide-range high-efficiency operation even with those optimized steady-state modulation strategies. Thus, another promising research direction for offering excellent steady-state performance is to develop new topology variants of DABC. For example, Dr. K.H. Loo and his team proposed several resonant immittance-based topologies for both single-phase and three-phase DABCs [83]–[89], which can achieve full-range soft-switching, minimum conduction loss, and high-efficiency operation over a wide range of operating conditions. As a result, topologies and modulation strategies are both important factors for optimizing steady-state performance and should be considered collectively. Nevertheless, for any DAB-like topologies, the adopted modulation scheme basically determines the steady-state performance and conversion efficiency.

2.2.2 Optimized Transient Modulation Strategies for Eliminating Transient DC Offsets in NR-DABC

The aforesaid modulation strategies mainly contribute to the improvement in steady-state performance. When they are used without transient trajectory planning, any PWM generator that attempts to update large-amplitude phase-shift increments or decrements directly (i.e., in one step) in the manner of CTPSM are susceptible to the issues of transient dc offsets and/or oscillations. Transient modulation, which is generally designed for improving the dynamic performance of DABC, is different from steady-state modulation and has become an important and fast-growing research theme. It has significant impacts on the transient performance of DABC, as any required modifications in the HF-link current are eventually accomplished through a sequence of switching events.

For NR-DABC, the problem of transient dc offsets arises from the fact that any asymmetry in the inductor volt-second product will give rise to magnetic flux imbalance that induces dc offsets, and hence the directly-adjusted transient switching pattern under CTPSM will lead to a monotonic increase in the volt-second product or flux linkage of the inductor during transient state. In order to eliminate transient dc offsets in NR-DABC, various OTPSM strategies have been successfully proposed for both SPS-modulated NR-DABC [90]–[103] and MPS-modulated NR-DABC [104]–[108], which can achieve dynamic volt-second balance in the energy-transfer inductor. The main advantage of OTPSM strategies is the ability to directly update a large-amplitude phase-shift increment/decrement within about one switching cycle and to limit inductor current as a protective measure. Despite some minor differences in design, the common principle of the existing OTPSM strategies is to design specific switching sequences that can seamlessly modify the trajectory of inductor current during transient state. According to the analysis presented in [108], the transient dc-offset elimination under MPS modulation schemes can be realized through generating suitably designed square-wave voltage in each half-bridge leg of NR-DABC. Hence, the theories of OTPSM developed for SPS modulation will form the basis for developing more advanced OTPSM strategies based on MPS modulation.

A comprehensive review of the prior-art SPS modulation based OTPSM strategies [90]–[103] is presented in this thesis. According to their modulation characteristics and DOF, characterized in terms of the number of adjustable positive and negative pulse widths during transient state, they can be classified into six categories, i.e., Types $A \sim F$. Note that the numeric subscripts attached to the type names (e.g., number 1 in A_1) are used to define different subtypes. One simulation example of each type of OTPSM can be found in Fig. 2.3, where the red line segments are the transient pulses that need to be adjusted and the measured transient average value (TAV) of i_L or $i_m^{'}$ is also labeled. Note that in order to measure i_m, an additional inductor whose inductance is equal to the transformer's magnetizing inductance is connected across the transformer's primary terminal. By directly measuring the current through this additional inductor, i_m will be replaced with $i_m^{'}$ in some simulation and experimental tests of this thesis, where $i_m^{'} \approx 0.5 i_m$.

Type-A OTPSM [90]–[94] and Type-B OTPSM [94]–[96] strategies originate from the principle of relative motion. Specifically, two or three edges are selected from v_{ab} and v_{cd} to asymmetrically distribute the total required phase-shift adjustment in order to achieve the desired peak value of i_L corresponding to the new steady state. For example, in Fig. 2.3(a), the falling edge of v_{ab} and the rising edge

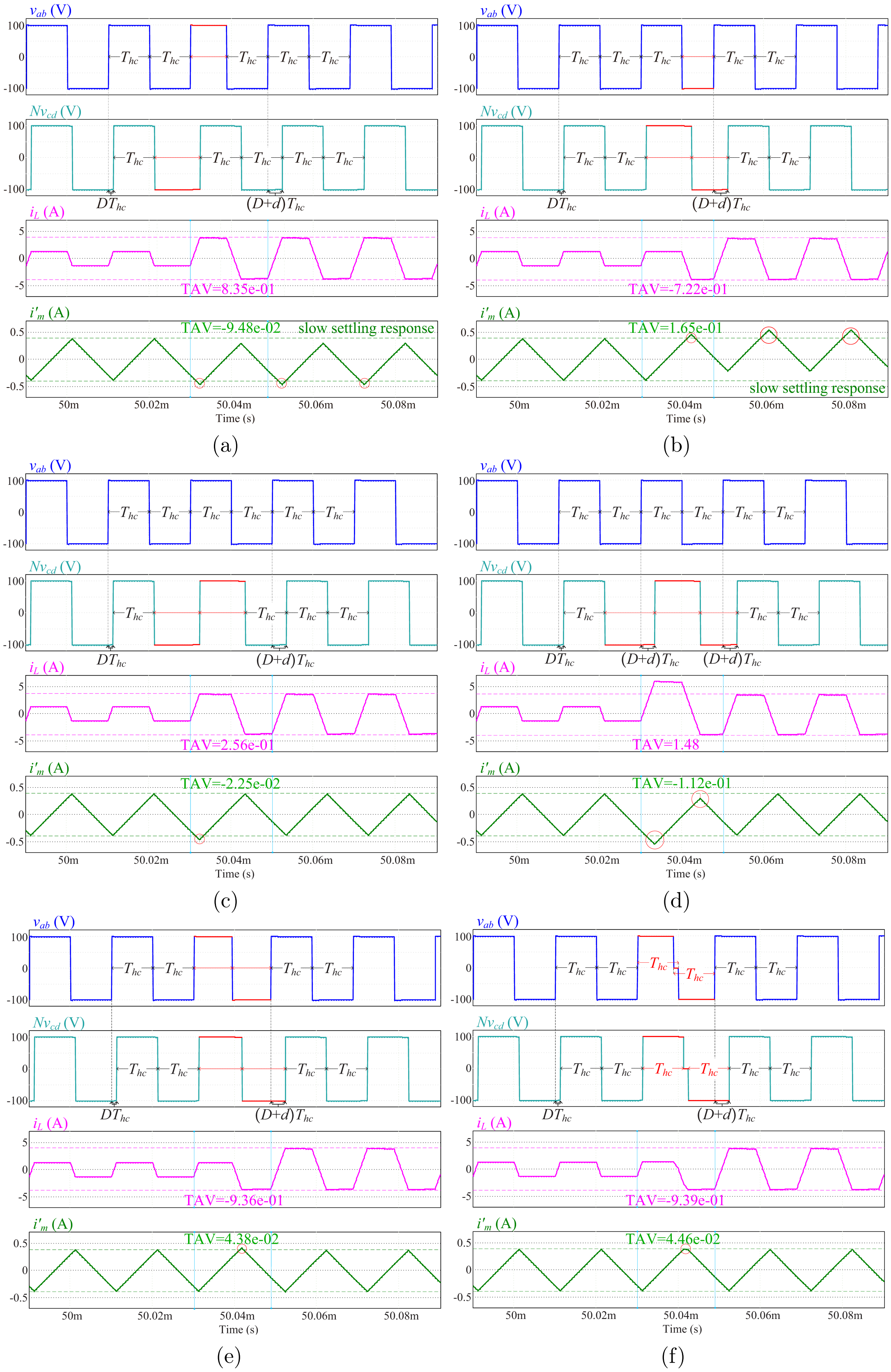

Fig. 2.3. Simulated open-loop transient response of NR-DABC under different types of OTPSM strategies ($D = 1/9$ and $d = 2/9$). (a) Type A_1 [90]. (b) Type B_1 [94]. (c) Type C_1 [97]. (d) Type D_1 [98]. (e) Type E_1 [100]. (f) Type F_1 [100].

of v_{cd} will move toward each other. However, as depicted in Figs. 2.3(a) (Type A_1 [90]) and (b) (Type B_1 [94]), although i_L can reach its new steady state within one switching cycle, excessive transient dc offset and long settling time are still exhibited by i_m, since the volt-second products on L_m under Type-A and Type-B OTPSM strategies are adjusted unevenly in resemblance to CTPSM. In addition, the transient pulse widths under these two types of OTPSM strategies are related to the voltage gain M of DABC, where $M = NV_2/V_1$. Hence, they are sensitive to converter parameters such as N, V_1, and V_2.

In contrast to the above two OTPSM strategies, the transient pulse widths of Type-C OTPSM [94],[97], Type-D OTPSM [98],[99], Type-E OTPSM [97],[100], and Type-F OTPSM [100]–[103] strategies are independent of M and determined only by the initial phase-shift ratio D and the phase-increment/decrement ratio d, and both i_L and i_m can reach their desired new steady states within one switching cycle. As exemplified in Figs. 2.3(c) (Type C_1 [97]), (d) (Type D_1 [98]), and (e) (Type E_1 [100]), Type-C and Type-E OTPSM strategies generate two equal-width transient pulses by consecutively moving two edges of v_{ab} and/or v_{cd}, while Type-D OTPSM strategies continuously generate three unequal-width transient pulses in v_{cd}. Unlike the other types of OTPSM strategies, as exemplified in Fig. 2.3(f) (Type F_1 [100]), Type-F OTPSM introduces zero-voltage durations into v_{ab} and/or v_{cd} during transient state, so that v_{ab} and/or v_{cd} become three-level voltages and the diagonal switches should be phase-shifted, which increases the complexity of its implementation. Unfortunately, according to the simulation results presented in Fig. 2.3, it should be specially noted that all Type-C to Type-F OTPSM strategies can lead to overshoots/undershoots in i_m, and the average values of both i_L and i_m during transient state are not zero.

In summary, although the settling time of i_L and/or i_m can be shortened by existing OTPSM strategies, due to their inherent design limitations, all of these strategies are unable to achieve zero dc offsets in both i_L and i_m during transient state. As a result, the adverse effects induced by transient dc offsets cannot be effectively mitigated by such existing OTPSM strategies, when they are implemented in a cycle-by-cycle manner. Eventually, since the non-zero transient dc offsets can appear at i_2 and I_o, the transient performance of closed-loop controlled NR-DABC will be degraded.

2.2.3 Optimized Transient Modulation Strategies for Eliminating Transient Oscillations in SR-DABC

The complex nonlinear dynamic behavior of SR-DABC is an interesting phenomenon. In order to overcome the issues associated with HF transient oscillations in SR-DABC, only a few studies have been conducted to investigate various control and modulation schemes. In [38], a dual-loop compensator is designed based on a small-signal model developed for SR-DABC. However, this study only suggests to select the controller's bandwidth to be much lower than the beat frequencies, which inevitably leads to slow transient responses. Hence, the methods based on classical control theory cannot provide satisfactory solutions against beat-frequency oscillations.

It is reasonable to believe that well-designed transient switching patterns can also modify the transient trajectories of resonant waveforms in DABSRC. However, due to the inherent differences in circuit characteristics, none of the OTPSM strategies developed for NR-DABC can be applied to suppress the transient oscillations in SR-DABC completely. This is because, unlike the piecewise-linear inductor current in NR-DABC that can directly reach a specific value by linearly adjusting the turn-on and turn-off pulse widths of some power switches, the trajectory of the non-linear resonant current in SR-DABC cannot be easily modified to follow the changes in pulse durations instantaneously due to the inertia of the resonant tank. Consequently, a challenging research topic is how to effectively and accurately modify the transient trajectories of resonant currents and voltages of

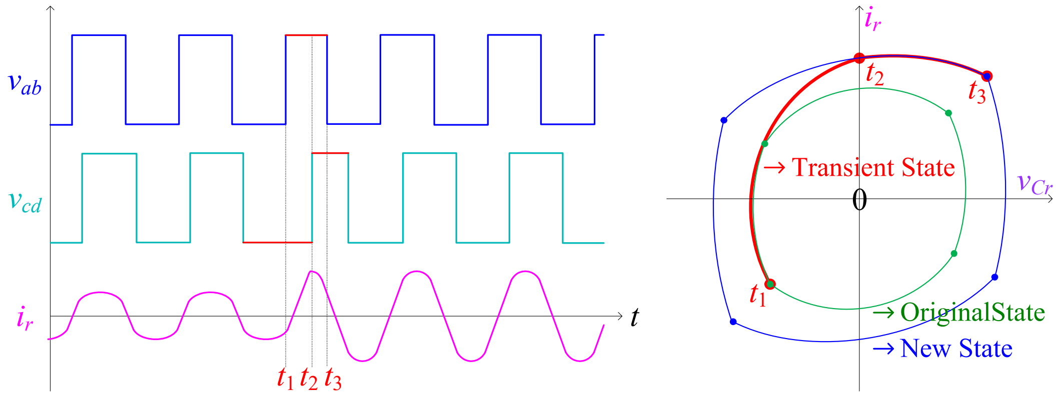

Fig. 2.4. Principle diagram of a trajectory-prediction-based transient modulation strategy for SR-DABC [109].

SR-DABC.

Recently, four OTPSM strategies were proposed in [109]–[111] for eliminating transient oscillations of SR-DABC, and they can actively modify the transient trajectory of resonant current as illustrated in Fig. 2.4. The core principle of these approaches is to determine appropriate switching events using complex trajectory-constrained equations. Unfortunately, closed-form expressions of their modulation laws are not available. In addition, similar to the majority of existing state-plane-trajectory control approaches developed for other resonant topologies [112]–[117], one typical disadvantage is that they require rich feedback information and several high-bandwidth sensors for trajectory planning and computation, which makes them difficult and expensive to implement, as well as sensitive to noise and measurement errors. Collectively, the previous OTPSM strategies for SR-DABC are not desirable due to the high complexity of their modulation laws, and research on this topic is still limited. The problem of transient oscillations in SR-DABC must be mitigated by designing simple and easy-to-implement transient modulation methods.

2.3 Literature Review of Control Strategies

In the previous subsection, the positive effects of OTPSM strategies on the dynamics of DABC are introduced. Although transient modulation design is important, when improving converter's transient performance, a general consideration is almost invariably the feedback control design. The commonly-used control strategies for DABC are proportional-integral (PI) based single-loop voltage control [118] and dual-loop current control [119], [120]. Although the small-signal dynamic models established in [121]–[123] can aid in tuning the PI-control parameters, the interaction between the two tuning parameters makes it challenging to simultaneously achieve fast and stable performance over the whole operating range.

In order to meet the requirements of fast load changes, feed-forward control can be combined with feedback control. In [124], a lookup table is used to decouple the complex non-linear relationship between phase-shift angle and load current, thereby implementing a fast feed-forward compensation for the next switching cycle. However, its control performance relies on the difference between actual and nominal circuit parameters. Another feed-forward control method known as virtual direct power control [125] has proven to be effective in cancelling the effects of circuit parameters, but its performance degrades significantly at light-load conditions.

Instead of using pre-calculated data like [124], the feed-forward control law can be further simplified by peak-current-mode control [126], [127] and current-mode feed-forward control [128], [129] solutions. They can respond to large-amplitude disturbances rapidly and actively clamp the envelope of the HF-link waveform of DABC without introducing excessive transient dc offsets and oscillations. Nevertheless, they are not desirable solutions because the inductor current of NR-DABC (or resonant current of SR-DABC) must be sampled by costly high-bandwidth sensors at a high sampling rate (i.e., at least twice the switching frequency). As a result, the usefulness of such approaches is rather restricted, especially in HF-operated DABCs. This problem also exists in some similar control techniques such as natural-switching-surface based boundary control [130] and deadbeat current control [131].

To address the limitations posed by conventional control schemes, some advanced controllers that have been successfully implemented previously including disturbance-observer-based controller [132], [133], sliding-mode controller [134], MPC [9], [41]–[45], etc. Among them, MPC has been extensively studied in both NR-DABC [9], [41]–[43] and SR-DABC [44], [45] due to its outstanding dynamic performance and ease of use. Compared with pure PI controllers, its response time and output voltage fluctuation can be significantly reduced. However, in exchange for fast transient response, the controller gain and bandwidth of MPC must be increased. Thus, the control variable (i.e., phase-shift angle) will undergo large-magnitude changes during transient state. Typically, under CTPSM, the higher the controller gain is, the larger the transient dc offsets and oscillations become. In order to limit the peak inductor/resonant current within a tolerance band, practical fast controllers are often integrated with specified constraint conditions or anti-windup design. For example, in [42], an additional constraint on the inductor current of NR-DABC is imposed by the MPC algorithm, but this inevitably shrinks the controller's bandwidth. Consequently, fast dynamics cannot be fully realized with MPC+CTPSM, and new fast control scheme needs to be devised.

2.4 Chapter Summary

The transient modulation approach and controller design both have impacts on DABC's dynamics. However, it can be found from recent overview studies [135], [136] that DABC's dynamics have been improved mostly as a result of advanced controller design. In these cases, the negative impacts of unsuitable transient modulation schemes under closed-loop conditions have been overlooked. As a result, enhancing the controller's performance alone without co-optimizing the transient phase-shift modulation method makes it difficult to achieve optimal dynamic performance. Unfortunately, the role of transient modulation on closed-loop controlled DABC remains unexplored and hence little understood, and most previous studies do not simultaneously take these two factors (i.e., controller and transient modulation) into account. Besides, the previous research has seldom examined possible solutions that can appropriately overcome the contradiction between fast control and transient dc offsets and oscillations in closed-loop controlled DABC without sensing the HF-link current. In light of the above, a promising direction is to integrate a fast controller (e.g., MPC) with a sensorless OTPSM strategy, such that the potential risk of modulation-induced dc offsets and oscillations in fast closed-loop controlled DABC can be mitigated without measuring the inductor/resonant current and the aforesaid limitations of MPC+CTPSM can also be overcome.

Although existing OTPSM techniques can assist to enhance DABC's dynamics, they have a number of significant limitations:

(1) Previous research neglected to investigate the underlying links between different types of OTPSM schemes, resulting in the development of several variants of similar methodologies.

(2) The existing OTPSM strategies for NR-DABC cannot achieve complete transient dc-offset elimination, as the average values of both the inductor current and transformer's magnetizing current are still non-zero during transient state. In addition, transient overshoots or undershoots can be observed in transformer's magnetizing current.

(3) Owing to the high implementation complexity of dynamically applying

existing OTPSM strategies in the PWM generator, their effectiveness is not yet verified in a fast closed-loop controlled DABC. As can be observed from the simulation and experimental results in almost all of these previous studies except [100], most of the existing OTPSM strategies have only been validated in open-loop conditions, in which case these strategies only need to be executed once rather than on a cycle-by-cycle basis, and hence their transient pulse widths must be pre-defined or pre-calculated. However, it is well understood that it is difficult or even impossible to reach a new steady state within only one switching cycle in a real-time closed-loop controlled DABC, particularly under large-amplitude disturbances. As external load disturbances are often uncertain, the practical usefulness of these previous methods when implemented in closed-loop systems is limited.

(4) A much-debated question is whether such OTPSM strategies can truly bring about positive effects on improving the dynamics of closed-loop controlled DABC. The OTPSM strategy proposed in [100] was verified with a single-loop voltage-mode PI controller. In order to demonstrate the benefit of the use of OTPSM, the gain of PI controller has to be significantly increased for generating large step changes in phase-shift ratio. However, a pure PI controller typically suffers from the trade-off between response time and stability margins. As demonstrated in [100], the results under a high-bandwidth PI controller plus OTPSM remained unsatisfactory, and the converter tended to become unstable under PI controller plus CTPSM due to a small stability margin. This implies that the combined use of OTPSM with a PI controller cannot fully deliver the anticipated dynamic performance, and such low-gain linear controllers are not effective to be used with OTPSM.

Overall, the effectiveness of OTPSM strategies when applied to fast closed-loop controlled DABC is not verified. The inadequacy of using a PI controller in realizing the full potential of OTPSM strategies is evident but its replacement by other more advanced high-gain controllers such as a MPC remains largely under-explored, thus preventing OTPSM from realizing its full benefits. More research is required to develop simple and effective OTPSM strategies for closed-loop controlled NR-DABC and SR-DABC.

Chapter 3

Optimal Transient Single-Phase-Shift Modulation for Transient DC-Offset Elimination

3.1 Introduction

As explained in Section 2.2.2, existing OTPSM techniques developed for NR-DABC have demonstrated limitations in their capability to realize zero transient dc offsets. Hence, to totally eliminate the transient dc offsets and make it more feasible for closed-loop controlled NR-DABC, a new OTPSM method is required.

By investigating the inherent operating principles of OTPSM, this chapter develops a set of unified equations governing essentially all the existing OTPSM strategies for SPS-modulated NR-DABC, and proposes a new sensorless method known as symmetric single-sided OTPSM (SS-OTPSM). To assess the validity of SS-OTPSM under closed-loop conditions, various combinations of transient modulation methods and MPCs are compared systematically and experimentally. The benefits of the proposed SS-OTPSM and the key contributions of this chapter are outlined below:

(1) It can completely eliminate the transient dc offsets in both inductor current and transformer's magnetizing current simultaneously, thus minimizing their negative effects on the dynamics of NR-DABC.

(2) It exhibits a significantly better performance in terms of transient dc-offset elimination capability in all open-loop cases.

(3) Benefiting from its symmetrical transient switching patterns, it is easy to implement SS-OTPSM in a cycle-by-cycle manner, thus facilitating its closed-loop realization and making it highly practical over other existing OTPSM strategies.

(4) An enhanced model predictive controller (EMPC), which is designed to be compatible with SS-OTPSM, is proposed to achieve optimal (i.e., ultra-fast and completely dc-offset-free) dynamics of NR-DABC.

The rest of this chapter is organized as follows. Section 3.2 derives the equivalent circuit and power transfer model of DABC. The principle of the proposed SS-OTPSM strategy is presented in Section 3.3. Section 3.4 presents the design of the proposed EMPC algorithm. Experimental results are shown in Section 3.5 to verify the performance of the proposed SS-OTPSM and EMPC, and conclusions are drawn in Section 3.6.

3.2 Equivalent Circuit and Power Transfer Model of NR-DABC

Fig. 3.1 shows the primary-referred equivalent circuits of NR-DABC. Fig. 3.1(a) represents an ideal NR-DABC, where the magnetizing inductance is assumed to be much larger than the total equivalent series inductance $L = L_p + N^2 L_s$, while Fig. 3.1(b) includes L_m by adopting the transformer's T equivalent model (T-model).

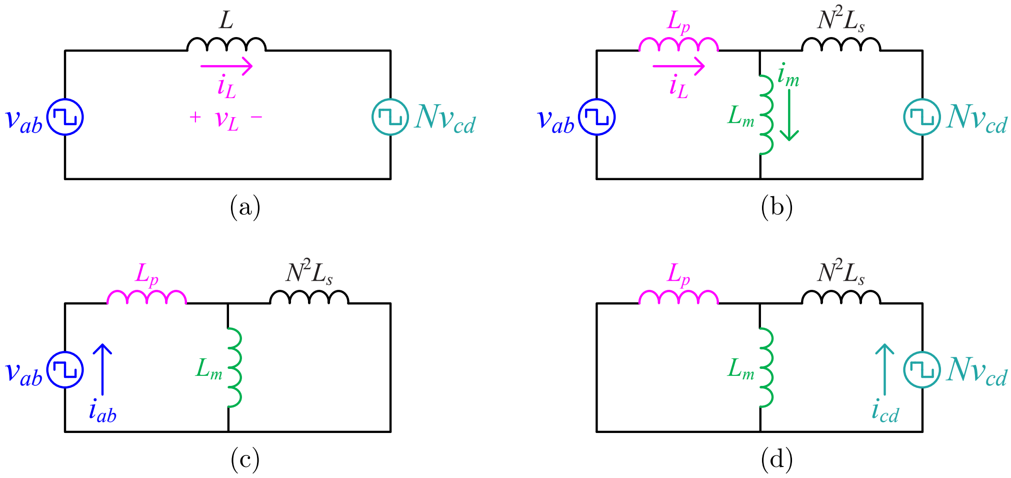

Fig. 3.1. Primary-referred equivalent circuits of NR-DABC. (a) Ideal equivalent circuit. (b) T-model equivalent circuit. Applying superposition principle. (c) Individual contribution due to v_{ab}. (d) Individual contribution due to Nv_{cd}.

Applying superposition principle to Fig. 3.1(b) gives Figs. 3.1(c) and (d). Thus, i_L and i_m can be expressed as

$$i_L = i_{ab} - \frac{L_m}{L_m + L_p} i_{cd} \tag{3.1}$$

$$i_m = \frac{N^2 L_s}{L_m + N^2 L_s} i_{ab} + \frac{L_p}{L_m + L_p} i_{cd} \tag{3.2}$$

where i_{ab} and i_{cd} are the current contributions due to each independent source (v_{ab} or v_{cd}) acting alone. This implies that i_L and i_m are functions of i_{ab} and i_{cd}, and their waveforms can be determined by applying superposition and analyzing the single-source equivalent circuits in Figs. 3.1(c) and (d). In general, $L_m \gg L_p$, and thus, (3.1) can be approximated as

$$i_L \approx i_{ab} - i_{cd}. \tag{3.3}$$

The average power transferred to the output/load can be computed from

$$P = \frac{1}{2T_{hc}} \int_0^{2T_{hc}} v_{ab}(t) i_L(t) \mathrm{d}t \approx \frac{NV_1V_2T_{hc}D(1-D)}{L} \tag{3.4}$$

where T_{hc} is one-half of the switching period and $D = \theta/\pi$ is the phase-shift ratio. It should be pointed out that (3.4) represents the ideal power transfer model, which does not consider dead-time effect which could lead to phase-shift error

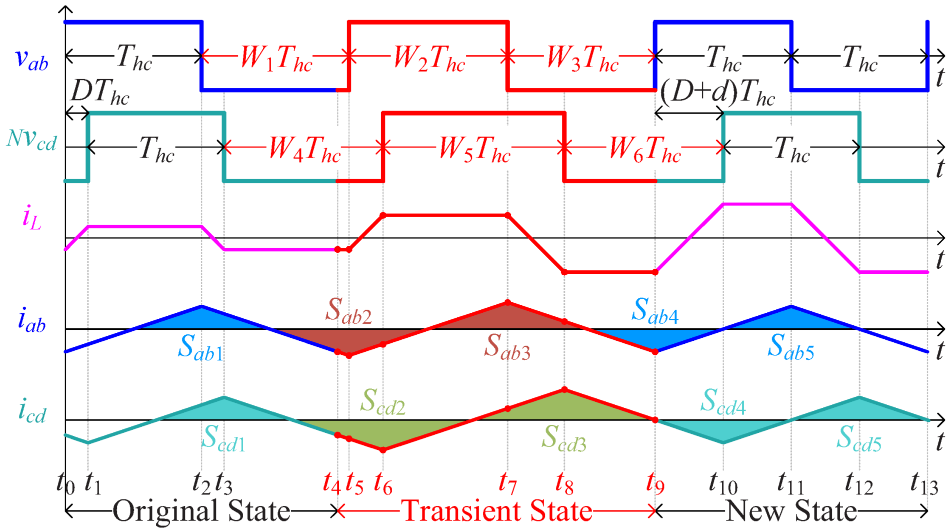

Fig. 3.2. Unified framework of OTPSM strategies for NR-DABC.

particularly at light load [137]. In addition, according to the study presented in [138], dead-time compensation methods can be easily integrated with OTPSM strategies, if necessary. Furthermore, the error in phase-shift ratio induced by dead-time effect can be automatically compensated by a closed-loop controller. Hence, dead-time effect is neglected in the following discussion.

3.3 Proposed Symmetric Single-Sided OTPSM (SS-OTPSM) Strategy for NR-DABC

The transmission power P given in (3.4) is a function of phase-shift ratio D. When P (or D) of NR-DABC is required to be changed, inappropriate transient modulation strategies (e.g., CTPSM) can lead to non-zero transient dc offsets in both the inductor current and transformer's magnetizing current. For this reason, CTPSM is undesirable and should be replaced by more advanced and appropriately designed OTPSM strategies.

3.3.1 Dynamic Volt-Second Balance

Section 2.2.2 has shown that the basic operation of Type-A to Type-E OTPSM strategies for NR-DABC is characterized by appropriately adjusting some of the positive and negative pulse widths of the two-level voltages (v_{ab} and v_{cd}) during transient state for meeting the dynamic volt-second balance requirement in the series inductor. To achieve this, as can be found from Fig. 3.2, there are in fact up to six transient pulse-width ratios, i.e., $W_1{\sim}W_6$, which can be manipulated in the waveforms of v_{ab} and v_{cd}.

Once the transient trajectory of i_L is successfully modified (by modulating $W_1{\sim}W_6$) to reach its new steady-state trajectory, i_L will enter and remain in the new periodic steady state indefinitely until the next transient event occurs. Typically, for all the previously mentioned OTPSM strategies, i_L will reach its new steady state in about one switching cycle, i.e., no later than t_9. This means that the problem encountered in designing OTPSM is to find the closed-form solutions for $W_1{\sim}W_6$ that will satisfy the boundary conditions at t_9:

- *Constraint* ①: The phase-shift ratio between the rising edges of v_{ab} and v_{cd} must be equal to $D + d$ at the end of the transient state, i.e., the time interval $t_{10} - t_9 = (t_{10} - t_0) - (t_9 - t_0) = (D + 1 + W_4 + W_5 + W_6)T_{hc} - (1 + W_1 + W_2 + W_3)T_{hc}$ should be equal to $(D + d)T_{hc}$. Hence,

$$W_1 + W_2 + W_3 + d = W_4 + W_5 + W_6. \tag{3.5}$$

- *Constraint* ②: The end point of the transient state is the initial point of the new steady-state cycle. Hence,

$$i_L(t_9) = i_L(t_{13}). \tag{3.6}$$

In general, the key objective of OTPSM is to determine the solution sets for the unknown modulation parameters $W_1{\sim}W_6$ based on the above two constraints.

Referring to [90], the boundary values of i_L in the original steady state (from

t_0 to t_4) and new steady state (from t_9 to t_{13}), namely, $i_L(t_0)$, $i_L(t_4)$, and $i_L(t_{13})$, are given by

$$i_L(t_0) = i_L(t_4) = -\frac{T_{hc}}{2L}[V_1 + (2D-1)NV_2] \tag{3.7}$$

$$i_L(t_{13}) = -\frac{T_{hc}}{2L}[V_1 + (2(D+d)-1)NV_2]. \tag{3.8}$$

From the voltage-current relationship of the equivalent series inductor L, i.e., $L\frac{di_L(t)}{dt} = v_L = v_{ab} - Nv_{cd}$, where v_L is the equivalent series inductor voltage, the intermediate values of i_L in the time interval $[t_4,\, t_9]$ can be obtained as

$$\begin{cases} i_L(t_5) &= i_L(t_4) + \frac{NV_2-V_1}{L}(t_5-t_4) \\ i_L(t_6) &= i_L(t_5) + \frac{V_1+NV_2}{L}(t_6-t_5) \\ i_L(t_7) &= i_L(t_6) + \frac{V_1-NV_2}{L}(t_7-t_6) \\ i_L(t_8) &= i_L(t_7) - \frac{V_1+NV_2}{L}(t_8-t_7) \\ i_L(t_9) &= i_L(t_8) + \frac{NV_2-V_1}{L}(t_9-t_8). \end{cases} \tag{3.9}$$

As can be observed from Fig. 3.2, the duration of transient process $[t_4,\, t_9]$ can be divided into five time intervals:

$$\begin{cases} t_5-t_4 &= (W_1-1)T_{hc} \\ t_6-t_5 &= (W_4-W_1+D)T_{hc} \\ t_7-t_6 &= (W_1+W_2-W_4-D)T_{hc} \\ t_8-t_7 &= (W_4+W_5-W_1-W_2+D)T_{hc} \\ t_9-t_8 &= (W_1+W_2+W_3-W_4-W_5-D)T_{hc}. \end{cases} \tag{3.10}$$

Substituting (3.7) and (3.10) into (3.9) gives

$$\begin{aligned} i_L(t_9) =& \frac{T_{hc}}{2L}[(1-2W_1+2W_2-2W_3)V_1 \\ &+(2W_1+2W_2+2W_3-4W_5-1-2D)NV_2]. \end{aligned} \tag{3.11}$$

To satisfy (3.6) (*Constraint* ②), let (3.8) be equal to (3.11), which results in

$$\begin{aligned} 0 =& (2 - 2W_1 + 2W_2 - 2W_3) \\ &+ (2W_1 + 2W_2 + 2W_3 - 4W_5 - 2 + 2d)M. \end{aligned} \tag{3.12}$$

A combination of (3.5) and (3.12) forms the general solution of OTPSM for NR-DABC. In theory, any solution set that can simultaneously satisfy (3.5) and (3.12) will make i_L reach a new steady state within one cycle. It can be verified that all Type-A to Type-E OTPSM strategies fulfill these two equations. However, (3.12) implies that if $W_1 \sim W_6$ cannot be completely decoupled from M, the transient pulse widths will be adversely affected by the noise and measurement errors in M. As has been pointed out in Section 2.2.2, Type-A and Type-B OTPSM strategies are prone to such problems.

To eliminate the dependence of M, both terms on the right-hand side of (3.12) should be zero. Hence,

$$\begin{cases} 1 + W_2 = W_1 + W_3 \\ W_1 + W_2 + W_3 + d = 1 + 2W_5. \end{cases} \tag{3.13}$$

Then, substituting (3.5) into (3.13) gives

$$\begin{cases} 1 + W_2 = W_1 + W_3 \\ 1 + W_5 = W_4 + W_6 \\ 2W_2 + d = 2W_5. \end{cases} \tag{3.14}$$

Since the relationships between $W_1 \sim W_6$ described by (3.14) are decoupled from M, (3.14) represents a general solution that can be used for developing sensorless (i.e., without being affected by M) OTPSM strategies. It is found that all Type-C to Type-E OTPSM strategies can be obtained as particular solutions of (3.14).

Equivalently, from the viewpoint of volt-second balance, the transient dc offset is resulted from imbalanced voltage-second product [94], [108]. Hence, if the magnetic fluxes of the series inductor L and magnetizing inductance L_m can be reset during transient state, the average values of the voltages across both L and L_m will be zero. By using superposition principle, the algebraic sums of the volt-second products caused by v_{ab} (in the time interval from t_0 to t_9) and v_{cd} (in the time interval from t_1 to t_{10}) should be individually equal to zero, that is

$$\begin{cases} V_1T_{hc}-V_1W_1T_{hc}+V_1W_2T_{hc}-V_1W_3T_{hc}=0 \\ NV_2T_{hc}-NV_2W_4T_{hc}+NV_5W_2T_{hc}-NV_2W_6T_{hc}=0. \end{cases} \tag{3.15}$$

Simplifying (3.15) and combining the result with (3.5) also leads to (3.14), which verifies that the fundamental principle of OTPSM is to establish a dynamic volt-second balance, i.e., the algebraic sum of the variations in the volt-second product of an inductor during transient state should be zero [94]. However, as can be observed from Fig. 2.3, even if a dynamic volt-second balance of both L and L_m is achieved under Type-C to Type-E OTPSM strategies, transient dc offsets still exist in i_L and i_m. This suggests that the dynamic volt-second balance is only a partial, i.e., necessary but not sufficient, condition required for eliminating transient dc offsets in both i_L and i_m. This condition can only guarantee that i_L and i_m will enter into their new steady states from t_9, i.e., within one cycle, but it cannot guarantee that their dc offsets during transient state are zero.

3.3.2 Complete Elimination of Transient DC Offsets

Note that previous studies have failed to demonstrate the effectiveness of their modulation methods in a strictly closed-loop controlled NR-DABC. Hence, the main objective of their designs is often merely to achieve dynamic volt-second balance in one switching cycle, and they have failed to completely eliminate transient dc offsets. According to (3.1) and (3.2), if the average values of i_{ab} and i_{cd} are zero during transient state (i.e., the transient waveforms of i_{ab} and i_{cd} are symmetrical about the time axis), no dc offsets will be produced in both i_L and i_m, which, in fact, is a necessary and sufficient condition for eliminating all transient dc offsets. More specifically, the integral values of i_{ab} and i_{cd} over the transient period should be zero. In other words, those shaded areas in Fig. 3.2 are required to satisfy:

$$\begin{cases} S_{ab1} = S_{ab4} = S_{ab5} \\ S_{ab2} = S_{ab3} \\ S_{cd1} = S_{cd4} = S_{cd5} \\ S_{cd2} = S_{cd3} \end{cases} \tag{3.16}$$

Solving (3.16) gives

$$\begin{cases} W_1 = W_3 \\ W_4 = W_6. \end{cases} \tag{3.17}$$

Combining (3.14) and (3.17) gives a more general and universal solution (3.18) that guarantees the elimination of dc offsets in both i_L and i_m during transient state.

$$\begin{cases} W_1 = W_3 = (1 + W_2)/2 \\ W_4 = W_6 = (1 + W_5)/2 \\ 2W_2 + d = 2W_5 \end{cases} \tag{3.18}$$

Although it is possible to derive various OTPSM strategies from (3.18), single-sided modulation is typically more attractive to engineers in practice due to simplicity, ease of implementation, and low hardware cost. When the pulse width of either v_{ab} or v_{cd} is set to a constant value of T_{hc}, there exist two simple particular solutions of (3.18), namely,

Type-I SS-OTPSM (v_{cd} *is unmodulated*):

$$\begin{cases} W_1 = W_3 = 1 - \frac{d}{4} \\ W_2 = 1 - \frac{d}{2} \\ W_4 = W_5 = W_6 = 1 \end{cases} \tag{3.19}$$

Type-II SS-OTPSM (v_{ab} *is unmodulated*):

$$\begin{cases} W_1 = W_2 = W_3 = 1 \\ W_4 = W_6 = 1 + \frac{d}{4} \\ W_5 = 1 + \frac{d}{2} \end{cases} \tag{3.20}$$

From (3.19) and (3.20), the algorithm implementation of SS-OTPSM is independent of any converter parameters and requires only the phase-shift increment or decrement d which is directly available from the controller; hence it requires no external sensing, i.e., being a sensorless solution, and can be implemented at low cost and low hardware complexity. When substituting $d=0$ into (3.19) and (3.20), $W_1 \sim W_6$ become 1, and hence SS-OTPSM is naturally compatible with conventional SPS modulation at steady state. It should be noted that, although the mathematical derivations of (3.19) and (3.20) are presented for the case of power increment ($d > 0$), i.e., increase in phase-shift ratio, the same equations are applicable to the case of power decrement ($d < 0$), i.e., decrease in phase-shift ratio. In addition, both Type-I and Type-II SS-OTPSM strategies do not distinguish between two power flow directions, and hence (3.19) and (3.20) are applicable to all cases of power flow conditions and each case will be simply treated as a case of increasing/decreasing power (or phase-shift ratio).

3.3.3 Performance and Implementation of SS-OTPSM

Fig. 3.3 presents the open-loop simulations under CTPSM, Type-I SS-OTPSM, and Type-II SS-OTPSM. Compared to CTPSM and the results of other OTPSM strategies presented in Fig. 2.3, the transient waveforms of i_L and i_m under both SS-OTPSM strategies show better symmetry due to the complete elimination of all transient dc offsets. By zooming out the transient waveforms under Type-I SS-OTPSM, as shown in Fig. 3.3(c), the transient peaks are significantly reduced. However, two small but detectable transient peaks can be observed in i_m in Fig.

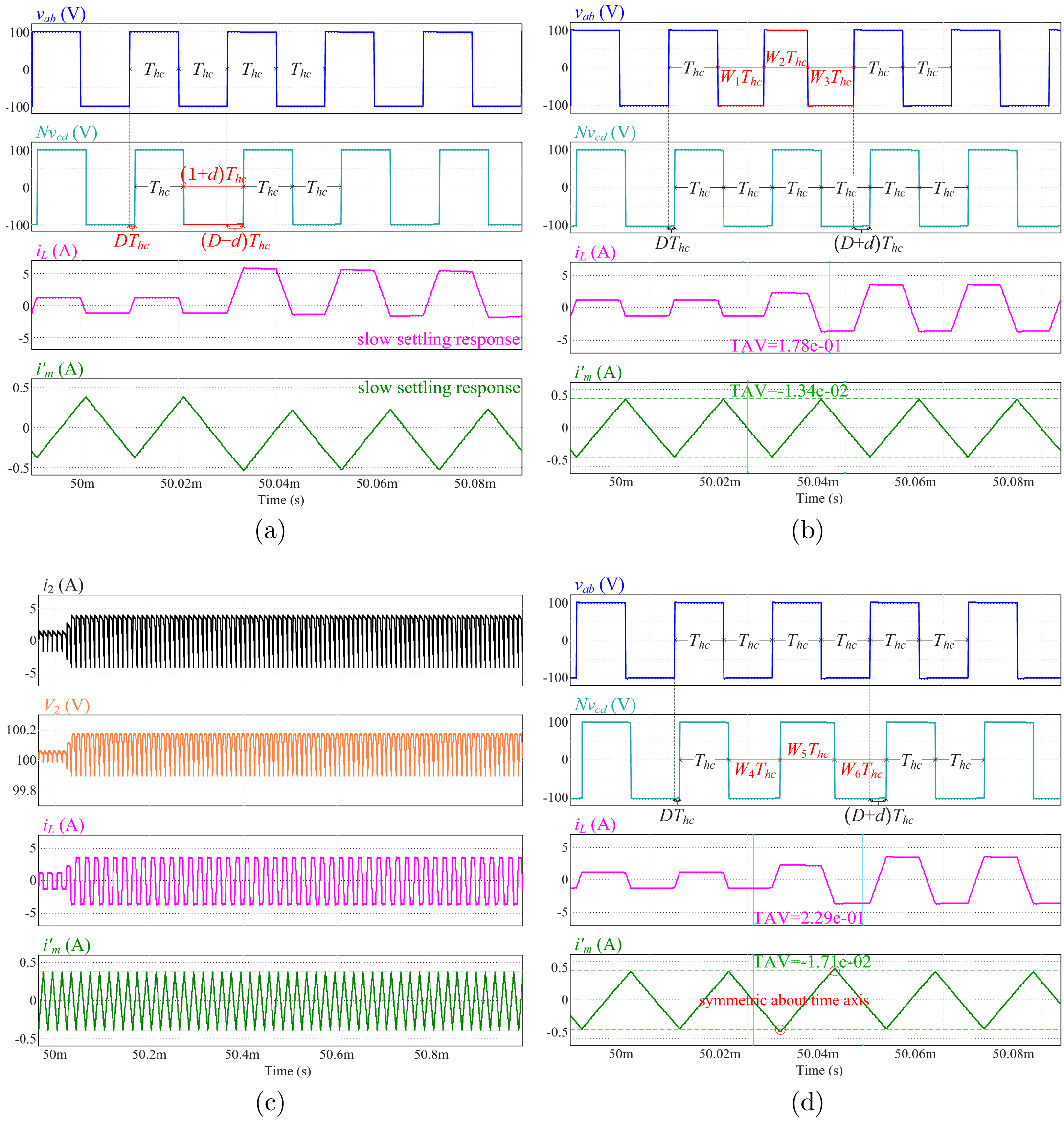

Fig. 3.3. Simulated open-loop transient response for an increase in the phase-shift ratio from $\frac{1}{9}$ to $\frac{1}{3}$ under CTPSM and SS-OTPSM strategies. (a) Transient waveforms under CTPSM. (b) Transient waveforms under Type-I SS-OTPSM. (c) Zoomed-out transient waveforms of i_2, V_2, i_L, and i_m under Type-I SS-OTPSM. (d) Transient waveforms under Type-II SS-OTPSM. The simulation parameters are as follows: $f_s = 50$ kHz, $V_1 = 100$ V, $V_2 = 100$ V, $L_p = 92$ μH, $L_s = 1.70$ μH, and $L_m = 650$ μH.

3.3(d), although the overall waveform remains symmetrical as a result of the elimination of transient dc offsets. It can be analyzed from (3.1) and (3.2) that i_{ab} and i_{cd} are equally important in determining i_L ($L_m \gg L_p$), while i_{cd} plays a more significant role in i_m since the secondary-side leakage inductance L_s can be neglected in most practical applications of NR-DABC. Therefore, any changes in v_{cd}

can lead to overshoots/undershoots and noticeable transient waveform changes in i_m, as shown in Figs. 2.3, 3.3(a), and 3.3(d). This observation reflects that (3.19), i.e., Type-I SS-OTPSM, which shows no such transient peaks (see Fig. 3.3(b)) is deemed more attractive for practical applications. For this reason, Type-I SS-OTPSM is selected as the default modulation scheme in the following discussion of SS-OTPSM. Furthermore, Fig. 3.4 shows the open-loop simulation results under different circuit parameters from those employed in Fig. 3.3. The findings demonstrate that Type-I SS-OTPSM is always effective to eliminate transient dc offsets of NR-DABC even when the parameters such as V_1 and L_p are changed, i.e., (3.19) is insensitive to the variation of system parameters except d.

The performances of various OTPSM strategies for NR-DABC are compared in Fig. 3.5 in a normalized form. The normalized percentages of improvement of different OTPSM strategies are obtained by computing the relative improvements with respect to CTPSM, where the data are summarized from Figs. 2.3 and 3.3. The abbreviations for the performance measurements are defined as follows: 1) PM1 – The maximum overshoot (or undershoot) of the positive (or negative) peak amplitude of the transient waveform of i_L; 2) PM2 – The absolute value of the dc offset (or average value) of i_L over the first transient cycle for open-loop tests, or the first five transient cycles for closed-loop tests; 3) PM3 – The maximum overshoot (or undershoot) of the positive (or negative) peak amplitude of the transient waveform of $i_m^{'}$; 4) PM4 – The absolute value of the dc offset (or average value) of $i_m^{'}$ over the first transient cycle for open-loop tests, or the first five transient cycles for closed-loop tests. It can be seen that Type-I SS-OTPSM performs the best in all four key aspects. The main features of different OTPSM strategies are summarized and listed in Table 3.1. It can be verified that all types of modulation strategies except Type-F OTPSM can be formulated by using (3.12) and (3.5), while Type-C to Type-E OTPSM and SS-OTPSM strategies can also be formulated by using (3.14). The expressions for the SS-OTPSM strategies, i.e.,

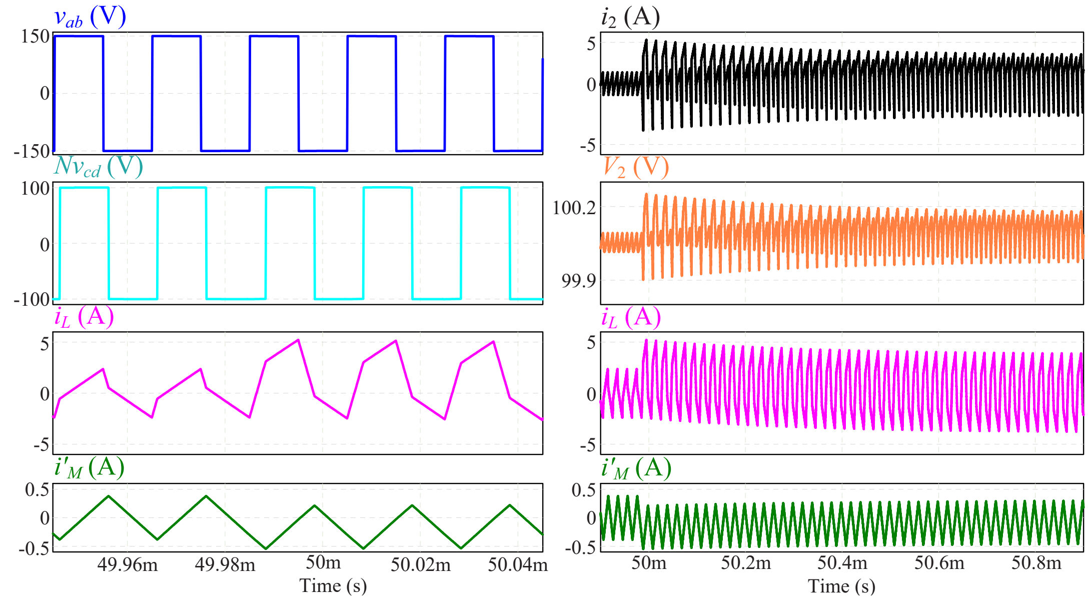

(a)

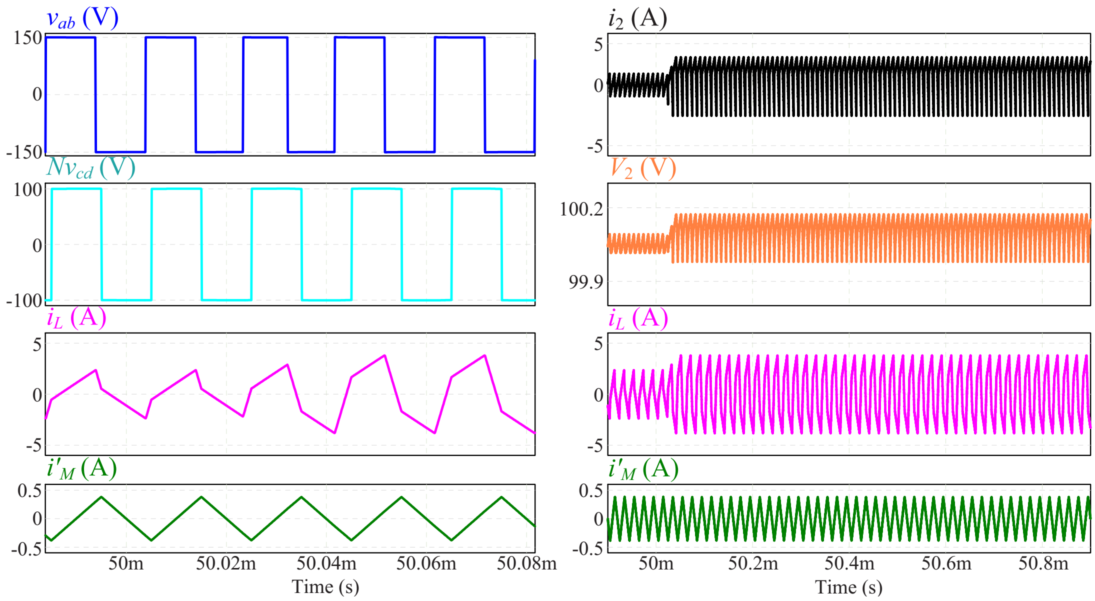

(b)

Fig. 3.4. Parameter sensitivity analysis for Type-I SS-OTPSM. Simulated open-loop transient response under (a) CTPSM and (b) Type-I SS-OTPSM. The simulation parameters are as follows: $f_s = 50$ kHz, $V_1 = 150$ V, $V_2 = 100$ V, $L_p = 150$ μH, $L_s = 1.70$ μH, $L_m = 650$ μH, and the phase-shift ratio is changed from $\frac{1}{9}$ to $\frac{1}{3}$.

(3.19), and (3.20), can be regarded as the optimum solutions of (3.14).

In addition to poorer performances as shown in Fig. 3.5, one major problem with the previous OTPSM strategies is their high implementation complexity. Due to their asymmetric modulation characteristics, it is difficult for the existing

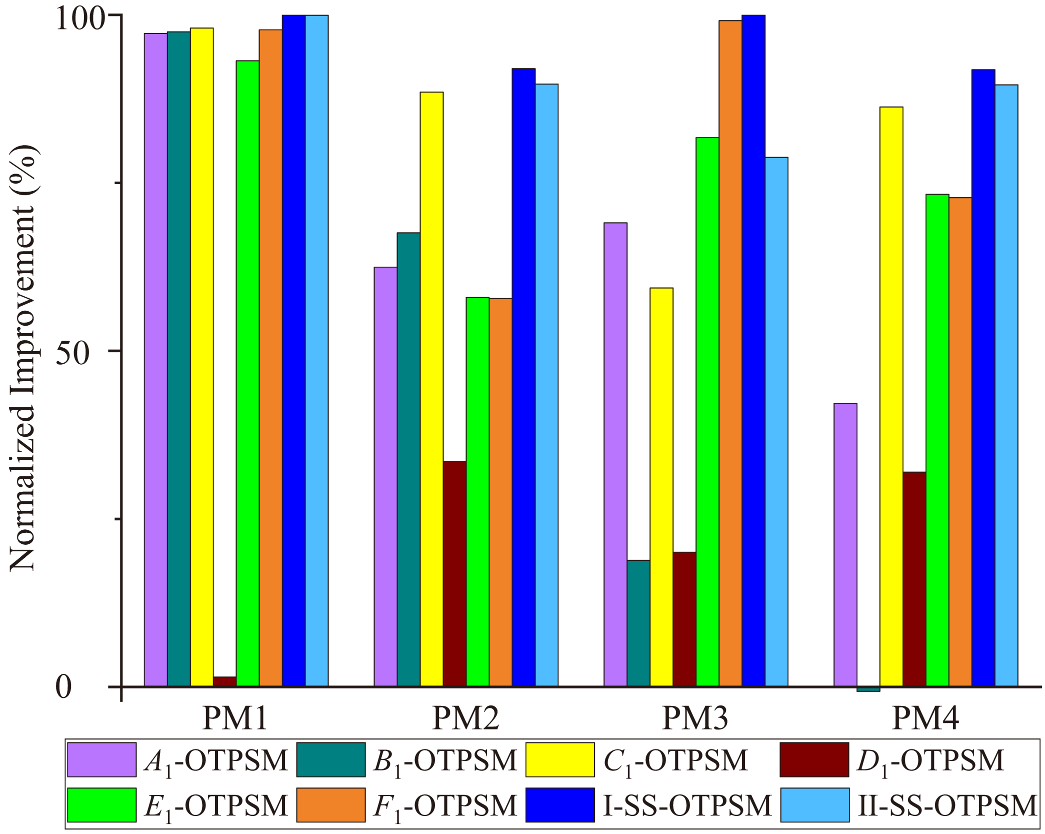

Fig. 3.5. Normalized performance evaluation of different OTPSM strategies in open-loop simulations for an increase in the phase-shift ratio from $\frac{1}{9}$ to $\frac{1}{3}$.

OTPSM strategies to synchronize their phase-shifted PWM carriers in a cycle-by-cycle manner, and little information is disclosed regarding their implementation in closed-loop configuration. Fig. 3.6 illustrates the implementation of the proposed Type-I SS-OTPSM in the PWM modules of microprocessor. v_{ab} and v_{cd} are generated by employing two triangular carriers, where Carrier 2 and Carrier 1 correspond to the master and slave PWM modules, respectively. When an interrupt event occurs, the phase-shift ratio between v_{ab} and v_{cd} should be updated to D+0.5d, and the (n+1)th period of v_{ab} should be updated to $(2-d)T_{hc}$. Redefining the transient response time T_t as $T_t = (2-d)T_{hc}$, the duty-cycle values of v_{ab} will always be fixed at $W_2T_{hc}/T_t = 0.5$, which ultimately makes it possible to change the pulse widths by only manipulating the PWM base frequency. With a constant duty ratio, triangle Carrier 1 has equal rise and fall times, and the resulting PWM waveform can be centered within each cycle.

Table 3.1 Main Features of Different Transient SPS Modulation Strategies for NR-DABC.

Type	DOF	Reference	W1	W2	W3	W4	W5	W6	Sensorless	Complexity	CE[†]
CTPSM	1	—	1	1	1	$1+d$	1	1	Yes	⋆	No
A_1 OTPSM	2	[90]	1	$1-\frac{dM}{M+1}$	1	$1+\frac{d}{M+1}$	1	1	No	⋆⋆⋆	No
A_2 OTPSM	2	[91]	1	1	$1-\frac{dM}{M+1}$	1	$1+\frac{d}{M+1}$	1	No	⋆⋆⋆	No
A_3 OTPSM	2	[91]	1	$1-\frac{dM}{M-1}$	1	1	$1-\frac{d}{M-1}$	1	No	⋆⋆⋆	No
A_4 OTPSM	2	[91]	1	1	$1-\frac{dM}{M-1}$	1	1	$1-\frac{d}{M-1}$	No	⋆⋆⋆	No
A_5 OTPSM	2	[92]	1	1	1	$1+\frac{d}{M+1}$	$1+\frac{dM}{M+1}$	1	No	⋆⋆⋆	No
A_6 OTPSM[§]	2	[93]	1 1	1 1	$1-\frac{d+2}{M+1}$ $1-\frac{d-2}{M+1}$	1 1	$1+\frac{(d+2)M}{M+1}$ $1+\frac{(d-2)M}{M+1}$	1 1	No	⋆⋆⋆⋆	No
A_7 OTPSM	2	[94]	$1-\frac{dM}{M-1}$	1	1	$1-\frac{d}{M-1}$	1	1	No	⋆⋆⋆	No
B_1 OTPSM	3	[94]	1	1	$1-d$	1	$1+\frac{d}{2M}$	$1-\frac{d}{2M}$	No	⋆⋆⋆⋆	No
B_2 OTPSM	3	[94]	1	$1+\frac{dM}{2}$	$1-\frac{dM}{2}$	1	$1+d$	1	No	⋆⋆⋆⋆	No
B_3 OTPSM	3	[95]	$1+\frac{\frac{\lvert D+d\rvert}{M}+D}{2}$	$1-\frac{\frac{\lvert D+d\rvert}{M}-D}{2}$	1	1	$1-\lvert D+d\rvert$	1	No	⋆⋆⋆⋆	No
B_4 OTPSM	3	[96]	$1+\frac{d}{2M}$	$1-\frac{d}{2M}$	1	$1+d$	1	1	No	⋆⋆⋆⋆	No
B_5 OTPSM	3	[96]	$1-\frac{d}{2M}$	$1+\frac{d}{2M}$	1	1	$1+d$	1	No	⋆⋆⋆⋆	No
C_1 OTPSM	2	[97]	1	1	1	$1+\frac{d}{2}$	$1+\frac{d}{2}$	1	Yes	⋆⋆	IE[‡]
C_2 OTPSM	2	[94]	$1-\frac{d}{2}$	$1-\frac{d}{2}$	1	1	1	1	Yes	⋆⋆	IE[‡]
D_1 OTPSM	3	[98]	1	1	1	$1+d$	$1+\frac{d}{2}$	$1-\frac{d}{2}$	Yes	⋆⋆⋆	IE[‡]
D_2 OTPSM	3	[99]	1	1	1	$1+\frac{d(d-2D+4)}{4(d+2)}$	$1+\frac{d}{2}$	$1+\frac{d(d+2D)}{4(d+2)}$	Yes	⋆⋆⋆	IE[‡]
E_1 OTPSM	4	[100]	1	$1-\frac{d}{4}$	$1-\frac{d}{4}$	1	$1+\frac{d}{4}$	$1+\frac{d}{4}$	Yes	⋆⋆⋆	IE[‡]
E_2 OTPSM[§]	4	[97]	$1-\frac{D+d}{2}$ $1+\frac{D}{2}$	$1-\frac{D+d}{2}$ $1+\frac{D}{2}$	1 1	$1-\frac{D}{2}$ $1+\frac{D+d}{2}$	$1-\frac{D}{2}$ $1+\frac{D+d}{2}$	1 1	Yes	⋆⋆⋆⋆	IE[‡]
F_1 OTPSM	6	[100]	—	—	—	—	—	—	Yes	⋆⋆⋆⋆⋆	IE[‡]
I SS-OTPSM	3	Proposed	$1-\frac{d}{4}$	$1-\frac{d}{2}$	$1-\frac{d}{4}$	1	1	1	Yes	⋆	Yes
II SS-OTPSM	3	Proposed	1	1	1	$1+\frac{d}{4}$	$1+\frac{d}{2}$	$1+\frac{d}{4}$	Yes	⋆	Yes

[§] Expressions in the first row satisfy $D>0$, $d<0$ and $D+d<0$, while expressions in the second row satisfy $D<0$, $d>0$ and $D+d>0$.
[⋆] Low ⋆, Moderate ⋆⋆, High ⋆⋆⋆, Very High ⋆⋆⋆⋆, Extreme ⋆⋆⋆⋆⋆.
[†] Complete elimination (CE) of transient dc offsets in both i_L and i_M. [‡] Incomplete elimination (IE).

In SS-OTPSM, the position of the sampling point can always be set at the midpoint of Carrier 1, such that the sampling and switching processes can be suitably synchronized. Synchronization allows the average sampled value to be exactly

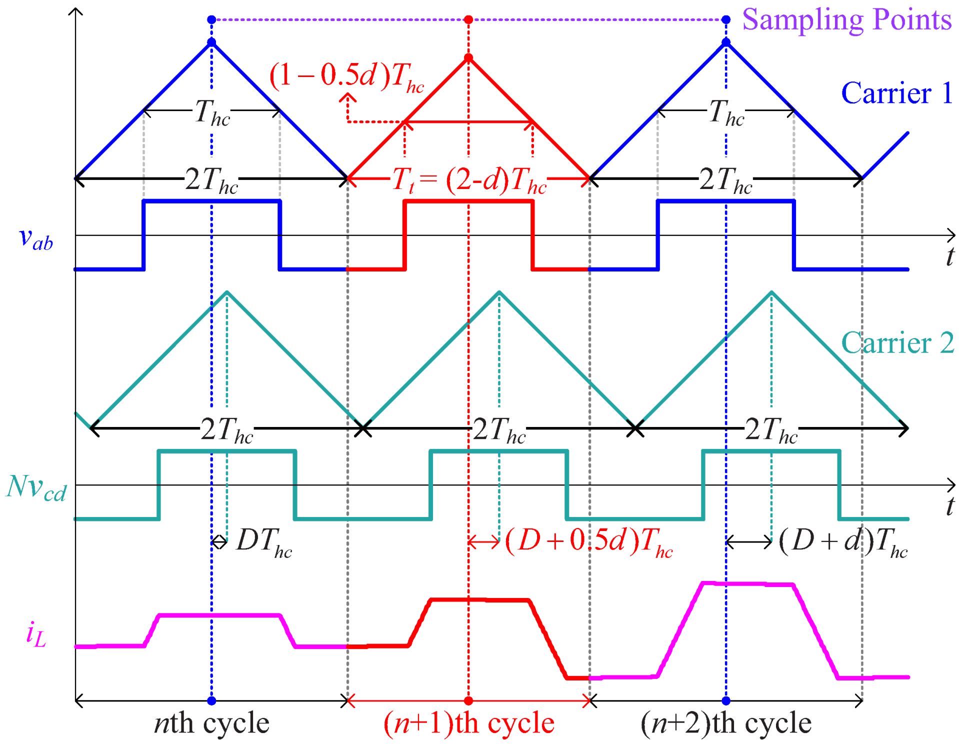

Fig. 3.6. Implementation details of Type-I SS-OTPSM on the PWM modules of a microprocessor platform.

reconstructed and are robust against phase-shift variations and switching noise. In contrast to this, the sampling point under other asymmetric modulation strategies are rarely located at a fixed position (e.g., the beginning or middle point) with respect to each modulation period, and hence the sampling signal is not perfectly synchronized with the carrier, resulting in aliasing effect and quantization noise in digitally controlled NR-DABC, especially when the sampling rate is chosen to be close to the switching frequency [139]. The aliasing-induced error between the dc component of the sampled value and the actual dc voltage/current may be non-negligible, thus degrading the closed-loop regulation accuracy and performance during both steady and transient states. By taking advantage of the symmetrical characteristic of the proposed SS-OTPSM, it is easy to reset the carriers after each execution, and achieve the synchronization between the sampling modules and PWM modules, which facilitates the continuous execution of SS-OTPSM in a closed-loop manner. This is a clear advantage of the proposed method over all existing ones.

3.4 Proposed Enhanced MPC for SS-OTPSM Modulated NR-DABC

In general, it is difficult for a single-voltage-loop PI controller to simultaneously meet stability requirements and achieve ultra-fast dynamics. As can be seen from Figs. 13 and 14 of [100], the dynamics under PI controller+Type-E_1 OTPSM were slow, and DABC tended to become unstable under PI controller+CTPSM. Thus, such OTPSM strategies are deemed unsuitable for use with a pure PI controller, as the low-gain linear PI controller often introduces only a relatively small change in the phase-shift ratio in every switching cycle to produce a smooth but slow dynamic response (see Fig. 14 of [100]). In such a case, no significant transient dc offsets will be introduced even by using CTPSM, and it is not possible to benefit from the superior transient performances of SS-OTPSM or OTPSM over CTPSM.

In our opinion, the proposed SS-OTPSM can be used in combination with any commonly-used controller. To evaluate the impacts of OTPSM and SS-OTPSM on closed-loop NR-DABC's dynamic performance, a high-gain, fast controller is required. For example, the advanced MPC can achieve faster and more satisfactory control performance than the PI controller. As investigated in [136], MPC was recognized as one of the most powerful control schemes for DABC, since the relationship between the phase shift ratio and output power is used as a feed-forward term in MPC to minimize the error between the actual and the desired output voltage. Thus, an MPC scheme, which is popular for its good control performance and ease of use, is adopted in this chapter.

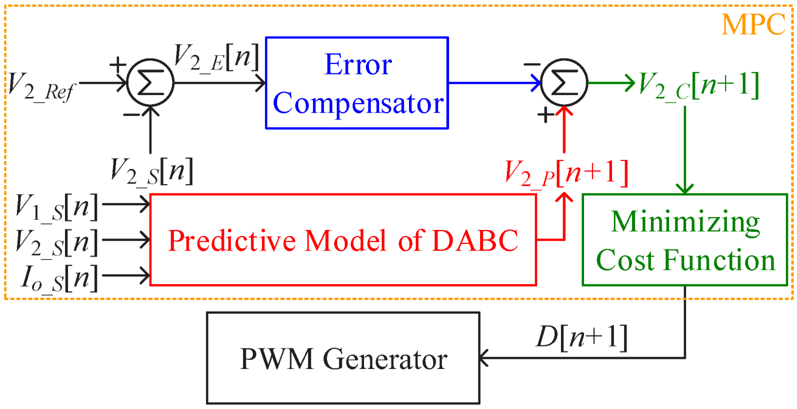

Fig. 3.7. Common block diagram of MPC.

3.4.1 Conventional MPC

Although different MPCs have been developed for NR-DABC, they can be generally depicted by the common block diagram in Fig. 3.7. V_{2_Ref} is the reference output voltage. $V_{1\_S}[n]$, $V_{2\_S}[n]$, and $I_{o\_S}[n]$ are the sampled values at the nth cycle, and they are used for generating the predicted output voltage $V_{2\_P}[n+1]$ according to a predictive model. $V_{2\_C}[n+1]$ is the corrected value of the output voltage after real-time error compensation. A given cost function J basically compares $V_{2\_C}[n+1]$ with V_{2_Ref} for calculating an optimal phase-shift ratio $D[n+1]$ for the next cycle that minimizes J. The major differences between the existing MPC schemes lie in their error compensators and cost functions. For example, in [9], a two-step prediction with a proportional compensator and a weighted cost function is implemented, while a one-step prediction using a PI compensator and a simple quadratic cost function are presented in [41]. To reduce computational burden, this chapter uses a simple scheme similar to that in [41].

Typically, the average value of i_2 (i.e., $\bar{i}_2$) can be predicted by the average power model of NR-DABC [9] and is approximated by

$$\bar{i}_2 = \frac{P}{V_2} = \frac{NV_1T_{hc}D(1-D)}{L}. \tag{3.21}$$

Hence, the dynamic behavior of V_2 is described by

$$C_o \frac{\mathrm{d}V_2}{\mathrm{d}t} = \bar{i}_2 - I_o = \frac{NV_1 T_{hc} D(1-D)}{L} - I_o. \tag{3.22}$$

The predicted output voltage at the (n+1)th cycle, i.e., $V_{2\_P}[n{+}1]$, can be obtained by discretizing (3.22) using the forward Euler approximation, which leads to

$$\begin{aligned} V_{2\_P}[n{+}1] \approx& V_{2\_S}[n] + 2T_{hc}{V_2}'[n] \\ =& V_{2\_S}[n] + \frac{2NT_{hc}^2 D(1{-}D)V_{1\_S}[n]}{LC_o} - \frac{2T_{hc}I_{o\_S}[n]}{C_o}. \end{aligned} \tag{3.23}$$

In this chapter, the cost function J is defined as

$$J = [V_{2\_Ref} - V_{2\_C}[n+1]]^2 \tag{3.24}$$

and the PI-based error compensator is given by (3.25)

$$K_p V_{2\_E}[n] + K_i \sum_{\tau=0}^{n} V_{2\_E}[\tau] \tag{3.25}$$

where $V_{2\_E}[n] = V_{2\_Ref} - V_{2\_S}[n]$ is the output voltage error, and $V_{2\_C}[n{+}1] = V_{2\_P}[n{+}1] - (K_p V_{2\_E}[n] + K_i \sum_{\tau=0}^{n} V_{2\_E}[\tau])$. Minimizing J yields the optimal phase-shift ratio

$$D[n+1] = \frac{1}{2}\left(1 - \sqrt{1 - \frac{4K_2}{K_1}}\right) \tag{3.26}$$

where

$$K_1 = \frac{2NT_{hc}^2 V_{1\_S}[n]}{LC_o} \tag{3.27}$$

$$K_2 = 2T_{hc}I_{o\_S}[n]/C_o + K_p^* V_{2\_E}[n] + K_i \sum_{\tau=0}^{n} V_{2\_E}[\tau] \tag{3.28}$$

and

$$K_p^* = K_p + 1. \tag{3.29}$$

(3.28) and (3.29) indicate that the presented controller attempts to correct the output voltage error V_{2_E} by an equivalent proportional gain K_p^* instead of K_p. Specifically, K_p^* determines the bandwidth of the control loop, suppresses sampling noise, and stabilizes the converter; while the integral gain K_i is used for eliminating steady-state tracking error.

3.4.2 Proposed EMPC Based on SS-OTPSM

A major problem with the above predictive model is that the average power computed from (3.4) is derived based on steady-state waveforms. Hence it cannot accurately predict the average power transferred to the load during transient period. Especially when a large step change in load occurs, the phase-shift ratio predicted by conventional model typically tends to deviate from the actual desired value, thus resulting in modelling error and longer transient response time. Hence, a refined model is required to describe the cycle-to-cycle dynamic properties of NR-DABC. However, since the initial or final value of i_L in each transient cycle is uncertain depending on many factors such as R_s, the transient average power under CTPSM is difficult to predict. This problem can be easily overcome by the proposed SS-OTPSM. Since the inductor current can be modulated to the desired value during each cycle, the average power of NR-DABC operating under SS-OTPSM can be correctly predicted and modelled cycle by cycle. If so, the predicted control variable (or phase-shift ratio) will be exactly proportional to the transferred power, and there is neither steady-state nor transient modelling error between them. To achieve this, an enhanced MPC (EMPC) as presented below that is compatible with SS-OTPSM is proposed in this chapter.

By referring to Fig. 3.6, the average power under SS-OTPSM over the (n+1)th cycle is given by

$$\begin{aligned} P^* &= \frac{1}{(2-d)T_{hc}} \int_0^{(2-d)T_{hc}} v_{ab}(t) i_L(t) \mathrm{d}t \\ &= \frac{NV_1V_2T_{hc}(8d - 9d^2 + 16D - 24Dd - 16D^2)}{4(2-d)L} \end{aligned} \tag{3.30}$$

which can be used to accurately predict the transient output power under SS-OTPSM. To compute the optimal phase-shift ratio, (3.31) gives the dynamic output voltage in continuous-time.

$$C_o \frac{\mathrm{d}V_2}{\mathrm{d}t} = \bar{i}_2 - I_o = \frac{P^*}{V_2} - I_o \tag{3.31}$$

Discretizing (3.31) with forward Euler method, the output voltage under SS-OTPSM can be predicted using (3.32).

$$V_{2\_P}^*[n{+}1] \approx V_{2\_S}[n] + 2T_{hc}(\frac{P^*}{C_o V_2} - \frac{I_{o\_S}[n]}{C_o}) \tag{3.32}$$

Substituting (3.32) into (3.24) and minimizing J, it can be shown that the refined optimal phase-shift ratio $D^*[n+1]$ employing EMPC is given by

$$\begin{aligned} D^*[n+1] = D[n] + d^* = &- \frac{2\sqrt{4(1+3D[n])K_1^2 - 2(7+6D[n])K_1K_2 + K_2^2}}{9K_1} \\ &+ \frac{(4-3D[n])K_1 + 2K_2}{9K_1}. \end{aligned} \tag{3.33}$$

Hence, compared to (3.26), a more accurate prediction of the optimal phase-shift ratio is given by (3.33).

Compared to conventional MPC, EMPC results in a more accurate prediction of the optimal phase-shift ratio, which is to be executed by SS-OTPSM. Otherwise, in the presence of significant error in the predicted optimal phase-shift ratio by conventional MPC, the performance merits of SS-OTPSM will also be adversely affected. This highlights the importance of co-optimization of controller and transient modulation designs in order to achieve a truly optimal dynamic performance.

3.4.3 Controller Design and Closed-Loop Simulation Results of Different Systems

To compare the dynamic performances of different combinations of controllers and transient modulation strategies, four cases are selected, i.e., MPC+CTPSM, MPC+E_1-OTPSM, MPC+SS-OTPSM and EMPC+SS-OTPSM, and two sets of K_p^* and K_i values are chosen according to the system requirements and bode plots, i.e., $\{K_{p1}^* = 0.07,\ K_{i1} = 0.3\}$ and $\{K_{p2}^* = 0.1,\ K_{i2} = 0.5\}$. In addition, the sampling

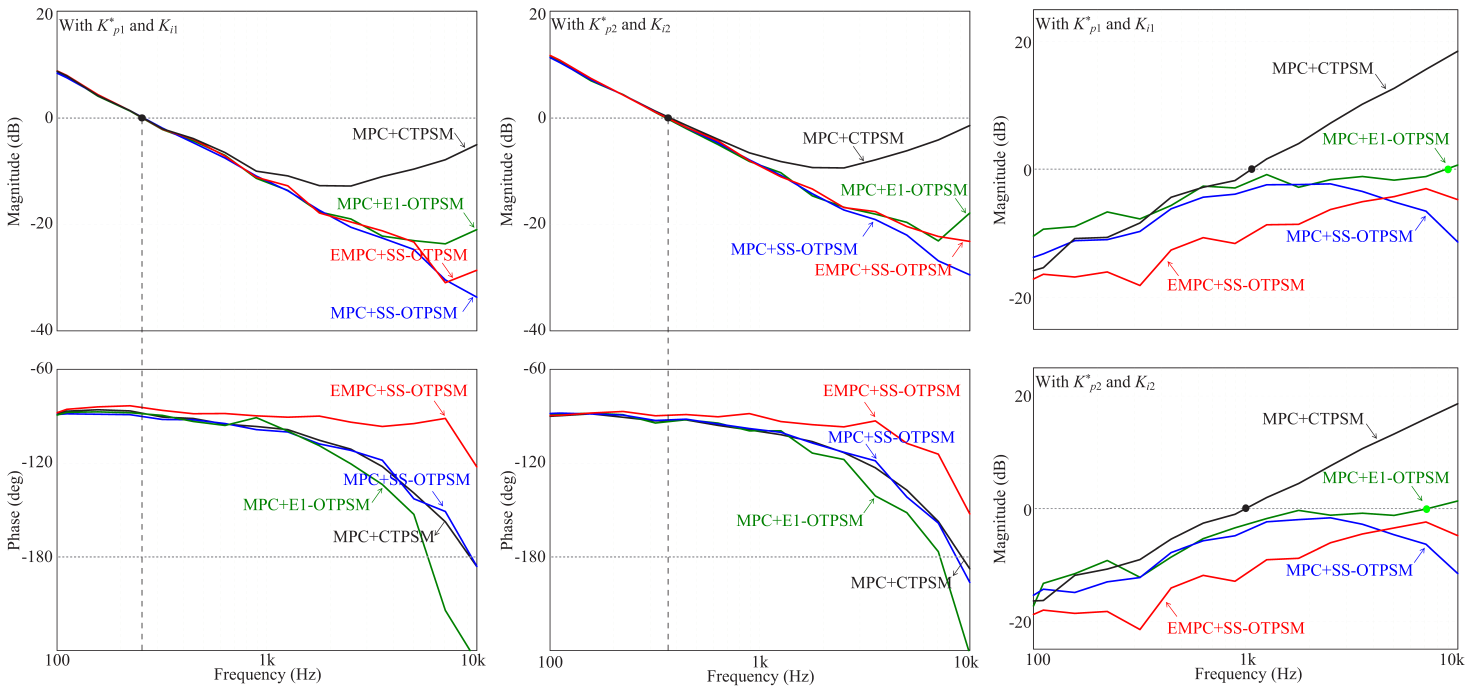

Fig. 3.8. Simulated loop gains and closed-loop output impedances under different systems. (a) Loop gains with K^*_{p1} and K_{i1}. (b) Loop gains with K^*_{p2} and K_{i2}. (c) Closed-loop output impedances.

frequency for both MPC and EMPC is set as the switching frequency, since all the sampled voltages and currents are dc signals, which do not need to use very high sampling rates.

Figs. 3.8(a) and (b) show the simulated loop gain, i.e., open-loop transfer function from $\hat{V}_{2\_E}(s)$ to $\hat{V}_2(s)$, with the two sets of control parameters, respectively. It can be seen that the system responses of the four cases are similar in the low-frequency region, and the difference mainly lies in the high-frequency region. Although the crossover frequencies and phase margin values of the four different systems are similar, SS-OTPSM is observed to possess a higher disturbance attenuation capability than CTPSM and E_1-OTPSM since the magnitude responses of MPC+SS-OTPSM and EMPC+SS-OTPSM decrease monotonically in the high-frequency region. Therefore, for similar phase margins, both MPC+SS-OTPSM and EMPC+SS-OTPSM exhibit significantly larger gain margins compared to the other two systems. As shown by the Bode plots, in the high-frequency region, the system's magnitude response under MPC+CTPSM is significantly higher than those of the other systems, and the system's phase response under MPC+E_1-OTPSM lags those of the other systems and becomes $-180°$ at a relatively low frequency, which makes them prone to stability problem. In summary, with the same control coefficients, the closed-loop controlled NR-DABC is expected to exhibit better stability and transient performances under MPC+SS-OTPSM and EMPC+SS-OTPSM.

In addition, the closed-loop output impedances of different systems are simulated by PSIM and shown in Fig. 3.8(c). It can be seen that the output impedance of the MPC+CTPSM system reaches 0 dB at about 1 kHz; the output impedance of the MPC+E_1-OTPSM system reaches 0 dB at 8.7 kHz with K_{p1}^* and K_{i1} and about 7 kHz with K_{p2}^* and K_{i2}; while the output impedances of both MPC+SS-OTPSM and EMPC+SS-OTPSM systems remain below 0 dB over a wide frequency range from 100 Hz to 10 kHz. MPC+E_1-OTPSM always exhibits a higher output impedance than MPC+SS-OTPSM and EMPC+SS-OTPSM. Compared with MPC+CTPSM and MPC+E_1-OTPSM, both MPC+SS-OTPSM and EMPC+SS-OTPSM are able to achieve a lower closed-loop output impedance, better stability, and hence better disturbance-rejection performance when subjected to large step-load changes.

As exemplified in Fig. 3.9, it is evident from the simulated closed-loop transient responses that the dc offsets arising from CTPSM are largely mitigated by E_1-OTPSM and SS-OTPSM, but the transient waveforms of i_L and $i_m^{'}$ under MPC+E_1-OTPSM still exhibit some noticeable asymmetry compared to SS-OTPSM. With the same control parameter values, EMPC+SS-OTPSM demonstrates the fastest transient response with zero dc offsets in both i_L and $i_m^{'}$, although its transient overshoots and undershoots are slightly higher than those under MPC+SS-OTPSM.

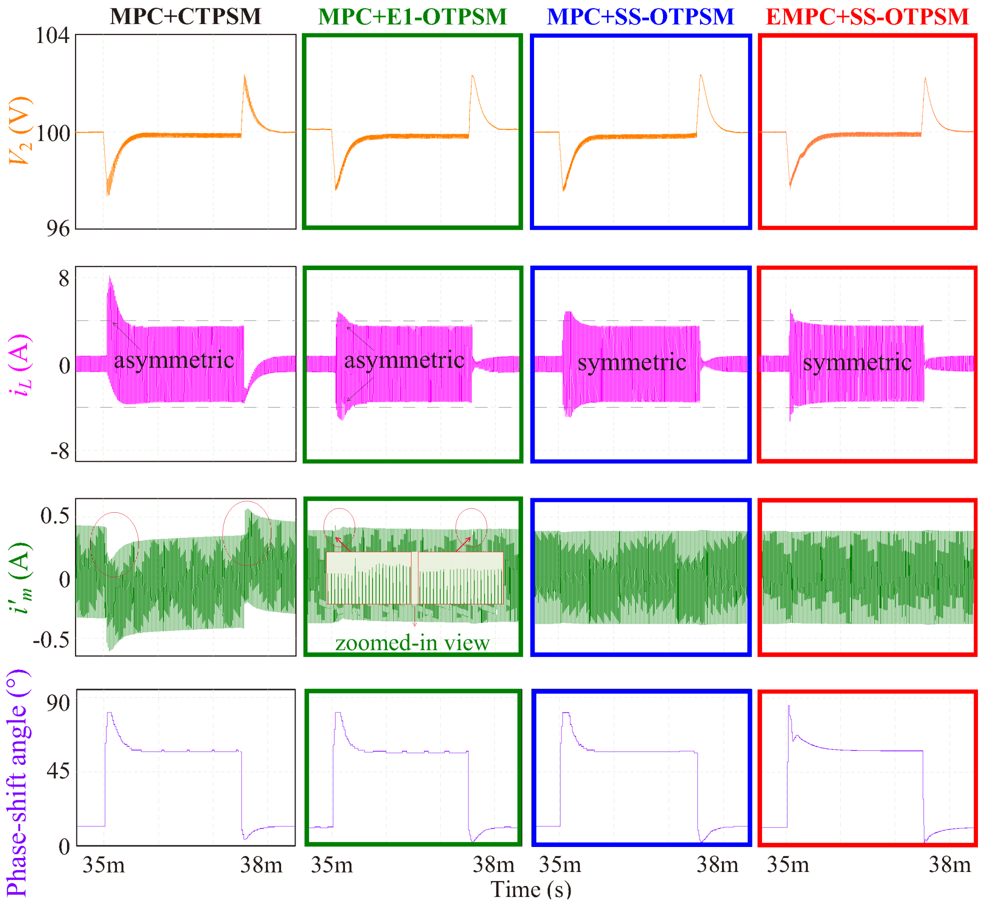

Fig. 3.9. Simulated closed-loop transient responses of different systems for step-load changes between 25% and 95% of the full load with K^*_{p2} and K_{i2}.

Furthermore, by zooming in the steady-state waveforms of V_2 and i_L of different systems under heavy-load condition, another interesting finding is that limit-cycle oscillations are observed under both MPC+CTPSM and MPC+E_1-OTPSM in steady state, while such oscillations are not observed under both MPC+SS-OTPSM and EMPC+SS-OTPSM. To illustrate this phenomenon, Fig. 3.10(a) shows the zoomed-in simulated steady-state waveforms with control parameters K^*_{p2} and K_{i2}. Although the integral term in the feedback loop can significantly eliminate steady-state error and help to reduce the amplitudes of limit-cycle oscillations to an acceptable level, such oscillations cannot be effectively attenuated if their frequencies are beyond the controller's bandwidth. Typically, the amplitude and frequency of limit-cycle oscillations depend strongly on the non-linear quantization effects caused by the interaction between the resolutions of PWM generator

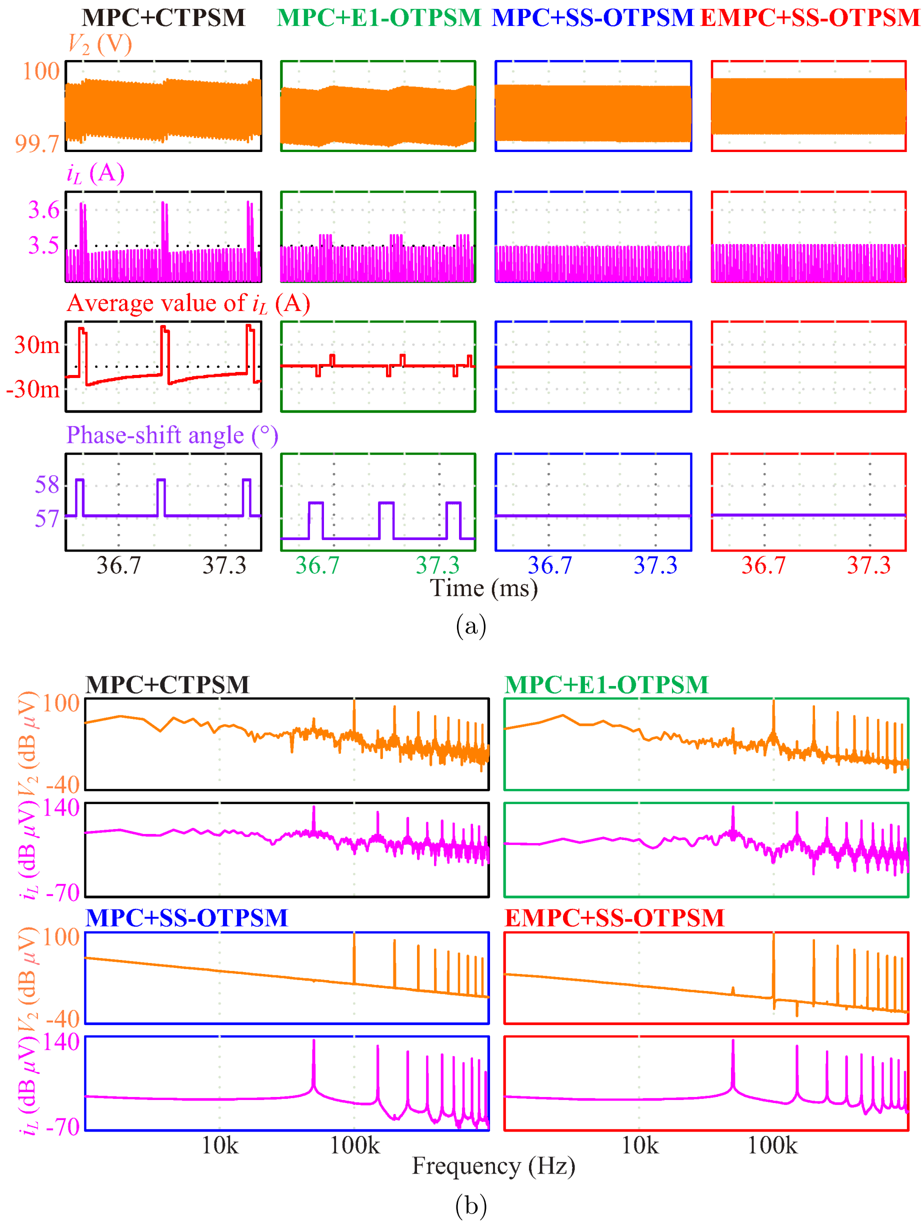

Fig. 3.10. Simulated steady-state waveforms under heavy-load condition with K^*_{p2} and K_{i2}. (a) Zoomed in steady-state waveforms of V_2, i_L, average value of i_L, and phase-shift angle. (b) FFT spectrum analysis of V_2 and i_L.

and sampling module [139]. According to the Fast Fourier Transform (FFT) analysis of V_2 and i_L shown in Fig. 3.10(b), some switching noise and spectral aliasing can be found in the spectrums under MPC+CTPSM and MPC+E_1-OTPSM, which are not seen under MPC+SS-OTPSM and EMPC+SS-OTPSM as they can achieve synchronous sampling. The aliasing effect can affect the regulation precision of output voltage and further lead to permanent small-amplitude disturbances

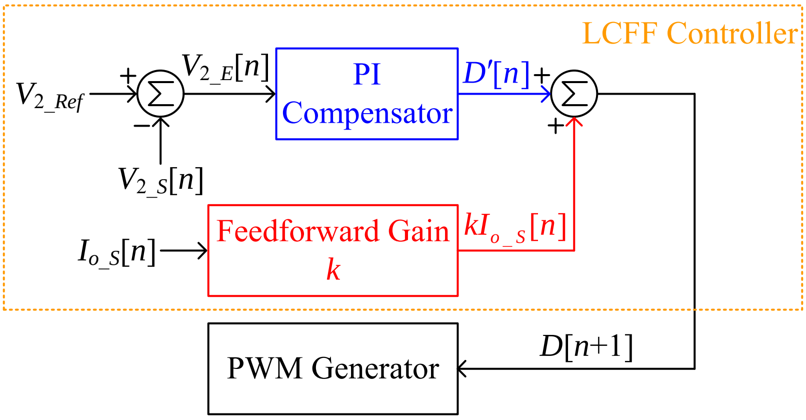

Fig. 3.11. Block diagram of LCFF control scheme.

in the control variable (i.e., phase-shift angle). Moreover, since any changes in the control variable may give rise to dc offsets, which cannot be completely eliminated by CTPSM or even E_1-OTPSM, considerable steady-state error can accumulate in the control loop. As shown in Fig. 3.10(a), the average value of i_L periodically oscillates around zero under MPC+CTPSM and MPC+E_1-OTPSM, while it is within the zero-error bin under MPC+SS-OTPSM and EMPC+SS-OTPSM. As demonstrated by the simulation results, in addition to enhancing transient response, both MPC+SS-OTPSM and EMPC+SS-OTPSM can achieve more precise regulation and suppress limit-cycle oscillations with the same control parameters since the aliasing effect can be neglected under SS-OTPSM. These above findings are evidences of the correctness of the theoretical analysis presented in the current and the last sections.

In addition, we selected a simple load-current feed-forward (LCFF) control scheme introduced in [125] and conducted a comparison with MPC+OTPSM. The block diagram of the selected LCFF controller can be found in Fig. 3.11. In this scheme, the phase-shift ratio D can be expressed as $D[n+1] = D^{'}[n] + kI_{o\_S}[n]$, where k is the feed-forward ratio of the load current $I_{o\_S}[n]$. In the following discussion, the proportional coefficient and integral coefficient of the PI compensator in LCFF controller are chosen as 0.45 and 0.008, respectively; the feed-forward ratio k is chosen as 24.

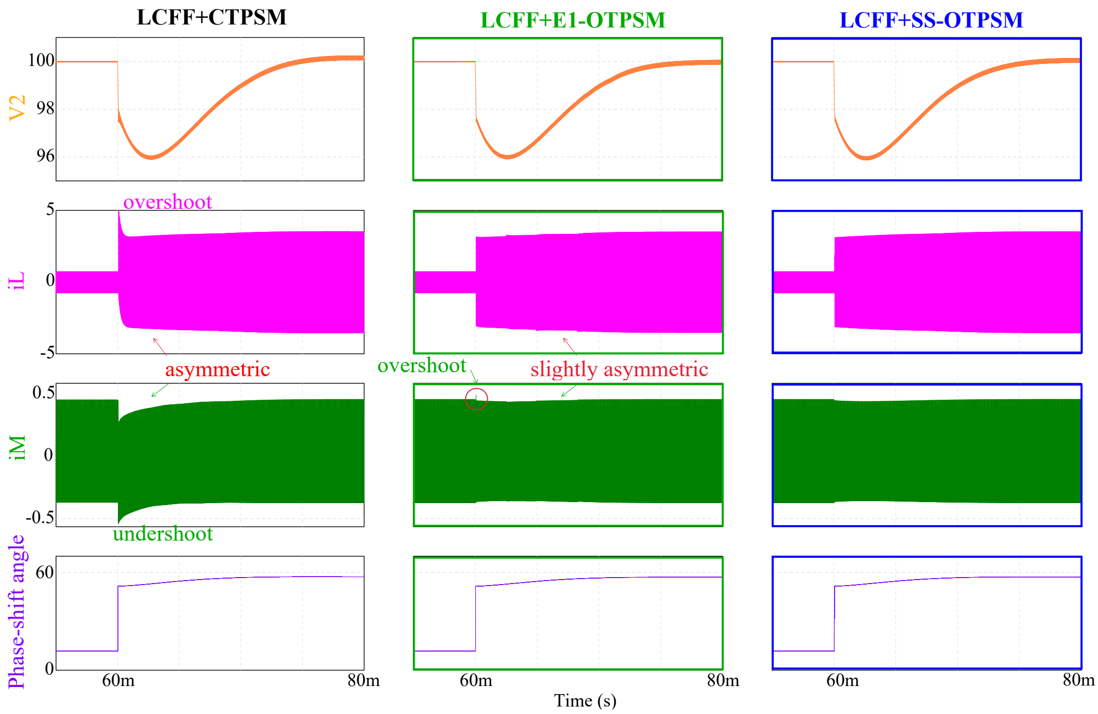

Fig. 3.12. Simulated closed-loop transient responses under LCFF controller plus different transient modulation strategies.

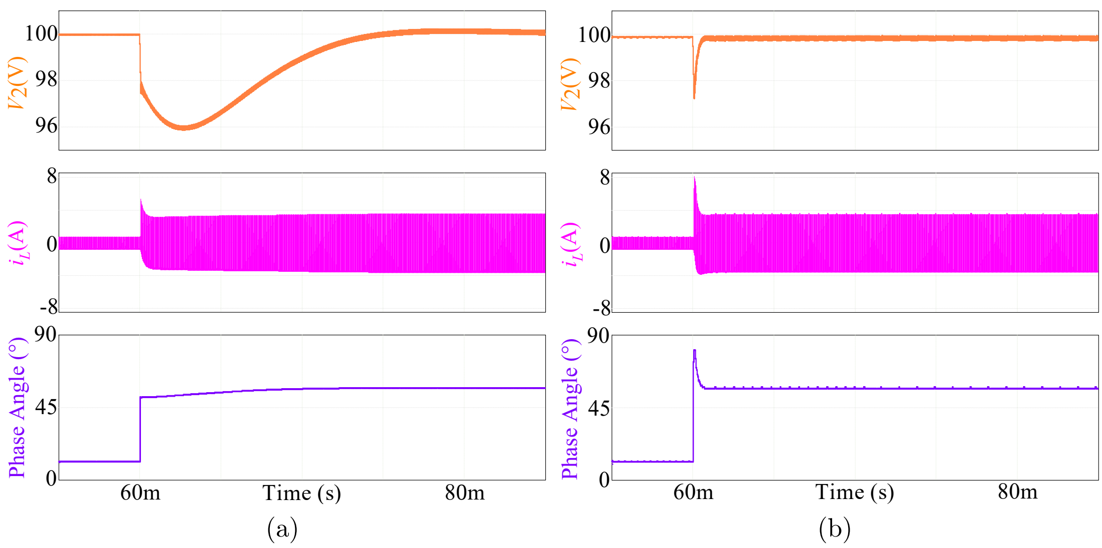

Fig. 3.13. A comparison between (a) LCFF Controller+CTPSM and (b) MPC+CTPSM.

The simulated transient responses of LCFF controller plus different transient modulation strategies are illustrated in Fig. 3.12. Comparisons between different closed-loop configurations are shown in Figs. 3.13 to 3.15. It can be seen from the dynamic response of phase-shift angle that the load-current feed-forward path

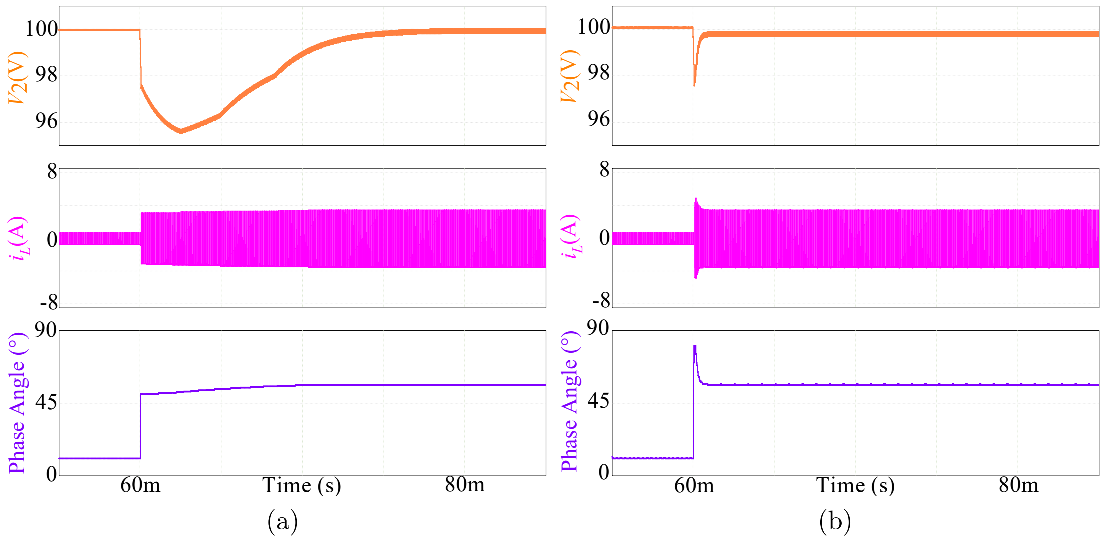

Fig. 3.14. A comparison between (a) LCFF Controller+E_1-OTPSM and (b) MPC+E_1-OTPSM.

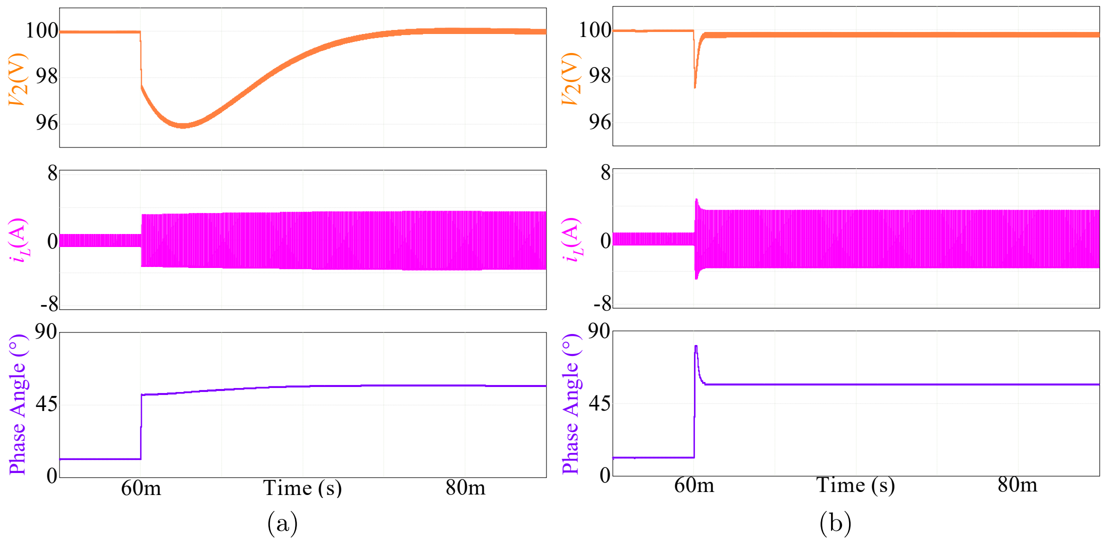

Fig. 3.15. A comparison between (a) LCFF Controller+SS-OTPSM and (b) MPC+SS-OTPSM.

plays a dominant role in control when the output voltage is far from the reference value, while the PI compensator starts to take effect when the output voltage is close to the reference value. Hence, the control performance of LCFF controller is generally less satisfactory than MPC, as the algorithm of MPC is based on the power transfer model of NR-DABC, which can quickly predict the desired phase-shift ratio. The above simulation results demonstrate once again that such

OTPSM strategies are inherently compatible with high-gain controllers such as MPC for realizing dc-offset-free and ultrafast dynamic responses. Even though OTPSM is compatible with many controllers, MPC is chosen in this work to test the effectiveness of OTPSM under extreme operating conditions involving abrupt and large-amplitude changes in the phase-shift angle.

3.5 Experimental Results

In order to verify the advantages of the proposed SS-OTPSM and EMPC, both open-loop and closed-loop experiments are carried out on a scaled-down prototype as shown in Fig. 3.16 with the key specifications listed in Table 3.2. In open-loop tests, both terminals of NR-DABC are connected with dc voltage sources, and additional resistors are connected in parallel to each source such that the direction of the power flow can be reversed. The phase-shift ratio is changed directly by giving command through a human-machine interaction software. In closed-loop tests, the output terminal is connected to resistive loads instead of a dc voltage source, and the load resistances can be switched by using a power MOSFET. The MPC or EMPC designed in Section 3.4 will determine the desired phase-shift ratio based on the sampled information.

According to Fig. 3.5 and Table 3.1, since Type-A, Type-B, Type-D, and Type-F OTPSM strategies do not show any significant advantages over other strategies, they will not be further discussed in this section. For performance comparisons, the two most-cited sensorless methods, i.e., Type-C_1 and Type-E_1 OTPSM strategies are implemented in open-loop experiments; Type-E_1 OTPSM is also implemented with a high-bandwidth MPC in closed-loop experiments as it is the only existing method that has been verified in closed-loop configuration, albeit with a low-bandwidth pure PI controller which is not suitable for use with OTPSM or SS-OTPSM.

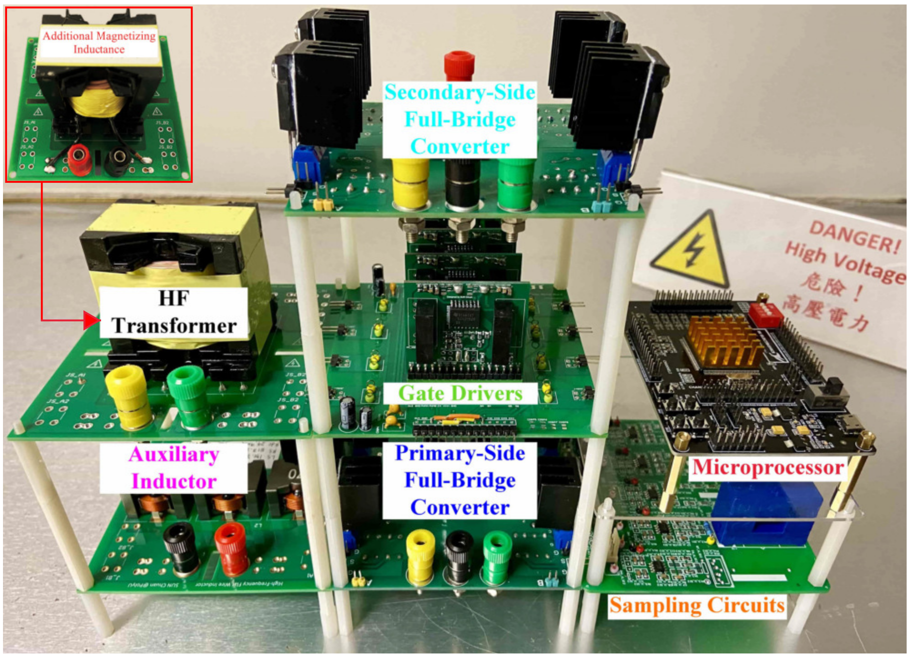

Fig. 3.16. Photograph of the experimental NR-DABC prototype.

Table 3.2 Circuit Parameters and Specifications Used in Chapter 3.

Symbol	Parameter Description	Value or Part Type
P_{max}	Rated Power	250 W
V_1	Input Voltage	100 V
V_2	Output Voltage	100 V
C_o	Output Capacitance	47 μF
R_L	Load Resistance	150/43 Ω
$N:1$	Transformer Ratio	1 : 1
L_m	Magnetizing Inductance	650 μH
R_m	ESR of L_m	260 mΩ
L_p	Primary Inductance	92 μH
R_p	ESR of L_p	211 mΩ
L_s	Secondary Inductance	1.7 μH
$S_x{\sim}Q_x$	Power Switches	UnitedSiC UJC06505K
f_s	Switching Frequency	50 kHz
–	Dead Time	250 ns
–	Voltage Sensing Circuit	Resistive Voltage Divider
–	Current Sensor	LEM LA 55-P
–	Microprocessor	TI TMS320F28335

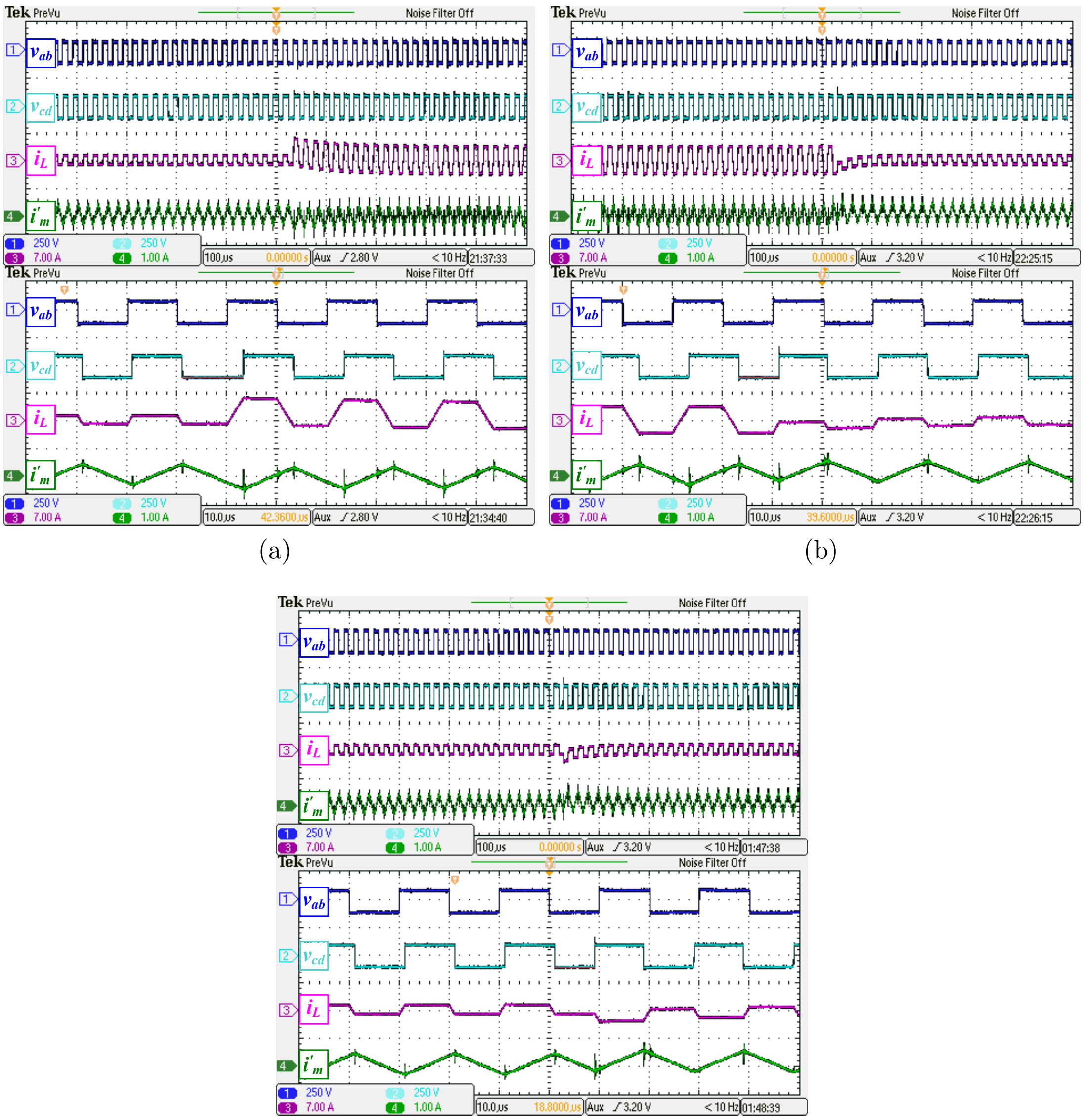

(a) (b)

(c)

Fig. 3.17. Open-loop experimental results under CTPSM. (a) The phase-shift ratio is changed from $\frac{1}{9}$ to $\frac{1}{3}$. (b) The phase-shift ratio is changed from $\frac{1}{3}$ to $\frac{1}{9}$. (c) The phase-shift ratio is changed from $\frac{1}{9}$ to $-\frac{1}{9}$.

3.5.1 Open-Loop Tests

Figs. 3.17 to 3.20 show the open-loop experimental results under CTPSM, the proposed SS-OTPSM, Type-C_1 OTPSM [97], and Type-E_1 OTPSM [100], respectively. Note that, by updating the phase-shift ratio from 1/9 to $-1/9$, the direction of power flow reverses in Figs. 3.17(c) and 3.18(c), and the experimental results confirmed that SS-OTPSM can be applied in all power flow conditions.

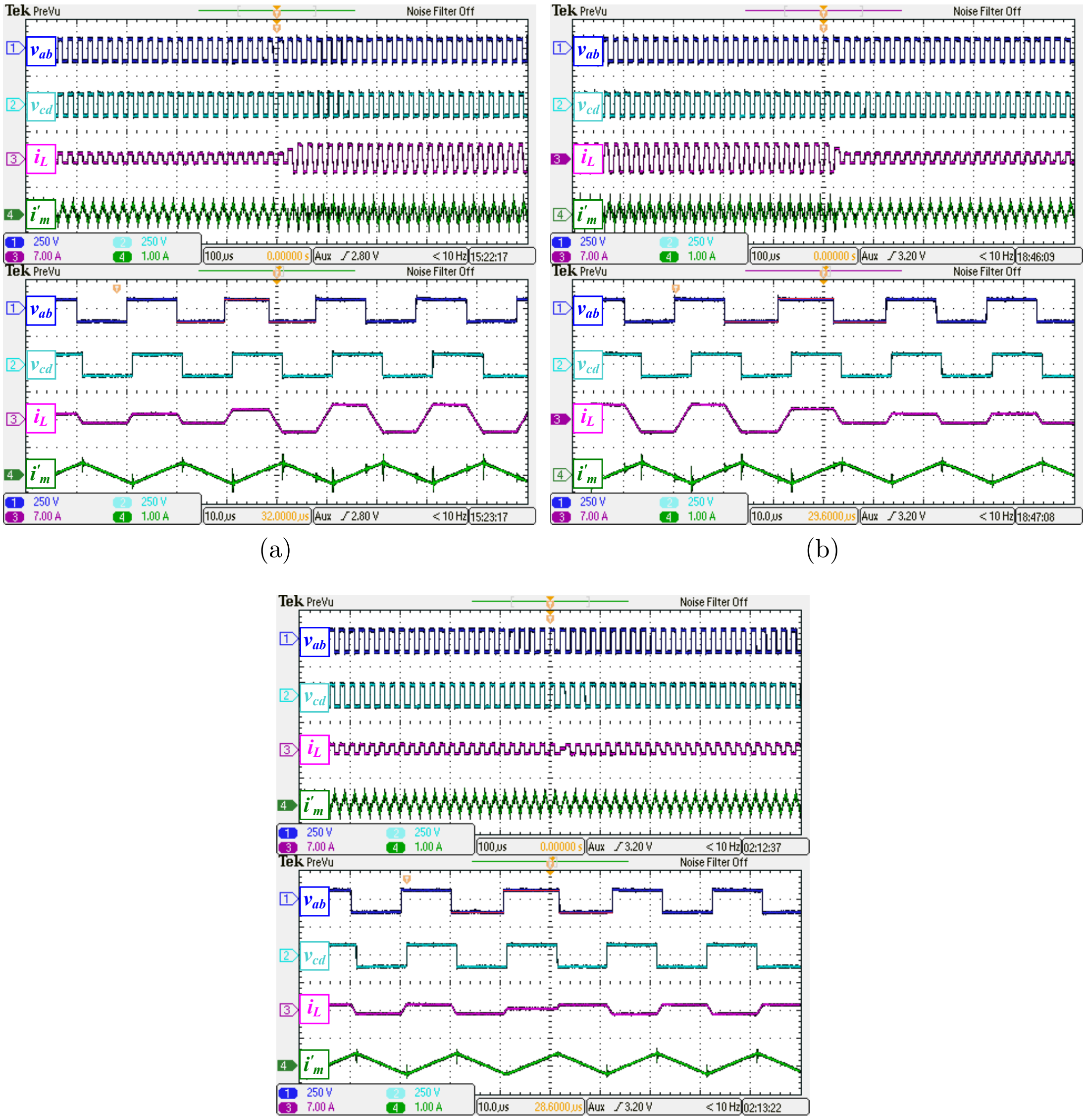

(a) (b)

(c)

Fig. 3.18. Open-loop experimental results under the proposed SS-OTPSM. (a) The phase-shift ratio is changed from $\frac{1}{9}$ to $\frac{1}{3}$. (b) The phase-shift ratio is changed from $\frac{1}{3}$ to $\frac{1}{9}$. (c) The phase-shift ratio is changed from $\frac{1}{9}$ to $-\frac{1}{9}$.

Extracting the performance data of open-loop experiments from Figs. 3.17 to 3.20, the performance evaluations of different transient modulation strategies are presented in Fig. 3.21. It can be seen that when there are abrupt and large-amplitude changes in phase-shift ratio, SS-OTPSM and OTPSM have shown a number of advantages over CTPSM. Under CTPSM, the transient waveforms of i_L and i_m' take several cycles to reach their new steady states, but it takes only about one cycle under SS-OTPSM and OTPSM to achieve the same states. In

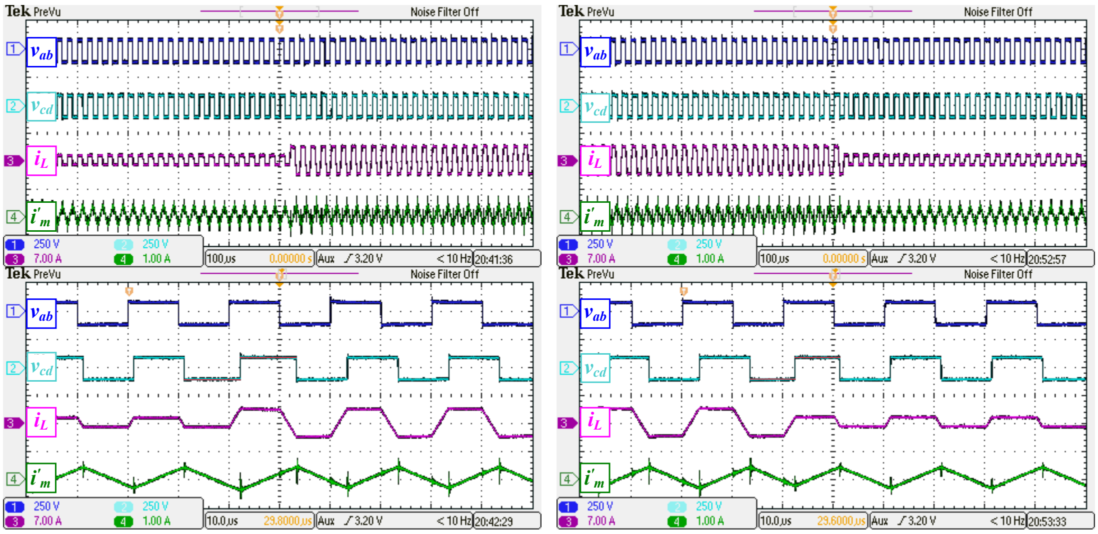

(a) (b)

Fig. 3.19. Open-loop experimental results under Type-C_1 OTPSM [97]. (a) The phase-shift ratio is changed from $\frac{1}{9}$ to $\frac{1}{3}$. (b) The phase-shift ratio is changed from $\frac{1}{3}$ to $\frac{1}{9}$.

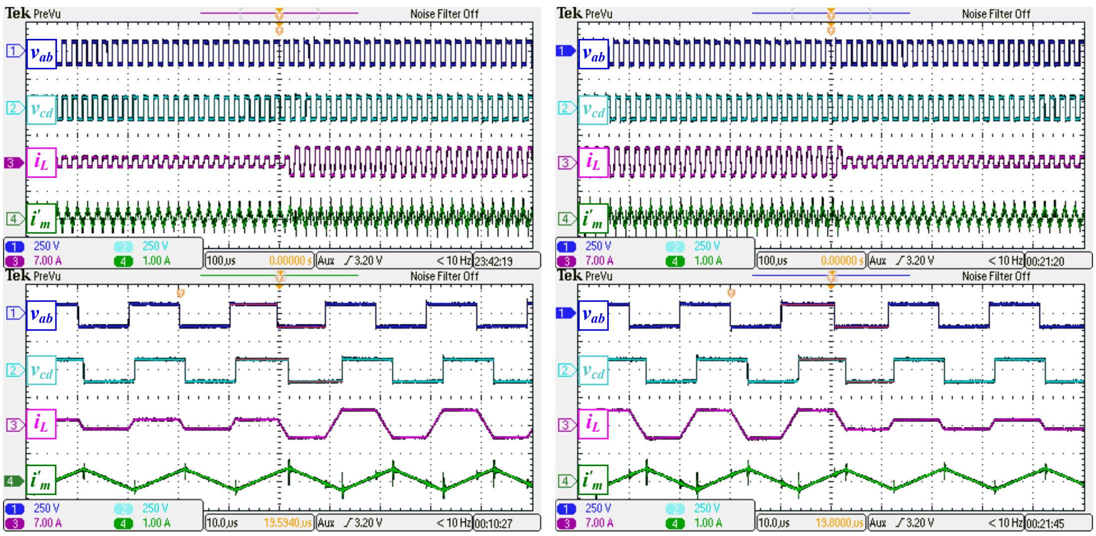

(a) (b)

Fig. 3.20. Open-loop experimental results under Type-E_1 OTPSM [100]. (a) The phase-shift ratio is changed from $\frac{1}{9}$ to $\frac{1}{3}$. (b) The phase-shift ratio is changed from $\frac{1}{3}$ to $\frac{1}{9}$.

addition, large peak overshoots/undershoots and excessive transient dc offsets in i_L and i_m' are eliminated under SS-OTPSM and OTPSM. As a result, the transient current stresses on the power devices are significantly reduced and the saturation of magnetic elements can be prevented.

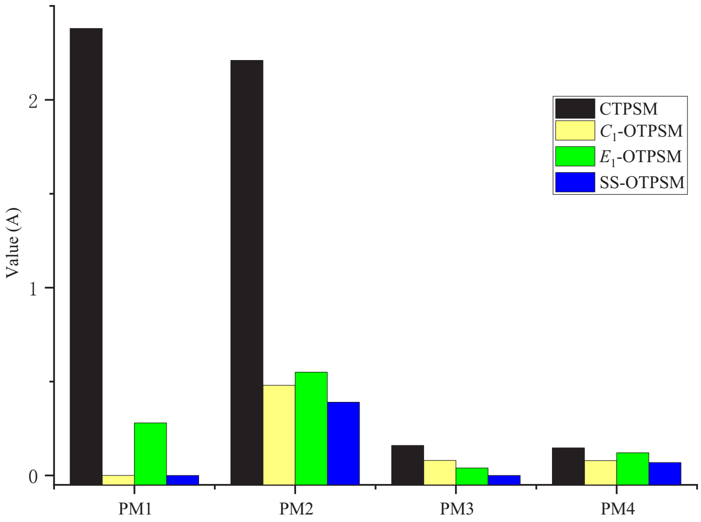

(a)

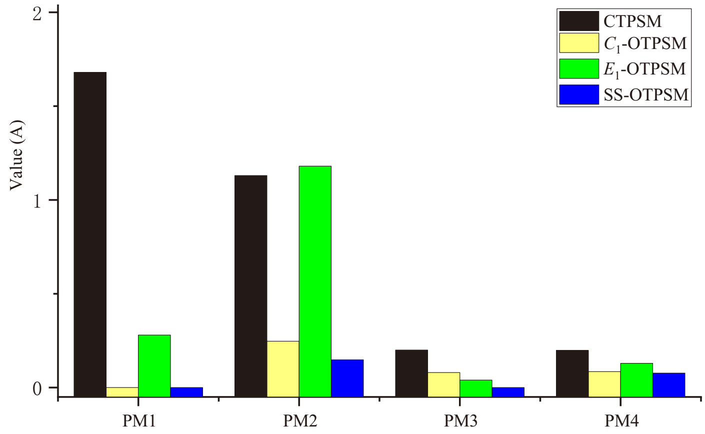

(b)

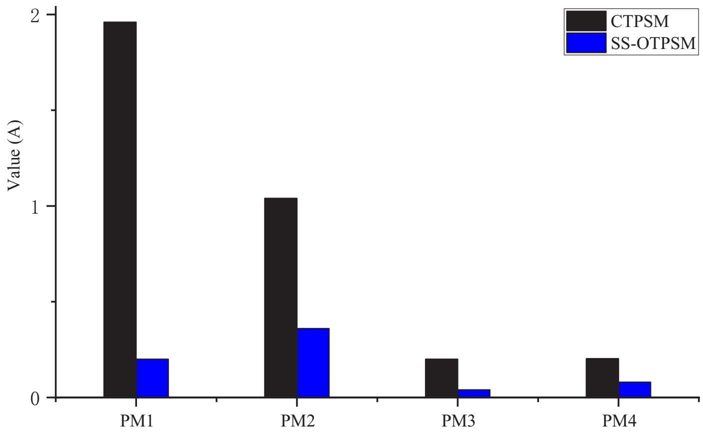

(c)

Fig. 3.21. Performance evaluation of different transient modulation strategies in open-loop experiments. (a) For an increase in the phase-shift ratio from $\frac{1}{9}$ to $\frac{1}{3}$. (b) For an decrease in the phase-shift ratio from $\frac{1}{3}$ to $\frac{1}{9}$. (c) The phase-shift ratio is changed from $\frac{1}{9}$ to $-\frac{1}{9}$.

It is worth noting that, besides achieving a lower dc offset in i_L, the dc offset and overshoot (or undershoot) in i_m' under SS-OTPSM are found to be significantly lower than those achieved with both Type-C_1 and Type-E_1 OTPSM strategies, since the transient operations of these two OTPSM strategies involve waveform changes in v_{cd}. Essentially, the proposed SS-OTPSM is a member of the class of OTPSM strategies. However, according to the performance evaluation described in Fig. 3.21, SS-OTPSM performs better than the other two OTPSM strategies due to its capability in further suppressing transient dc offsets in both i_L and i_m

simultaneously. This finding is consistent with the open-loop simulation results presented in Fig. 3.5 and the theoretical analysis of SS-OTPSM and OTPSM.

Compared with all the existing OTPSM strategies, SS-OTPSM is more readily implemented in a cycle-by-cycle manner in microprocessors due to its conceptual simplicity and lower implementation complexity, which makes it inherently suitable for practical use. In the next subsection, the performance of SS-OTPSM will be further examined by closed-loop experiments.

3.5.2 Closed-Loop Tests

To compare the closed-loop dynamic performances under MPC+CTPSM, MPC+E_1-OTPSM, MPC+SS-OTPSM, and EMPC+SS-OTPSM, experimental results of step-load changes between 25% and 95% of the full load are shown in Figs. 3.22 to 3.25, where the maximum output voltage deviation (i.e., Max ΔV_2) and settling time are annotated. The control parameters of $\{K^*_{p1} = 0.07,\ K_{i1} = 0.3\}$ are used for the tests shown in Figs. 3.22 and 3.23, and $\{K^*_{p2} = 0.1,\ K_{i2} = 0.5\}$ which correspond to a fast-loop configuration, are depicted in Figs. 3.24 and 3.25. It should be noted that the control parameters and experimental conditions used in the subfigures of Figs. 3.22 to 3.25 are identical. The performance data of these closed-loop experiments are extracted and compared in Fig. 3.26 in terms of PM1$\sim$PM4.

Generally, the experimental transient responses depicted in Figs. 3.22 to 3.25 match closely with the simulation results shown in Fig. 3.9. As expected, excessive overshoots (or undershoots) and transient dc offsets are observed in both i_L and i'_m under MPC+CTPSM, and these dc offsets have significant influences on the high-frequency-link waveforms such as the ripples of V_2, which results in the largest output voltage deviation in all different cases. As shown in Figs. 3.24 and 3.25, these issues become even more apparent in the case of increased bandwidth, i.e., with K^*_{p2} and K_{i2}. In contrast to this, all such problems as-

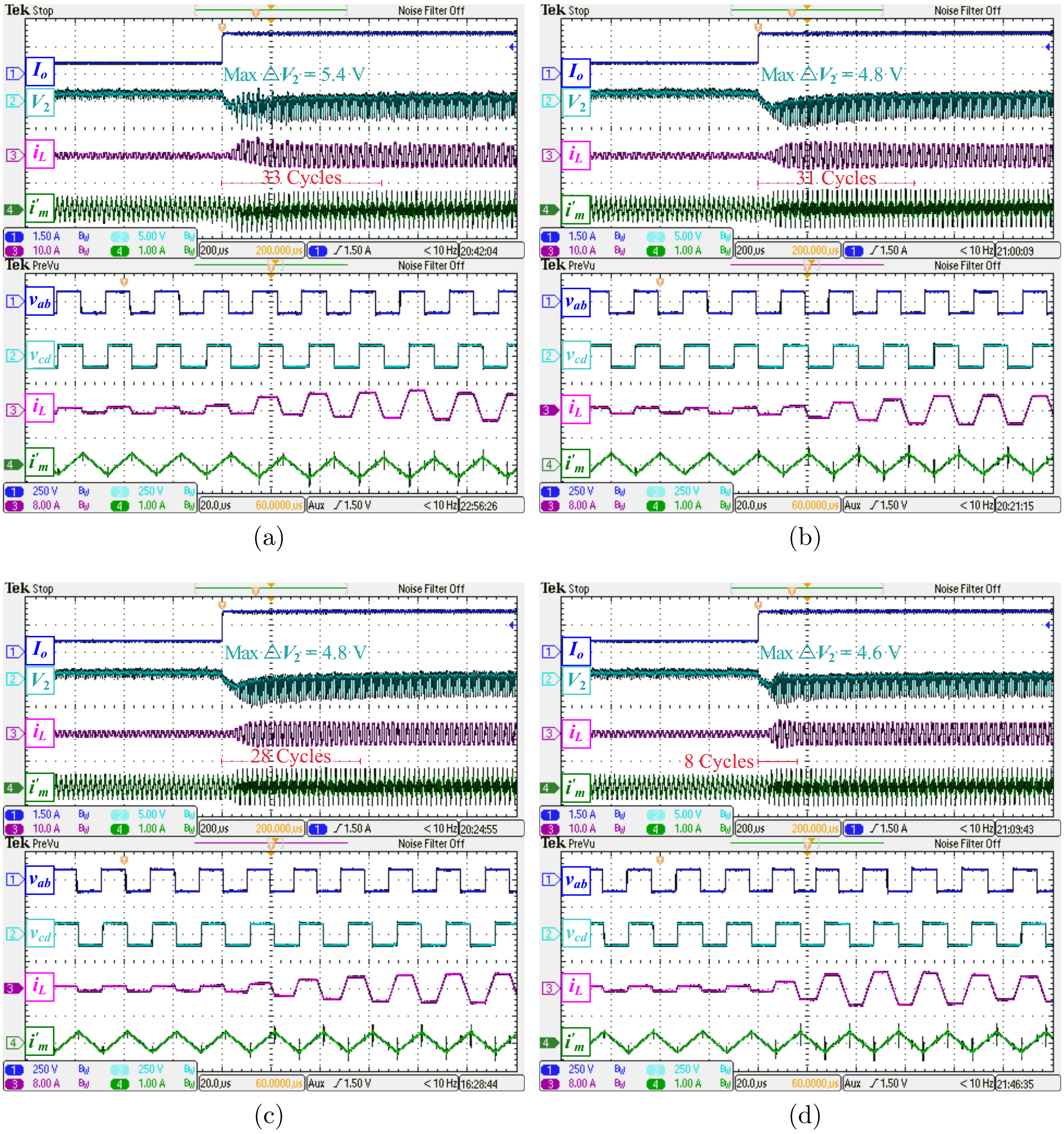

Fig. 3.22. Experimental closed-loop transient responses for a step change in the load from 25% to 95% with $\{K_{p1}^{*}=0.07,\ K_{i1}=0.3\}$ under (a) MPC+CTPSM, (b) MPC+E_1-OTPSM, (c) MPC+SS-OTPSM, and (d) EMPC+SS-OTPSM.

sociated with transient dc offsets are largely suppressed under E_1-OTPSM and SS-OTPSM. According to Fig. 3.26, and the results of performance comparison suggest that MPC+SS-OTPSM outperforms MPC+CTPSM and MPC+E_1-OTPSM in the four key performance aspects, i.e., PM1∼PM4. It is also observed that the settling times under MPC+CTPSM are always the longest compared to other systems, and the settling times under MPC+SS-OTPSM are always shorter than those under MPC+E_1-OTPSM. As a result, compared with the conventional

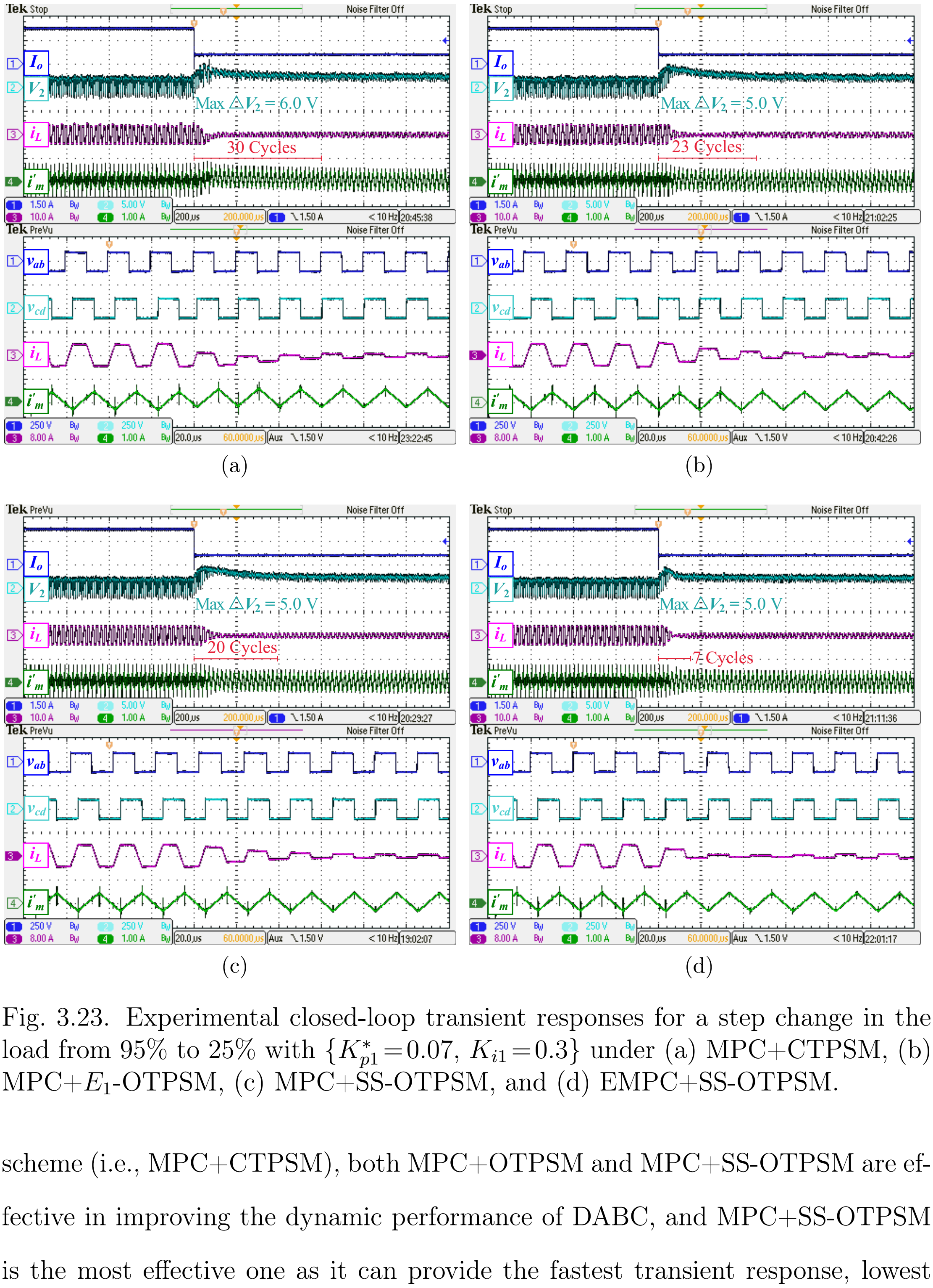

(a) (b) (c) (d)

Fig. 3.23. Experimental closed-loop transient responses for a step change in the load from 95% to 25% with $\{K_{p1}^{*}=0.07,\ K_{i1}=0.3\}$ under (a) MPC+CTPSM, (b) MPC+E_1-OTPSM, (c) MPC+SS-OTPSM, and (d) EMPC+SS-OTPSM.

scheme (i.e., MPC+CTPSM), both MPC+OTPSM and MPC+SS-OTPSM are effective in improving the dynamic performance of DABC, and MPC+SS-OTPSM is the most effective one as it can provide the fastest transient response, lowest transient dc offsets, and smallest overshoots/undershoots in all cases.

However, although transient dc offsets can be significantly reduced, the settling times achieved under both MPC+E_1-OTPSM and MPC+SS-OTPSM are only several cycles shorter than those achieved under MPC+CTPSM. As anal-

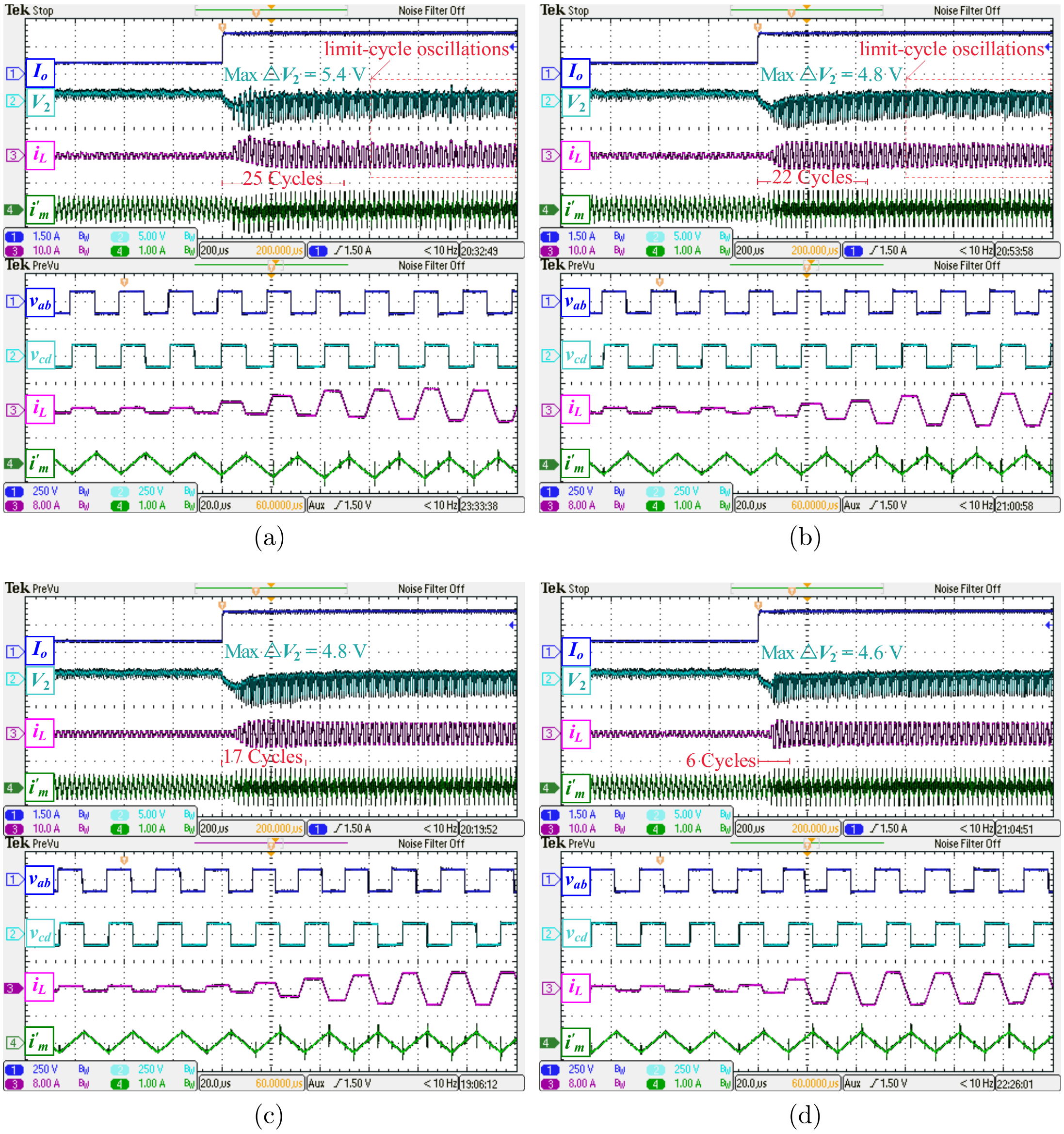

Fig. 3.24. Experimental closed-loop transient responses for a step change in the load from 25% to 95% with $\{K^*_{p2}=0.1,\ K_{i2}=0.5\}$ under (a) MPC+CTPSM, (b) MPC+E_1-OTPSM, (c) MPC+SS-OTPSM, and (d) EMPC+SS-OTPSM.

ysed in Subsection 3.4.2 and Subsection 3.4.3, a refined EMPC that matches the transient operation of SS-OTPSM is required to fully realize its potential benefits. Referring to the experimental results shown in Figs. 3.22 to 3.25, under EMPC+SS-OTPSM, the settling times can be significantly reduced to $6 \sim 8$ cycles with no obvious increase in the overshoot/undershoot of i_L and i'_m, and the output voltage deviation is also the smallest compared with other systems, which verifies the positive contribution of the proposed EMPC in realizing the benefits of SS-

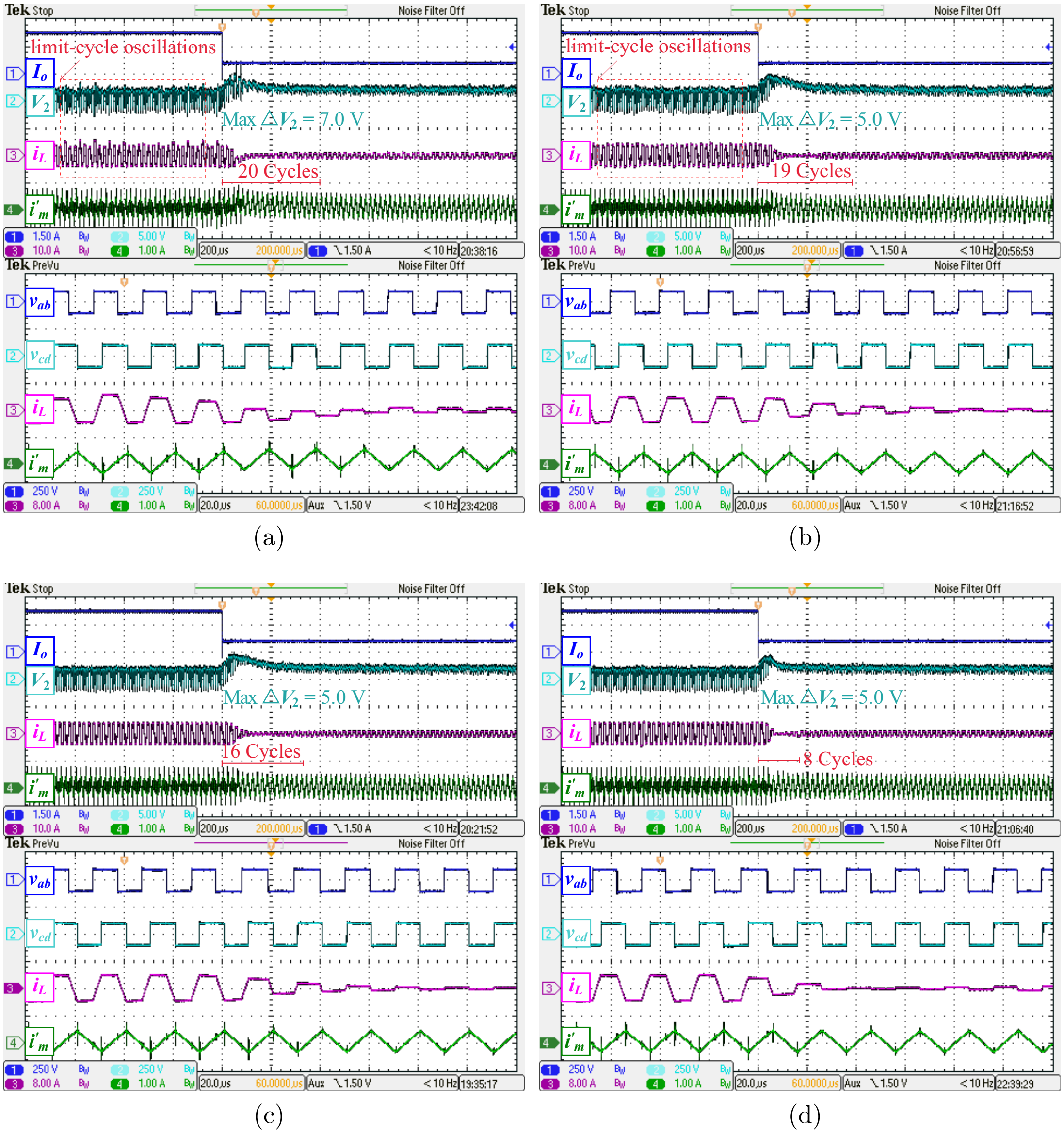

Fig. 3.25. Experimental closed-loop transient responses for a step change in the load from 95% to 25% with $\{K^*_{p2}=0.1,\ K_{i2}=0.5\}$ under (a) MPC+CTPSM, (b) MPC+E_1-OTPSM, (c) MPC+SS-OTPSM, and (d) EMPC+SS-OTPSM.

OTPSM to the fullest without further modification of control parameters. In all cases, EMPC+SS-OTPSM minimizes the trajectory tracking error and optimizes the inductor current (as well as the magnetizing current) to ensure minimum transient response time and waveform distortions, thus enabling an optimal transient performance of an MPC-controlled NR-DABC.

In addition, as can be seen from Figs. 3.24(a), 3.24(b), 3.25(a), and 3.25(b), there are small-amplitude limit-cycle oscillations in the steady-state waveforms of

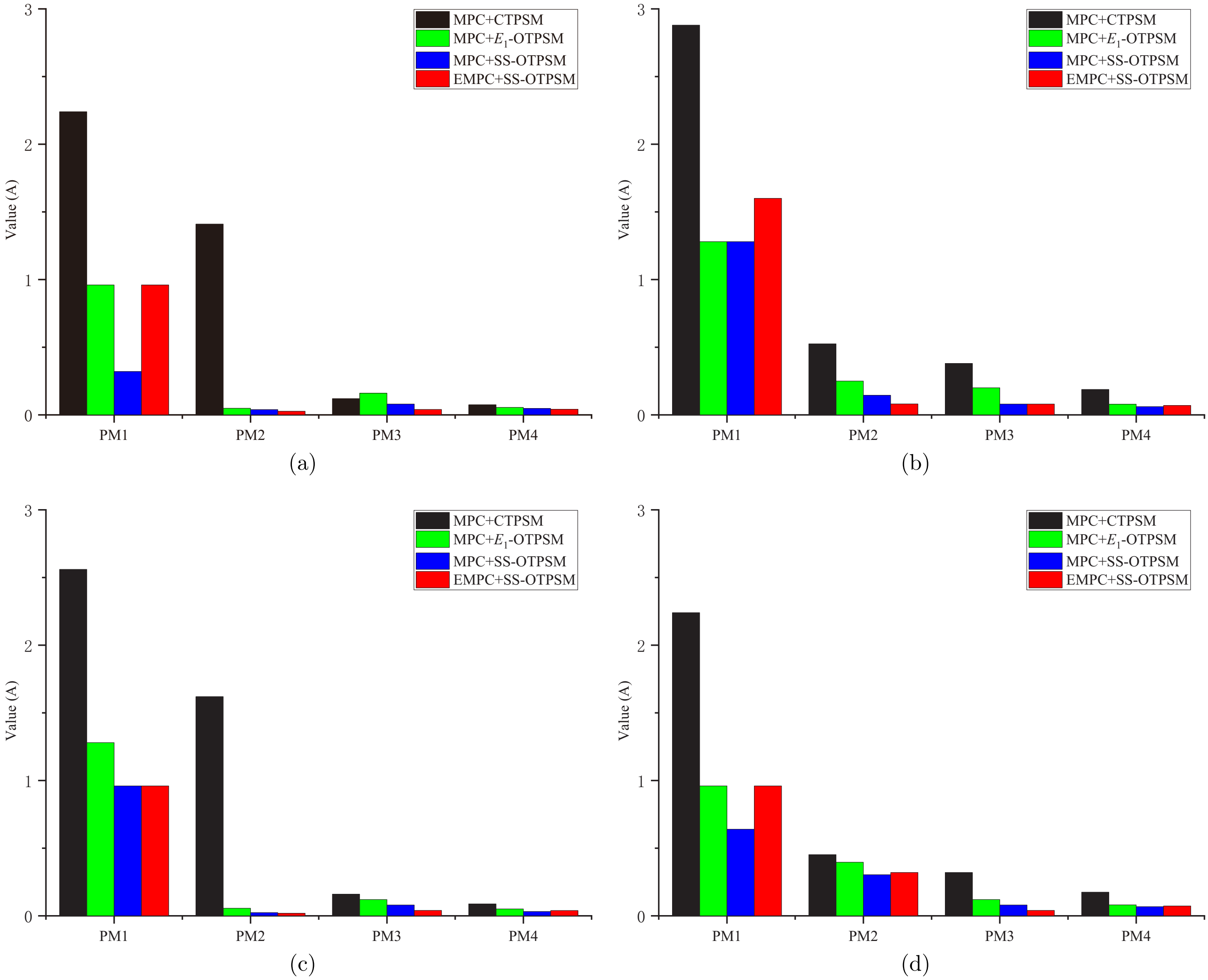

Fig. 3.26. Performance evaluation of closed-loop experiments. (a) Load step-up transition with $\{K^*_{p1} = 0.07,\ K_{i1} = 0.3\}$. (b) Load step-down transition with $\{K^*_{p1} = 0.07,\ K_{i1} = 0.3\}$. (c) Load step-up transition with $\{K^*_{p2} = 0.10,\ K_{i2} = 0.5\}$. (d) Load step-down transition with $\{K^*_{p2} = 0.10,\ K_{i2} = 0.5\}$.

V_2 and i_L under MPC+CTPSM and MPC+E_1-OTPSM, which are similar to the observations in Fig. 3.10(a). As explained previously, these low-frequency oscillations are caused by the presence of accumulated errors due to aliasing effect, and the presence of residual transient dc offsets. In general, an incompatible transient modulation tends to introduce switching noise, quantization noise, multiple time delays, etc., to the control loop, which ultimately results in reduced stability and hence degraded steady-state and transient performances in DABC. Since the volt-second product on the energy-transfer inductor and magnetizing inductor can be more precisely balanced under SS-OTPSM, it is more robust than CTPSM and E_1-OTPSM in terms of error compensation and control performance. Hence, a major advantage of SS-OTPSM is its ease of use and compatibility with high-bandwidth (or high-gain) controllers for achieving fast convergence to new steady states without oscillation when implemented in closed-loop configuration.

3.6 Chapter Summary

This chapter comprehensively overviews the existing OTPSM strategies for SPS modulated NR-DABC under a unified transient-modulation framework. The presented theoretical analysis reveals that satisfying dynamic volt-second balance alone does not guarantee the complete elimination of transient dc offsets in both energy-transfer and transformer's magnetizing inductors during transient state, unless the time-averaged values of i_{ab} and i_{cd} over the transient state are maintained at zero. A symmetric single-sided OTPSM (SS-OTPSM) strategy is then proposed based on this theory. As confirmed by simulation and experimental results, the newly proposed SS-OTPSM demonstrates its superiority over CTPSM and other existing OTPSM strategies in its total elimination of the transient dc offsets in both energy-transfer and transformer's magnetizing inductors under all different open-loop operating conditions. It is by far the simplest and most effective OTPSM strategy unmatched by all existing OTPSM-based strategies.

This chapter also reveals the importance of controller design on the effectiveness of transient modulation. When conventional power calculation associated with steady-state operation is adopted for implementing MPC+SS-OTPSM, the significant error present in the power calculation has led to an erroneous prediction of the optimal phase-shift ratio, and hence a sub-optimal performance of SS-OTPSM similar to the performances of CTPSM and older OTPSM strategies.

It has been successfully demonstrated that, through the use of an augmented power calculation matching the operation of SS-OTPSM and its application in an enhanced MPC (EMPC), a remarkable improvement in transient performance has been achieved where the settling time is reduced by over 50%. Overall, through the co-optimization of SS-OTPSM and EMPC, truly optimal dynamics of NR-DABC can be achieved easily and cost effectively.

Chapter 4

Trajectory-Switching Modulation for Suppression of Transient Oscillations

4.1 Introduction

In Chapter 3, effective OTPSM strategies for eliminating transient dc offsets in NR-DABC are discussed, but they cannot be used for attenuating HF transient oscillations in SR-DABC as the resonant current of SR-DABC is a non-linear function of the phase-shift angle (or control variable), which is different from the inductor current of NR-DABC.

In this chapter, a novel trajectory-switching modulation (TSM) strategy is proposed. To verify its advantages over CTPSM, the transient performances under both modulation strategies when applied to an MPC-controlled SR-DABC are presented and compared, and their simulation and experimental results are systematically analyzed. The benefits of the proposed TSM and the key contributions of this chapter are outlined below:

(1) It is compatible with fast and large-amplitude changes in the phase-shift

angle of SR-DABC, enabling it to swiftly reach a new steady state (ideally within about one switching cycle) following the external disturbances without inducing noticeable HF transient oscillations.

(2) Unlike existing trajectory control methods, no voltage and current information is required for the implementation of the proposed method, thus eliminating the need for additional costly high-bandwidth sensors.

(3) This chapter presents the first practical demonstration of the closed-loop implementation of transient modulation strategy in SR-DABC and its effectiveness in suppressing HF transient oscillations.

(4) Unlike existing feedback control designs with which control bandwidth must be limited to prevent the occurrence of HF transient oscillations, the elimination of such oscillations by the proposed TSM method enables the implementation of high-gain, high-bandwidth fast controller in SR-DABC to achieve superior transient performance.

The rest of this chapter is organized as follows. Section 4.2 describes the basic operation of SPS modulation for SR-DABC. The principle of operation of the proposed TSM strategy is presented in Section 4.3. In Section 4.4, a detailed system modelling and MPC design are presented, followed by simulations and experimental results in Section 4.5. Finally, conclusions are drawn in Section 4.6.

4.2 Basic Operation of SPS Modulation in SR-DABC

Fig. 1.7(a) shows the power stage of a SR-DABC using T-model transformer. In order to focus on the analysis of transient oscillatory dynamics of SR-DABC, the transformer's magnetizing inductance is assumed to be very large and neglected in this chapter. In addition, since R_s is small in practice, its effect is often negligible.

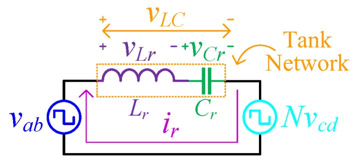

Fig. 4.1. Simplified equivalent circuit of SR-DABC.

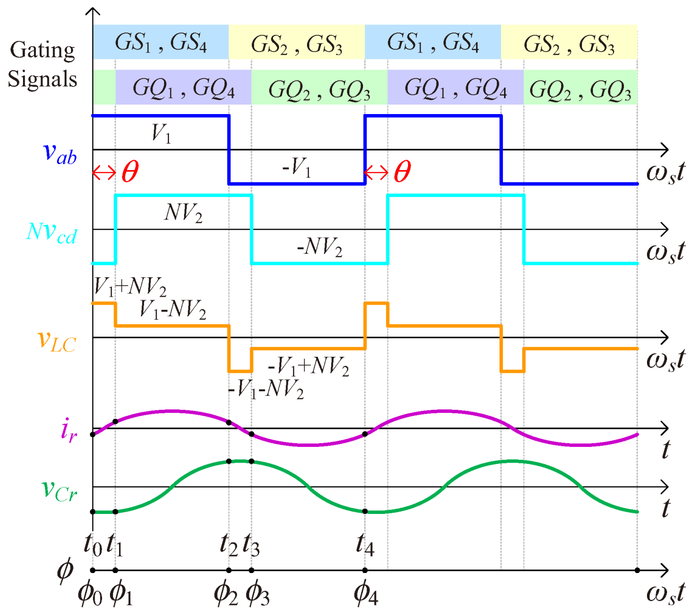

Fig. 4.2. Steady-state time-domain waveforms of SR-DABC under SPS modulation.

Thus, the condition $R_s^2 \ll 4L_r/C_r$ holds true, and a simplified equivalent circuit of SR-DABC can be obtained as shown in Fig. 4.1, which is second-order and underdamped.

4.2.1 Time-Domain Analysis of Steady-State Operation Under SPS Modulation

Fig. 4.2 shows the steady-state time-domain waveforms of SR-DABC under SPS modulation. It can be seen that θ determines the waveform of v_{LC}, thus controlling the voltage applied to the series resonant tank. Referring to Fig. 4.1, the L_r-C_r series resonant network is excited by a multi-level voltage $v_{LC} = v_{ab} - Nv_{cd}$. Applying Kirchhoff's voltage law (KVL) to the equivalent circuit in Fig.

4.1 yields

$$\begin{aligned} v_{LC} &= L_r \frac{\mathrm{d}i_r(t)}{\mathrm{d}t} + \frac{1}{C_r}\int_0^t i_r(t)\mathrm{d}t + v_{Cr}(0) \\ \Rightarrow 0 &= L_r \frac{\mathrm{d}^2 i_r(t)}{\mathrm{d}t^2} + \frac{1}{C_r} i_r(t). \end{aligned} \tag{4.1}$$

To solve (4.1), i_r can be generally assumed to have the following form:

$$i_r(t) = A_i \cos(\omega_r(t - t_i)) + B_i \sin(\omega_r(t - t_i)) \tag{4.2}$$

or

$$i_r\left(\frac{\phi}{\omega_s}\right) = A_i \cos\frac{\phi - \phi_i}{F} + B_i \sin\frac{\phi - \phi_i}{F} \tag{4.3}$$

for t in the time interval $[t_i, t_{i+1}]$, where A_i and B_i are constants to be determined and $\omega_r = 1/(\sqrt{L_r C_r})$ is the angular resonant frequency. $\phi_i = \omega_s t_i$ is the angular displacement at time t_i, where $\omega_s = 2\pi f_s$ is the angular switching frequency and i = 1, 2, 3, ... indicates the ith trajectory-switching point.

Substituting (4.3) into (4.1) gives

$$v_{Cr}\left(\frac{\phi}{\omega_s}\right) = \frac{1}{C_r}\int_0^t i_r(t)\mathrm{d}t + v_{Cr}(0) = v_{LC} - \left(-A_i \sin\frac{\phi-\phi_i}{F} + B_i \cos\frac{\phi-\phi_i}{F}\right) Z_r \tag{4.4}$$

where $Z_r = \sqrt{L_r/C_r}$ is defined as the characteristic impedance. Then, $A_i = i_r(\phi_i/\omega_s)$ and $B_i = (v_{LC} - v_{Cr}(\phi_i/\omega_s))/Z_r$ can be obtained by letting $\phi = \phi_i$ in (4.3) and (4.4), which gives the general analytical expressions of i_r and v_{Cr} as

$$i_r\left(\frac{\phi}{\omega_s}\right) = i_r\left(\frac{\phi_i}{\omega_s}\right)\cos\frac{\phi-\phi_i}{F} + \frac{v_{LC} - v_{Cr}\left(\frac{\phi_i}{\omega_s}\right)}{Z_r}\sin\frac{\phi-\phi_i}{F} \tag{4.5}$$

$$v_{Cr}\left(\frac{\phi}{\omega_s}\right) = v_{LC}\cdot\left(1 - \cos\frac{\phi-\phi_i}{F}\right) + v_{Cr}\left(\frac{\phi_i}{\omega_s}\right)\cos\frac{\phi-\phi_i}{F} + Z_r \cdot i_r\left(\frac{\phi_i}{\omega_s}\right)\sin\frac{\phi-\phi_i}{F}. \tag{4.6}$$

The sine and cosine terms in (4.5) and (4.6) can be combined by using trigonometric identities to give (4.7), which indicates that the two-dimensional (2D) state-plane diagram shown in Fig. 4.3 is graphically described by piecewise circular arcs.

$$Z_r^2 i_r^2\left(\frac{\phi}{\omega_s}\right) + \left(v_{Cr}\left(\frac{\phi}{\omega_s}\right) - v_{LC}\right)^2 = Z_r^2 i_r^2\left(\frac{\phi_i}{\omega_s}\right) + \left(v_{Cr}\left(\frac{\phi_i}{\omega_s}\right) - v_{LC}\right)^2 \tag{4.7}$$

Due to the steady-state operation of SPS modulation, the waveforms of i_r and

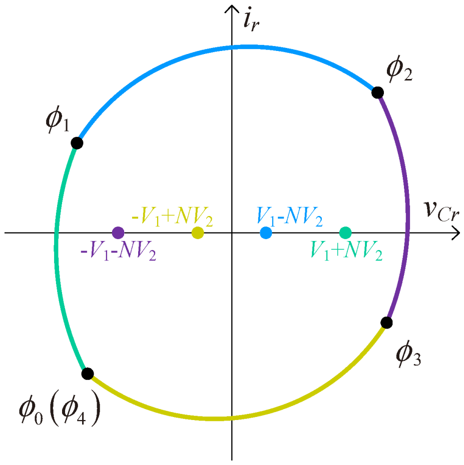

Fig. 4.3. Steady-state state-plane diagram of SR-DABC under SPS modulation.

v_{Cr} are symmetrical comprising four distinct time intervals in one switching cycle. It can be observed from Fig. 4.3 that point $\phi_0(\phi_4)$ and point ϕ_2 are symmetrical about the origin, so as point ϕ_1 and point ϕ_3. Hence,

$$\begin{cases} i_r\left(\dfrac{\phi_0}{\omega_s}\right) = -i_r\left(\dfrac{\phi_2}{\omega_s}\right), v_{Cr}\left(\dfrac{\phi_0}{\omega_s}\right) = -v_{Cr}\left(\dfrac{\phi_2}{\omega_s}\right) \\ i_r\left(\dfrac{\phi_1}{\omega_s}\right) = -i_r\left(\dfrac{\phi_3}{\omega_s}\right), v_{Cr}\left(\dfrac{\phi_1}{\omega_s}\right) = -v_{Cr}\left(\dfrac{\phi_3}{\omega_s}\right). \end{cases} \tag{4.8}$$

By substituting (4.8) into (4.5) and (4.6), the values of $i_r(\phi_i/\omega_s)$ and $v_{Cr}(\phi_i/\omega_s)$ at different trajectory-switching points ϕ_i can be solved exactly. For example,

$$i_r\left(\frac{\phi_0}{\omega_s}\right) = \frac{1}{Z_r}\left[NV_2 \sec\left(\frac{\pi}{2F}\right)\sin\left(\frac{\pi-2\theta}{2F}\right) - V_1 \tan\left(\frac{\pi}{2F}\right)\right] \tag{4.9}$$

$$v_{Cr}\left(\frac{\phi_0}{\omega_s}\right) = NV_2\left[1-\cos\left(\frac{\theta}{F}\right) - \sin\left(\frac{\theta}{F}\right)\tan\left(\frac{\pi}{2F}\right)\right] \tag{4.10}$$

and other instantaneous values of i_r and v_{Cr} at any time can be obtained accordingly.

4.2.2 Transient-State Operation of SPS Modulation

During transient state, the phase-shift angle of SR-DABC is generally updated from its initial value θ in the current cycle to $\theta + \delta$ before the end of the next switching cycle, where $\delta = \Delta\theta$ is the angle increment or decrement. The transient-state operation of SPS modulation (i.e., CTPSM) is illustrated in Fig. 4.4, where

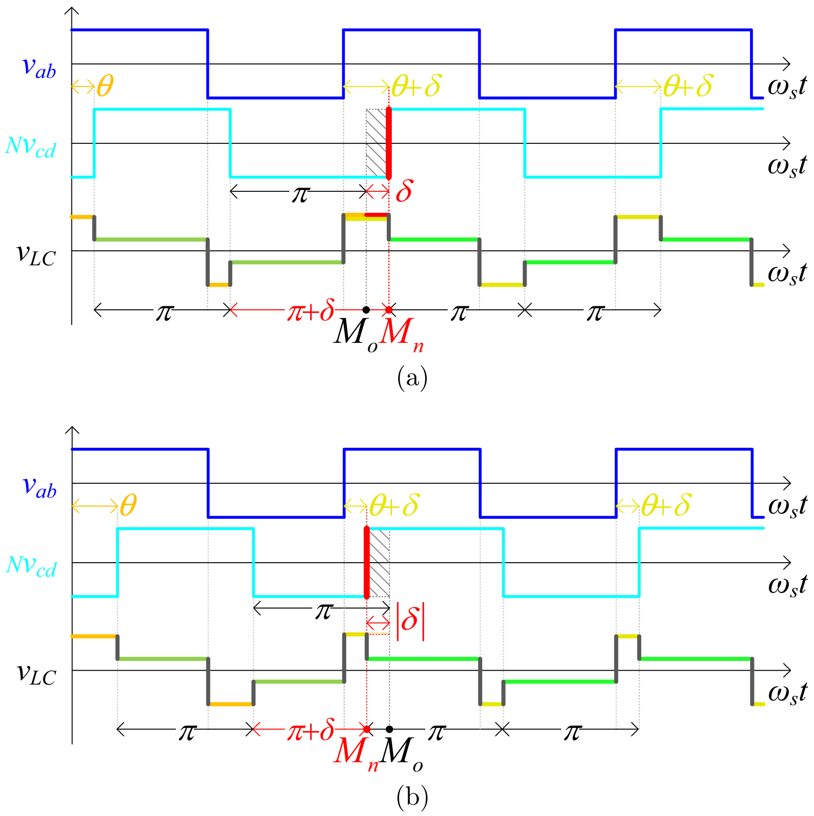

Fig. 4.4. Conventional transient-state operation of SPSM (CTPSM) for (a) $\delta > 0$. (b) $\delta < 0$.

the transient low-level duration of v_{cd} will be increased ($\delta > 0$) or decreased ($\delta < 0$) by $|\delta|$, i.e., the turn-on instances of Q_1 and Q_4 are adjusted from point M_o to point M_n, in order to realize a desired new phase-shift angle $\theta + \delta$.

Despite its popularity, the impact of CTPSM on the transient behavior of SR-DABC, however, has not been thoroughly investigated in the literature. To better examine the large-scale transient behavior of SR-DABC under CTPSM, open-loop simulations (with both sides of the converter connected to dc voltage sources and other converter parameters specified in Table 4.1) were performed on Powersim (PSIM) software and the results are presented in Fig. 4.5. In Figs. 4.5(a) and (b), the converter is operated in forward power modes; in Fig. 4.5(c), the direction of power flow changes from the forward mode to the reverse mode.

It is evident from the simulation results shown in Fig. 4.5 that CTPSM generally leads to large-amplitude HF transient oscillations which exist in all resonant

Table 4.1 Circuit Parameters and Specifications Used in Chapter 4.

Item	Description
Rated Output Power P_{max}	250 W
Input Voltage V_1	100 V
Output Voltage V_2	100 V
Output Capacitance C_o	47 μF
Load Resistance R_L	100/45 Ω
Transformer Turns Ratio $N:1$	1 : 1
Resonant Inductance L_r	321 μH
Equivalent series resistance of L_r	211 mΩ
Resonant Capacitance C_r	45 nF
Resonant Frequency f_r	41.8756 kHz
Switching Frequency f_s	50 kHz
Dead Time	300 ns
Switches $S_1{\sim}S_4$ and $Q_1{\sim}Q_4$	UnitedSiC UJC06505K
Drain-Source ON Resistance	45 mΩ
Gate Driver	TI UCC21520
Op Amp for ADC	TI TL082
Voltage Transducer	Two-Resistor Voltage Divider
Current Transducer	LEM LA 55-P
Microprocessor	TI TMS320F28335
Simulation Software	PSIM 12.0.4

tank voltage and current waveforms (e.g., i_r, v_{Cr} and v_{Lr}). The oscillations are caused by the excitation of the resonant tank by a step change in v_{LC} resulting from a step increase or decrease of the low-level duration of v_{cd}. Since the resonant tank will absorb or release abundant energy at that transient moment, the periodic tank-energy balance will be broken suddenly. Taking the frequency spectrum of the transient resonant current i_r, as shown in Fig. 4.6, reveals that it contains an additional component at the resonant frequency $f_r = \omega_r/(2\pi)$ which is superimposed with the dominant component at the switching frequency f_s. The switching frequency component is known to originate from the forced response of the second-order L_r-C_r-R_r resonant tank due to the terminal voltages v_{ab} and v_{cd}, while the resonant frequency component emerges from the natural response of the

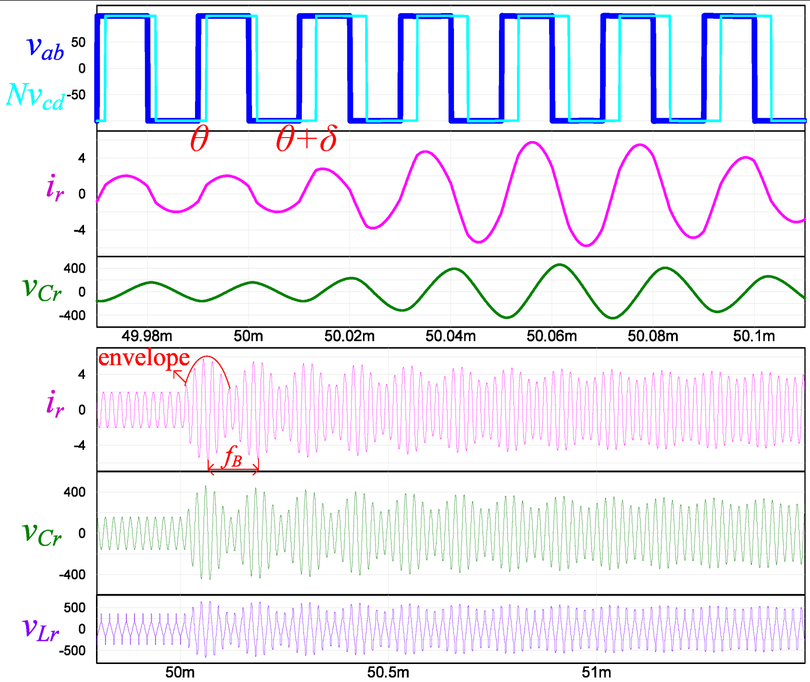

(a)

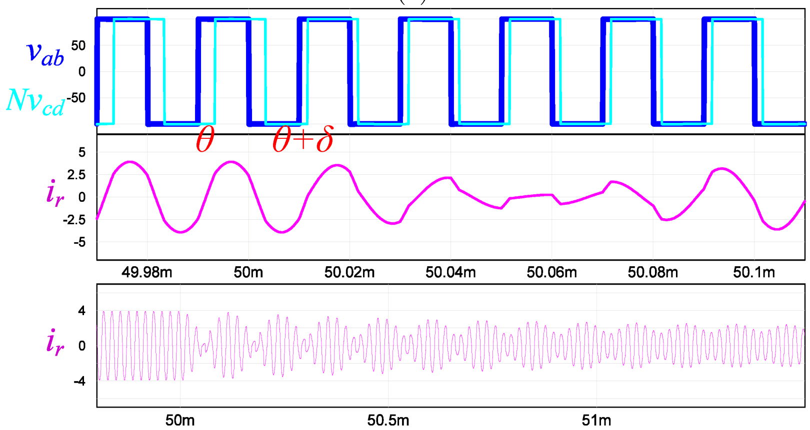

(b)

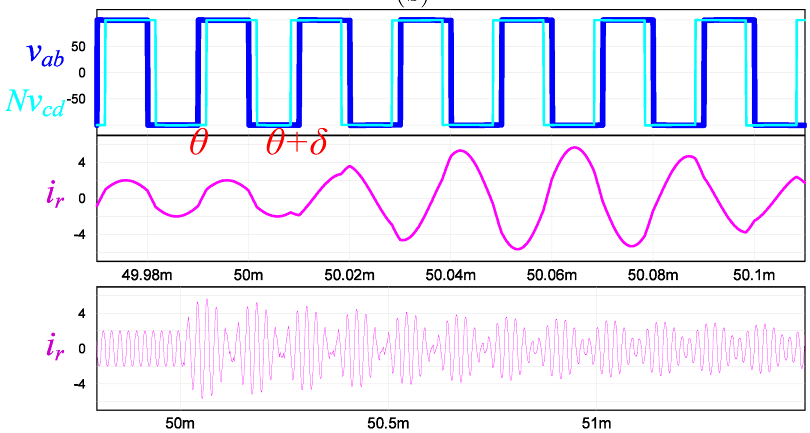

(c)

Fig. 4.5. Simulated transient responses of SR-DABC under CTPSM. (a) Step-load increase: $\theta = \pi/6$, $\delta = \pi/6$ and $\theta + \delta = \pi/3$. (b) Step-load decrease: $\theta = \pi/3$, $\delta = -\pi/6$ and $\theta + \delta = \pi/6$. (c) Step change of power flow direction: $\theta = \pi/6$, $\delta = -\pi/3$ and $\theta + \delta = -\pi/6$.

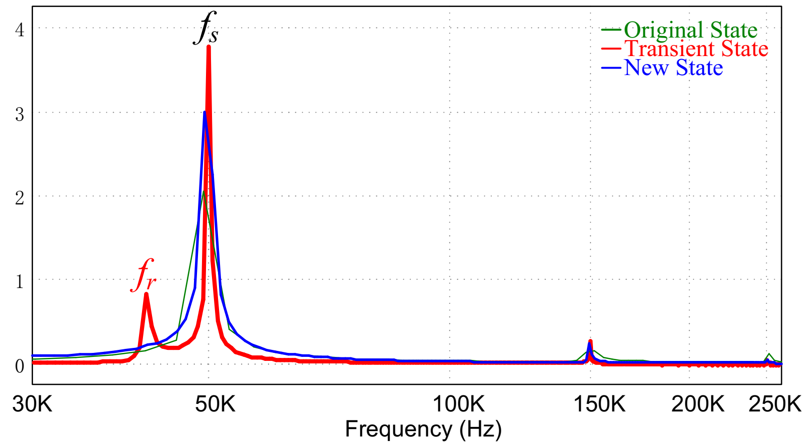

Fig. 4.6. Frequency spectrum of resonant current i_r under different states.

resonant tank when excited by a step change in v_{LC}.

The oscillations occur at the beat frequency, which result from the interaction between the switching-frequency and resonant-frequency components in the series resonant tank during transient state. By the effect of the beat phenomenon, the superposition of the two sinusoidal components produces a resultant wave with an envelope that fluctuates at the beat frequency $f_B = f_s - f_r$ [39]. For all the simulated cases shown in Fig. 4.5, the switching frequency f_s and the resonant frequency f_r are 50 kHz and 41.8 kHz, respectively, hence the theoretical beat frequency is 8.2 kHz, which closely matches with the frequency of the envelopes of the simulated transient waveforms. For a second-order L_r-C_r-R_r resonant circuit, its natural response will decay exponentially with a time constant $2L_r/R_r$, accompanied by a decaying amplitude of the envelope, as the short-lived burst of energy is dissipated by R_r.

It should be noted a large step change in δ will lead to large-amplitude HF transient oscillations which will impose high voltage and current stresses on all the power stage components of SR-DABC, and may even damage them. These oscillations reflect the main drawback of CTPSM and the problem is typically avoided by gradually updating the phase-shift angle so that the phase-shift angle is varied by a small increment/decrement between two consecutive switching cycles. Clearly, this is not a desirable solution as it leads to slow converter's dynamic response. The problem must be mitigated by designing a new transient-state modulation method.

4.3 Proposed Trajectory-Switching Modulation (TSM) Strategy for SR-DABC

As the impedance, and hence the natural response, of the resonant tank usually cannot be altered, a more effective method for the suppression of HF transient oscillations is to modify the resonant tank's forced response by actively shaping its input excitation (v_{LC}) with an appropriate transient switching sequence. The following subsections will describe the designs of the proposed transient switching sequences for the cases of increasing and decreasing power in Figs. 4.7 and 4.8, respectively. The superscript associated with the phase angle ϕ, e.g. "I" in ϕ_0^{I}, is used to denote the operation mode under TSM.

4.3.1 Increasing Power ($\delta > 0$)

The case of $\delta > 0$ corresponds to an increase of power. By referring to an example of updating a positive value of δ under TSM, as shown in Fig. 4.7(a), there are two modulation parameters involved, i.e., the transient phase-shift angle (β_1) between v_{ab} and v_{cd} and the positive pulse width (γ_1) of v_{cd}, which can be adjusted during transient state to alter the trajectories of v_{Cr} and i_r while v_{ab} is kept unchanged as a 50% duty-cycle square wave. Both parameters, β_1 and γ_1, are modulated via a multi-step process during each switching cycle to update the phase-shift angle from the original steady-state value θ to the new steady-state value $\theta + \delta$. By means of a multi-step updating process, a sudden surge of injected energy to the resonant tank is therefore prevented. On the contrary, for CTPSM, as previously depicted in Fig. 4.4, only the transient phase-shift angle is modulated (i.e., $\beta_1 = \theta + \delta$) while the duty cycle of v_{cd} is always kept as 0.5,

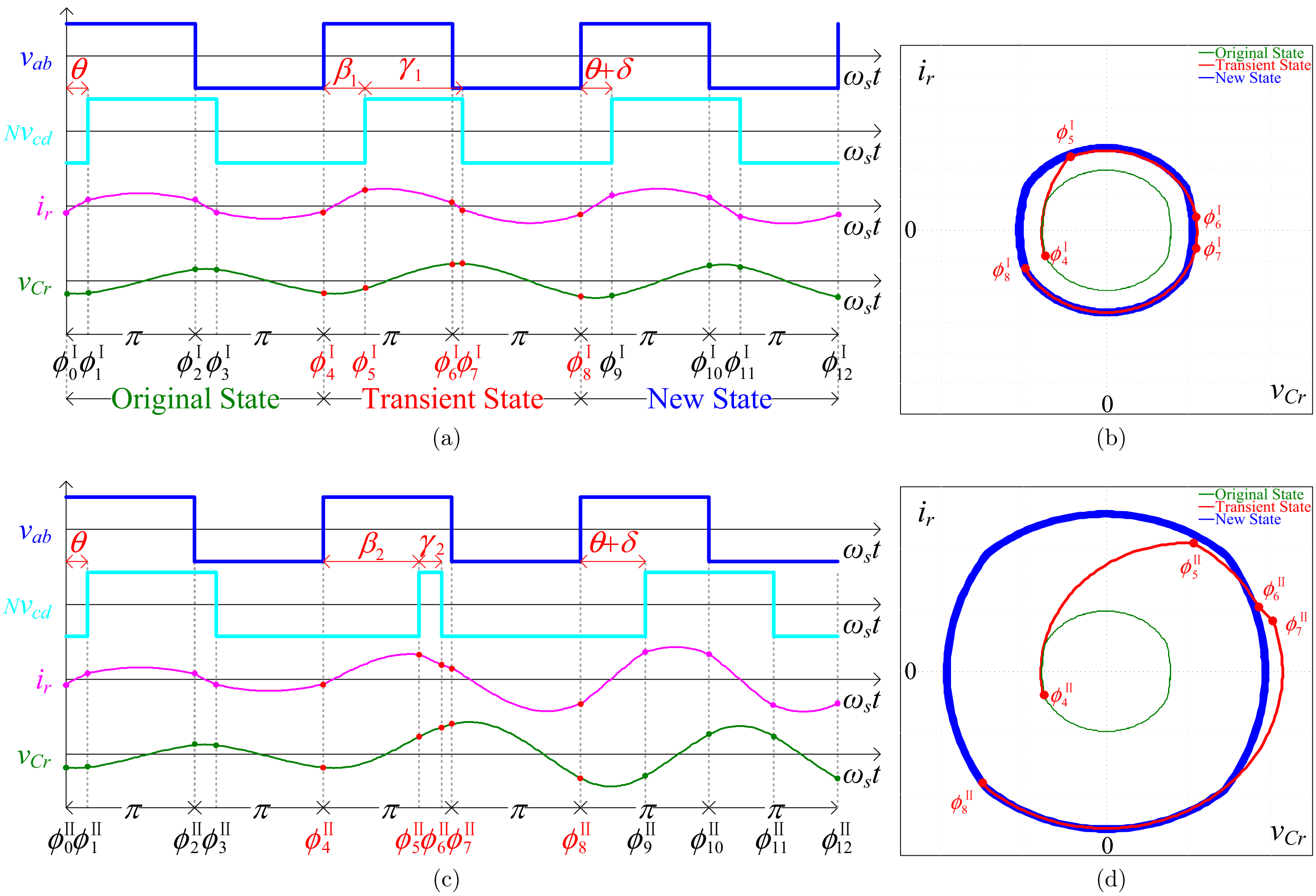

Fig. 4.7. The proposed TSM for $\delta > 0$. (a) Mode I, (c) Mode II. 2D state-plane diagrams under TSM ($\delta > 0$). (b) Mode I. (d) Mode II.

which causes a sudden injection of energy to the resonant tank that triggers the undesirable HF transient oscillations.

According to [113], the instantaneous tank energy (e_T) is given by $e_T = (C_r {v_{Cr}}^2 + L_r {i_r}^2)/2$, which is proportional to the square of the radius of the state-plane trajectory associated with the current state. The underlying principle of TSM can be explained by referring to the state-plane diagram shown in Fig. 4.7(b). Since e_T can be modified by modulating β_1 and γ_1, i.e. by turning on and off the secondary-side switches in appropriate ways, the transient trajectories of i_r and v_{Cr} should accordingly be altered in a deterministic way (by modulating β_1 and γ_1) to enable them to acquire their new steady-state trajectories at a

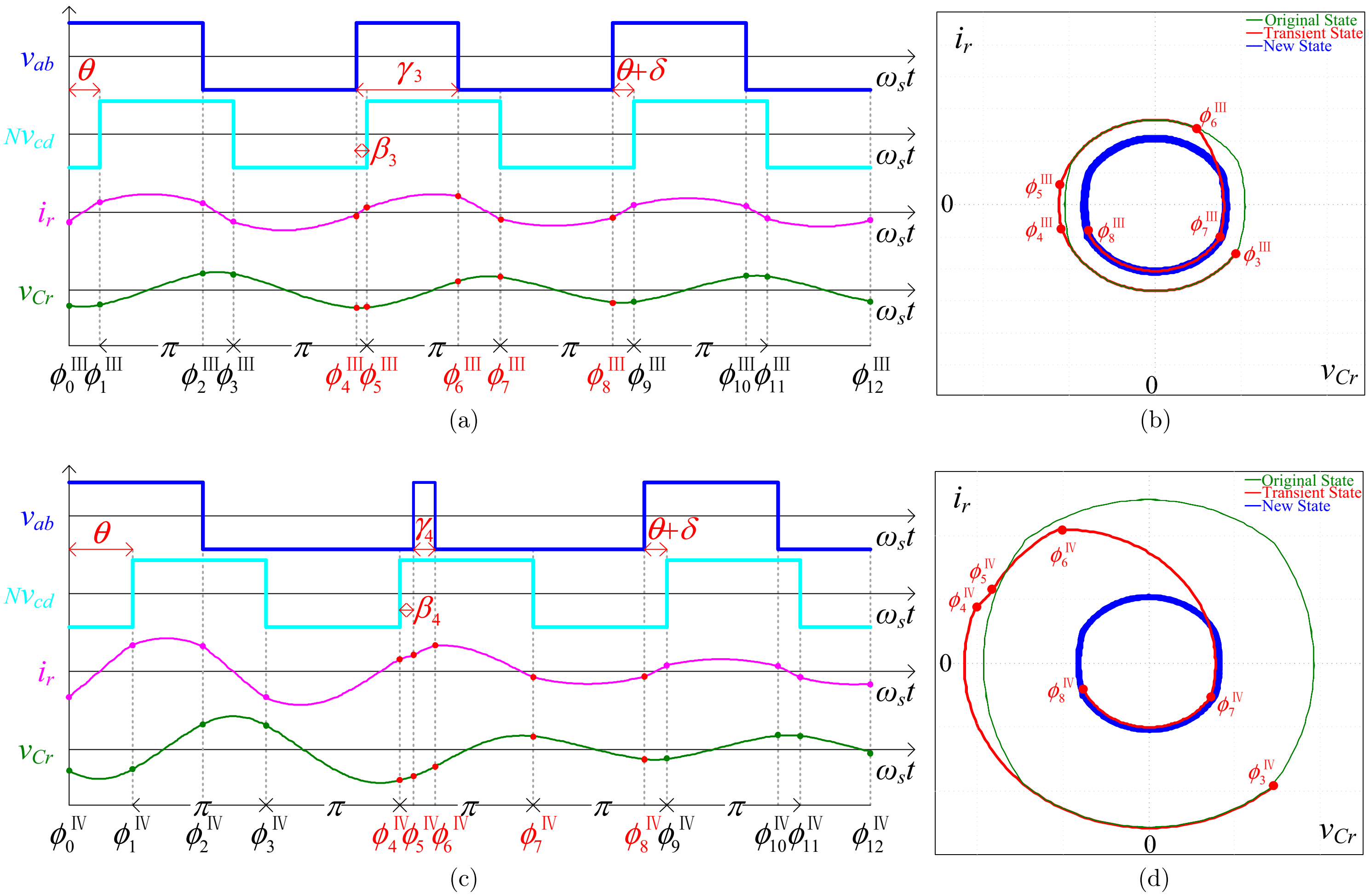

Fig. 4.8. The proposed TSM for $\delta < 0$. (a) Mode III. (c) Mode IV. 2D state-plane diagrams under TSM ($\delta < 0$). (b) Mode III. (d) Mode IV.

specified time, e.g. at the end of one switching cycle, and once they enter the new state trajectories (without oscillation), they should remain there until the next transient event/command occurs. If i_r and v_{Cr} can reach their new steady states in one switching cycle, oscillations are eliminated and settling time is shortened significantly. Therefore, in order to eliminate HF transient oscillations, the boundary values of v_{Cr} and i_r at the beginning and the end of the transient process, i.e., $\phi_4^{\mathrm{I}}/\omega_s$ and $\phi_8^{\mathrm{I}}/\omega_s$, should be equal to their original and new steady-state values corresponding to the phase-shift angle θ and $\theta + \delta$, respectively. This can be achieved by finding the solutions for β_1 and γ_1 that satisfy the boundary conditions at $\phi_4^{\mathrm{I}}/\omega_s$ and $\phi_8^{\mathrm{I}}/\omega_s$. Once these solutions are found, an optimal transient switching sequence (as well as transient state-plane trajectories) can be constructed that completes the transient process in one switching cycle.

Under TSM, the transient process which begins at $\phi_4^{\mathrm{I}}/\omega_s$ and ends at $\phi_8^{\mathrm{I}}/\omega_s$ can be divided into four intervals, namely, $\phi_5^{\mathrm{I}}-\phi_4^{\mathrm{I}}=\beta_1$, $\phi_6^{\mathrm{I}}-\phi_5^{\mathrm{I}}=\pi-\beta_1$, $\phi_7^{\mathrm{I}}-\phi_6^{\mathrm{I}}=\beta_1+\gamma_1-\pi$, and $\phi_8^{\mathrm{I}}-\phi_7^{\mathrm{I}}=2\pi-\beta_1-\gamma_1$. It is assumed that the terminal voltages V_1 and V_2 are constant during the transient process, which is reasonable given the very short duration, i.e., one switching cycle, of the transient process. To determine the instantaneous values of v_{Cr} and i_r at the intermediate points between $\phi_4^{\mathrm{I}}/\omega_s$ and $\phi_8^{\mathrm{I}}/\omega_s$, i.e., $i_r(\phi_5^{\mathrm{I}}/\omega_s)\sim i_r(\phi_8^{\mathrm{I}}/\omega_s)$ and $v_{Cr}(\phi_5^{\mathrm{I}}/\omega_s)\sim v_{Cr}(\phi_8^{\mathrm{I}}/\omega_s)$, (4.5) and (4.6) are applied in an iterative manner. The lower boundary values can be found from the original steady-state values $i_r(\phi_4^{\mathrm{I}}/\omega_s)=i_r(\phi_0^{\mathrm{I}}/\omega_s)$ and $v_{Cr}(\phi_4^{\mathrm{I}}/\omega_s)=v_{Cr}(\phi_0^{\mathrm{I}}/\omega_s)$ from (4.9) and (4.10), respectively. The upper boundary values can be found after four iterations as

$$\begin{aligned} i_r\left(\frac{\phi_8^{\mathrm{I}}}{\omega_s}\right) =& -\frac{4NV_2}{Z_r}\cos\left(\frac{2\beta_1+\gamma_1-4\pi}{2F}\right)\sin\left(\frac{\gamma_1}{2F}\right) \\ &+\frac{NV_2}{Z_r}\sec\left(\frac{\pi}{2F}\right)\sin\left(\frac{5\pi-2\theta}{2F}\right)-\frac{V_1}{Z_r}\tan\left(\frac{\pi}{2F}\right) \end{aligned} \tag{4.11}$$

$$\begin{aligned} v_{Cr}\left(\frac{\phi_8^{\mathrm{I}}}{\omega_s}\right) =& 4NV_2\sin\left(\frac{2\beta_1+\gamma_1-4\pi}{2F}\right)\sin\left(\frac{\gamma_1}{2F}\right) \\ &+NV_2\left[1-\sec\left(\frac{\pi}{2F}\right)\cos\left(\frac{5\pi-2\theta}{2F}\right)\right]. \end{aligned} \tag{4.12}$$

As the objective is to eliminate HF transient oscillations, $i_r(\phi_8^{\mathrm{I}}/\omega_s)$ and $v_{Cr}(\phi_8^{\mathrm{I}}/\omega_s)$ must be equal to their new steady-state values at $\phi_{12}^{\mathrm{I}}/\omega_s$. Hence,

$$\begin{aligned} i_r\left(\frac{\phi_8^{\mathrm{I}}}{\omega_s}\right) &= i_r\left(\frac{\phi_{12}^{\mathrm{I}}}{\omega_s}\right) \\ &=\frac{1}{Z_r}\left[NV_2\sec\left(\frac{\pi}{2F}\right)\sin\left(\frac{\pi-2\theta-2\delta}{2F}\right)-V_1\tan\left(\frac{\pi}{2F}\right)\right] \end{aligned} \tag{4.13}$$

$$\begin{aligned} v_{Cr}\left(\frac{\phi_8^{\mathrm{I}}}{\omega_s}\right) &= v_{Cr}\left(\frac{\phi_{12}^{\mathrm{I}}}{\omega_s}\right) \\ &=NV_2\left[1-\cos\left(\frac{\theta+\delta}{F}\right)-\sin\left(\frac{\theta+\delta}{F}\right)\tan\left(\frac{\pi}{2F}\right)\right] \end{aligned} \tag{4.14}$$

which are obtained by replacing θ by $\theta+\delta$ in both (4.9) and (4.10).

Combining (4.11) with (4.13), and (4.12) with (4.14), gives

$$\sec\frac{\pi}{2F}\sin\frac{2\pi+\delta}{2F}\cos\frac{2\theta+\delta-3\pi}{2F}=2\sin\frac{\gamma_1}{2F}\cos\frac{2\beta_1+\gamma_1-4\pi}{2F} \tag{4.15}$$

$$\sec\frac{\pi}{2F}\sin\frac{2\pi+\delta}{2F}\sin\frac{2\theta+\delta-3\pi}{2F}=2\sin\frac{\gamma_1}{2F}\sin\frac{2\beta_1+\gamma_1-4\pi}{2F}. \tag{4.16}$$

Dividing (4.16) by (4.15) and simplifying the resulting equation leads to

$$\beta_1=\frac{\pi+2\theta+\delta-\gamma_1}{2}. \tag{4.17}$$

Finally, substituting β_1 from (4.17) into (4.15) or (4.16) yields

$$\gamma_1=2F\cdot\arcsin\left[\frac{1}{2}\sec\left(\frac{\pi}{2F}\right)\sin\left(\frac{2\pi+\delta}{2F}\right)\right]. \tag{4.18}$$

Thus, (4.17) and (4.18) give the closed-form solutions for γ_1 and β_1 that satisfy the boundary conditions for producing oscillation-free transition from the original to the new steady states. It is evident that both γ_1 and β_1 are functions of the normalized frequency $F = f_s/f_r$, θ, and δ only, which greatly simplifies the implementation of TSM as no sensing is required for other converter parameters, such as N, V_1, V_2, i_r, v_{Cr}, which are typically required by the existing trajectory control methods. The problems of high implementation complexity and high cost which characterize the existing trajectory control methods are thus overcome by the proposed TSM method. Finally, it should be noted that, although two operation modes are depicted in Fig. 4.7, there is no fundamental difference between them. This is evident from the above analysis which does not distinguish the two operation modes in the mathematical derivation of (4.17) and (4.18), thus the same equations are applicable to both operation modes, which again highlights the simplicity of the proposed TSM method.

4.3.2 Decreasing Power ($\delta < 0$)

The feasible solution region of (4.18) for $\gamma_1 > 0$ is plotted in Fig. 4.9, where the dashed lines define the maximum allowable δ in each execution of TSM. It can be seen that there is no feasible solution when $\delta < 0$ and F is small, although

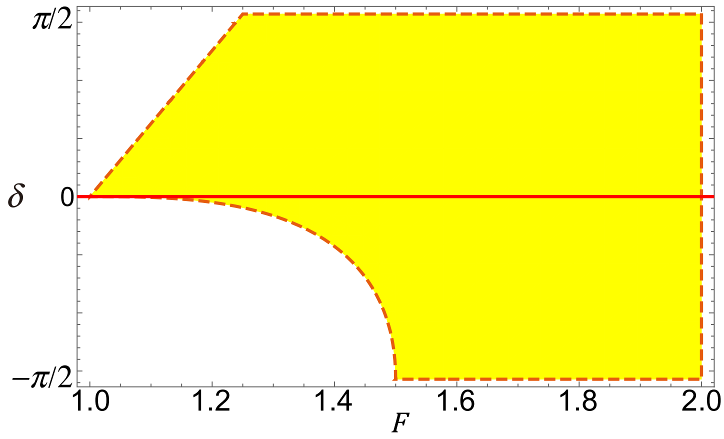

Fig. 4.9. Feasible solution region of (4.18).

the proposed method still works well for large F. To enlarge its feasible operating region, therefore, the proposed TSM method is modified as shown in Fig. 4.8(a) for $\delta < 0$, where the roles of v_{ab} and v_{cd} are reciprocated. With the modified TSM method, when power is decreased, i.e. $\delta < 0$, v_{cd} is kept unchanged as a 50% duty-cycle square wave at fixed frequency, while the positive pulse width γ_3 of v_{ab} and the phase-shift angle β_3 between v_{ab} and v_{cd} are modulated to eliminate HF transient oscillations during transient state. It can be shown that by following the same method of analysis as detailed in Subsection 4.3.1, the solutions for β_3 and γ_3 can be determined as given by (4.19) and (4.20). Again, it should be noted that there is no fundamental difference between the two operation modes, i.e., Mode III and Mode IV, depicted in Fig. 4.8, thus the same equations are applicable to both operation modes.

$$\beta_3 = \frac{\pi - 2\theta - \delta - \gamma_3}{2} \tag{4.19}$$

$$\gamma_3 = 2F \cdot \arcsin\left[\frac{1}{2}\sec\left(\frac{\pi}{2F}\right)\sin\left(\frac{2\pi - \delta}{2F}\right)\right] \tag{4.20}$$

4.3.3 Unified Form of TSM

The following relationships can be summarized from Fig. 4.7 and Fig. 4.8:

(1) $\phi_5^{\mathrm{I}} - \phi_3^{\mathrm{I}} = (\pi - \theta) + \beta_1$;

(2) $\phi_9^{\mathrm{I}} - \phi_7^{\mathrm{I}} = \pi - (\beta_1 + \gamma_1 - \pi) + (\theta + \delta)$;

(3) $\phi_5^{\mathrm{II}} - \phi_3^{\mathrm{II}} = (\pi - \theta) + \beta_2$;

(4) $\phi_9^{\mathrm{II}} - \phi_6^{\mathrm{II}} = (\pi - \beta_2 - \gamma_2) + \pi + (\theta + \delta)$;

(5) $\phi_4^{\mathrm{III}} - \phi_2^{\mathrm{III}} = \theta + (\pi - \beta_3)$;

(6) $\phi_8^{\mathrm{III}} - \phi_6^{\mathrm{III}} = (\pi - (\gamma_3 - \beta_3)) + (\pi - (\theta + \delta))$;

(7) $\phi_5^{\mathrm{IV}} - \phi_2^{\mathrm{IV}} = \theta + \pi + \beta_4$;

(8) $\phi_8^{\mathrm{IV}} - \phi_6^{\mathrm{IV}} = (\pi - \beta_4 - \gamma_4) + (\pi - (\theta + \delta))$.

By combining the above relationships with (4.17) and (4.19), β_1, β_2, β_3, and β_4 can be eliminated, thus resulting in

$$\begin{cases} \phi_5^{\mathrm{I}} - \phi_3^{\mathrm{I}} = \phi_9^{\mathrm{I}} - \phi_7^{\mathrm{I}} = (3\pi - \gamma_1 + \delta)/2 \\ \phi_5^{\mathrm{II}} - \phi_3^{\mathrm{II}} = \phi_9^{\mathrm{II}} - \phi_6^{\mathrm{II}} = (3\pi - \gamma_2 + \delta)/2 \\ \phi_4^{\mathrm{III}} - \phi_2^{\mathrm{III}} = \phi_8^{\mathrm{III}} - \phi_6^{\mathrm{III}} = (3\pi - \gamma_3 - \delta)/2 \\ \phi_5^{\mathrm{IV}} - \phi_2^{\mathrm{IV}} = \phi_8^{\mathrm{IV}} - \phi_6^{\mathrm{IV}} = (3\pi - \gamma_4 - \delta)/2 \end{cases} \tag{4.21}$$

which can be unified as

$$\begin{aligned} &\phi_5^{\mathrm{I}} - \phi_3^{\mathrm{I}} = \phi_9^{\mathrm{I}} - \phi_7^{\mathrm{I}} = \phi_5^{\mathrm{II}} - \phi_3^{\mathrm{II}} = \phi_9^{\mathrm{II}} - \phi_6^{\mathrm{II}} \\ =&\phi_4^{\mathrm{III}} - \phi_2^{\mathrm{III}} = \phi_8^{\mathrm{III}} - \phi_6^{\mathrm{III}} = \phi_5^{\mathrm{IV}} - \phi_2^{\mathrm{IV}} = \phi_8^{\mathrm{IV}} - \phi_6^{\mathrm{IV}} \\ =&(3\pi - \gamma + |\delta|)/2. \end{aligned} \tag{4.22}$$

Similarly, the pulse width γ of the transient-modulated square-wave voltage, i.e., v_{ab} for $\delta < 0$ and v_{cd} for $\delta > 0$, defined by (4.18) and (4.20) can be unified as

$$\gamma = 2F \cdot \arcsin\left[\frac{1}{2}\sec\left(\frac{\pi}{2F}\right)\sin\left(\frac{2\pi + |\delta|}{2F}\right)\right]. \tag{4.23}$$

Consequently, a unified form of the proposed TSM method given by (4.22) and (4.23) is obtained which is applicable to all four operation modes depicted in Figs. 4.7 and 4.8. Fig. 4.10 shows its implementation in a microprocessor

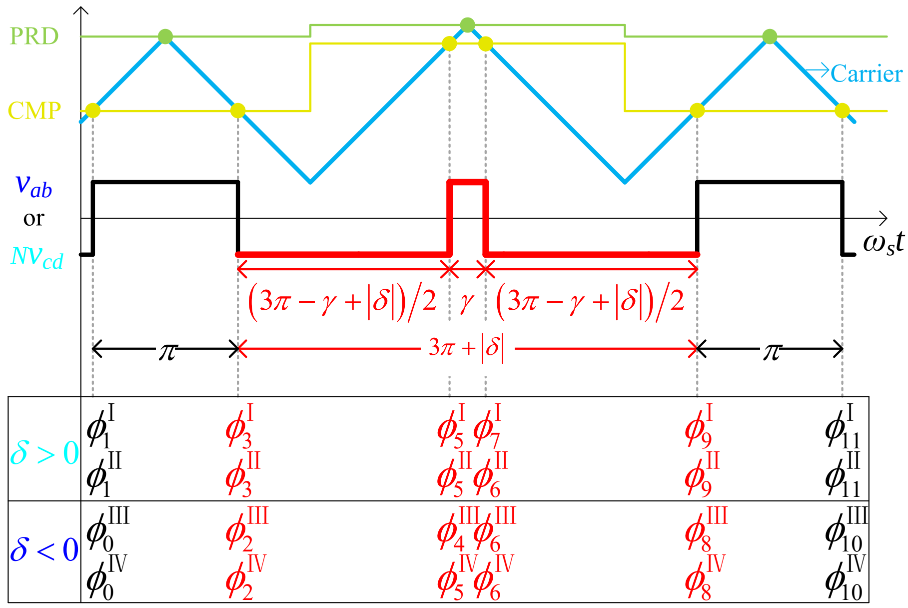

Fig. 4.10. Unified form of TSM and its switching processes.

by modifying the instantaneous values of the period (PRD) and counter-compare (CMP) registers and generating a floating triangular carrier signal during transient states.

Although the presented analysis and discussion focus on the case of forward power flow, the results are equally applicable to other cases, including increase/decrease of power in reverse power flow and reversal of power flow direction, as all these cases can be treated from the viewpoint of increasing or decreasing the phase-shift angle δ. For example, when a SR-DABC transitions from forward power flow to reverse power flow, a negative change of δ, i.e., $\delta < 0$, is involved, and such a scenario is readily handled by (4.19) and (4.20), or the unified equations (4.22) and (4.23).

To verify the effectiveness of the proposed TSM method, the open-loop transient responses of a SR-DABC under TSM are simulated and the results are presented in Fig. 4.11. To enable a fair comparison with the results shown in Fig. 4.5, the same converter parameters are used and the same cases involving both $\delta > 0$ and $\delta < 0$ are simulated. It is clear that, under the action of TSM, the transient resonant current i_r and resonant capacitor voltage v_{Cr} converge rapidly

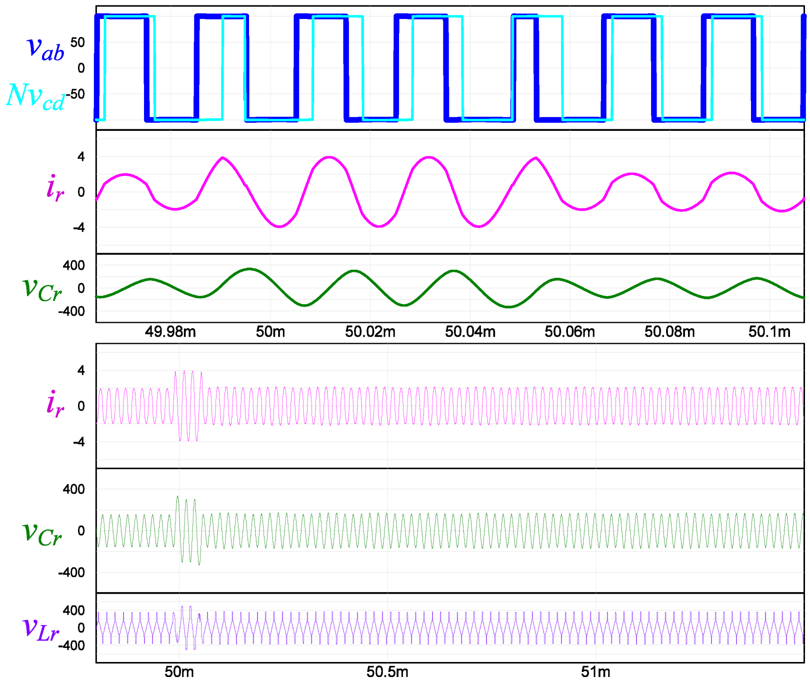

(a)

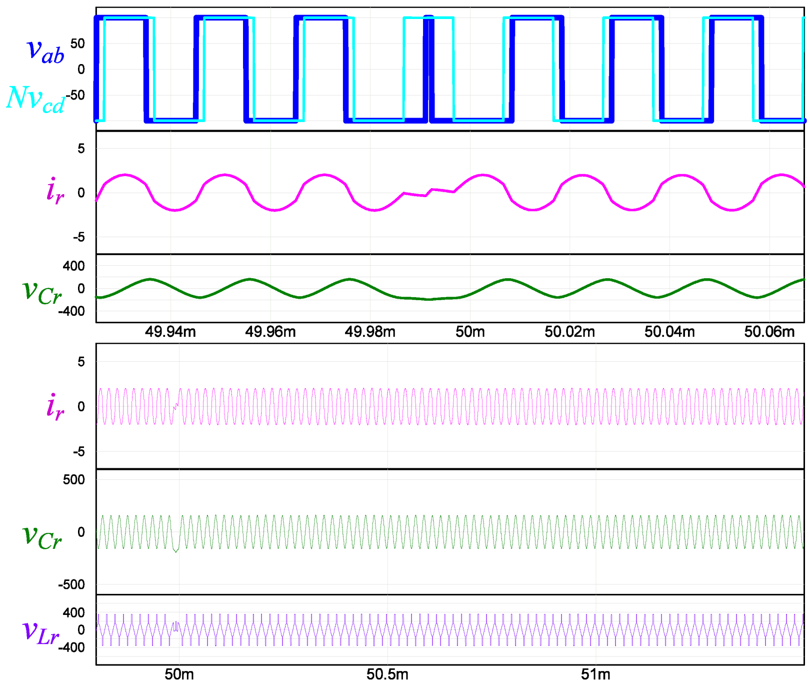

(b)

Fig. 4.11. Simulated open-loop transient responses under TSM. (a) The phase-shift angle is changed from $\pi/6$ to $\pi/3$ and back to $\pi/6$. (b) The phase-shift angle is changed from $\pi/6$ to $-\pi/6$.

to their new steady-state values within one switching cycle without causing any visible HF transient oscillations. To verify this point, the transient state-plane

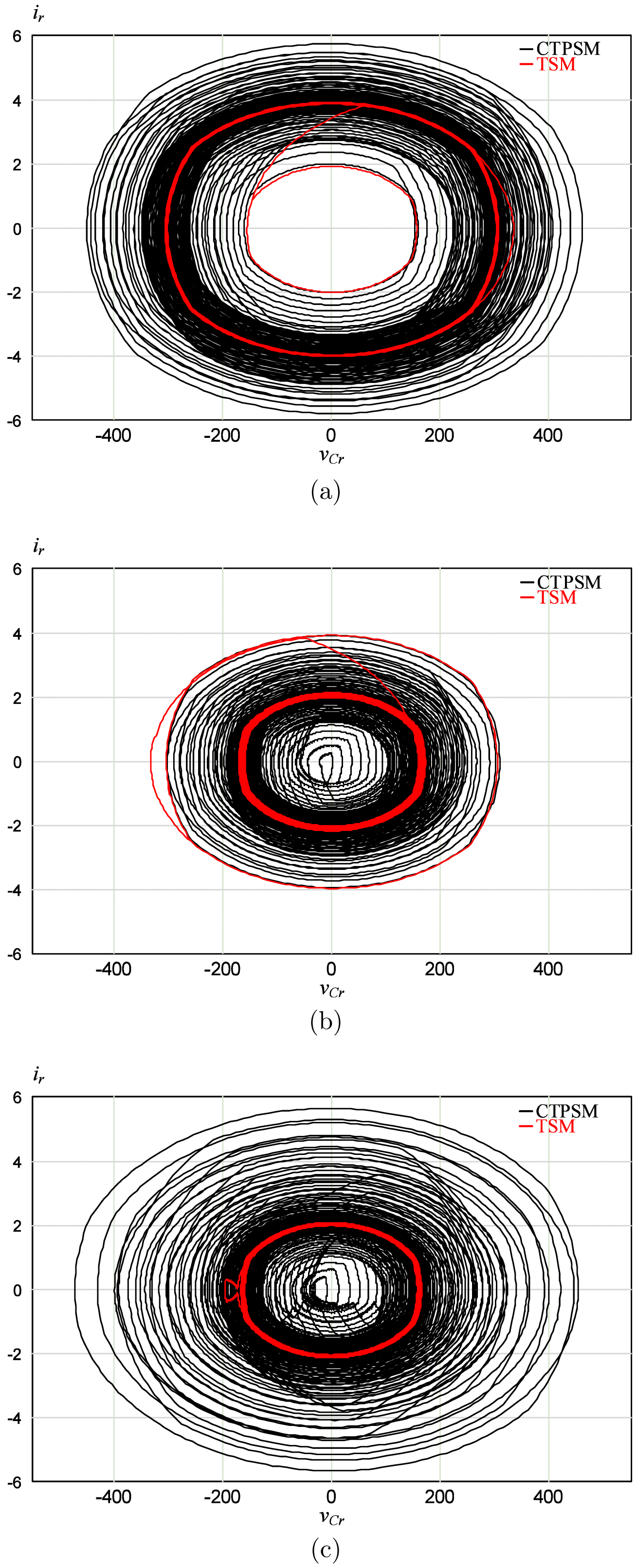

Fig. 4.12. Transient open-loop state-plane diagrams of SR-DABC under CTPSM and TSM. (a) $\theta = \pi/6$, $\delta = \pi/6$ and $\theta + \delta = \pi/3$. (b) $\theta = \pi/3$, $\delta = -\pi/6$ and $\theta + \delta = \pi/6$. (c) $\theta = \pi/6$, $\delta = -\pi/3$ and $\theta + \delta = -\pi/6$.

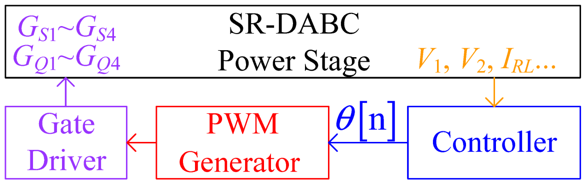

Fig. 4.13. Block diagram of a typical closed-loop controlled SR-DABC.

diagrams of i_r and v_{Cr} for all three cases under CTPSM and TSM are plotted in Fig. 4.12 for a better visualization. It is clear from these plots that i_r and v_{Cr} under CTPSM generally undergo many cycles of oscillations before settling at their new steady-state trajectories, whereas i_r and v_{Cr} under TSM are seen to approach their new steady-state trajectories smoothly and directly with essentially no oscillations. Thus, the voltage and current stresses experienced by the converter's power stage components are significantly reduced, leading to a major improvement in their long-term reliability.

4.4 MPC Design for SR-DABC

The block diagram of a typical closed-loop controlled SR-DABC is shown in Fig. 4.13. The controller aims to maintain a constant output voltage V_2 in the presence of load variations, by modulating the phase-shift angle $\theta[n]$ between v_{ab} and v_{cd}, while the PWM generator is used for realizing TSM or CTPSM. In general, a high-gain controller leads to a smaller steady-state tracking error, but it also gives rise to a more abrupt and larger transient variation in $\theta[n]$ which tends to produce undesirable large-amplitude HF transient oscillations when CTPSM is used. Consequently, CTPSM is only suitable for use with a low-gain controller which will introduce only a small change in $\theta[n]$ in every switching cycle to produce a smooth but slow dynamic response of SR-DABC. To evaluate its practical advantages, therefore, TSM should be combined with a high-gain, fast controller such as MPC which will subject the TSM-based PWM generator to more stringent operating requirements and thereby verifying its superiority in performance. MPC has recently been proven to be a powerful controller with fast reference tracking ability [9], [41], [44]. When applied to SR-DABC, its main function is to determine an optimal phase-shift angle $\theta[n]$ that minimizes a cost function (e.g., output voltage tracking error) over a given prediction time horizon (e.g., one switching cycle) with the aid of the converter's dynamic model. In this section, an MPC will be designed for a SR-DABC with the specifications given in Table 4.1.

By using fundamental harmonic approximation (FHA) method [31], the transferred power P of a SR-DABC can be approximated by (4.24),

$$P = \frac{1}{T_s}\int_0^{T_s} v_{ab}(t) i_r(t) \mathrm{d}t \overset{\text{FHA}}{\approx} \frac{8NV_1V_2\sin\theta}{\pi^2 X_r} \tag{4.24}$$

where $T_s = 1/f_s$ is the switching period and $X_r = \omega_s L_r - 1/(\omega_s C_r)$ is the equivalent impedance of the series resonant network.

At the output node in Fig. 1.7(a), a first-order differential equation (4.25) can be formulated that describes the dynamic behavior of V_2, where $\bar{i}_2 = P/V_2$ is the average value of i_2 over one switching period.

$$C_o\frac{\mathrm{d}V_2}{\mathrm{d}t} = \bar{i}_2 - I_o = \frac{8NV_1\sin\theta}{\pi^2 X_r} - \frac{V_2}{R_L} \tag{4.25}$$

Discretizing (4.25) by using forward Euler approximation yields (4.26) which can be used to predict the converter's output voltage at the next time step.

$$\begin{aligned} V_2[n+1] &= V_2[n] + V_2{}'[n]T_s \\ &= V_2[n] + \frac{8NV_1\sin\theta}{\pi^2 X_r C_o f_s} - \frac{V_2[n]}{R_L C_o f_s} \end{aligned} \tag{4.26}$$

In order to accurately track the output reference voltage $V_{2,ref}$ and minimize output voltage deviation, a quadratic cost function J can be introduced and formulated as $J = [V_{2,ref} - V_2[n+1]]^2$, which should be minimized to determine the optimal control variable (i.e., phase-shift angle) for the next time step. Based on the gradient descent method, the cost function J can be minimized when its gradient (∇J) is equal to zero.

$$\nabla J = 0 \tag{4.27}$$

Hence, the optimal phase-shift angle can be expressed as

$$\theta[n+1]=\arcsin\left[\frac{\pi^2 X_r C_o f_s}{8NV_1[n]}\left[V_{2,ref}-V_2[n]+\frac{V_2[n]}{R_L C_o f_s}\right]\right]. \tag{4.28}$$

Then, the measured load current $I_o[n]$ can be used instead of the term $\frac{V_2[n]}{R_L}$ in (4.28) to add a load-current feed-forward path for further enhancing dynamic response. This gives a modified expression of the predicted phase-shift angle $\theta[n+1]$,

$$\theta[n+1]=\arcsin\left[\frac{\pi^2 X_r C_o f_s}{8NV_1[n]}\left[v_e[n]+\frac{I_o[n]}{C_o f_s}\right]\right] \tag{4.29}$$

where $v_e[n] = V_{2,ref} - V_2[n]$ is defined as the error voltage.

Expanding (4.29) in a one-dimensional Taylor series around the steady-state operating point, and removing higher-order non-linear terms, leads to

$$\hat{\theta}=W\left[\hat{v}_e[n]+\frac{\hat{I}_{RL}[n]}{C_o f_s}\right]\Bigg/\sqrt{1-\left[W\left[v_e[n]+\frac{I_o[n]}{C_o f_s}\right]\right]^2} \tag{4.30}$$

where W is given by $W=\frac{\pi^2 X_r C_o f_s}{8NV_1[n]}$, and the symbol $\hat{}$ denotes small-signal quantities.

However, the idealized equation (4.30) cannot be directly used for closed-loop control due to the HF noise associated with v_e and the presence of some unmodeled effects (e.g., power losses, sensing errors, power harmonics, etc.), which may affect the closed-loop regulation and even stability of the converter system. A PI compensator is required to compensate for the unmodeled effects as well as to act as a low-pass filter for attenuating HF noise and ensuring closed-loop stability. The overall transfer function of MPC with the inclusion of PI compensator is therefore given by

$$G_{\mathrm{MPC}}(s) = \frac{W\left[\hat{v}_e[n]\left(K_p+\frac{K_i}{s}\right)+\frac{\hat{I}_{RL}[n]}{C_o f_s}\right]}{\sqrt{1-\left[\frac{W I_o[n]}{C_o f_s}\right]^2}}. \tag{4.31}$$

Here, the proportional gain K_p plays a dominant role in determining the closed-loop performance of the converter, such as bandwidth, response speed, and stability. As discussed, some unmodeled effects always exist, thus an integral gain K_i

should be included to eliminate steady-state error without significantly altering the dynamic properties of the converter.

Next, (4.25) is perturbed and linearized to yield the small-signal differential equation relating phase-shift angle $\hat{\theta}$ (i.e., δ) and output voltage $\hat{V}_2$.

$$C_o \frac{\mathrm{d}\hat{V}_2}{\mathrm{d}t} = \frac{8N}{\pi^2 X_r} \left(V_1 \hat{\theta} \cos\theta + \hat{V}_1 \sin\theta \right) - \frac{\hat{V}_2}{R_L} \tag{4.32}$$

Taking the Laplace transform of (4.32) and setting $\hat{V}_1 = 0$ yields the control-to-output transfer function $G_{V_2\theta}(s)$.

$$G_{V_2\theta}(s) = \frac{\hat{V}_2(s)}{\hat{\theta}(s)} = \frac{8NV_1 R_L \cos\theta}{\pi^2 X_r \left(1 + sC_o R_L\right)} \tag{4.33}$$

Fig. 4.14(a) shows the overall control block diagram of the proposed MPC, where the transfer functions of the constituent blocks are defined below:

$$G_{\mathrm{PI}}(s) = K_p + \frac{K_i}{s} \tag{4.34}$$

$$G_c(s) = W \Bigg/ \sqrt{1 - \left[\frac{W I_o[n]}{C_o f_s}\right]^2} \tag{4.35}$$

$$G_d(s) = e^{-sT_d} \tag{4.36}$$

Note that T_d is the inherent time delay introduced by the zero-order hold effect in digital implementation and $G_d(s)$ represents its Laplace transform. G_c is the modulation gain relating error voltage to phase-shift angle.

Finally, the closed-loop transfer function of an MPC-controlled SR-DABC, i.e., transfer function from $\hat{V}_{2,ref}(s)$ to $\hat{V}_2(s)$, is given by (4.37),

$$G(s) = \frac{T(s)}{1 + T(s)} \tag{4.37}$$

where

$$T(s) = \frac{G_{\mathrm{PI}}(s) G_c(s) G_d(s) G_{V_2\theta}(s)}{1 - G_c(s) G_d(s) G_{V_2\theta}(s) / \left(R_L C_o f_s\right)} \tag{4.38}$$

is the loop gain.

To verify the effectiveness of the proposed TSM method under different controller configurations, two sets of PI parameters are designed to yield two control loop bandwidths with a crossover frequency of 158 Hz and 550 Hz, respectively,

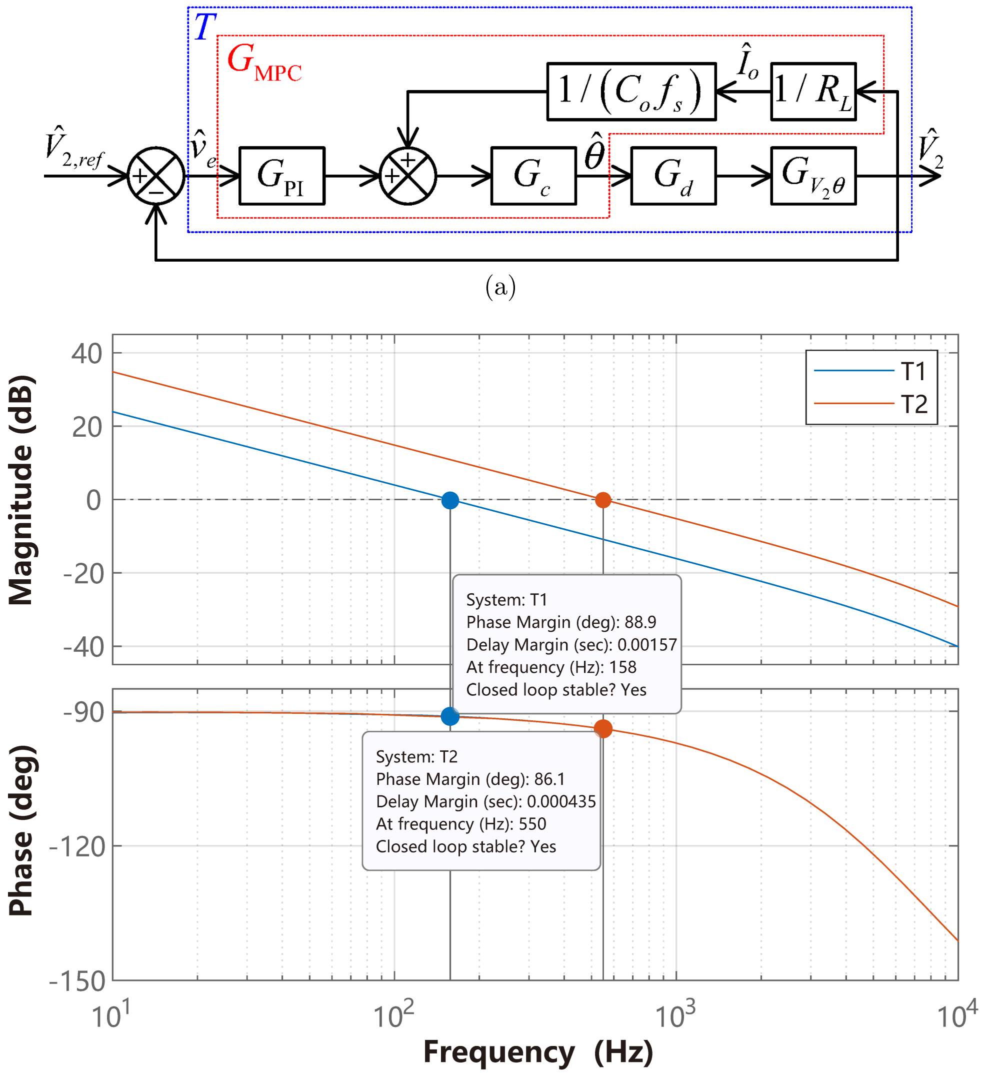

Fig. 4.14. Closed-loop MPC design for SR-DABC. (a) Overall control block diagram. (b) Bode plot of loop gain $T(s)$.

and the corresponding PI parameters are $\{T_1\text{: } K_p = 0.02,\ K_i = 0.005\}$ and $\{T_2\text{: } K_p = 0.07,\ K_i = 0.01\}$. The bode plots of T_1 and T_2 are shown in Fig. 4.14(b). It can be seen that both controller configurations are well designed with abundant phase margins, i.e., of 88.9° for T_1 and 86.1° for T_2, and hence good stability. Additionally, TSM which only operates during transient states does not alter the pole locations prescribed by the controller, and hence does not affect the stability of the designed closed-loop SR-DABC. However, since it is unnecessary to trigger TSM when δ is very small (as it will not give rise to large-amplitude transient

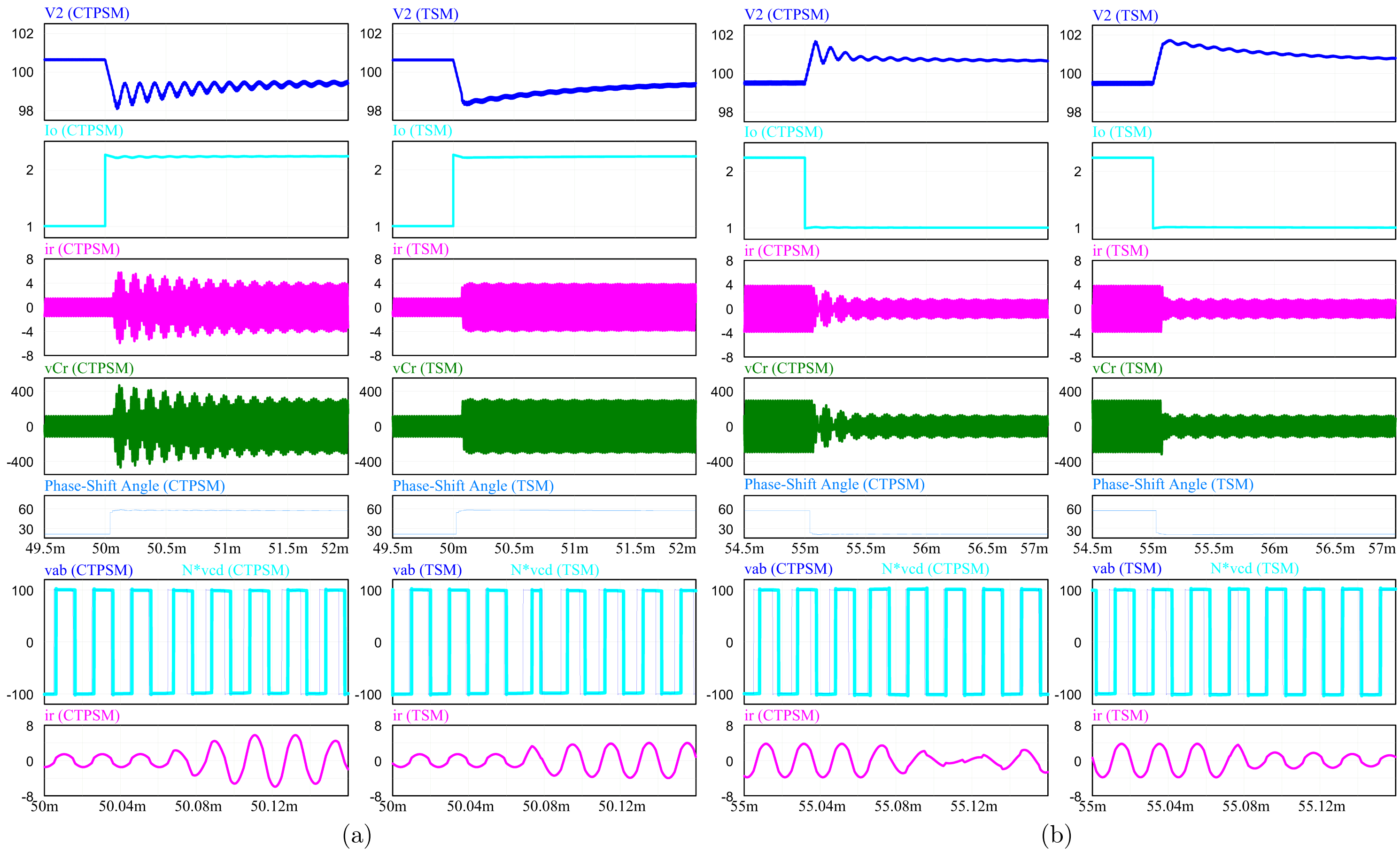

Fig. 4.15. Simulated closed-loop transient responses under MPC with T_1 ($K_p = 0.02$, $K_i = 0.005$). (a) Load step-up. (b) Load step-down.

oscillations), a minimum threshold δ_{th} can be set below which TSM will not be triggered.

Figs. 4.15 and 4.16 show the simulated transient responses of SR-DABC implemented with CTPSM and TSM for two sets of PI parameters. Fig. 4.15 corresponds to the slow-loop configuration T_1, whereas Fig. 4.16 corresponds to the fast-loop configuration T_2. As expected, it can be observed from these simulation results that SR-DABC under CTPSM generally suffers from severe HF transient oscillations during step-load changes, whereas SR-DABC under TSM exhibits no or only very weak transient oscillations during the same step-load changes as the trajectories of i_r and v_{Cr} are controlled by TSM to reach their new steady-state values rapidly. However, due to the inclusion of parasitic elements in the simu-

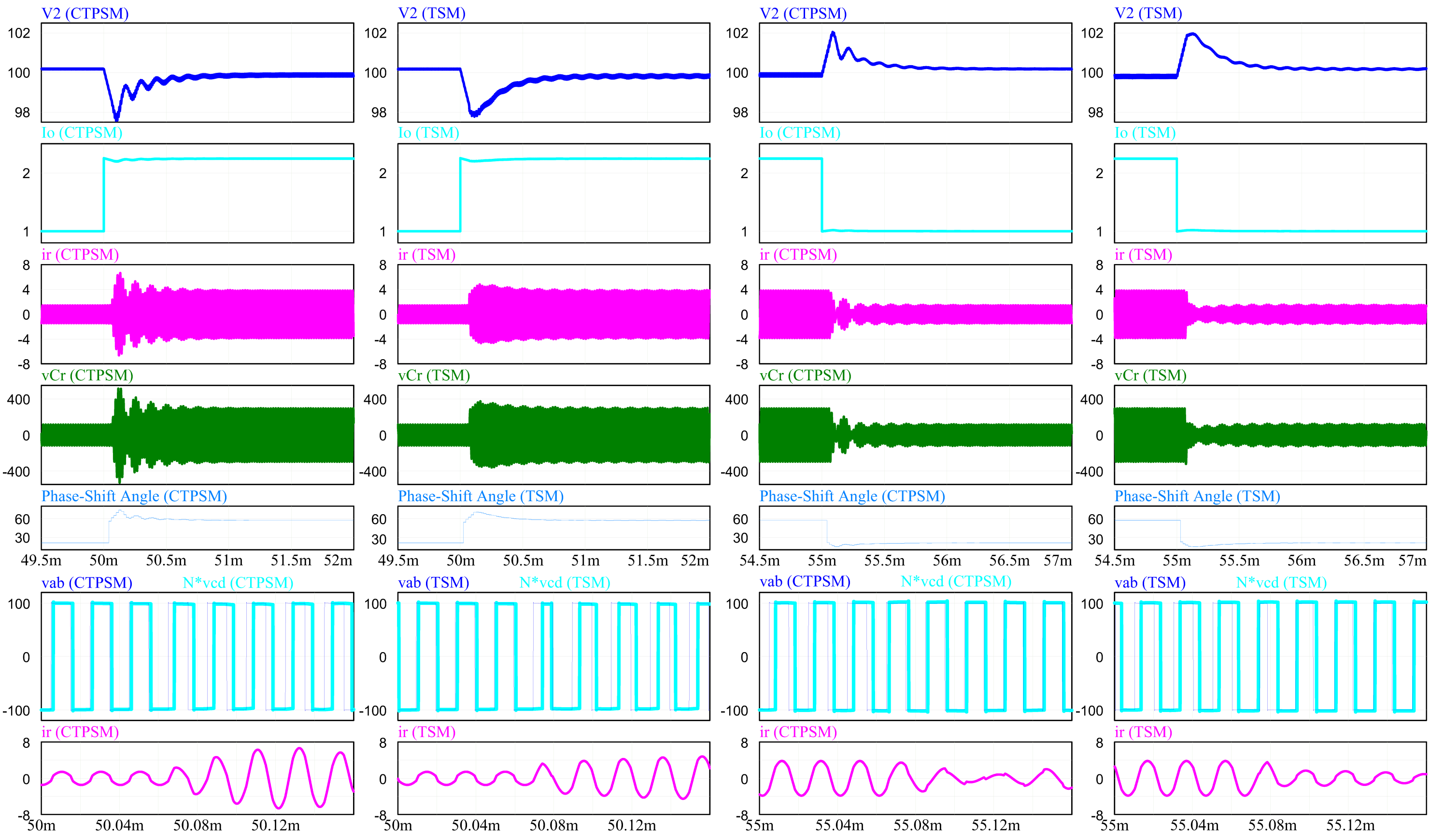

Fig. 4.16. Simulated closed-loop transient responses under MPC with T_2 ($K_p = 0.07$, $K_i = 0.01$). (a) Load step-up. (b) Load step-down.

lated SR-DABC which are not considered in the derivation of (4.23), there exists an incomplete suppression of HF transient oscillations by TSM in Figs. 4.15 and 4.16 leading to the existence of some small-amplitude residual oscillations in i_r and v_{Cr}. Another important observation is that, by comparing Figs. 4.15 and 4.16, faster control loop (T_2) tends to cause more severe HF transient oscillations (i.e., higher transient peak amplitudes of i_r and v_{Cr}) under CTPSM, whereas the performance of TSM is less sensitive to control loop bandwidth as a result of the cycle-by-cycle planning of the trajectories of i_r and v_{Cr} in response to changes in the phase-shift angle.

As shown in Fig. 4.14(a), except for the control parameters of PI compensator, the values of R_L, C_o, and f_s all have a great effect on the closed-loop performance.

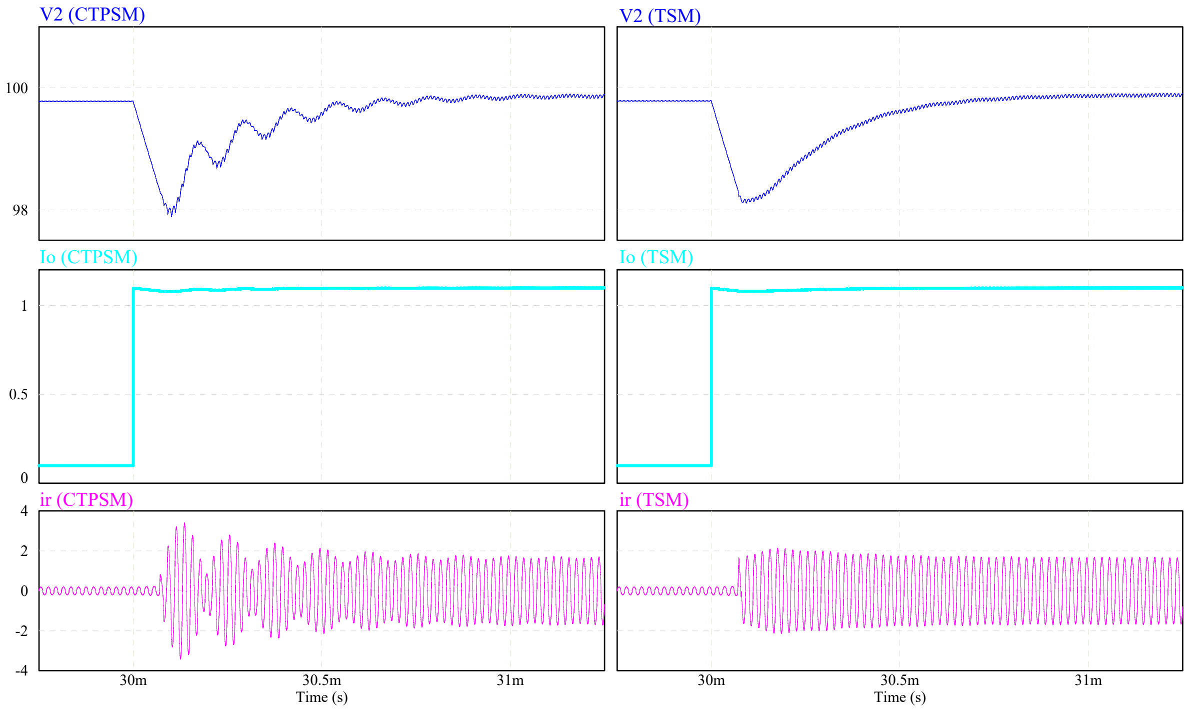

(a)

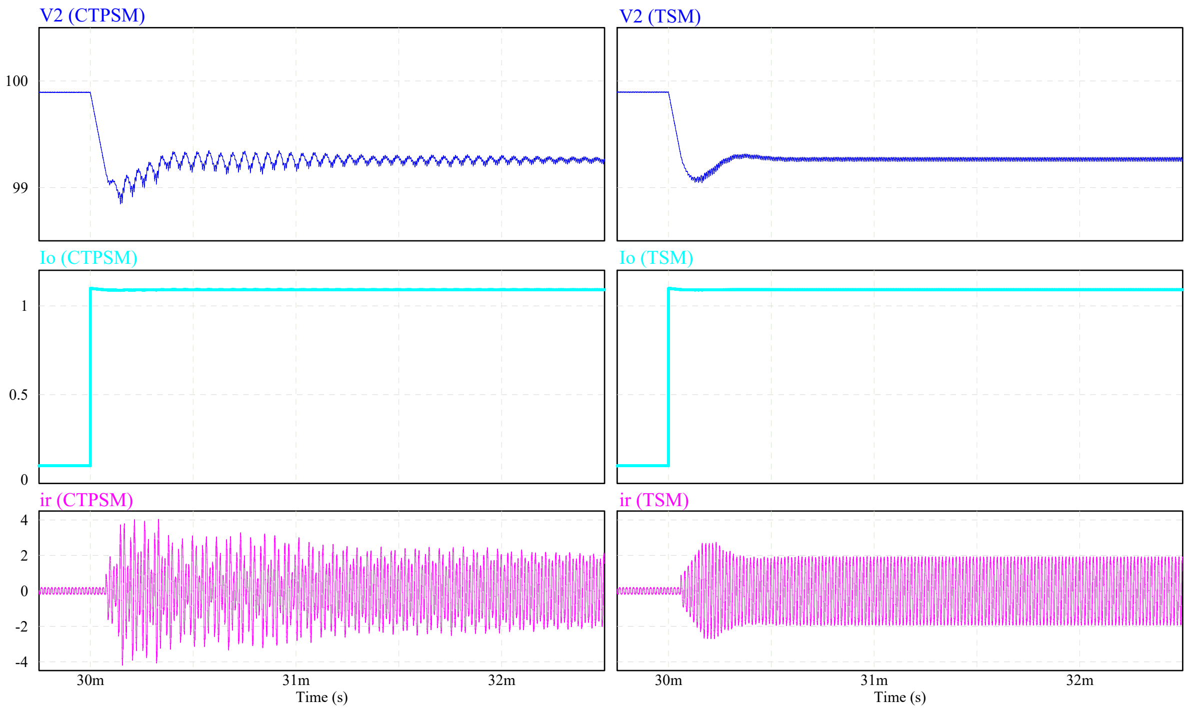

(b)

Fig. 4.17. Simulated closed-loop transient responses under MPC with modified parameters. (a) $C_o = 47\mu$F, $R_L = 1000/90.9\Omega$, $f_s = 50$ kHz, $K_p = 0.07$, and $K_i = 0.01$ (i.e., T_2). (b) $C_o = 100\mu$F, $R_L = 1000/90.9\Omega$, $f_s = 60$ kHz, $K_p = 0.3$, and $K_i = 0.9$.

To further validate the impacts caused by the variations of these parameters, two more closed-loop simulation tests with modified parameters are demonstrated in Fig. 4.17. The R_L (i.e., $R_L = 1000/90.9\Omega$) used in Fig. 4.17(a) is different from that in Figs. 4.18 and 4.19 (i.e., $R_L = 100/45\Omega$). R_L, C_o, f_s, K_p, and K_i used in Fig. 4.17(b) are all modified. It can be found from Fig. 4.17, MPC+TSM performs better dynamic performances than MPC+CTPSM under both cases, which suggests that TSM is able to achieve oscillation-free closed-loop dynamics even when some of the circuit and control parameters are changed. It should be noted that the load disturbance and output capacitance mainly have impacts on the response of the controller, instead of the effectiveness of the proposed transient modulation method (i.e., TSM), which is generally insensitive to the variation of system parameters in a fixed-frequency modulated SR-DABC, and its performance heavily depends on the amplitude of the step change in the control variable (i.e., phase-shift angle).

4.5 Experimental Verifications

The objective of this section is to validate the effectiveness of the proposed TSM under various dynamic conditions by comparing it to CTPSM. A scaled-down laboratory prototype as shown in Fig. 4.18 has been constructed for the purpose. The hardware specifications and simulation parameters are listed in Table 4.1. Two types of experiments are performed in this section: open-loop and closed-loop, and their implementation flowcharts are shown in Fig. 4.19, where z^{-1} denotes a unit delay in z-Transform. Hence, the current phase-shift angle is $\theta[n] = z^{-1}\theta[n+1]$ and the increment is $\delta = \theta[n+1] - \theta[n]$. For open-loop experiments (see Fig. 4.19(a)), no feedback loop is implemented and step changes in the phase-shift angle are directly applied to SR-DABC through a human-machine interaction (HMI) software. When $\delta \neq 0$, the phase-shift angle is updated by CTPSM or TSM according to the decision of the "TSM Selector", otherwise it waits for the next

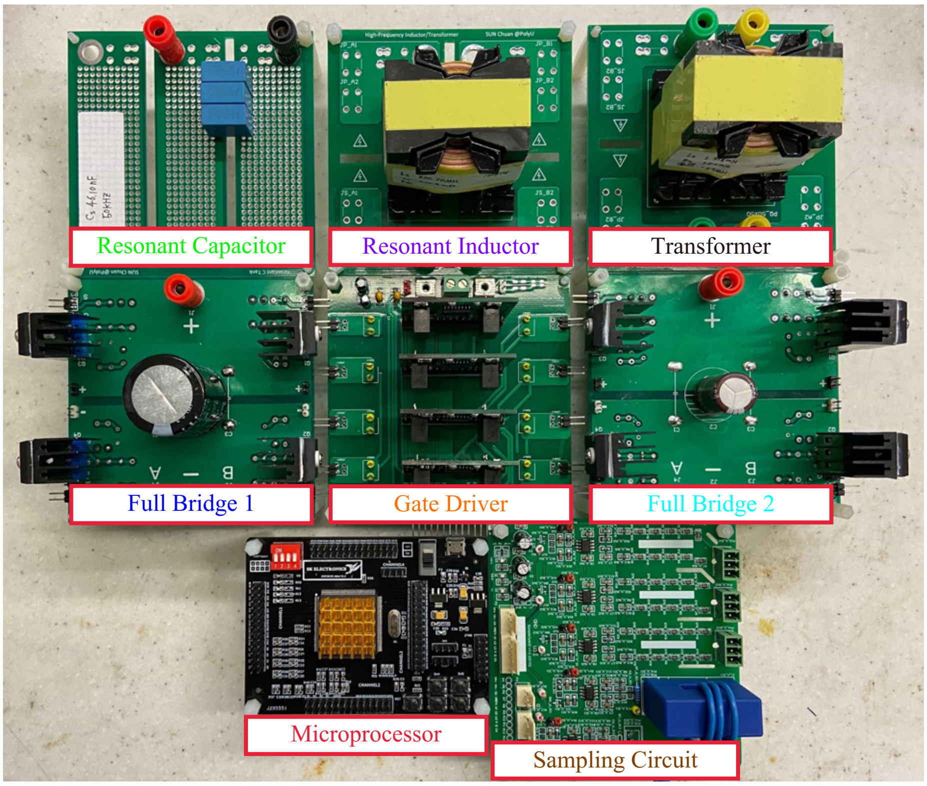

Fig. 4.18. Photograph of the experimental SR-DABC prototype.

command. For closed-loop experiments (see Fig. 4.19(b)), the phase-shift angle is computed by the MPC designed in Section 4.4. As TSM should be activated during transient state only, a minimum $|\delta| = \delta_{th}$ is defined above which TSM is activated, otherwise CTPSM is activated instead. It should be noted that, due to the finite bandwidth of MPC, the rate of change of the phase-shift angle in closed-loop experiments is always slower than that in open-loop experiments, thus it can be said that open-loop experiments enable us to test the performances of CTPSM and TSM under extreme operating conditions involving abrupt and large-amplitude changes in the phase-shift angle.

4.5.1 Open-Loop Tests

Fig. 4.20(a) and Fig. 4.20(b) show the open-loop experimental transient responses of a SR-DABC under CTPSM and TSM, respectively, when the phase-shift angle is increased from $\pi/6$ to $\pi/3$. As can be seen from Fig. 4.20(a), under

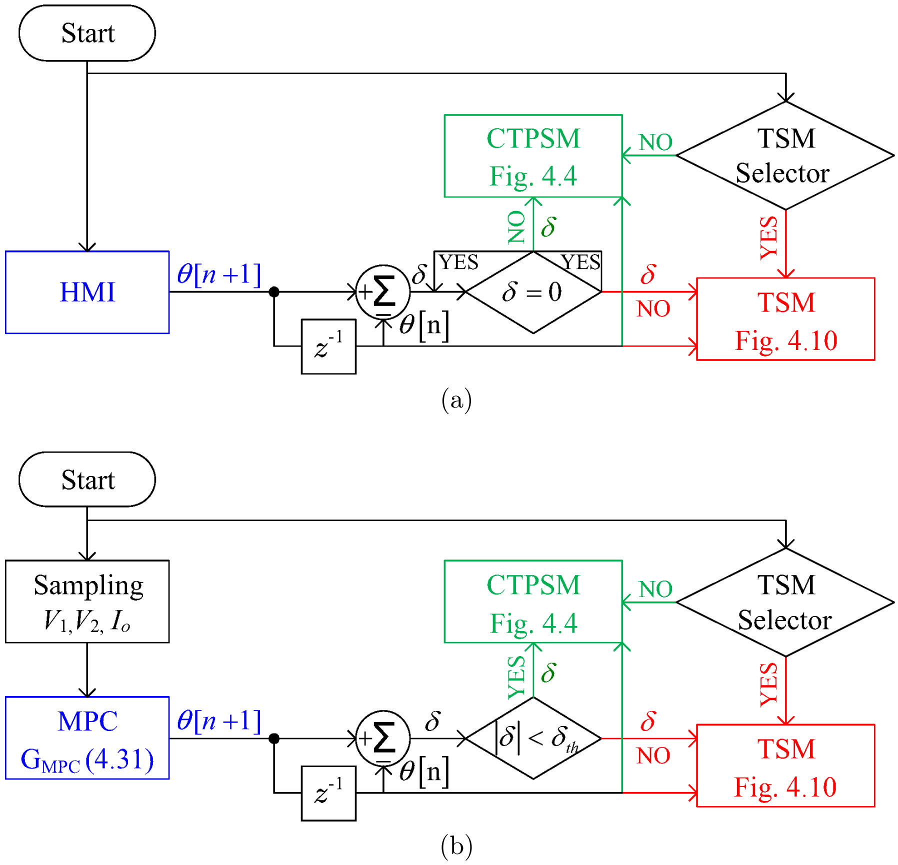

Fig. 4.19. Implementation flowcharts. (a) Open-loop configuration. (b) Closed-loop configuration.

CTPSM, the resulting HF transient oscillations continue for approximately 40 cycles before i_r reaches the new steady state. More importantly, the original and the new steady-state amplitudes of i_r are 2.00 A and 3.90 A, respectively, but its peak transient amplitude can reach as high as 5.70 A, leading to high current stress on the power stage components. On the contrary, as shown in Fig. 4.20(b), i_r reaches the new steady state in about one switching cycle under TSM without causing any visible transient oscillations.

Fig. 4.21 shows the measured transient responses when the phase-shift angle is decreased from $\pi/3$ to $\pi/6$, while Fig. 4.22 shows the measured transient responses when the direction of power flow is reversed by changing the phase-shift angle from $\pi/6$ to $-\pi/6$. Similar as before, with CTPSM, i_r suffers from severe HF transient oscillations under these conditions, resulting in peak transient current amplitudes

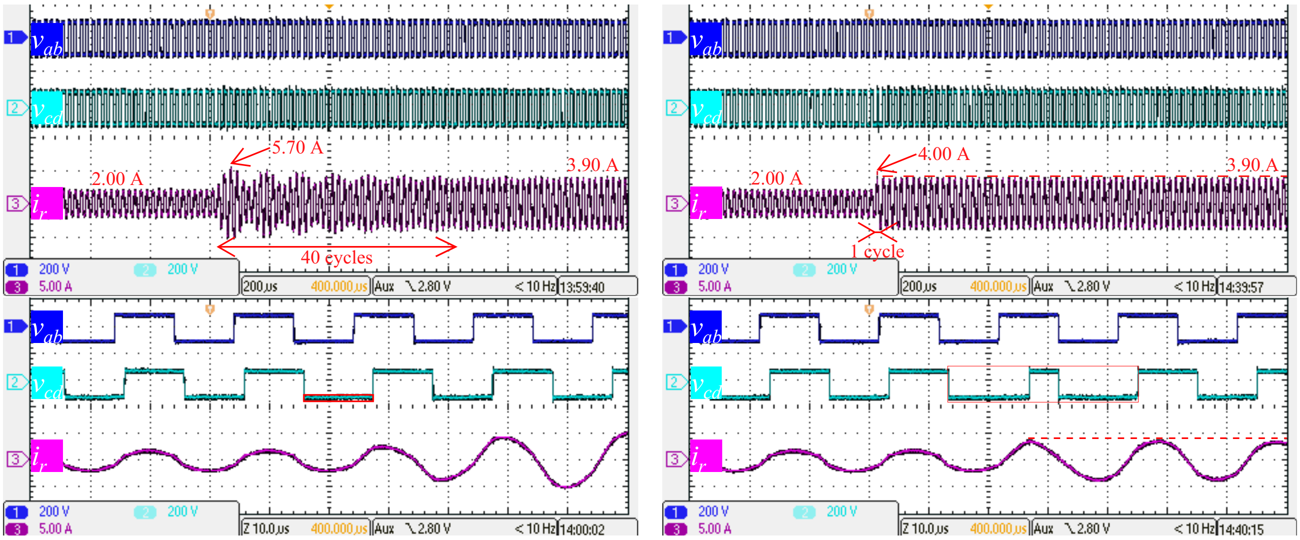

(a) (b)

Fig. 4.20. Open-loop experimental results when the phase-shift angle is changed from $\pi/6$ to $\pi/3$. (a) Under CTPSM (c.f. simulation results in Fig. 4.5(a)). (b) Under TSM (c.f. simulation results in Fig. 4.11(a)).

that are significantly higher than the steady-state values. On the contrary, no visible transient oscillations are observed in the case of SR-DABC under TSM as the trajectory of i_r has been planned to transit smoothly from the original to the new steady state in about one switching cycle.

As a result, it can be concluded that TSM has demonstrated an excellent performance in suppressing HF transient oscillations even under abrupt and large-amplitude changes in the phase-shift angle. This verifies its suitability for adoption in closed-loop design with fast controller such as MPC. The objective of the next subsection is to verify the performance of TSM under closed-loop conditions when regulated by an MPC.

4.5.2 Closed-Loop Tests

In practice, SR-DABC is generally operated in closed-loop configuration, therefore the performance of TSM under closed-loop conditions is of greater practical interest and should be thoroughly verified. Thus, both simulation and experimen-

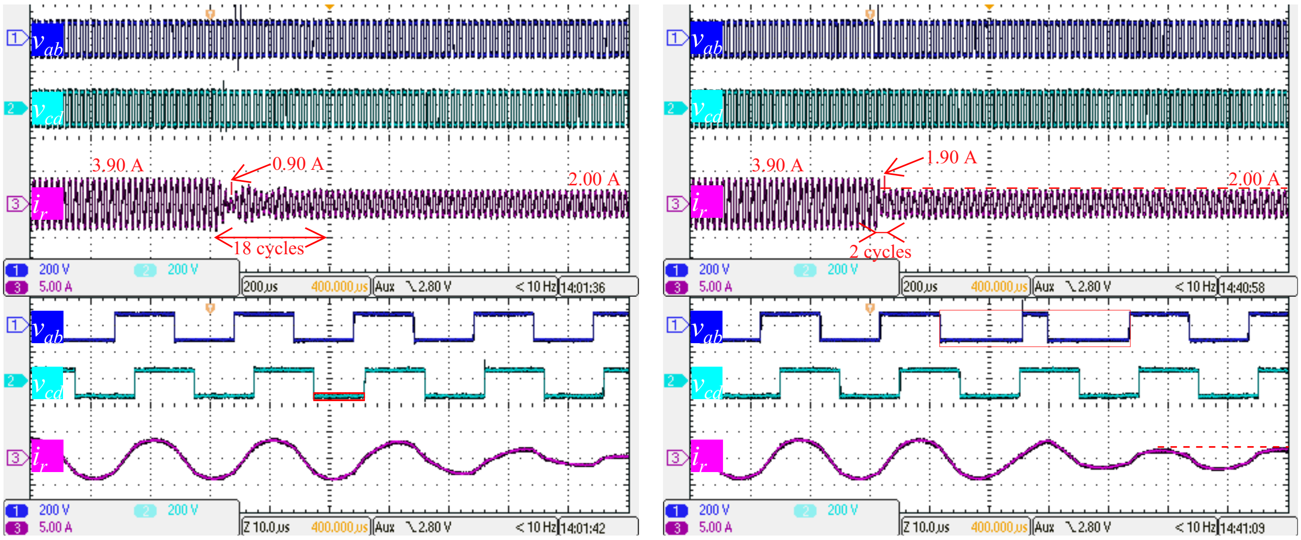

(a) (b)

Fig. 4.21. Open-loop experimental results when the phase-shift angle is changed from $\pi/3$ to $\pi/6$. (a) Under CTPSM (c.f. simulation results in Fig. 4.5(b)). (b) Under TSM (c.f. simulation results in Fig. 4.11(a)).

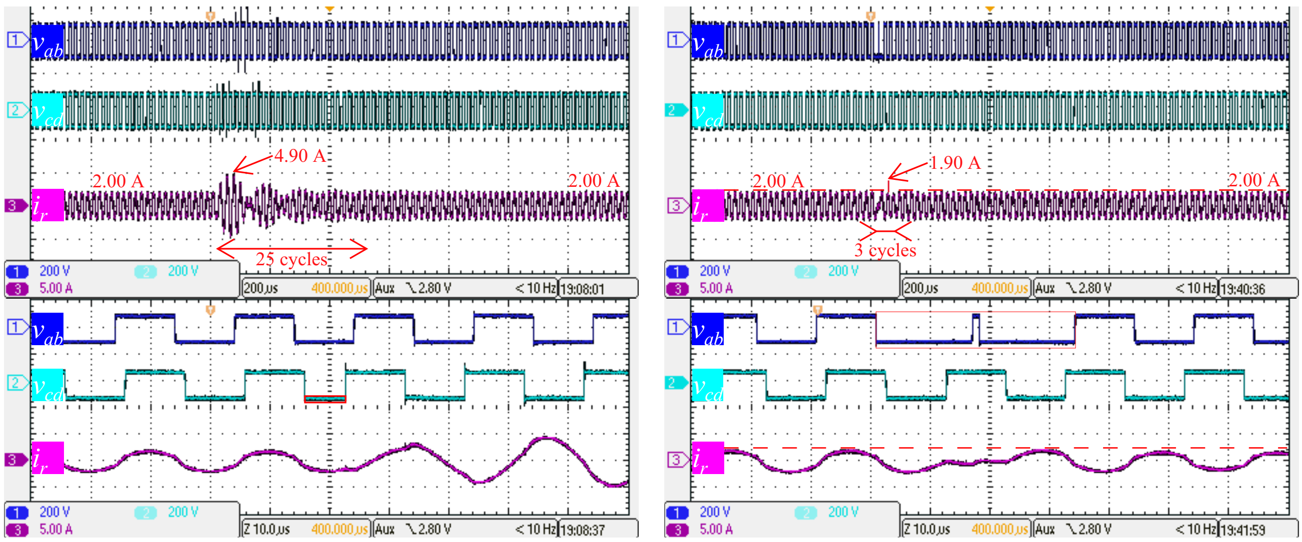

(a) (b)

Fig. 4.22. Open-loop experimental results when the phase-shift angle is changed from $\pi/6$ to $-\pi/6$. (a) Under CTPSM (c.f. simulation results in Fig. 4.5(c)). (b) Under TSM (c.f. simulation results in Fig. 4.11(b)).

tal results are presented for a closed-loop SR-DABC implemented with TSM. To highlight the merits of TSM, comparisons are made with a closed-loop SR-DABC implemented with CTPSM. As discussed previously, MPC is selected as the feed-

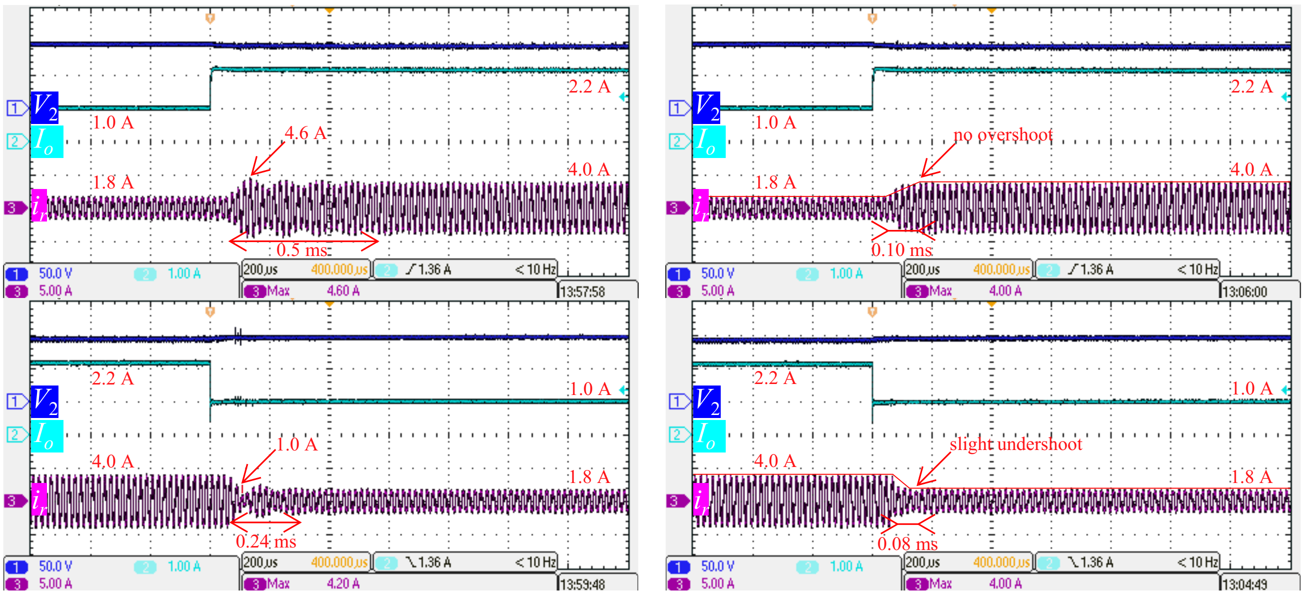

(a) (b)

Fig. 4.23. Experimental step-load transient responses under (a) MPC+CTPSM, (b)MPC+TSM. (T_1: $K_p = 0.02$, $K_i = 0.005$).

back controller in these simulations and experiments due to its fast control action which is intended to introduce large-amplitude changes in the phase-shift angle when performing closed-loop regulation [44]. For all the simulations and experiments presented in this subsection, the output voltage of SR-DABC is regulated by MPC under step-load changes between 1 A and 2.2 A.

Figs. 4.23 and 4.24 show the experimental results corresponding to the simulated cases depicted in Figs. 4.15 and 4.16. Generally, the experimentally measured transient responses under CTPSM and TSM for both slow-loop and fast-loop configurations match closely with the simulated transient responses. For CTPSM, a transient peak amplitude of 4.6 A is observed for i_r, i.e., 15% higher than the steady-state amplitude of 4.0 A, under step-load increase 1 A $\rightarrow$ 2.2 A, and it takes approximately 0.50 ms to reach the new steady state under the slow-loop configuration. Under the fast-loop configuration, the transient peak amplitude of i_r has increased to 7.2 A, i.e., 71% higher than the steady-state amplitude of 4.2 A, and it takes a much longer time (0.32 ms) to reach the new steady state.

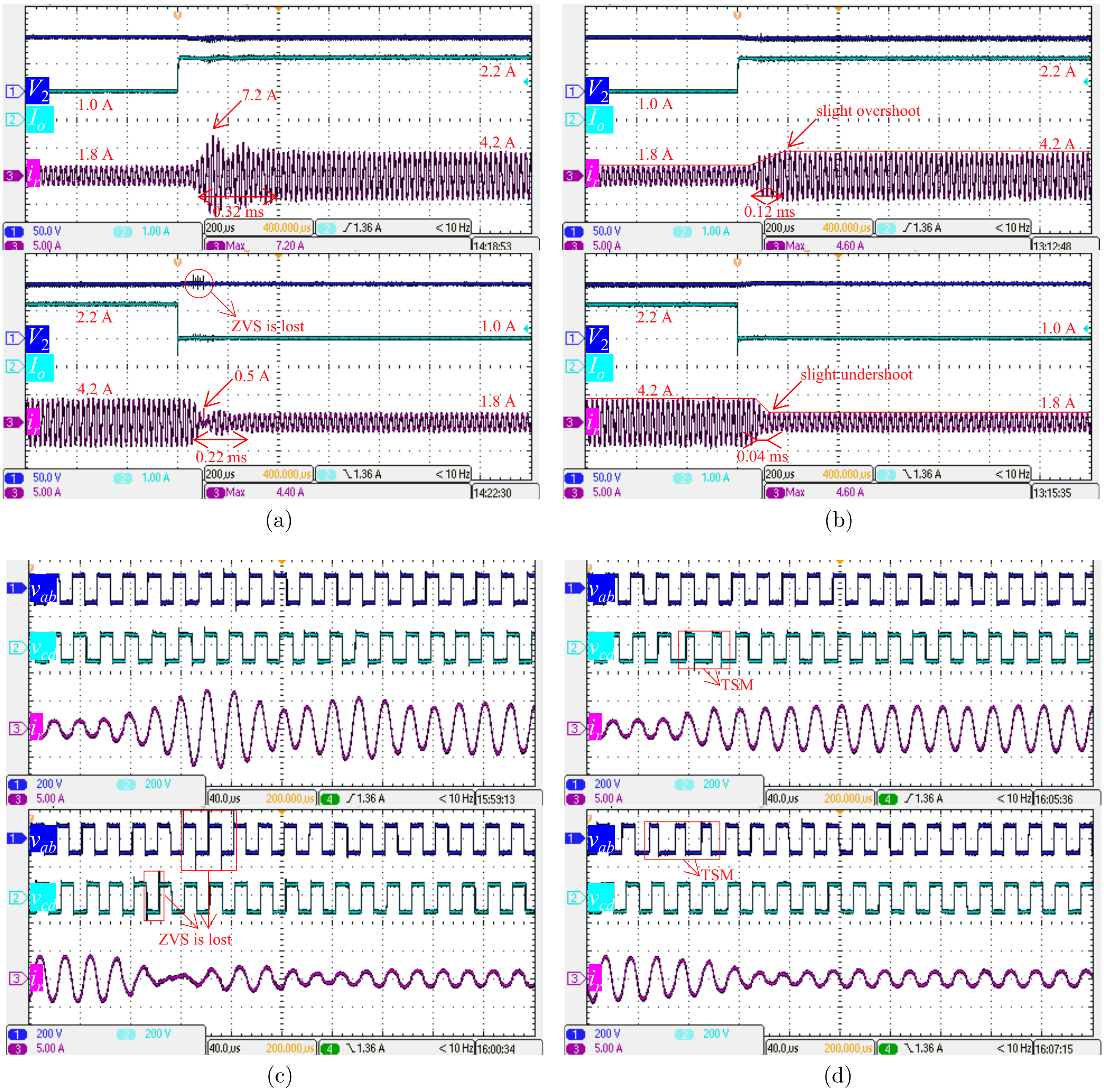

Fig. 4.24. Experimental step-load transient responses under (a) MPC+CTPSM, (b) MPC+TSM. Zoomed-in waveforms of v_{ab}, v_{cd}, and i_r under (c) MPC+CTPSM, (d) MPC+TSM. (T_2: $K_p = 0.07$, $K_i = 0.01$)

These observations again highlight the incompatibility of CTPSM with high-gain (fast) controller as it tends to introduce more severe HF transient oscillations as the control loop bandwidth increases and the phase-shift angle changes more rapidly. Under step-load decrease 2.2 A $\rightarrow$ 1 A, a severe undershoot is observed in i_r at the onset of transient response, and the degree of undershoot is observed to worsen with increasing control loop bandwidth, i.e., up to 1.3 A (72%) undershoot is resulted under the fast-loop configuration, to the extent that large spikes are produced on the output voltage V_2 leading to a degradation in the output voltage quality. These transient voltage spikes are associated with the loss of ZVS, as shown in Fig. 4.24(c), resulting from small phase-shift angles under MPC+CTPSM. For step-load decrease, i_r takes 0.24 ms and 0.22 ms, respectively, to reach the new steady state under the slow-loop and fast-loop configurations. It should be noted that the above observations also apply to v_{Cr} (since $i_r = C_r \frac{\mathrm{d}v_{Cr}}{\mathrm{d}t}$) so the transient waveforms of v_{Cr} are omitted here due to space constraint.

On much the contrary, regardless of control loop bandwidth, no visible overshoot and undershoot are observed in i_r (as well as v_{Cr}) during step-load increase and decrease when TSM is applied instead of CTPSM. For example, under the slow-loop configuration T_1, i_r is observed to reach the new steady state smoothly and rapidly in approximately 0.10 ms and 0.08 ms during step-load increase and decrease, i.e. 80% and 67% reduction compared to CTPSM, respectively. It is also observed that the settling time of i_r under TSM remains more or less the same for both slow-loop and fast-loop configurations, thus verifying the insensitivity of TSM's operation to controller configuration, making it ready for integration with any fast controller for realizing oscillation-free fast dynamic performance of SR-DABC for many emerging power electronic applications requiring stringent bus voltage regulation, such as power supplies for data centers and electric vehicles. As exemplified in Fig. 4.24(d), the zoomed-in waveforms of v_{ab}, v_{cd}, and i_r confirm the proper operation of TSM during transient states, indicating once again that the operation of TSM is decoupled from the actual controller configuration, thus providing greater flexibility in the design and implementation of fast controller for SR-DABC while ensuring the realization of oscillation-free transient responses in all cases.

To facilitate a comparison between CTPSM and TSM, all simulation and ex-

Table 4.2 Performance Comparison of CTPSM and TSM under Open-Loop Conditions.

		Modulation	POS/PUS	ST
$\theta = \pi/6$ $\delta = \pi/6$	Simulation	CTPSM	POS 1.85 A	167 cycles
		TSM	POS 0.06 A	001 cycle
	Experiment	CTPSM	POS 1.80 A	040 cycles
		TSM	POS 0.10 A	001 cycle
$\theta = \pi/3$ $\delta = -\pi/6$	Simulation	CTPSM	PUS 1.63 A	134 cycles
		TSM	PUS 0.06 A	001 cycle
	Experiment	CTPSM	PUS 1.10 A	018 cycles
		TSM	PUS 0.10 A	002 cycles
$\theta = \pi/6$ $\delta = -\pi/3$	Simulation	CTPSM	POS 3.31 A	149 cycles
		TSM	PUS 0.07 A	001 cycle
	Experiment	CTPSM	POS 2.90 A	025 cycles
		TSM	PUS 0.10 A	003 cycles

perimental results discussed above are summarized in Tables 4.2 and 4.3. The main results are presented in the last two columns, where POS and PUS stand for "peak overshoot" and "peak undershoot", respectively, and ST stands for "settling time". It is evident from the tabulated results that the POS/PUS and ST associated with TSM are significantly lower compared to the figures associated with CTPSM, which confirms the effectiveness of TSM in suppressing HF transient oscillations and achieving fast convergence to new steady states. Except for a few cases, there is generally close agreement between the simulated and experimental results with the slight discrepancies predominantly due to parasitic components, parameter deviations, dead-time effects, power losses, etc.

4.5.3 Parameter Sensitivity Analysis

In practice, the values of the resonant components can deviate from their nominal values due to manufacturing tolerances, temperature effects, component aging, etc. From (4.23), it can be seen that the transient modulation parameter γ

Table 4.3 Performance Comparison of CTPSM and TSM under Closed-Loop Conditions.

		Modulation	POS/PUS	ST
Load step-up transition under MPC with T_1	Simulation	CTPSM	POS 1.95 A	1.92 ms
		TSM	POS 0.24 A	0.38 ms
	Experiment	CTPSM	POS 0.60 A	0.50 ms
		TSM	POS 0.00 A	0.10 ms
Load step-down transition under MPC with T_1	Simulation	CTPSM	PUS 1.30 A	0.84 ms
		TSM	PUS 0.27 A	0.33 ms
	Experiment	CTPSM	PUS 0.80 A	0.24 ms
		TSM	PUS 0.20 A	0.08 ms
Load step-up transition under MPC with T_2	Simulation	CTPSM	POS 3.12 A	0.68 ms
		TSM	POS 0.97 A	0.46 ms
	Experiment	CTPSM	POS 3.00 A	0.32 ms
		TSM	POS 0.40 A	0.12 ms
Load step-down transition under MPC with T_2	Simulation	CTPSM	PUS 1.33 A	0.43 ms
		TSM	PUS 0.63 A	0.12 ms
	Experiment	CTPSM	PUS 1.30 A	0.22 ms
		TSM	PUS 0.20 A	0.04 ms

is a function of the normalized frequency F ($F = f_s/f_r$). Although f_s is constant for a fixed-frequency operated SR-DABC, variations in L_r and/or C_r can lead to changes in f_r, and hence F. To understand the effect of variation in F, the feasible solution region of TSM for different F values are plotted in Fig. 4.25, from which it can be seen that the maximum allowable δ in each execution decreases with decreasing F, implying that when this occurs the operation of TSM is limited to small step changes in phase-shift angle in each execution.

To further evaluate the performance of TSM under parameter variations, a detailed parameter sensitivity analysis (PSA) is performed whereby the transient responses of SR-DABC are simulated for different C_r under both open-loop and closed-loop conditions, and the corresponding POS/PUS and ST are recorded and plotted in Figs. 4.26 and 4.27, respectively. Fig. 4.26 depicts the open-loop PSA

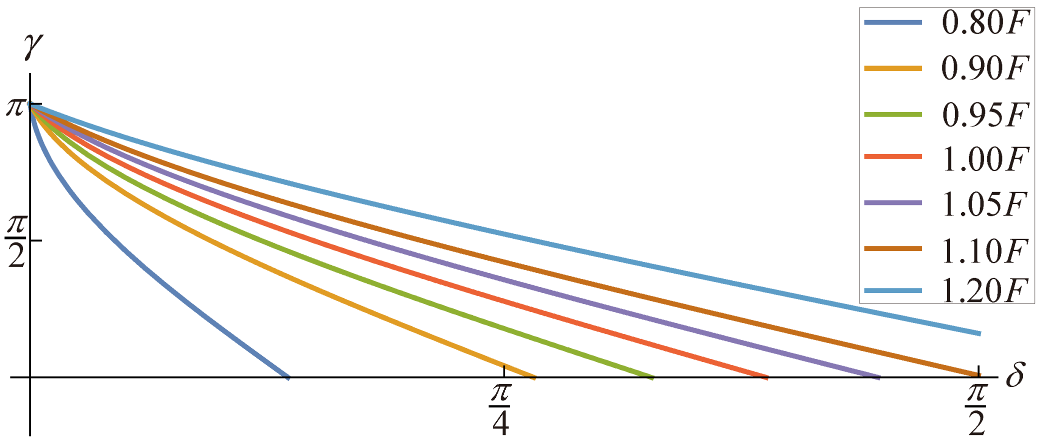

Fig. 4.25. Effect of variation in F on the feasible solution region of TSM.

results for an increase in phase-shift angle from $\pi/6$ to $\pi/3$, whereas Fig. 4.27 depicts the closed-loop PSA results for a step-load increase from 1 A to 2.2 A, where $C_{r,N}$ is defined as the normalized resonant capacitance with respect to the nominal capacitance. Despite the wide-range variation of C_r, it is evident that the POS/PUS and ST resulting from TSM remain consistently lower than those resulting from CTPSM, which confirms the effectiveness of TSM even after taking the effect of parameter variation into consideration.

4.6 Chapter Summary

A new sensor-less trajectory control method known as TSM is proposed to mitigate the problem of HF transient oscillations in SR-DABC arising from CTPSM. As these HF transient oscillations typically take many switching cycles to decay before the converter reaches its new steady states, a truly fast dynamic response cannot be achieved by employing high-gain controller alone without considering the design of the underlying transient modulation strategy in parallel. In fact, it can be seen from Figs. 4.23 and 4.24, an inappropriately designed transient modulation strategy is likely to worsen the dynamic response of SR-DABC, especially when a higher-gain controller is employed. As demonstrated by both simulations and experiments, this study has shown that, by combining the proposed TSM

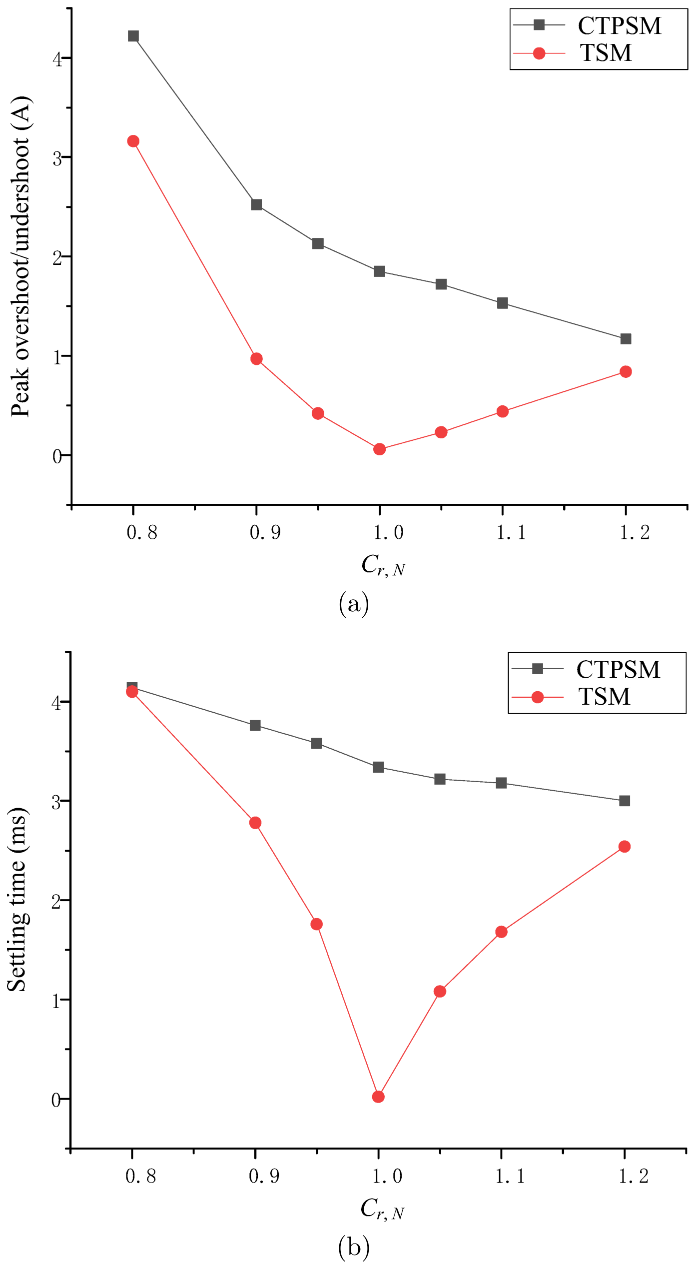

Fig. 4.26. Open-loop PSA results for an increase in phase-shift angle from $\pi/6$ to $\pi/3$. (a) Peak overshoot/undershoot. (b) Settling time.

method with a high-gain controller such as MPC, oscillation-free dynamic response can be readily achieved in SR-DABC without requiring costly sensors and complex trajectory calculations, such that the transient peak-to-peak amplitude of resonant current is reduced and time-optimal transient performances can be obtained. This work represents the first attempt in the related literature to highlight the role of transient modulation and its importance in achieving high-quality and

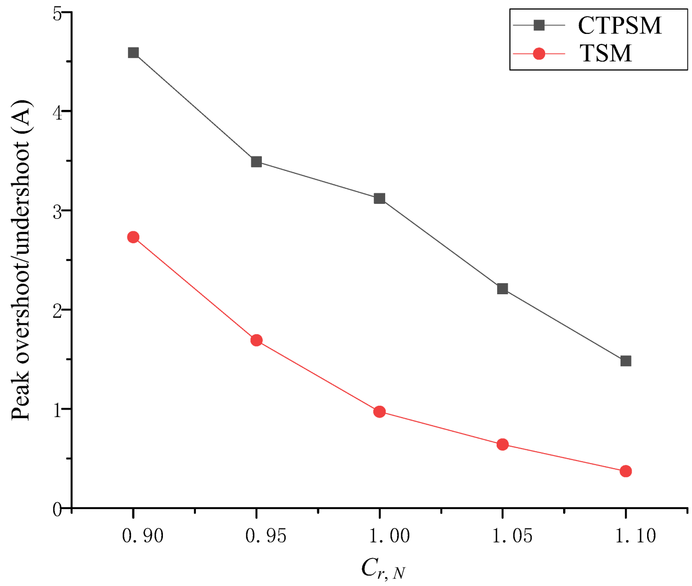

(a)

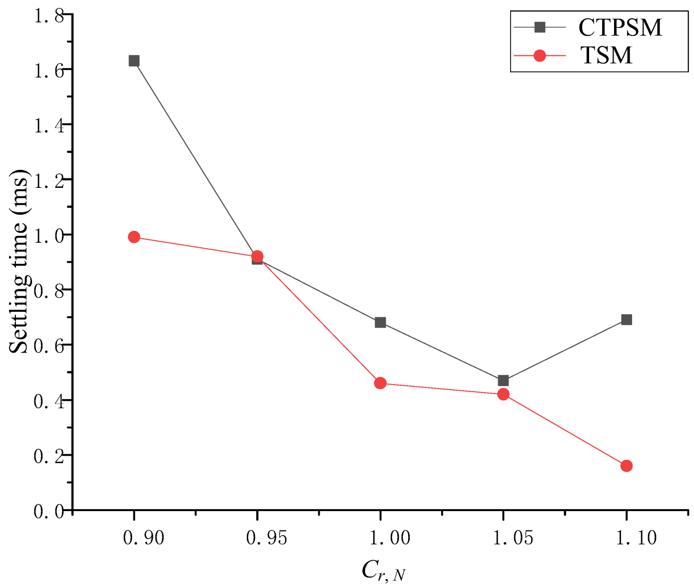

(b)

Fig. 4.27. Closed-loop PSA results for a step-load increase from 1 A to 2.2 A. (a) Peak overshoot/undershoot. (b) Settling time.

ultrafast dynamic response in SR-DABC under both open-loop and closed-loop conditions.

Chapter 5

Generalized Trajectory-Switching Modulation for DC-Offset-Free and Oscillation-Free Transient Response

5.1 Introduction

In Chapter 4, a transient SPS modulation scheme known as TSM can provide accurate closed-form expressions of the transient pulse widths for suppressing HF transient oscillations without using additional sensors, which is a more desirable solution than the ones presented in [109]–[111]. However, the feasible solution region of TSM becomes restricted when the applied switching frequency (f_s) approaches the resonant frequency (f_r). In order to achieve a wider operating range under TSM, v_{cd} is modified when increasing the phase-shift angle, while v_{ab} is modified when decreasing the phase-shift angle, which makes it inconvenient to use in MPS-modulated SR-DABC. Obviously, it is also unfeasible to extend the transient modulation methods presented in [109]–[111] to MPS-modulated SR-DABC.

Thus, an evident limitation with the existing OTPSM strategies for SR-DABC is that they are designed to be compatible with SPS modulation only. Since SPS modulation has limitations in ZVS range, peak current stress, backflow power, etc., at different converter gains and power levels, it is worthwhile to develop a transient modulation strategy for MPS gating schemes. Another key limitation of existing schemes is that all of them cannot eliminate the transient dc offset in transformer's magnetizing current, which will result in a longer settling time and potential risk of transformer's core saturation, thus inevitably degrading the dynamic performance of SR-DABC.

To overcome these limitations, this chapter proposes a novel transient modulation strategy known as generalized TSM (GTSM), which is formulated for general MPS-modulated SR-DABC. The benefits of the proposed GTSM and the key contributions of this chapter are outlined below:

1. It can be applied universally to any MPS gating schemes, operation modes, and power-flow directions, making it compatible with essentially most applications.

2. It represents the first method that can suppress the transient oscillations and dc offsets simultaneously.

3. Unlike other existing technique (TSM [140]), GTSM can be utilized effectively even when the switching-to-resonant frequency ratio $F = f_s/f_r$ is small. Hence, the designed transient pulse widths of GTSM are easily modified with respect to a fixed reference signal.

4. The algorithm of GTSM is guided by a set of analytical expressions and does not require any voltage or current feedback (i.e., sensorless), which facilitates its cycle-by-cycle implementation in an accurate and cost-effectively manner under closed-loop conditions.

Table 5.1 Comparison of different transient modulation schemes for SR-DABC.

Desirable properties	GTSM	TSM [140]	Methods in [109]–[111]
Oscillation Suppression	✓	✓	✓
DC-offset Elimination	✓	×	×
Generic Method	✓	×	×
Analytical Expression	✓	✓	×
Sensorless Algorithm	✓	✓	×
Closed-loop Implementation	✓	✓	×
Wide Feasible Region	✓	×	Not applicable

5. A combined use of GTSM and MPC is presented for demonstrating the merits of GTSM under closed-loop conditions when coupled with a fast controller.

6. An online parameter estimation method is employed to ensure both GTSM and MPC can adaptively work well when the resonant tank's parameters are not precisely known or deviate significantly from the nominal values.

Table 5.1 compares different transient modulation techniques for DABSRC. As GTSM can achieve all desirable properties, it is an ideal and by far the most effective scheme for SR-DABC.

The rest of this chapter is organized as follows. Section 5.2 describes an independent half-bridge equivalent circuit model of TPS-modulated SR-DABC and the conventional transient modulation scheme. The fundamental principle of the proposed GTSM strategy is presented in Section 5.3. In Section 5.4, a closed-loop model predictive control design for MPS-modulated SR-DABC is presented, followed by a method for online estimation of resonant tank's parameters in Section 5.5. Experimental results and data analysis are shown in Section 5.6, and conclusions are drawn in Section 5.7.

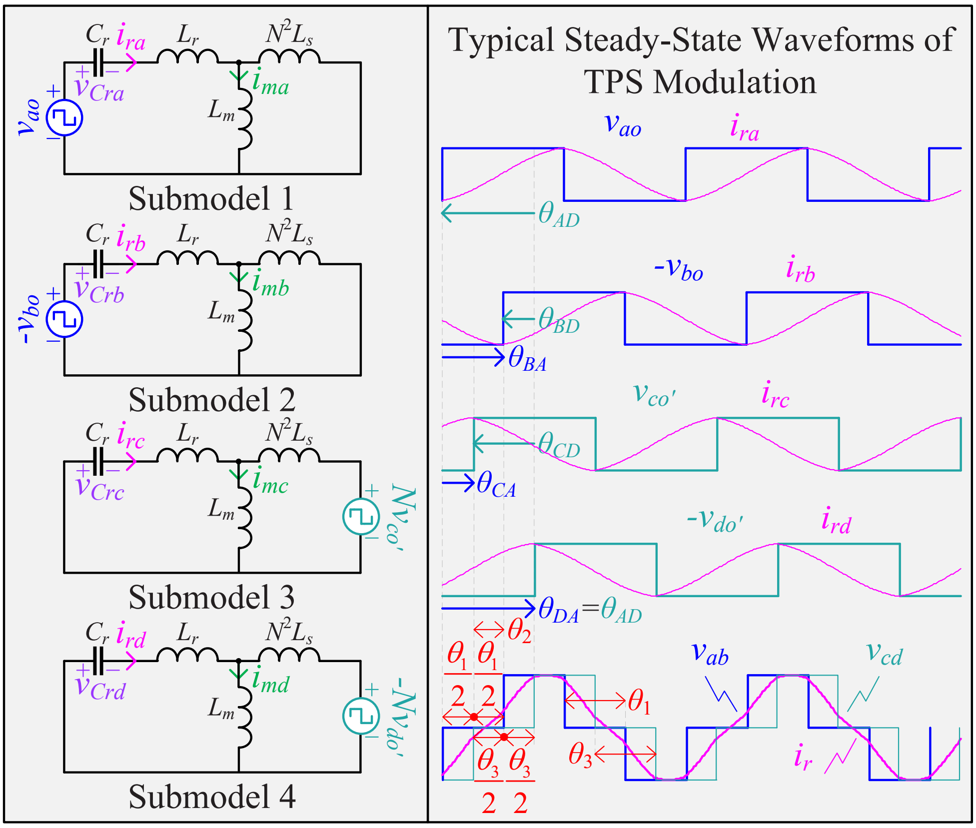

Fig. 5.1. Independent half-bridge equivalent model and steady-state waveforms of TPS-modulated SR-DABC.

5.2 Independent Half-Bridge Equivalent Model of SR-DABC

The resonant capacitor of SR-DABC can, to a certain degree, help to block the dc bias in the resonant current during steady state [31], but it cannot suppress the transient dc offset to prevent the transformer from saturation. Thus, as depicted in Fig. 1.7(a), a practical circuit schematic of SR-DABC based on T-model transformer is considered in this chapter.

As shown in Fig. 5.1, referring to the analyses presented in [108], v_{ab} and v_{cd} under any commonly used phase-shift modulation schemes can be seen as produced by four half-bridge square-wave generators (i.e., v_{ao}, $-v_{bo}$, $v_{co'}$, and $-v_{do'}$), which are phase-shifted from each other by $\{\theta_{BA}, \theta_{CA}, \theta_{DA}\}$ (i.e., with respect to v_{ao}) or

Table 5.2 Relationships Between Different Definitions of Phase-Shift Angles.

Reference Signal	Phase-Shift Relationship
v_{ao}	$\theta_{BA} = \theta_1$ $\theta_{CA} = \theta_2 + 0.5 * (\theta_1 - \theta_3)$ $\theta_{DA} = \theta_2 + 0.5 * (\theta_1 + \theta_3)$
$-v_{do'}$	$\theta_{AD} = \theta_2 + 0.5 * (\theta_1 + \theta_3)$ $\theta_{BD} = \theta_2 + 0.5 * (\theta_3 - \theta_1)$ $\theta_{CD} = \theta_3$

$\{\theta_{AD}, \theta_{BD}, \theta_{CD}\}$ (i.e., with respect to $-v_{do'}$) for achieving different power levels and flow directions. Therefore, a SR-DABC can be further decomposed into four independent half-bridge equivalent circuit submodels, which helps us in analyzing the resonant current i_r, magnetizing current i_m, and resonant capacitor voltage v_{Cr} by calculating the contribution of each independent excitation source separately. Using the superposition theorem yields

$$\begin{cases} i_r = i_{ra} + i_{rb} + i_{rc} + i_{rd} \\ i_m = i_{ma} + i_{mb} + i_{mc} + i_{md} \\ v_{Cr} = v_{Cra} + v_{Crb} + v_{Crc} + v_{Crd}. \end{cases} \tag{5.1}$$

Accordingly, by applying mesh analysis to for example submodel 2 and submodel 3, we obtain

$$i_{mb} = \frac{N^2 L_s}{L_m + N^2 L_s} i_{rb} \tag{5.2}$$

$$i_{mc} = (\frac{1}{\omega_s^2 L_m C_r} - \frac{L_r}{L_m}) i_{rc} \tag{5.3}$$

where $\omega_s = 2\pi f_s$.

Typically, under TPS modulation, the following definitions of phase-shift angles are adopted: $\theta_1 \in [0, \pi]$ and $\theta_3 \in [0, \pi]$ as the inner phase-shift angles of the primary and secondary bridges, and $\theta_2 \in [-\pi/2, \pi/2]$ as the outer phase-shift angle. In our case, based on the selected reference signal, i.e., either v_{ao} or $-v_{do'}$,

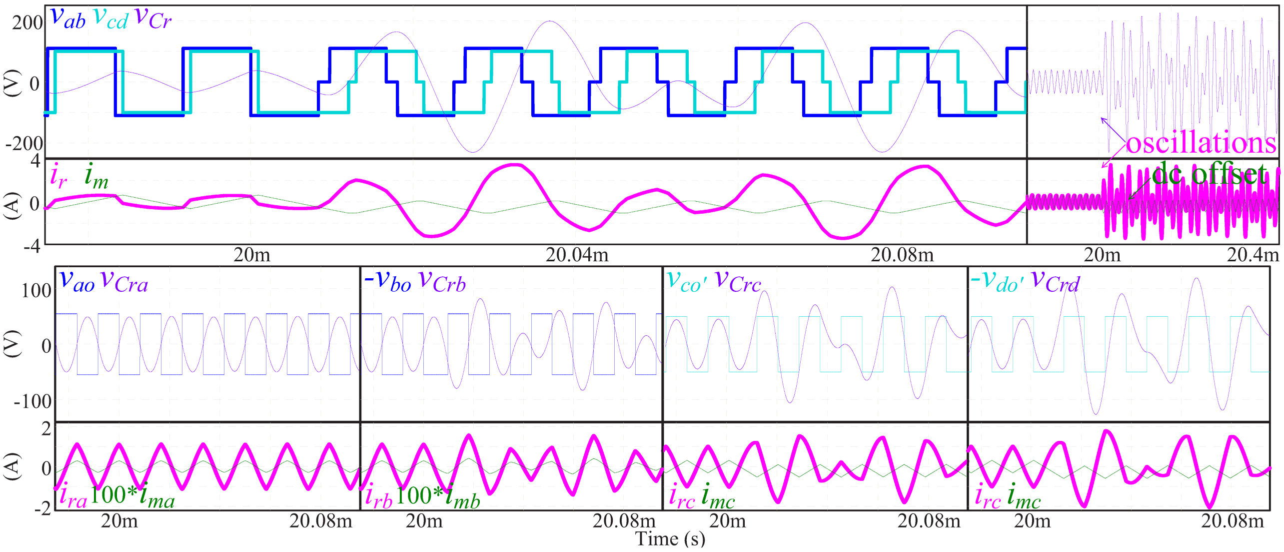

(a)

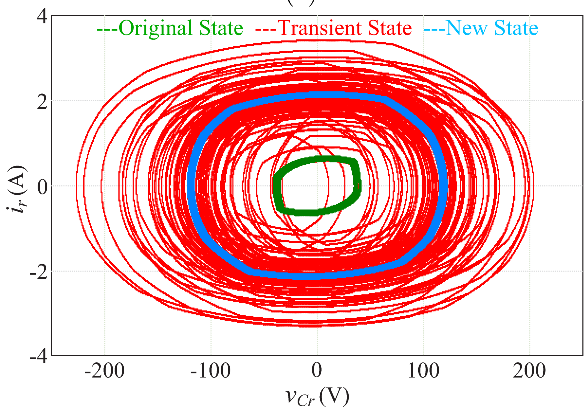

(b)

Fig. 5.2. An open-loop simulation example from SPS mode to TPS mode under CTPSM with $V_1 = 110$ V, $V_2 = 100$ V, $f_s = 60$ kHz, and $F = 1.54$. (a) Simulated transient waveforms. (b) v_{Cr}-i_r state-plane diagram under CTPSM.

the relationships between different phase-shift angles are tabulated in Table 5.2. In general, for MPS-based CTPSM, v_{ao} is set as a frequency-fixed 50% duty-cycle square-wave reference signal. During transient state, the low-level durations of $-v_{bo}$, $v_{co'}$, and $-v_{do'}$ are directly increased/decreased by $\Delta\theta_{BA}$, $\Delta\theta_{CA}$, and $\Delta\theta_{DA}$, respectively, with respect to v_{ao}. However, it is known that the direct adjustments of θ_{BA}, θ_{CA}, and θ_{DA} (or the three control variables θ_1, θ_2, and θ_3) will induce complex dynamics in i_r, i_m, v_{Cr}, etc.

Fig. 5.2 presents an open-loop simulation example of how these phase-shift angles are updated by CTPSM. It is assumed that the desired phase-shift increments/decrements are $\Delta\theta_1$, $\Delta\theta_2$, and $\Delta\theta_3$. In this simulation test, the scenario

Table 5.3 Circuit Parameters and Specifications Used in Chapter 5.

Symbol	Parameter Description	Value or Part Type
V_1	Input Voltage	110-125 V
V_2	Output Voltage	100 V
C_o	Output Capacitance	47 μF
R_L	Load Resistance	50/200 Ω
$N:1$	Transformer's Turns Ratio	1 : 1
L_m	Magnetizing Inductance	650 μH
L_r	Resonant Inductance	321 μH
L_s	Secondary Inductance	1.70 μH
C_r	Resonant Capacitance	52 nF
f_s	Switching Frequency	50-60 kHz
f_r	Resonant Frequency	38.96 kHz
S_x~Q_x	Power Switches	UnitedSiC UJC06505K
–	Dead Time	250 ns
–	Gate Driver	TI UCC21520
–	Current Transducer	LEM LA 55-P
–	Voltage Transducer	Resistive Divider
–	Microprocessor	TI TMS320F28335
–	DAC Module	Microchip MCP4921
–	Simulation Platform	Powersim PSIM

$\theta_1 = 0$, $\theta_2 = \pi/9$, $\theta_3 = 0$, $\Delta\theta_1 = \pi/6$, $\Delta\theta_2 = 11\pi/36$, and $\Delta\theta_3 = \pi/9$, i.e., a transition from SPS mode to TPS mode is simulated. In addition, $V_1 = 110$ V, $V_2 = 100$ V, $f_s = 60$ kHz, $f_r = 38.96$ kHz, the switching-to-resonant frequency ratio $F = f_s/f_r = 1.54$, and other simulation parameters can be found in Table 5.3. It can be seen from Fig. 5.2(a) that high-frequency transient oscillations are induced in i_{rb}, i_{rc}, i_{rd}, i_r, v_{Crb}, v_{Crc}, v_{Crd}, and v_{Cr}, and excessive transient dc offsets appear in i_{mb}, i_{mc}, i_{md}, and i_m. However, such situations do not arise in the branch currents and voltages of submodel 1. This suggests that only when a direct pulse-width adjustment occurs in any of these independent square-wave voltages will transient oscillations and dc offsets be generated in SR-DABC. Based on the state-plane diagram shown in Fig. 5.2(b), the transient voltage and current stresses can reach nearly twice the new steady-state values under open-loop simulations, which increases the device stress, risk of system failure, and electro-magnetic interference (EMI) noise. As all problems are attributed to the use of CTPSM, more advanced transient phase-shift modulation scheme should be studied.

5.3 Proposed Generalized Trajectory-Switching Modulation (GTSM) Strategy

A fundamental property illustrated by the analysis presented in Section 5.2 is that, although the currents and voltages in different submodels exhibit different degrees of transient behaviors, if oscillation-free and dc-offset-free transient responses are achieved in each of these four submodels by separately applying an appropriate transient square-wave excitation to the submodel, smooth transitions can be achieved in i_r, i_m, and v_{Cr} simultaneously by the principle of superposition. As an illustration example, we will analyse the transient response of one submodel such as submodel 3 with excitation source $v_{co'}$. As labelled in Fig. 5.3(a), for the proposed GTSM, there are four transient modulation variables, namely, α_1, α_2, α_3, and α_4. Instead of using CTPSM to directly update the phase-shift increment in one step, the proposed GTSM attempts to execute the phase-shift adjustment in multiple steps, which means that more DOF are available for trajectory planning and control by GTSM during transient state. The key point of the proposed GTSM is that the ac-link current and voltage trajectories of SR-DABC should be modified by α_1, α_2, α_3, and α_4 to fulfil the boundary conditions for realizing oscillation-free transition [140] and dynamic volt-second balance for eliminating transient dc offset [108], [141].

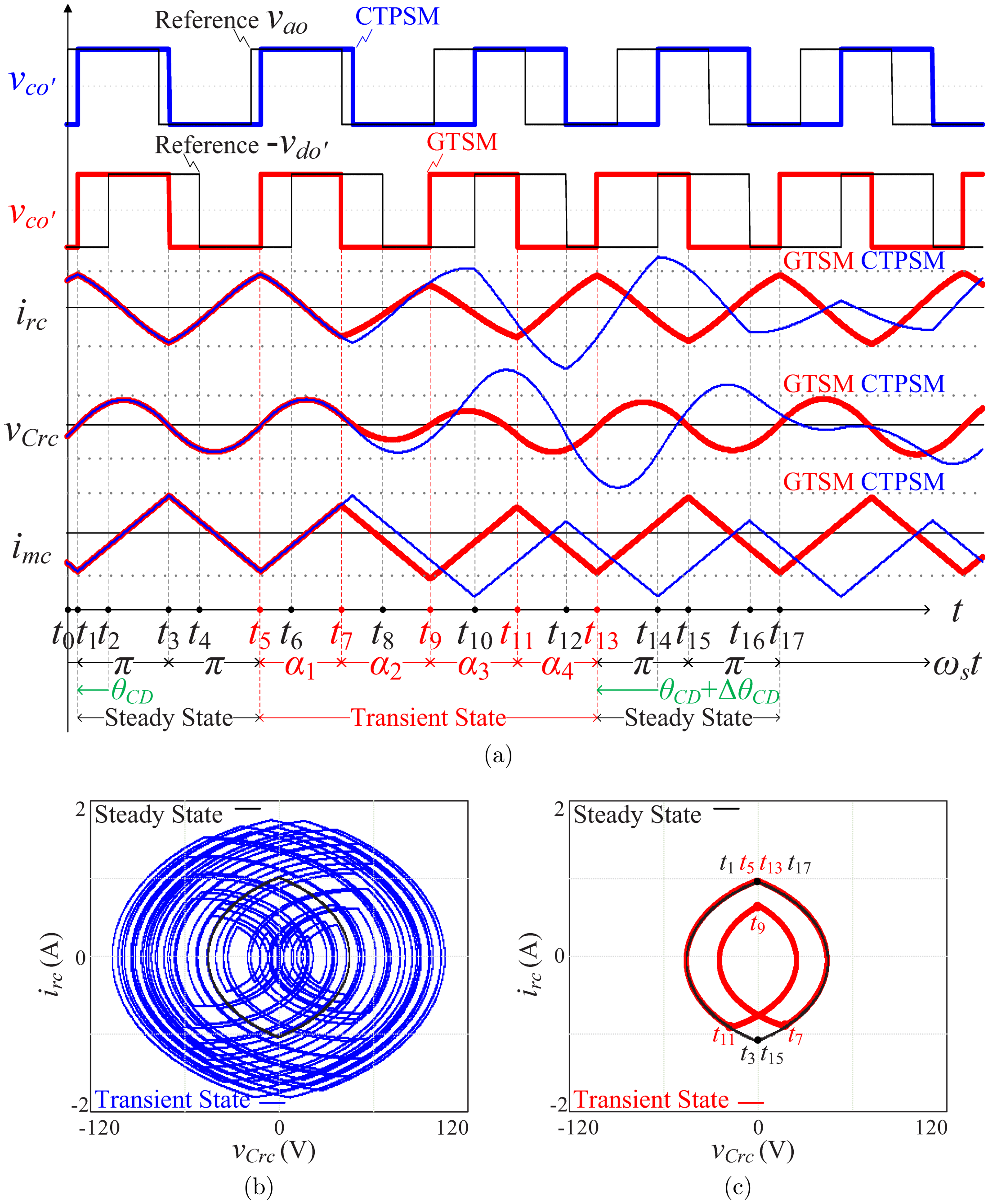

Fig. 5.3. (a) Theoretical transient waveforms with CTPSM and the proposed GTSM in submodel 3. (b) v_{Crc}-i_{rc} state-plane diagram under CTPSM. (c) v_{Crc}-i_{rc} state-plane diagram under GTSM.

5.3.1 Elimination of Transient DC Offset

Typically, if v_{ao} is selected as the reference signal under CTPSM, the direct changes in $-v_{bo}$, $v_{co'}$, and $-v_{do'}$ during transient state will inevitably lead to excessive transient dc offsets in i_{mb}, i_{mc}, and i_{md}. However, according to (5.2), the transient dc offsets in i_{ma} and i_{mb} are relatively small, and i_{mc} and i_{md} will have stronger influences on i_m due to $L_m > L_r \gg L_s$ in most applications of SR-DABC. As any transient operation in the secondary-side voltages may result in large-amplitude transient current in i_{mc} and/or i_{md} and long settling time, it is suggested that $-v_{do'}$ is fixed and used as the reference signal and phase-shift adjustments are accomplished through the modifications of v_{ao}, $-v_{bo}$, and $v_{co'}$. For this reason, $-v_{do'}$ is set as a fixed reference signal under GTSM, and θ_{AD}, θ_{BD}, and θ_{CD} are expressed in terms of θ_1, θ_2, and θ_3 as given in Table 5.2.

However, the setting of appropriate reference signal alone cannot eliminate the transient dc offset in i_m. In fact, (5.2) and (5.3) also show that the current flowing through the magnetizing inductance branch (e.g., i_{mb} or i_{mc}) is directly proportional to the current flowing through the L_r-C_r resonant network branch (e.g., i_{rb} or i_{rc}). Hence, supposing that the submodel circuits are purely inductive, to eliminate transient dc offset in i_{mc}, a dynamic volt-second balance should be imposed on $v_{co'}$ [108]. Consequently, in submodel 3, a constraint condition of the volt-second balance during transient state is given by

$$\begin{aligned} &Nv_{co'}\alpha_1 - Nv_{co'}\alpha_2 + Nv_{co'}\alpha_3 - Nv_{co'}\alpha_4 = 0 \\ &\qquad \Rightarrow \alpha_1 - \alpha_2 + \alpha_3 - \alpha_4 = 0. \end{aligned} \tag{5.4}$$

In addition, to ensure that the transient state ends no later than t_{13} under GTSM, it can be found from Fig. 5.3(a) that a phase-shift constraint is required as given by (5.5).

$$\omega_s(t_{13} - t_5) = \alpha_1 + \alpha_2 + \alpha_3 + \alpha_4 = 4\pi - \Delta\theta_{CD} \tag{5.5}$$

Combining (5.4) and (5.5) leads to

$$\alpha_1 + \alpha_3 = \alpha_2 + \alpha_4 = 2\pi - 0.5\Delta\theta_{CD} \tag{5.6}$$

and the use of (5.6) will ensure that i_{mc} enters its new steady state before t_{13}.

As discussed in Chapter 3 [141], in order to minimize the adverse effects caused by transient dc offset, it is important to minimize the time-averaged value of

i_{mc} (i.e., $\bar{i_{mc}}$) over the transient state. By applying constraint (5.6), $\bar{i_{mc}}$ can be simplified and expressed as

$$\begin{aligned}\bar{i_{mc}} &= \frac{1}{t_{13}-t_5}\int_{t_5}^{t_{13}} i_{mc}\mathrm{d}t \\ &= \frac{NV_2}{2L_m}\left(-\frac{T_s}{4}+\frac{2\pi-0.5\Delta\theta_{CD}}{2}-\frac{\alpha_2\alpha_3}{2\pi-0.5\Delta\theta_{CD}}\right)\end{aligned} \tag{5.7}$$

where $T_s = 1/f_s$ is the switching period. It can be deduced from (5.7) that for a given $\Delta\theta_{CD}$, $\bar{i_{mc}}$ reaches its minimum value only when $\alpha_2 = \alpha_3$ and both α_2 and α_3 are set to their maximum possible values, namely, (5.8).

$$\alpha_2 = \alpha_3 = \max(\alpha_2) = \max(\alpha_3) \tag{5.8}$$

Thus, (5.8) is the optimal solution of (5.6) for eliminating transient dc offset and achieving a minimum $\bar{i_{mc}}$ during transient state.

5.3.2 Elimination of High-Frequency Transient Oscillations

It should be noted that with (5.6) and/or (5.8), the values of α_1, α_2, α_3, and α_4 cannot be uniquely determined. In other words, (5.6) merely guarantees the elimination of transient dc offset but cannot guarantee the elimination of transient oscillations in i_{rc} and v_{Cr}.

Referring to the previous research work reported in Chapter 4 [140], the analytical expressions of i_r and v_{Cr} for an ideal L_r-C_r tank can be obtained by applying Kirchhoff's voltage law to the equivalent circuit of SR-DABC. Similarly, by neglecting the magnetizing inductance L_m of submodel 3, i.e., L_m is treated as open circuit, i_{rc} and v_{Crc} are expressed by (5.9) and (5.10), respectively,

$$i_{rc}(t) = i_{rc}(t_i)\cos(\omega_r(t-t_i)) + ((-Nv_{co'}) - v_{Crc}(t_i))\sin(\omega_r(t-t_i))/Z_r \tag{5.9}$$

$$\begin{aligned}v_{Crc}(t) =& v_{Crc}(t_i)\cos(\omega_r(t-t_i)) + Z_r i_{rc}(t_i)\sin(\omega_r(t-t_i)) \\ &+ (-Nv_{co'})(1-\cos(\omega_r(t-t_i)))\end{aligned} \tag{5.10}$$

where $Z_r = \sqrt{L_r/C_r}$ represents the characteristic impedance of the resonant tank,

$\omega_r = 1/\sqrt{L_r C_r} = 2\pi f_r$ is the angular resonant frequency, and the subscript $i = 1, 2, 3, \ldots$ is used to indicate the time nodes.

Due to the symmetrical characteristics of the steady-state waveforms shown in Fig. 5.3, the initial steady-state values of i_{rc} and v_{Crc} at the beginning of the transient state (t_5) are given by

$$i_{rc}(t_5) = i_{rc}(t_1) = -i_{rc}(t_3) = NV_2 \tan(\pi/2/F)/2/Z_r \tag{5.11}$$

$$v_{Crc}(t_5) = v_{Crc}(t_1) = -v_{Crc}(t_3) = 0 \tag{5.12}$$

and the values of $i_{rc}(t_5)$ and $v_{Crc}(t_5)$ are constant for a given set of circuit parameters and operating conditions. All of the following instantaneous values of i_{rc} and v_{Crc} at other time instances can be found by iteratively applying (5.9) and (5.10). For example, the upper boundary values of i_{rc} and v_{Crc} at the end of the transient state (t_{13}) are given by (5.13) and (5.14), respectively.

$$\begin{aligned} i_{rc}(t_{13}) = {} & \frac{NV_2}{2Z_r} \sec[\frac{\pi}{2F}](\sin[\frac{\pi - 2(\alpha_1 + \alpha_2 + \alpha_3 + \alpha_4)}{2F}] \\ & + 2\cos[\frac{\pi}{2F}](\sin[\frac{\alpha_4}{F}] - \sin[\frac{\alpha_3 + \alpha_4}{F}] + \sin[\frac{\alpha_2 + \alpha_3 + \alpha_4}{F}])) \end{aligned} \tag{5.13}$$

$$\begin{aligned} v_{Crc}(t_{13}) = {} & \frac{NV_2}{2} \sec[\frac{\pi}{2F}](\cos[\frac{\pi - 2(\alpha_1 + \alpha_2 + \alpha_3 + \alpha_4)}{2F}] \\ & + \cos[\frac{\pi}{2F}](1 - 2(\cos[\frac{\alpha_4}{F}] - \cos[\frac{\alpha_3 + \alpha_4}{F}] + \cos[\frac{\alpha_2 + \alpha_3 + \alpha_4}{F}]))) \end{aligned} \tag{5.14}$$

As the objective of GTSM is to suitably design the transient pulse widths (i.e., α_1 to α_4) to fulfil the required phase-shift adjustments (5.5) commanded by the controller while ensuring that the transient values of v_{Crc} and i_{rc} can reach the targeted new steady-state values at the designated time (e.g., t_{13}) and will remain in the same convergent state after that. The sufficient and necessary condition for effectively suppressing the transient oscillations in i_{rc} and v_{Crc} is that their new steady-state values at t_{13} should be equal to their initial steady-state values at t_5.

Hence,

$$\begin{cases} i_{rc}(t_{13}) = i_{rc}(t_5) \\ v_{Crc}(t_{13}) = v_{Crc}(t_5). \end{cases} \tag{5.15}$$

It should be noted that since $C_r \Delta v_{Crc} = \int i_{rc} \mathrm{d}t$, $v_{Crc}(t_{13}) = v_{Crc}(t_5)$ in fact guarantees a dynamic amp-second balance in the resonant capacitor. Substituting (5.11), (5.12), (5.13), and (5.14) into (5.15) leads to (5.16) and (5.17)

$$\begin{aligned} &\cos[\frac{\pi}{2F}](\sin[\frac{\alpha_4}{F}] - \sin[\frac{\alpha_3+\alpha_4}{F}] + \sin[\frac{\alpha_2+\alpha_3+\alpha_4}{F}]) \\ =&\sin[\frac{\alpha_1+\alpha_2+\alpha_3+\alpha_4}{2F}]\cos[\frac{\alpha_1+\alpha_2+\alpha_3+\alpha_4-\pi}{2F}] \end{aligned} \tag{5.16}$$

$$\begin{aligned} &\cos[\frac{\pi}{2F}](\cos[\frac{\alpha_4}{F}] - \cos[\frac{\alpha_3+\alpha_4}{F}] + \cos[\frac{\alpha_2+\alpha_3+\alpha_4}{F}]) \\ =&\cos[\frac{\alpha_1+\alpha_2+\alpha_3+\alpha_4}{2F}]\cos[\frac{\alpha_1+\alpha_2+\alpha_3+\alpha_4-\pi}{2F}] \end{aligned} \tag{5.17}$$

which are used as the current and voltage constraints, respectively, for GTSM. A combination of (5.5), (5.16), and (5.17) in fact forms a 4-DOF general solution for the suppression of transient oscillations in i_{rc} and v_{Crc}, and solving these three simultaneous equations yields a simplified constraint condition given by (5.18).

$$2\cos[\frac{\alpha_3+\alpha_4-\alpha_1}{2F}]\sin[\frac{\alpha_2}{2F}] = \sin[\frac{2\pi-0.5\Delta\theta_{CD}-\alpha_4}{F}] \tag{5.18}$$

5.3.3 GTSM — An Optimal 4-DOF Transient Phase-Shift Modulation for Oscillation-Free and DC-Offset-Free Dynamics

Based on the analysis presented in Sections 5.3.1 and 5.3.2, the realization of oscillation-free and dc-offset-free dynamics in submodel 3 should simultaneously satisfy at least two constraints, i.e., (5.6) and (5.18), in order to achieve the stated objectives before t_{13}. Substituting (5.6) into (5.18) gives

$$\cos[\frac{\alpha_3+\alpha_4-\alpha_1}{2F}] = \cos[\frac{\alpha_2}{2F}] \tag{5.19}$$

and hence $\alpha_3+\alpha_4-\alpha_1=\pm\alpha_2$. Through a careful analysis, only one particular solution set, i.e., the proposed GTSM (5.20), is found to be practically feasible given that the transient pulse widths must be greater than zero.

$$\begin{cases} \alpha_1=\alpha_4=2\pi-0.5\Delta\theta_{CD}-\alpha_2 \\ \alpha_2=\alpha_3=F\arccos[\dfrac{1+\cos[\dfrac{3\pi-\Delta\theta_{CD}}{2F}]\sec[\dfrac{\pi}{2F}]}{2}] \end{cases} \tag{5.20}$$

Figs. 5.3(b) and (c) illustrate the simulated v_{Crc}-i_{rc} state-plane diagrams under CTPSM and GTSM, respectively. Compared with CTPSM, the transient trajectories under GTSM can converge rapidly (one to two switching cycles) to the steady-state elliptic trajectory (i.e., the black curve) without any overshoots and oscillations. Besides, (5.20) also specifies the boundary values of α_2 and α_3 needed to minimize the transient dc offset in accordance with (5.8). As evident from (5.20), no sensor is required by the proposed GTSM, and it only relies on F (a nearly constant parameter) and the phase-shift increment or decrement ($\Delta\theta_{CD}$) obtained from the controller. The symmetrical PWM pattern of GTSM also facilitates its cycle-by-cycle implementation in the PWM modules inside the microcontroller.

Similarly, by substituting $\Delta\theta_{CD}$ with $\Delta\theta_{AD}$ and $\Delta\theta_{BD}$ into (5.20), the GTSM schemes for submodels 1 and 2 (i.e., v_{ao}, $-v_{bo}$) can be obtained similarly, while submodel 4 is excited by a square-wave voltage $-v_{do'}$ of 50% duty cycle. By separately applying GTSM to the four submodels which guarantees their smooth transitions from the old to the new steady states, an overall oscillation-free and dc-offset-free transient response can be ensured for MPS-modulated SR-DABC.

5.3.4 Performance Evaluation of Different Transient Modulation Strategies for SR-DABC

The transient modulation strategies reported in the prior works [109]–[111] require the adjustments of the high- and/or low-level durations of both v_{ab} and v_{cd}

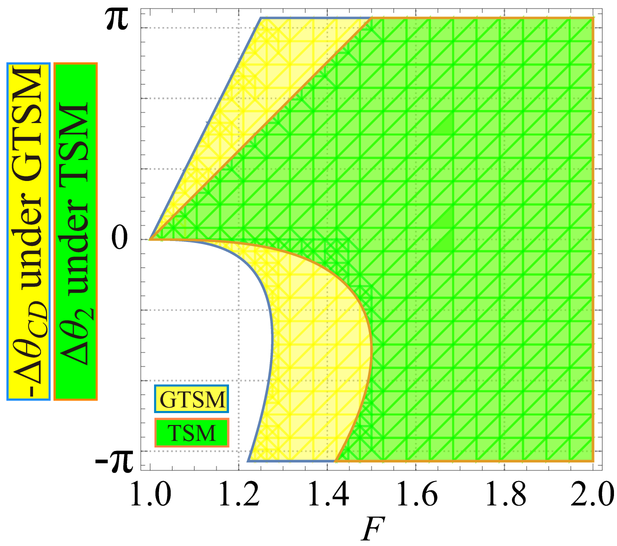

Fig. 5.4. Feasible regions of GTSM and TSM.

during each execution, which leads to high implementation complexity and complicated relationships between modulation variables. The transient pulse widths under these methods cannot be decoupled from the state variables and feedback information of SR-DABC, and there are generally no analytical solutions available for implementation, hence numerical solutions are used instead. However, in closed-loop implementation of SR-DABC, it is impossible to obtain the precise transient pulse widths in each switching cycle due to discretization error, which causes the performances and effectiveness of these methods to degrade in practice.

It can be further verified that the 3-DOF TSM strategy proposed in Chapter 4 [140] is a particular solution of the generalized 4-DOF strategy given by (5.18) of this chapter, and there exists no feasible 2-DOF modulation schemes for (5.18) where two of the four modulation variables are π. By letting $\{\alpha_1 > 0,\ \alpha_2 > 0,\ \alpha_3 > 0,\ \alpha_4 > 0\}$, the feasible regions of both TSM and GTSM are compared in Fig. 5.4. In case of a sufficiently large F, there are solutions for both $\Delta\theta_2 > 0$ and $\Delta\theta_2 < 0$, and hence TSM can be applied in any submodels without changing the reference signal. However, when F is small, the feasible region of TSM becomes narrow and there is no solution for $\Delta\theta_2 < 0$, in which case the reference signal of TSM should be changed to avoid a negative phase-shift change. This is the reason of

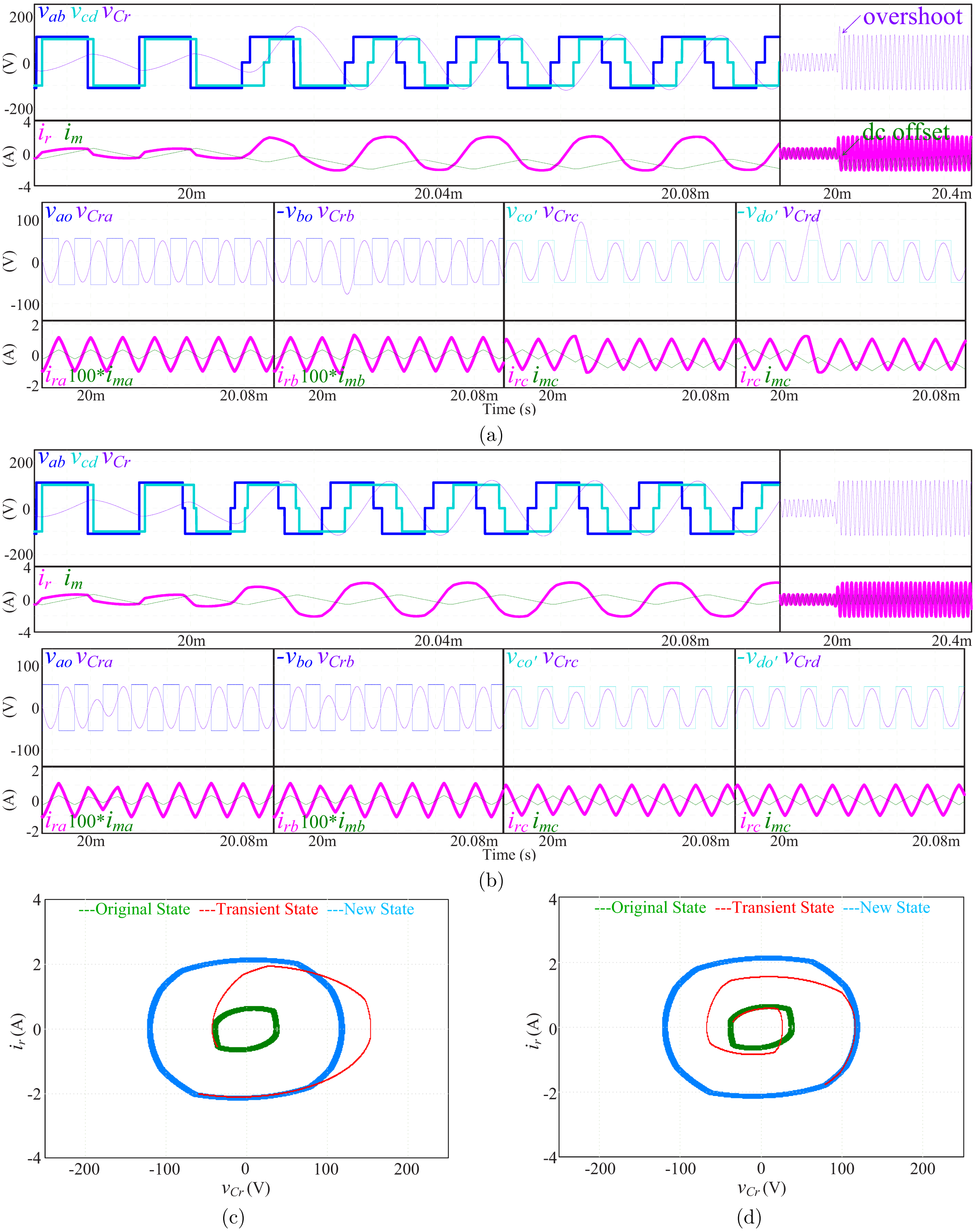

Fig. 5.5. The open-loop simulation examples from SPS mode to TPS mode under TSM [140] and GTSM with $V_1 = 110$ V, $V_2 = 100$ V, $f_s = 60$ kHz, and $F = 1.54$. Simulated transient waveforms under (a) TSM and (b) GTSM. v_{Cr}-i_r state-plane diagrams under (c) TSM and (d) GTSM.

why TSM is implemented in v_{cd} for $\Delta\theta_2 > 0$ and v_{ab} for $\Delta\theta_2 < 0$ in [140], which makes it extremely difficult to apply TSM to MPS-modulated SR-DABC when F is small. It can be seen from Fig. 5.4 that the proposed GTSM can be utilized over a wide range of f_s (i.e., it produces feasible solutions for small F), and its feasible region is much larger than that of TSM. Hence, GTSM can be applied in any of the submodels without altering the relation between the reference excitation source and the other excitation sources. This makes GTSM easy to use in MPS-modulated SR-DABC, which is an important advantage of GTSM over all existing transient modulation methods presented in [109]–[111], [140].

Figs. 5.5(a) and (b) show the simulated transient waveforms of SR-DABC under TSM and GTSM with large F ($F = 1.54$). Other circuit parameters are the same as those used in Fig. 5.2. It can be seen that although TSM is able to suppress transient oscillations, it still leads to excessive transient dc offsets in i_m and some overshoots in v_{Cr}, while GTSM can achieve a transient performance without overshoot, transient dc offset, and transient oscillations. From the state-plane diagrams shown in Figs. 5.5(c) and (d), GTSM constantly produces lower-energy trajectories of i_r and v_{Cr}, as the transient trajectories under GTSM are closer to the desired new-steady-state trajectories. Therefore, GTSM represents a significant improvement over TSM, even when F is large.

Going one step further, when $F \to \infty$, traditional NR-DABC can be regarded as a special case of SR-DABC with infinite C_r [32]. Accordingly, by taking the limits, (5.20) can be simplified to (5.21) for eliminating the transient dc offsets in both inductor and transformer's magnetizing currents of a conventional NR-DABC, which demonstrates the generality of the proposed solution (5.20).

$$\begin{cases} \alpha_1 = \alpha_4 = \pi - 0.5\Delta\theta_{CD} \\ \alpha_2 = \alpha_3 = \lim\limits_{F\to\infty} F \arccos[\dfrac{1+\cos[\dfrac{3\pi-\Delta\theta_{CD}}{2F}]\sec[\dfrac{\pi}{2F}]}{2}] = \pi \end{cases} \tag{5.21}$$

Accordingly, the three transient modulation variables of TSM reported in [140] can be simplified to $\{\pi+0.25\Delta\theta_2, \pi+0.5\Delta\theta_2, \pi+0.25\Delta\theta_2\}$ when F approaches infinity, which is equivalent to the Type-II SS-OTPSM proposed in Chapter 3. However, it should be noted that, in general, the constraints for transient dc-offset elimination in NR-DABC are linear equations, whereas the constraints for transient oscillation suppression in SR-DABC are non-linear transcendental equations. Thus, although both TSM and GTSM can be applied for eliminating the transient dc offsets of NR-DABC by letting $F \rightarrow \infty$, they are not the best solutions for using in NR-DABC. On the other hand, the designs of transient modulation schemes developed for NR-DABC (e.g., the methods reported in [105], [106], [108], [141]) are not applicable and different to those of SR-DABC. Besides, the prior transient modulation schemes proposed for SR-DABC in [109]–[111], [140] were designed to eliminate transient oscillations only, hence they have failed to eliminate the transient dc offset especially in i_m, which is more important for NR-DABC. For example, when $F \neq \infty$ (i.e., in a SR-DABC), TSM [140] can eliminate transient oscillations in i_r of SR-DABC but fails to eliminate transient dc offset in i_m. In fact, compared with the simulation result shown in Fig. 5.2(a) under CTPSM, TSM causes a more severe transient dc offset in i_m as can be seen from Fig. 5.5(b).

In summary: 1) GTSM has a wide operating range and can simultaneously achieve oscillation-free and dc-offset-free convergence to the new steady state within one to two switching cycles in MPS-modulated SR-DABC. It is viewed as the most effective transient modulation scheme for SR-DABC up to date. 2) Until now, the proposed GTSM strategy is the only unified approach capable of simultaneously eliminating transient oscillations and dc offsets in both MPS-modulated NR-DABC and SR-DABC. 3) A transient modulation scheme developed for SR-DABC may be applicable to NR-DABC (e.g., GTSM), but the inverse is not true. 4) Except for the proposed TSM and GTSM, all existing transient modulation schemes developed for SR-DABC cannot be used to eliminate transient dc offsets in i_r and i_m of NR-DABC ($F \rightarrow \infty$), but TSM cannot eliminate the transient dc offset in i_m of SR-DABC ($F \neq \infty$).

5.4 Model Predictive Control With Minimum-RMS-Current Operation

Although the above open-loop simulation results enable us to compare the transient performances of CTPSM and GTSM in response to single-step changes in phase-shift angles, SR-DABC is generally operated in closed-loop configuration in practice. Thus, to demonstrate its practical values, the proposed GTSM should be implementable on a cycle-by-cycle basis under closed-loop conditions. It should be noted that the proposed GTSM can be implemented with any controller, but as explained in Chapters 3 and 4 [140], [141], fast controllers are preferred since their inherently wide control bandwidth will induce abrupt and large-amplitude changes in phase-shift angles. Therefore, in this article, the transient performance of GTSM under closed-loop conditions is verified using a high-gain MPC with minimum-RMS-current operation similar to the one developed for MPS-modulated NR-DABC in [43]. A step-by-step closed-loop controller design is presented in this section.

By applying FHA analysis [31], the fundamental components of v_{ab} and Nv_{cd} are expressed by (5.22) and (5.23), and hence the resonant current i_r can be approximated by (5.24)

$$v_{ab} \approx \frac{4V_1}{\pi} \cos\left[\frac{\theta_1}{2}\right] \sin\left[\omega_s t\right] \tag{5.22}$$

$$Nv_{cd} \approx \frac{4NV_2}{\pi} \cos\left[\frac{\theta_3}{2}\right] \sin\left[\omega_s t - \theta_2\right] \tag{5.23}$$

$$i_r \approx \frac{4V_1(M\cos\left[\frac{\theta_3}{2}\right]\cos\left[\omega_s t - \theta_2\right] - \cos\left[\frac{\theta_1}{2}\right]\cos\left[\omega_s t\right])}{\pi X_r} \tag{5.24}$$

where $X_r = \omega_s L_r - 1/(\omega_s C_r)$ is the equivalent impedance and $M = NV_2/V_1$ is defined as the voltage gain of SR-DABC. Next, the RMS value of i_r, (i.e., i_{r_RMS})

and the output active power (i.e., P_o) can be calculated from (5.25) and (5.26), respectively.

$$\begin{aligned} i_{r\_\mathrm{RMS}} &= \sqrt{\frac{1}{T_s}\int_0^{T_s} i_r^2 \mathrm{d}t} \\ &= \frac{2\sqrt{2}V_1}{\pi X_r}\sqrt{\begin{aligned}&\cos^2\left[\tfrac{\theta_1}{2}\right] + M^2\cos^2\left[\tfrac{\theta_3}{2}\right] \\ &-2M\cos\left[\tfrac{\theta_1}{2}\right]\cos\left[\tfrac{\theta_3}{2}\right]\cos\left[\theta_2\right]\end{aligned}} \end{aligned} \tag{5.25}$$

$$\begin{aligned} P_o &= \frac{1}{T_s}\int_0^{T_s} v_{ab}\cdot i_r \mathrm{d}t \\ &= \frac{8NV_1V_2}{\pi^2 X_r}\sin\left[\theta_2\right]\cos\left[\frac{\theta_1}{2}\right]\cos\left[\frac{\theta_3}{2}\right] \end{aligned} \tag{5.26}$$

Typically, in order to maintain a high efficiency during steady state, i_{r_RMS} will be selected as the main optimization objective in SR-DABC for minimizing conduction loss. The optimal steady-state phase-shift angles can be obtained by solving the constrained minimization problem, i.e., (5.27).

$$\begin{aligned} &\underset{\theta_1,\theta_2,\theta_3}{\text{minimize}} \quad i_{r\_\mathrm{RMS}}(\theta_1,\theta_2,\theta_3) \\ &\text{subject to} \quad P_o(\theta_1,\theta_2,\theta_3) = P_{o\_d},\ \left|P_{o\_d}\right| \le P_{o\_max} \end{aligned} \tag{5.27}$$

where P_{o_d} is defined as the desired steady-state output power, and $P_{o\_max} = 8NV_1V_2/(\pi^2 X_r)$ is the theoretical maximum transmission power. The optimal solution sets can be written as follows: for Case 1 ($M>1$ and $\left|P_{o\_n}\right| \le \sqrt{1-1/(M^2)}$), (5.28) is valid; for Case 2 ($M<1$ and $\left|P_{o\_n}\right| \le \sqrt{1-M^2}$), (5.29) is valid; for Case 3 (other operating regions), (5.30) is valid. Please note that $P_{o\_n} = P_{o\_d}/P_{o\_max}$ is defined as the normalized output power.

$$\begin{cases} \theta_1 = 0 \\ \theta_2 = \arctan\left[P_{o\_n}\cdot M\right] \\ \theta_3 = 2\arccos\left[\sqrt{1/(M^2)+P_{o\_n}^2}\right] \end{cases} \tag{5.28}$$

$$\begin{cases} \theta_1 = 2\arccos\left[\sqrt{M^2 + P_{o\_n}^2}\right] \\ \theta_2 = \arctan\left[P_{o\_n}/M\right] \\ \theta_3 = 0 \end{cases} \tag{5.29}$$

$$\begin{cases} \theta_1 = 0 \\ \theta_2 = \arcsin\left[P_{o\_n}\right] \\ \theta_3 = 0 \end{cases} \tag{5.30}$$

Although the solution sets of (5.27), i.e., (5.28)-(5.30), can also be found in [45], [52], the solution procedure is not accessible, and the results given in [45] contain some errors. Thus, in this chapter, we provide the details of the solution procedure to find the optimal θ_1, θ_2, and θ_3 for achieving a minimum i_{r_RMS}. The constrained optimization problem in (5.27) is often solved by using the method of Lagrange multipliers [52], and the procedure can be divided into three main steps.

(1) Step 1: A Lagrangian function is constructed as follows:

$$\mathcal{L}(\theta_1, \theta_2, \theta_3, \lambda) = i_{r\_\mathrm{RMS}} + \lambda(P_o - P_{o\_d}) \tag{5.31}$$

where variable $\lambda \neq 0$ is a Lagrange multiplier.

(2) Step 2: Differentiating $\mathcal{L}$ with respect to θ_1, θ_2, θ_3, and λ, and equating the results to zero, we have

$$\nabla\mathcal{L}(\theta_1, \theta_2, \theta_3, \lambda) = 0. \tag{5.32}$$

(3) Step 3: By solving (5.32), we can obtain the four equations corresponding to $\partial_{\theta_1}\mathcal{L}=0$, $\partial_{\theta_2}\mathcal{L}=0$, $\partial_{\theta_3}\mathcal{L}=0$, and $\partial_{\lambda}\mathcal{L}=0$. If $\theta_1 \neq \pi$ and $\theta_3 \neq \pi$, $\partial_{\theta_2}\mathcal{L} = 0$ leads to (5.33), and λ can be found accordingly.

$$\frac{\pi \tan\theta_2}{2\lambda V_1} = \sqrt{1 + \cos\theta_1 + M^2(1 + \cos\theta_3) - 4M\cos\tfrac{\theta_1}{2}\cos\theta_2\cos\tfrac{\theta_3}{2}} \tag{5.33}$$

Substituting (5.33) into $\partial_{\theta_1}\mathcal{L} = 0$ and $\partial_{\theta_3}\mathcal{L} = 0$, and then simplifying the results yields (5.34) and (5.35), respectively.

$$\sin\frac{\theta_1}{2}\left[\cos\frac{\theta_1}{2}\cot\theta_2 - M\cos\frac{\theta_3}{2}\csc\theta_2\right] = 0 \tag{5.34}$$

$$\sin\frac{\theta_3}{2}\left[M\cos\frac{\theta_3}{2}\cot\theta_2 - \cos\frac{\theta_1}{2}\csc\theta_2\right] = 0 \tag{5.35}$$

In addition, $\partial_\lambda \mathcal{L} = 0$ gives $P_o = P_{o\_d}$, and hence

$$P_{o\_n} = \frac{P_{o\_d}}{P_{o\_max}} = \cos\frac{\theta_1}{2}\cos\frac{\theta_3}{2}\sin\theta_2. \tag{5.36}$$

We now have three cases to simultaneously satisfy (5.34), (5.35), and (5.36).

Case 1: If $\theta_1 = 0$ and $\theta_3 \neq 0$, (5.34) always holds, and (5.35) and (5.36) can be simplified to (5.37) and (5.38), respectively.

$$M\cos\frac{\theta_3}{2}\cos\theta_2 = 1 \tag{5.37}$$

$$P_{o\_n} = \cos\frac{\theta_3}{2}\sin\theta_2 \tag{5.38}$$

Thus, we can obtain (5.28) by solving (5.37) and (5.38). It is apparent from (5.37) that (5.28) only exists when $M > 1$. In addition, as the range of validity of inverse cosine function (arccos) is limited to $[-1, 1]$, the solution of θ_3 in (5.28) is valid only when $\left|P_{o\_n}\right| \leq \sqrt{1 - 1/(M^2)}$. In fact, if $\left|P_{o\_n}\right| > \sqrt{1 - 1/(M^2)}$, θ_3 will approach zero.

Case 2: If $\theta_1 \neq 0$ and $\theta_3 = 0$, (5.35) always holds, and (5.34) and (5.36) can be simplified to (5.39) and (5.40), respectively.

$$M = \cos\frac{\theta_1}{2}\cos\theta_2 \tag{5.39}$$

$$P_{o\_n} = \cos\frac{\theta_1}{2}\sin\theta_2 \tag{5.40}$$

Similarly, we can obtain (5.29) by solving (5.39) and (5.40). According to (5.39) and the range of validity of arccos, (5.29) only exists when $M < 1$ and $\left|P_{o\_n}\right| \leq \sqrt{1 - M^2}$. In addition, when $\left|P_{o\_n}\right| > \sqrt{1 - M^2}$, θ_1 will approach zero.

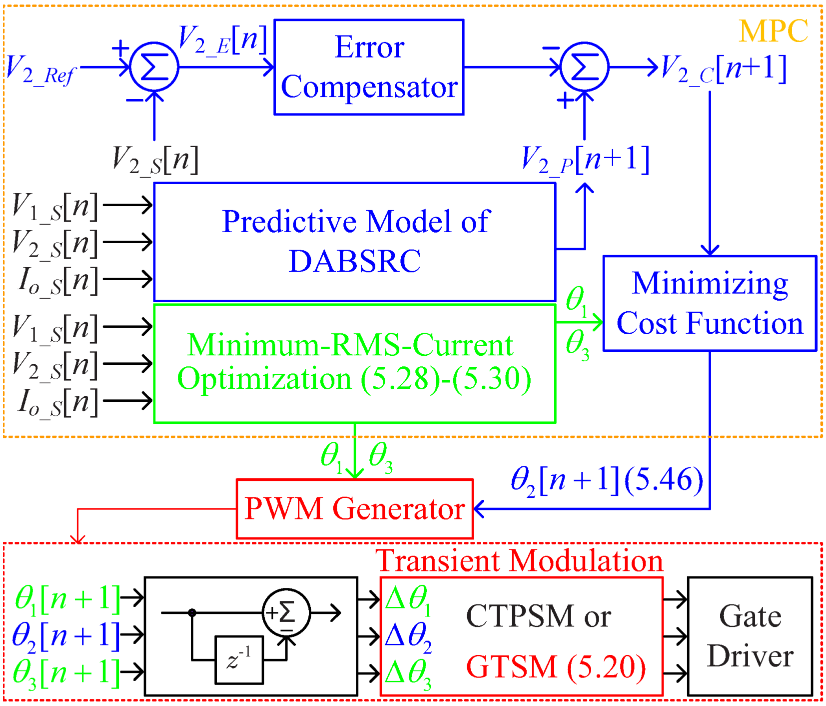

Fig. 5.6. Block diagram of MPC with minimum-RMS-current optimization.

Case 3: If $\theta_1 = 0$ and $\theta_3 = 0$, both (5.34) and (5.35) always hold, and (5.36) can be simplified to

$$P_{o\_n} = \sin\theta_2 \tag{5.41}$$

which yields (5.30) applicable to the other cases not covered by Case 1 and Case 2.

Nevertheless, it should be highlighted that the expressions of optimal θ_1, θ_2, and θ_3 given by (5.28)-(5.30) cannot be directly used to form a closed-loop controller as they are steady-state solutions. A simple control scheme for MPS-modulated SR-DABC used in this chapter is depicted in Fig. 5.6. With this control scheme, V_{2_Ref} is defined as the reference output voltage; $V_{1\_S}[n]$, $V_{2\_S}[n]$, and $I_{o\_S}[n]$ are the sampled values of V_1, V_2, and I_o obtained via a 12-bit analog-to-digital converters (ADCs); $V_{2\_P}[n+1]$ is the predicted output voltage for the next, i.e., $(n+1)$th, cycle; $V_{2\_E}[n]$ is the error/deviation between the output voltage and its reference; $V_{2\_C}[n+1]$ is defined as the predicted output voltage after correction.

A standard quadratic cost function $\mathcal{J}$ of MPC is given by:

$$\mathcal{J} = \left(V_{2\_Ref} - V_{2\_C}[n+1]\right)^2. \tag{5.42}$$

When implementing the control loop, the outer phase-shift angle θ_2 is computed to find a cost-minimizing control strategy, while the inner phase-shift angles θ_1 and θ_3 are directly determined using (5.28)-(5.30).

In fact, the basic principles and design methods for the MPCs used in Chapters 3-5 are very similar. The main difference between these three controllers is that they are designed for SPS-modulated NR-DABC, SPS-modulated SR-DABC, and MPS-modulated SR-DABC, respectively, and hence they should use different power prediction models, i.e., expressions of the transmission or output power of the converter. In general, the predictive model of MPS-modulated SR-DABC is established based on the average power model, i.e., (5.26), from which the dynamics of V_2 can be obtained as

$$\begin{aligned} C_o\frac{\mathrm{d}V_2}{\mathrm{d}t} &= \frac{P_o}{V_2} - I_o \\ &= \frac{8NV_1}{\pi^2 X_r}\sin\left[\theta_2\right]\cos\left[\frac{\theta_1}{2}\right]\cos\left[\frac{\theta_3}{2}\right] - I_o \end{aligned} \tag{5.43}$$

where C_o is the total output capacitance. $V_{2\_P}[n{+}1]$ can be obtained by discretizing (5.43) using the forward Euler method, which results in

$$\begin{aligned} V_{2\_P}[n+1] =& V_{2\_S}[n] + \frac{\mathrm{d}V_{2\_S}[n]}{\mathrm{d}t}T_s \\ =& V_{2\_S}[n] + \frac{8NV_{1\_S}[n]\sin\theta_2\cos\frac{\theta_1}{2}\cos\frac{\theta_3}{2}}{\pi^2 X_r C_o f_s} - \frac{I_{o\_S}[n]}{C_o f_s}. \end{aligned} \tag{5.44}$$

Generally, in order to compensate for the unmodeled effects, a proportional–integral (PI) compensator should be used, and the compensator's output is added to $V_{2\_P}[n+1]$ to produce $V_{2\_C}[n+1]$. Thus,

$$V_{2\_C}[n+1] = V_{2\_P}[n+1] - \left(K_p V_{2\_E}[n] + K_i\sum_{\tau=0}^{n} V_{2\_E}[\tau]\right) \tag{5.45}$$

where K_p and K_i are, respectively, the proportional and integral gains to be designed, and $V_{2\_E}[n] = V_{2\_Ref} - V_{2\_S}[n]$. Finally, minimizing $\mathcal{J}$, i.e., $\bigtriangledown\mathcal{J} = 0$, yields

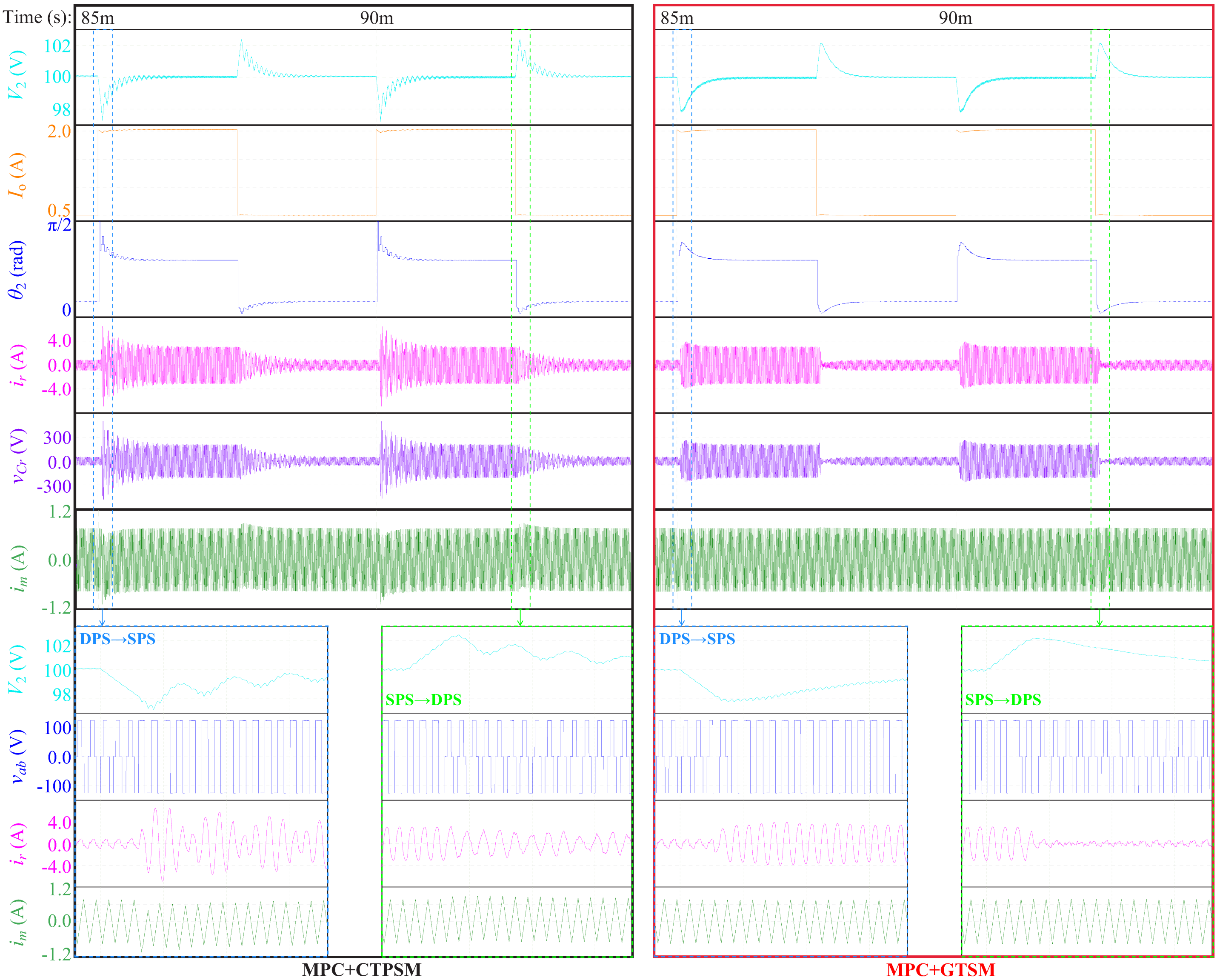

Fig. 5.7. Simulated closed-loop transient waveforms under 200-Hz 0.5-to-2 A pulsed-power loads. $V_1 = 125$ V, $V_2 = 100$ V, $f_s = 50$ kHz, $F = 1.2835$, $K_p^* = 0.08$, and $K_i = 0.00008$.

the predicted optimal outer phase-shift angle (or control variable)

$$\theta_2[n+1] = \arcsin\left[\frac{\pi^2 X_r C_o f_s}{8NV_{1\_S}[n]\cos\frac{\theta_1}{2}\cos\frac{\theta_3}{2}}\left(\frac{I_{o\_S}[n]}{C_o f_s} + K_p^* V_{2\_E}[n] + K_i \sum_{\tau=0}^{n} V_{2\_E}[\tau]\right)\right] \tag{5.46}$$

where $K_p^* = K_p + 1$ is the equivalent proportional gain. Evidently, the dynamics of SR-DABC are affected by the choices of K_p^* and K_i. In general, larger values of K_p^* and K_i lead to higher closed-loop bandwidth and hence faster dynamic response.

As shown in Fig. 5.6, the output voltage of SR-DABC can be regulated by the MPC designed above with minimum-RMS-current operation, while the PWM generator determines the strategy to update $\Delta\theta_1$, $\Delta\theta_2$, and $\Delta\theta_3$ either by CTPSM or GTSM. Fig. 5.7 shows the simulated closed-loop transient waveforms under MPC+CTPSM and MPC+GTSM with 200-Hz pulsed-power loads, where the load current periodically changes between 0.5 A and 2.0 A. Other key specifications are given as follows: $V_1 = 125$ V, $V_2 = 100$ V, $C_o = 47$ μF, $f_s = 50$ kHz, $F = 1.2835$, and the PI control parameters are $K_p^* = 0.08$ and $K_i = 0.00008$. It can be seen that the overshoots and undershoots in i_r, v_{Cr}, and i_m under MPC+CTPSM are significantly larger than those under MPC+GTSM, and smoother transient waveforms are achieved under MPC+GTSM. The simulation results clearly demonstrate that transient oscillations, dc offsets, settling times of i_r, v_{Cr}, and i_m can be significantly minimized by GTSM, thus contributing positively to improving the dynamics of SR-DABC.

5.5 Online Estimation of Resonant Frequency

Due to aging effects, environmental conditions (e.g., temperature and humidity), manufacturing tolerances, etc., the actual values of C_r and L_r may deviate from their nominal values, which can result in deviation in the resonant frequency f_r of SR-DABC. It can be observed from (5.20) and (5.46) that both algorithms of GTSM and MPC are related to X_r and $F = f_s/f_r$, respectively. Thus, f_r is the most important converter parameter that determines both F and X_r. In most studies, f_r is regarded as having a constant value; nevertheless, in order to achieve the anticipated performance of the proposed GTSM, the effects of parameter deviations should not be ignored. To emulate the cases under resonant frequency deviations, the preset value of F in the GTSM program codes is modified, while the actual circuit parameters are kept unchanged.

Fig. 5.8 shows the simulated open-loop transient state-plane trajectories for

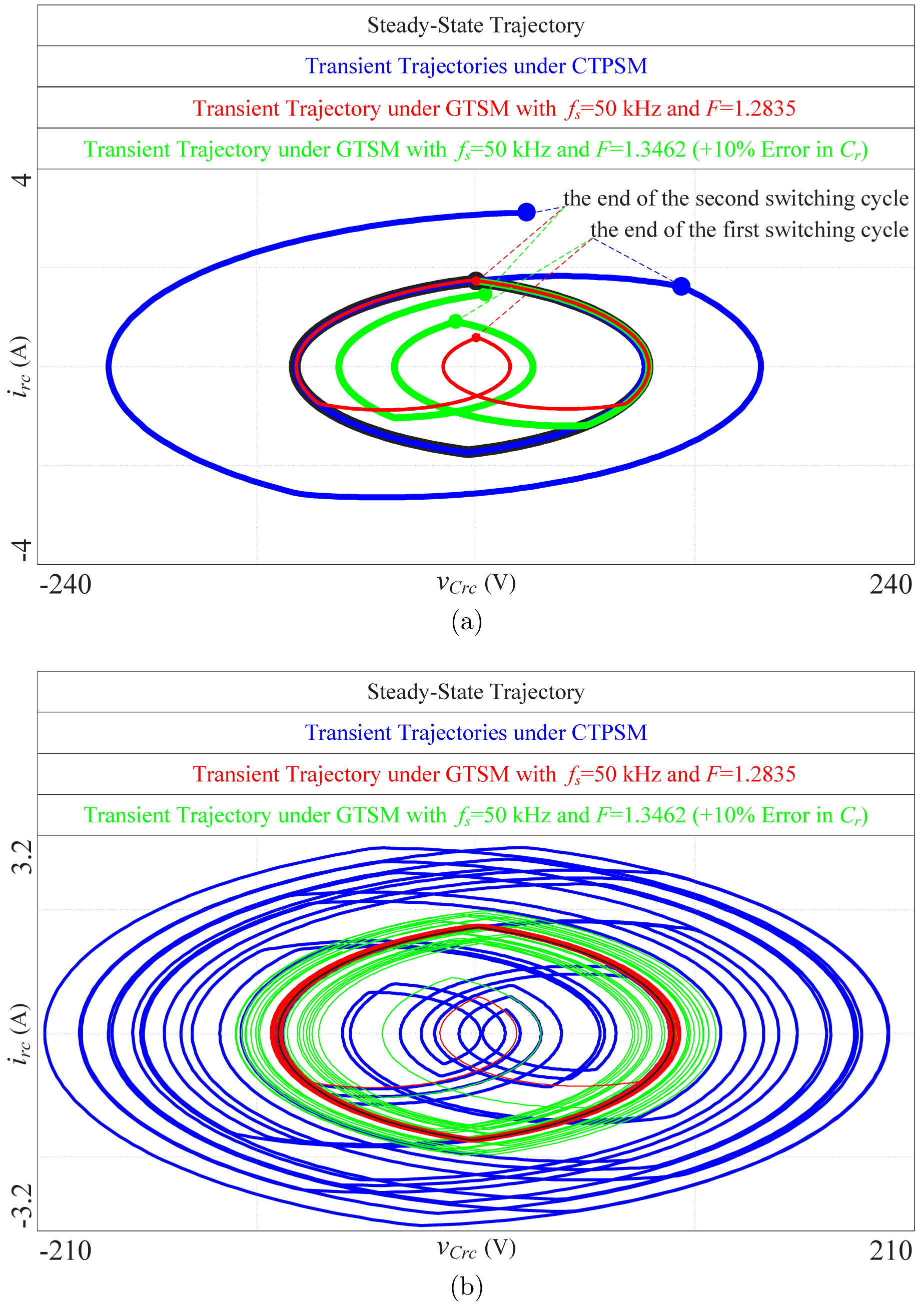

Fig. 5.8. Simulated transient v_{Crc}-i_{rc} state-plane diagrams in submodel 3 under open-loop conditions, where $\Delta\theta_3 = \pi/3$ (i.e., $\Delta\theta_{CD} = \pi/3$), $f_s = 50$ kHz, and $F = 1.2835$ (nominal value) or $F = 1.3462$ (+10% error in C_r). (a) Transient v_{Crc}-i_{rc} state-plane diagrams of the first two switching cycles. (b) Transient v_{Crc}-i_{rc} state-plane diagrams of 25 switching cycles.

$\Delta\theta_3 = \pi/3$ (or $\Delta\theta_{CD} = \pi/3$) in submodel 3 with $F = 1.2835$ (nominal value). If there exists a $+10\%$ error in the resonant capacitance C_r (i.e., $F = 1.3462$), the resulting error in transient pulse widths will lead to small deviations from the desired transient trajectory (i.e., red curve), and the associated transient v_{Crc}-i_{rc}

trajectory (i.e., green curve) can converge to the steady-state trajectory (i.e., black curve) within two switching cycles (see Fig. 5.8(a)). As shown in Fig. 5.8(b), although the error in F leads to a certain degradation in performance, GTSM can still effectively suppress transient oscillations when compared to CTPSM. In addition, even with deviation in F, it can still effectively eliminate transient dc offsets in i_m, as (5.6) always holds. Thus, in general, although the performance of GTSM may degrade with a larger error in f_r or F, it still outperforms CTPSM in terms of transient performance.

Nevertheless, as illustrated in Fig. 5.4, if the errors in C_r and L_r result in a quite small F, GTSM will lose its effect for some cases. Besides, in the presence of significant deviations in X_r and F from the nominal values, the dynamic performance of closed-loop controlled SR-DABC could be severely affected if its modulator and controller cannot adapt to changes in X_r and F. For these reasons, an accurate value of f_r should be determined to achieve optimal dynamics in SR-DABC. There are various automatic resonant-frequency tracking techniques proposed for this purpose [142], [143]. In this article, we adopted a simple perturb and observe (P&O) method, which is similar to that proposed in [144], to estimate X_r and F.

Neglecting all power losses,

$$P_o = V_2 * I_o \tag{5.47}$$

and substituting (5.47) into (5.26) gives the estimation of X_r under TPS modulation

$$X_r = \frac{8NV_1}{\pi^2 I_o} \sin[\theta_2] \cos\left[\frac{\theta_1}{2}\right] \cos\left[\frac{\theta_3}{2}\right]. \tag{5.48}$$

In general, the exact values of C_r and L_r in a SR-DABC may not be known but they can be treated as constant during the brief parameter identification process. As X_r changes with switching frequency f_s only, f_s must be perturbed to produce different values of X_r. In theory, for a given switching frequency f_{s_i}, its corresponding impedance X_{r_i} is given by

$$X_{r\_i} = \sqrt{L_r/C_r}\left(F_i - 1/F_i\right) = Z_r\left(F_i - 1/F_i\right), \tag{5.49}$$

where $F_i = f_{s\_i}/f_r$. Define the nominal impedance X_{r_n} as

$$X_{r\_n} = \sqrt{L_r/C_r}\left(F_n - 1/F_n\right) = Z_r\left(F_n - 1/F_n\right), \tag{5.50}$$

where f_{s_n} is the nominal switching frequency, and hence $F_n = f_{s\_n}/f_r$.

Combining (5.49) and (5.50), the estimated f_r and F (i.e., f_{r_e} and F_{n_e}) can be obtained from (5.51) and (5.52), respectively.

$$f_{r\_e} = \sqrt{\frac{X_{r\_ie}f_{s\_i}f_{s\_n}^2 - X_{r\_ne}f_{s\_i}^2 f_{s\_n}}{X_{r\_ie}f_{s\_i} - X_{r\_ne}f_{s\_n}}} \tag{5.51}$$

$$F_{n\_e} = \sqrt{\frac{f_{s\_n}\left(X_{r\_ie}f_{s\_i} - X_{r\_ne}f_{s\_n}\right)}{f_{s\_i}\left(X_{r\_ie}f_{s\_n} - X_{r\_ne}f_{s\_i}\right)}} \tag{5.52}$$

It should be emphasized that X_{r_ie} and X_{r_ne} used in (5.51) and (5.52) are the estimated values of X_{r_i} and X_{r_n} computed according to (5.48). By incorporating (5.48) and (5.52) into MPC and the proposed GTSM, respectively, the problems associated with parameter deviations can be mitigated. It should be noted that the accuracy of the parameter identification is affected by the accuracy of the power model of SR-DABC, i.e., (5.26). As suggested by [144], a higher accuracy is achieved with SPS modulation. Thus, the parameter estimation algorithm is executed when SR-DABC is operated with SPS modulation.

5.6 Experimental Verification

As shown in Fig. 5.9, a scaled-down experimental prototype of SR-DABC is constructed to validate the proposed GTSM. The circuit parameters used in the prototype are listed in Table 5.2. The nominal switching frequency f_{s_n} in all experiments is set as 50 kHz (i.e., F_n = 1.2835 and X_{r_n} = 39.6317). In this article, we directly measure the magnetizing current through an auxiliary inductor, such that the measured current is $i_m/2$. It should be pointed out that the additional

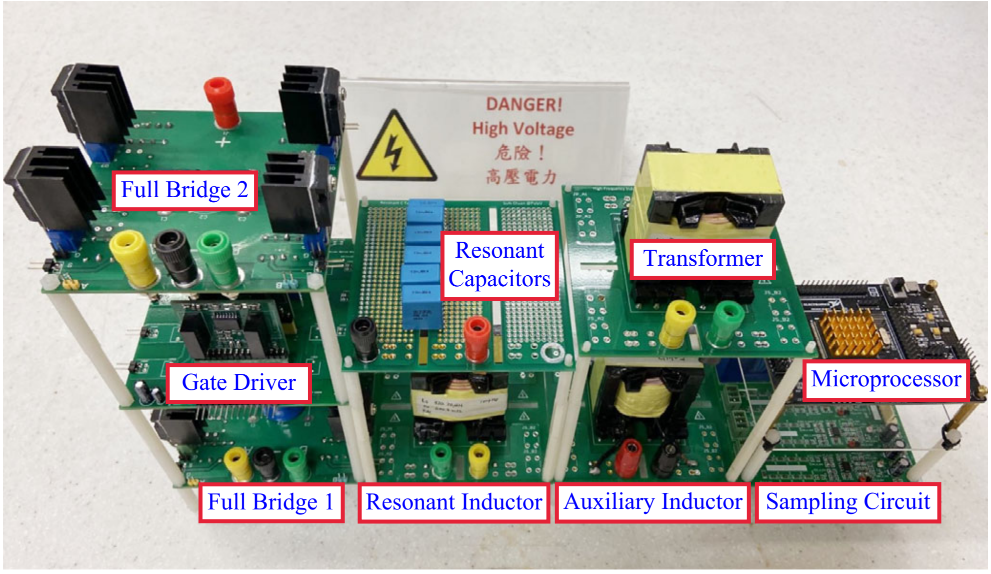

Fig. 5.9. Photograph of laboratory prototype of SR-DABC.

magnetizing inductance is much larger than the power transfer inductance L_r and the transformer's leakage inductance, and hence it has negligible influence on the performance of SR-DABC. In addition, it is used only during the experimentation stage and can be omitted in practical implementation. The resonant capacitor C_r often needs to endure a high voltage in SR-DABC, hence it is important to investigate the voltage stress of C_r. However, due to the limitations of oscilloscope channels, v_{Cr} is not directly measured in experiments as it generally has a similar profile as i_r.

As our work represents the first attempt to discourse the role of optimized transient modulation strategy in achieving high-quality dynamic response in MPS-modulated SR-DABC, the proposed GTSM is merely compared with CTPSM in all experimental test cases.

5.6.1 Open-Loop Tests

In open-loop tests, both the input and output terminals of SR-DABC are connected with dc voltage sources, which provides an ideal test environment equivalent to an infinite control bandwidth for evaluating the theoretical performances of CTPSM and GTSM. Both transient modulation strategies are executed only once with predefined $\Delta\theta_1$, $\Delta\theta_2$, and $\Delta\theta_3$.

Three open-loop transition cases, i.e., increasing power (Case I), decreasing power (Case II), and reversing power flow direction (Case III) are demonstrated in detail. It can be seen from Fig. 5.10 that GTSM can simultaneously mitigate transient oscillations and dc offsets in all cases. The maximum overshoots in i_r and i_m are reduced by 50% to 100% with GTSM, thus minimizing transient voltage and current stresses on the power devices and ensuring smooth transient operation. GTSM also enables SR-DABC to seamlessly reach the desired new steady state within a few switching cycles. The results shown in Fig. 5.10 also match with our theoretical analysis in Section 5.2 and Section 5.3 as well as the findings from simulation results, which demonstrate the importance of effective transient modulation in optimizing the dynamic performance of SR-DABC. In addition, although GTSM cannot guarantee transient ZVS, it enables SR-DABC to reach the new steady state more rapidly and achieve steady-state ZVS instead. Thus, it can be found from Fig. 5.10 that, compared with GTSM, voltage spikes in v_{ab} and v_{cd} under CTPSM sustain for a longer period of time which could degrade the reliability of the power switches.

5.6.2 Closed-Loop Tests

In closed-loop tests, the output terminal is connected to a purely resistive load R_L, and the output voltage is regulated by the MPC designed in Section 5.4. All tests are conducted under large-amplitude step-load changes between 0.5 A and 2.0 A. According to the analysis of minimum-RMS-current operation, SR-DABC should work under DPS mode at light load (i.e., 0.5 A) and SPS mode at heavy load (i.e., 2.0 A). Since the phase-shift angles are computed in real time under closed-loop conditions, both CTPSM and GTSM are implemented on a cycle-by-cycle basis. The update frequency of the PWM generator and sampling frequencies

Fig. 5.10. Experimental open-loop transient waveforms with $V_1 = 110$ V, $V_2 = 100$ V, $f_s = 50$ kHz, and $F = 1.2835$. (a) Case I: Increasing power accompanied by a transition from TPS mode to DPS mode (i.e., $\theta_1 = 2\pi/15$, $\theta_2 = 11\pi/60$, $\theta_3 = \pi/10$, $\Delta\theta_1 = \pi/15$, $\Delta\theta_2 = 11\pi/60$, and $\Delta\theta_3 = -\pi/10$). (b) Case II: Decreasing power accompanied by a transition from SPS mode to TPS mode (i.e., $\theta_1 = 0$, $\theta_2 = 7\pi/15$, $\theta_3 = 0$, $\Delta\theta_1 = 2\pi/15$, $\Delta\theta_2 = -\pi/6$, and $\Delta\theta_3 = \pi/5$). (c) Case III: Reversing power flow direction accompanied by a transition from DPS mode to SPS mode (i.e., $\theta_1 = 0$, $\theta_2 = \pi/4$, $\theta_3 = \pi/10$, $\Delta\theta_1 = 0$, $\Delta\theta_2 = -23\pi/60$, and $\Delta\theta_3 = -\pi/10$).

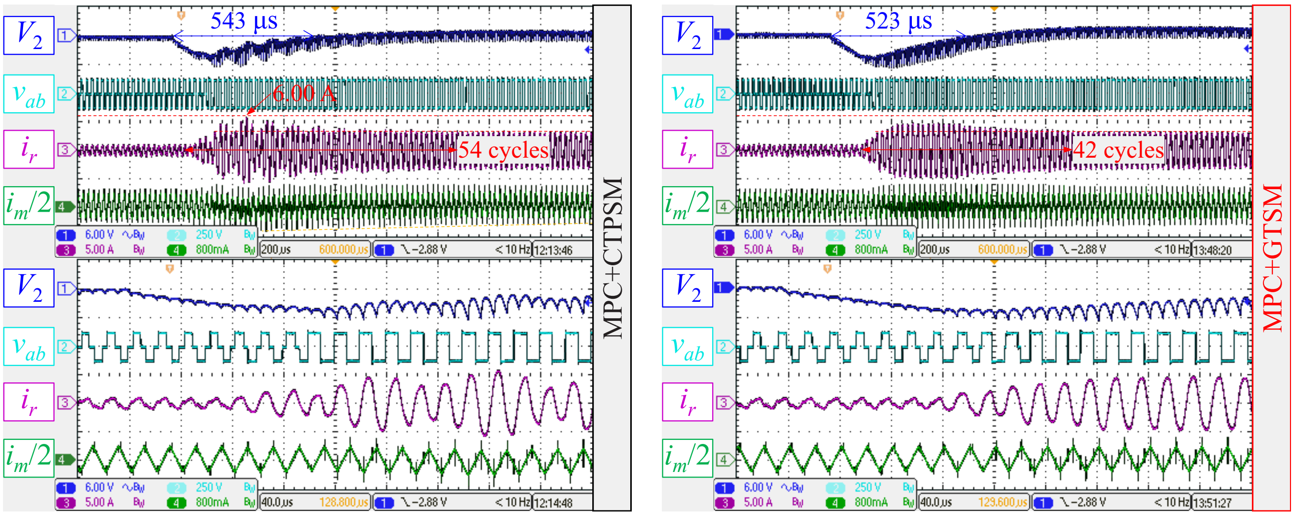

(a) (b)

Fig. 5.11. Experimental closed-loop transient waveforms for a step-up load change from 0.5 to 2 A with $\{K_p^* = 0.055,\ K_i = 0.0015\}$ under (a) MPC+CTPSM and (b) MPC+GTSM. $V_1 = 125$ V, $V_2 = 100$ V, $f_s = 50$ kHz, $F = 1.2835$, and $X_r = 39.6317$.

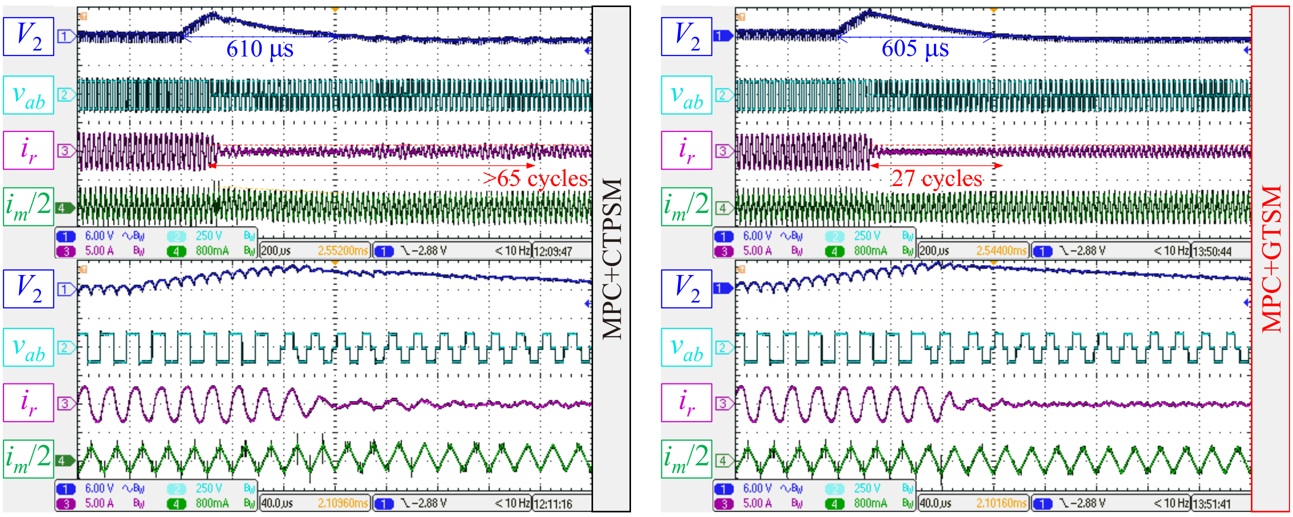

(a) (b)

Fig. 5.12. Experimental closed-loop transient waveforms for a step-down load change from 2 to 0.5 A with $\{K_p^* = 0.055,\ K_i = 0.0015\}$ under (a) MPC+CTPSM and (b) MPC+GTSM. $V_1 = 125$ V, $V_2 = 100$ V, $f_s = 50$ kHz, $F = 1.2835$, and $X_r = 39.6317$.

of ADCs are set as f_s, while the algorithm of MPC is executed every two switching cycles $(0.5/f_s)$. Three sets of control parameters (i.e., $\{K_p^* = 0.055,\ K_i = 0.0015\}$, $\{K_p^* = 0.08,\ K_i = 0.002\}$, and $\{K_p^* = 0.15,\ K_i = 0.004\}$) are selected to comprehensively compare the transient performances of SR-DABC under MPC+CTPSM and

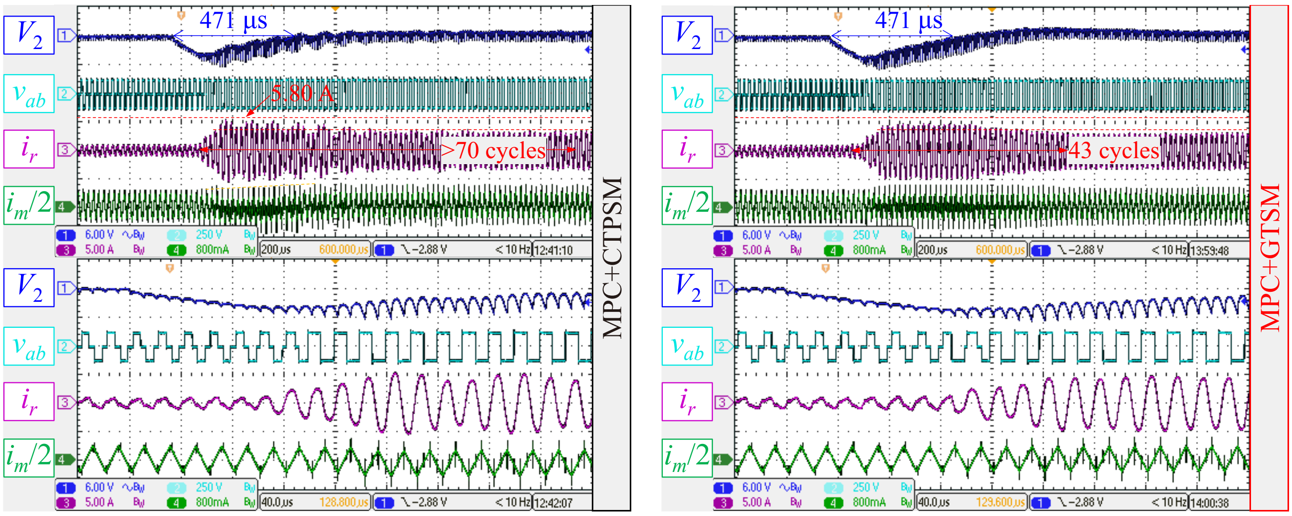

(a) (b)

Fig. 5.13. Experimental closed-loop transient waveforms for a step-up load change from 0.5 to 2 A with $\{K_p^*=0.08,\ K_i=0.002\}$ under (a) MPC+CTPSM and (b) MPC+GTSM. $V_1=125$ V, $V_2=100$ V, $f_s=50$ kHz, $F=1.2835$, and $X_r=39.6317$.

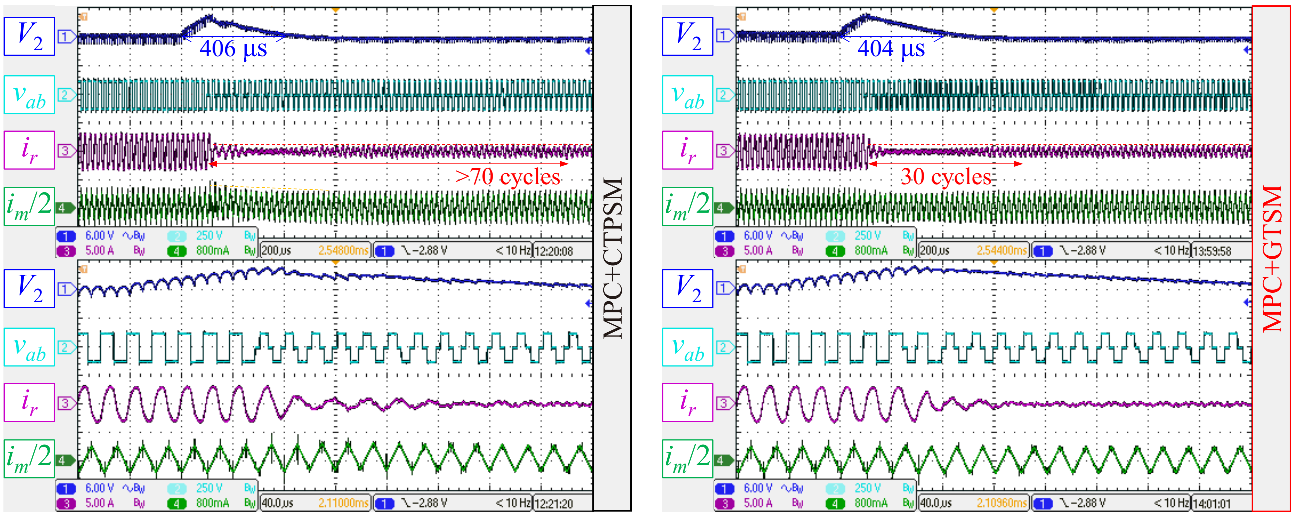

(a) (b)

Fig. 5.14. Experimental closed-loop transient waveforms for a step-down load change from 2 to 0.5 A with $\{K_p^*=0.08,\ K_i=0.002\}$ under (a) MPC+CTPSM and (b) MPC+GTSM. $V_1=125$ V, $V_2=100$ V, $f_s=50$ kHz, $F=1.2835$, and $X_r=39.6317$.

MPC+GTSM. The experimental closed-loop transient waveforms of SR-DABC implemented with different control parameters are shown in Figs. 5.11-5.16.

As can be seen from the experimental results, the maximum voltage deviations under both MPC+CTPSM and MPC+GTSM with different control pa-

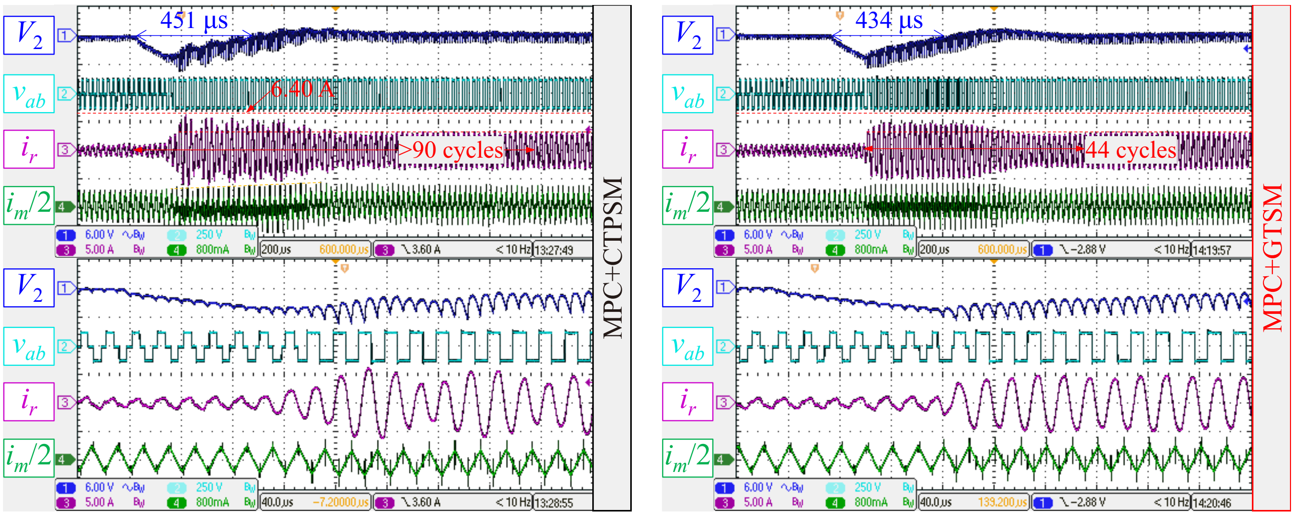

(a) (b)

Fig. 5.15. Experimental closed-loop transient waveforms for a step-up load change from 0.5 to 2 A with $\{K_p^* = 0.15,\ K_i = 0.004\}$ under (a) MPC+CTPSM and (b) MPC+GTSM. $V_1 = 125$ V, $V_2 = 100$ V, $f_s = 50$ kHz, $F = 1.2835$, and $X_r = 39.6317$.

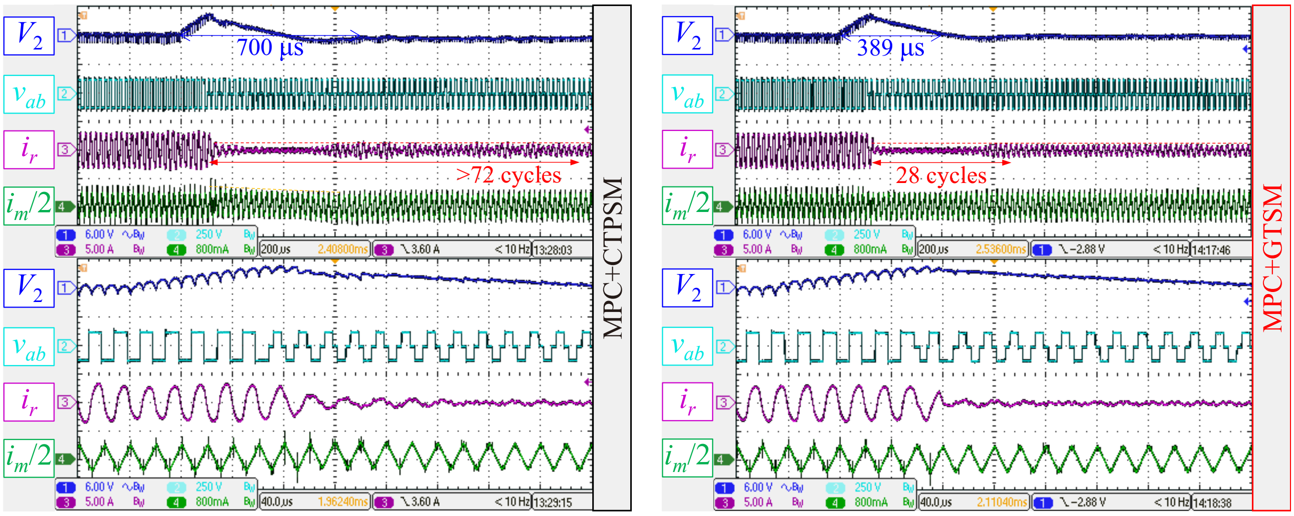

(a) (b)

Fig. 5.16. Experimental closed-loop transient waveforms for a step-down load change from 2 to 0.5 A with $\{K_p^* = 0.15,\ K_i = 0.004\}$ under (a) MPC+CTPSM and (b) MPC+GTSM. $V_1 = 125$ V, $V_2 = 100$ V, $f_s = 50$ kHz, $F = 1.2835$, and $X_r = 39.6317$.

rameters do not differ significantly from each other as the voltage deviations are mainly determined by the value of the output capacitance. The recovery time of the output voltage generally decreases with increasing controller's bandwidth (i.e., K_p^*), but MPC+GTSM leads to shorter recovery time as compared with

MPC+CTPSM. If we carefully examine the waveforms of i_r and i_m, the actual settling times of i_r and i_m increase with increasing controller's bandwidth under MPC+CTPSM. Moreover, as shown in Figs. 5.12(a) and 5.16(a), the output voltage under MPC+CTPSM continuously oscillates about the reference voltage for a relatively long time due to the inaccurate trajectory tracking caused by CTPSM. Compared with MPC+CTPSM, the settling times of both i_r and i_m can be significantly reduced by MPC+GTSM and they are not sensitive to the controller's bandwidth, as they can approach their new steady-state values rapidly without undergoing any transient oscillations and dc offsets. Another important observation is that MPC+CTPSM shows large-amplitude overshoots in both i_r and i_m especially under the cases of step-up load changes, and such issues become more severe with higher controller's bandwidth. On the contrary, the overshoots can be effectively suppressed by MPC+GTSM and do not change noticeably with different control parameters. Meanwhile, as the high-frequency resonant current is translated to the output current of SR-DABC after rectification, the output voltage quality is much improved as a consequence under MPC+GTSM and does not suffer from any transient oscillations. These experimental results also agree well with the closed-loop simulation results shown in Fig. 5.7. Overall, the quality of SR-DABC's waveforms deteriorates with increasing controller's bandwidth under MPC+CTPSM, while they are consistently maintained at high quality under MPC+GTSM. It can therefore be safely concluded that GTSM is more compatible with high-gain, high-bandwidth, and fast controller due to its ability to drive SR-DABC to new steady state swiftly with no transient oscillations and dc bias.

5.6.3 Parameter Sensitivity Tests

To ensure a meaningful parameter sensitivity test, the initial values of X_r and F in the program codes of MPC and GTSM are deliberately set to some incorrect values, and the SR-DABC is constantly operated under SPS mode.

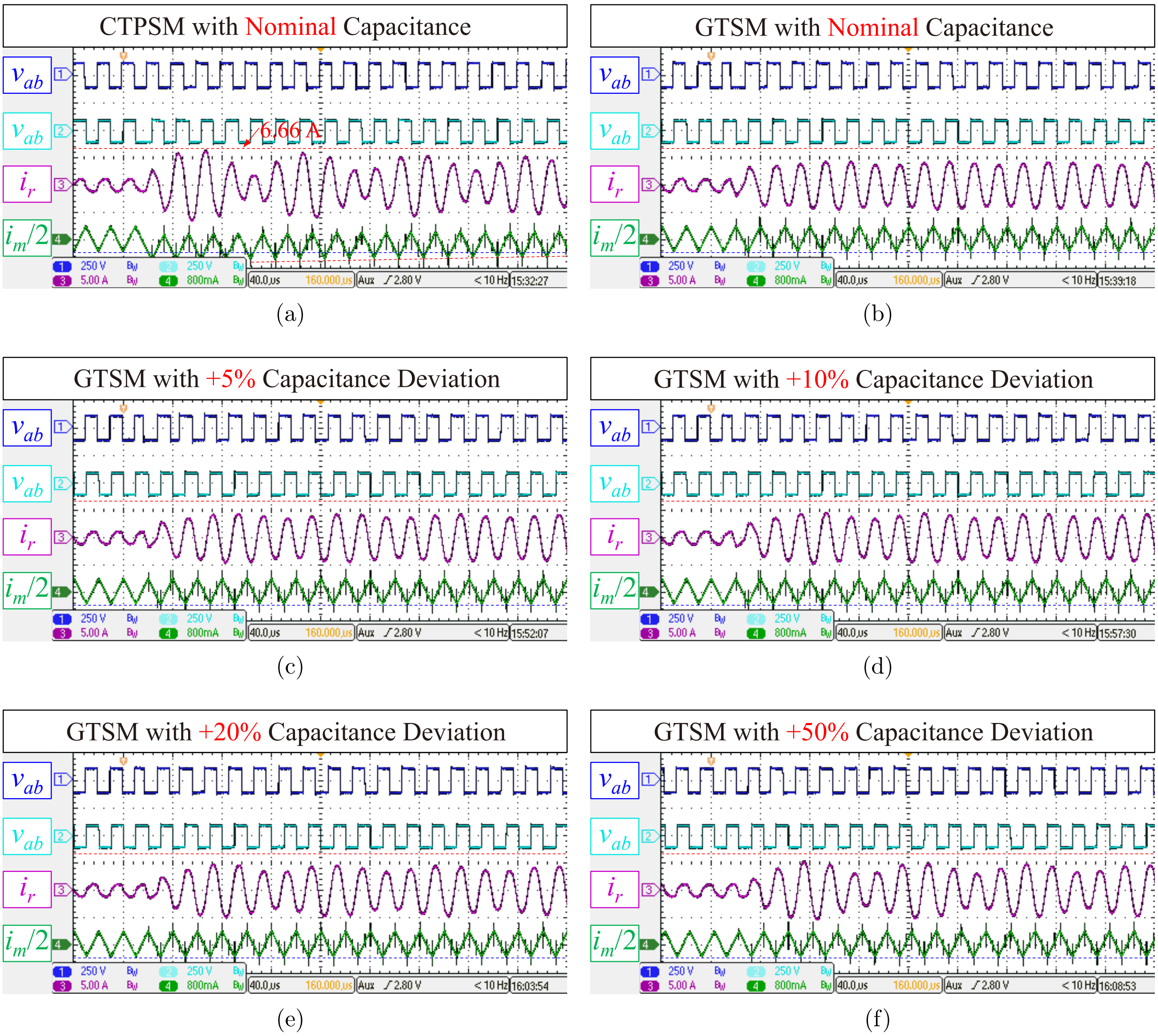

Fig. 5.17. Experimental open-loop transient waveforms under CTPSM and GTSM while considering different capacitance errors. $V_1 = 110$ V, $V_2 = 100$ V, $f_s = 50$ kHz, $\theta_1 = \Delta\theta_1 = 0$, $\theta_3 = \Delta\theta_3 = 0$, $\theta_2 = \pi/9$, and $\Delta\theta_2 = 4\pi/9$. (a) CTPSM with nominal capacitance (i.e., $F = 1.2835$), (b) GTSM with nominal capacitance, (c) GTSM with +5% capacitance deviation (i.e., $F = 1.3152$), (d) GTSM with +10% capacitance deviation (i.e., $F = 1.3462$); (e) GTSM with +20% capacitance deviation (i.e., $F = 1.4060$); (f) GTSM with +50% capacitance deviation (i.e., $F = 1.5720$).

Fig. 5.17 shows the open-loop transient experiments with CTPSM and GTSM considering the presence of errors in the resonant capacitance. It is apparent that if the capacitance error is no more than 20%, GTSM can still effectively

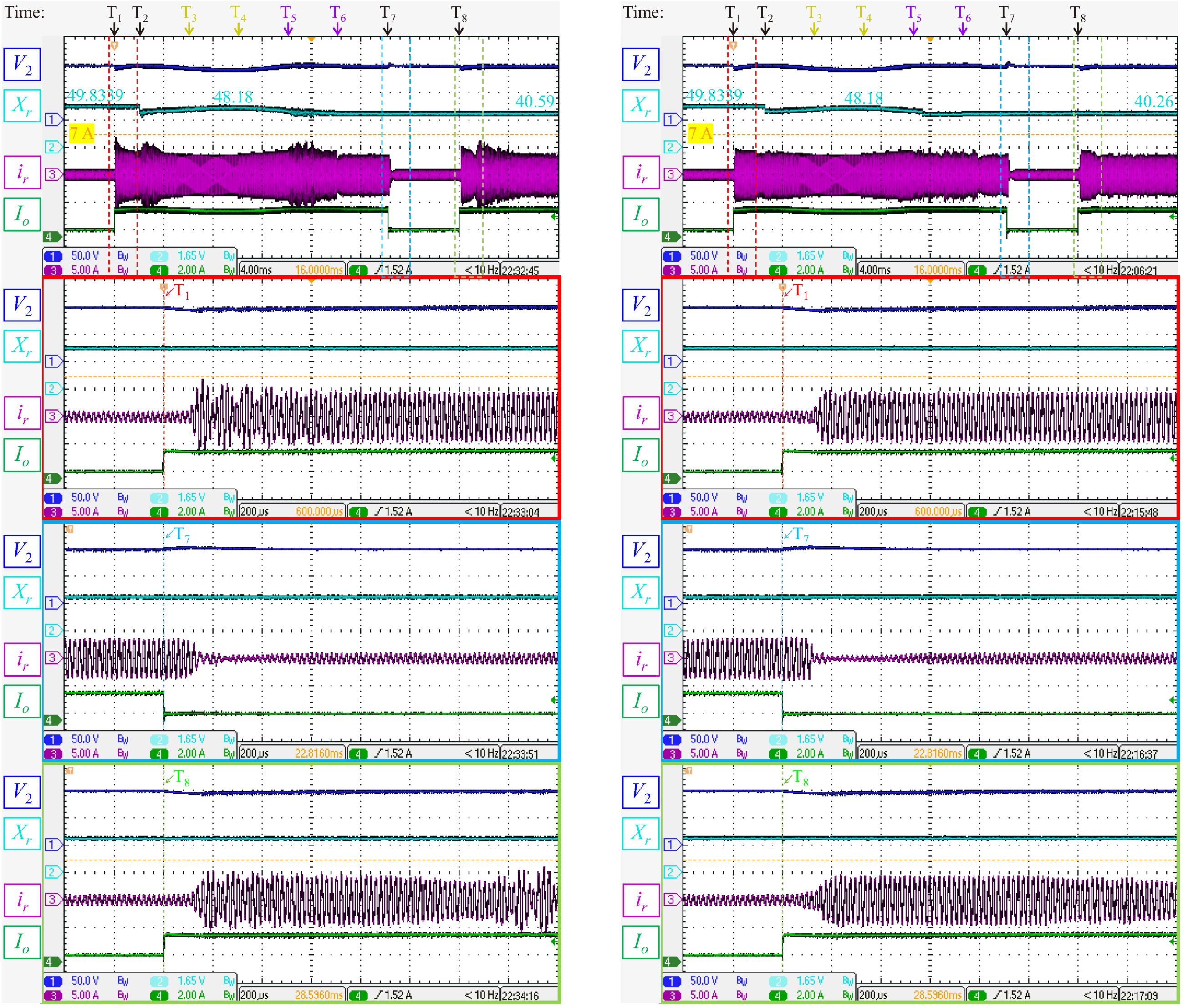

MPC+CTPSM

(a)

MPC+GTSM

(b)

Fig. 5.18. Experimental closed-loop online estimation of X_r and F. Transient waveforms for step load changes between 0.5 and 2 A are shown under (a) MPC+CTPSM and (b) MPC+GTSM. $V_1 = 110$ V, $V_2 = 100$ V, $K_p^* = 0.08$, $K_i = 0.002$, $f_{s\_n} = 50$ kHz, $f_{s\_i} = 52$ kHz, initial (incorrect) values of $X_r = 49.8339$ and $F = 1.4060$.

suppress the transient oscillations and overshoots in i_r. Even if the capacitance error increases to 50%, GTSM still achieves a better transient performance over CTPSM. In addition, the transient dc offset in i_m is effectively eliminated by GTSM in all cases. Thus, it can be concluded that GTSM is inherently not sensitive to parameter deviations.

Fig. 5.18 illustrates the experimental online estimation of X_r and F under closed-loop conditions. The changes in X_r are monitored through a digital-to-analog converter (DAC) module and can be observed from Channel 2's waveforms. The initial (incorrect) values of X_r and F are set as 49.8339 and 1.4060, respectively, which deviate from the nominal values ($X_{r\_n} = 39.6317$ and $F_n = 1.2835$). Before T_1, the converter works with incorrect X_r and F at a light load. At T_1, the load is suddenly changed, and the converter operates at a heavy load. By zooming in the waveforms around T_1, it can be found that even with the incorrect X_r and F, the transient oscillations and overshoots in i_r under MPC+GTSM are much smaller than those under MPC+CTPSM. At T_2, the system has reached the steady state, and the switching frequency will gradually increase to f_{s_i} from f_{s_n} until T_3. The online estimation of X_{r_i} starts from T_3 and will last until T_4, and the estimated values are recorded every two switching cycles. After data processing, the average value of X_{r_i}, i.e., X_{r_ie} can be obtained, which is regarded as the estimated value of X_{r_i} corresponding to f_{s_i}. From T_4, the switching frequency is gradually restored to the nominal value f_{s_n} until T_5. From T_5 to T_6, online estimation restarts, and the estimated impedance X_{r_ne} corresponding to f_{s_n} can be obtained similarly as X_{r_ie}. With X_{r_ie} and X_{r_ne} available, the estimated nominal value of F (i.e., F_{n_e}) can be calculated from (5.52) accordingly. At T_6, the estimated values of X_{r_ne} and F_{n_e} are incorporated into MPC and GTSM, and the execution of parameter estimation comes to an end. The values of X_{r_ne} under MPC+CTPSM and MPC+GTSM are 40.59 and 40.26, respectively, which are close to the actual nominal value $X_{r\_n} = 39.6317$. To verify the dynamics after correction of X_r and F, a step-down load transient is initiated at T_7, followed by a step-up load transient at T_8. As can be seen from the zoomed-in transient waveforms around T_7 and T_8, similar to the results reported in Section 5.6.2, MPC+GTSM always shows a significantly better transient performance over MPC+CTPSM. In addition, for the cases of step-up load transients, the maximum overshoots at T_8 under both MPC+CTPSM and MPC+GTSM are reduced compared to those at T_1, which demonstrates the effectiveness of the online parameter estimation procedure.

5.7 Chapter Summary

In summary, this chapter confirms again the suitability of state-plane-trajectory-based modulation strategies for regulating the energy state of the resonant tank of SR-DABC. The proposed GTSM represents the first method that can realize the stated objective, i.e., fast, oscillation-free, and dc-offset-free transition from old to new steady state in MPS-modulated SR-DABC. In addition, the proposed algorithm of GTSM is sensorless, formulated in analytical form, and insensitive to deviations in resonant tank's parameters, which facilitates its real-time closed-loop implementation in practical applications. Both open-loop and closed-loop test results demonstrate the superior performance of GTSM over CTPSM. When combined with advanced control algorithm such as MPC, which requires fast settling time on a cycle-by-cycle basis in order to deliver the anticipated performance, the proposed GTSM represents a much more effective method compared to CTPSM in terms of achieving fast and smooth (transient oscillation-free and dc-offset-free) responses to extremely fast control actions commanded by MPC or other advanced control algorithms.

Chapter 6

Conclusions and Suggestions for Future Research

In this thesis, several novel optimized transient modulation and control strategies have been proposed to enhance the transient performance of DABC. Collectively, the proposed solutions have made new contributions and demonstrated clear advantages over the other existing methods in the literature. Simulation and experimental results demonstrated that such OTPSM strategies are inherently compatible with high-gain controllers such as MPC for realizing dc-offset-free, oscillation-free, and ultrafast transient responses in DABC, and they are highly attractive for applications requiring fast dynamics. This chapter summarizes the major contributions and makes suggestions for future research.

6.1 Main Contributions

The major contributions of this thesis can be concluded as follows:

(1) Although extensive research has been carried out on the OTPSM strategies for NR-DABC, the proposed SS-OTPSM shows significant differences in the design objectives, theories, and performances. In Chapter 3, a set of unified equations, i.e., (3.5) and (3.12), governing all the existing SPS-

based OTPSM strategies are developed. A new condition enabling a full elimination of all transient dc offsets is introduced to further enhance the theoretical framework of OTPSM, which gave birth to the simplest and most effective OTPSM strategy for NR-DABC, i.e., SS-OTPSM (3.18), to date. SS-OTPSM can completely and simultaneously eliminate the transient dc offsets in both inductor current (i_L) and transformer's magnetizing current (i_m), which demonstrates a significant benefit compared to all existing strategies. It is also worth noting that according to the principle of superposition [108], the proposed SS-OTPSM can be extended to MPS-modulated NR-DABC, and hence SS-OTPSM has the advantage of good compatibility with different gating schemes. More importantly, previous studies have not treated the closed-loop implementation of their methods in detail and failed to demonstrate their effectiveness in a fast closed-loop controlled NR-DABC. This problem is successfully addressed by the proposed SS-OTPSM+MPC, as SS-OTPSM is particularly suitable for implementation in a cycle-by-cycle manner.

(2) Another practical significance of Chapter 3 lies in the optimization of the dynamic performance of NR-DABC through the co-optimization of transient modulation and controller designs (i.e., SS-OTPSM+EMPC), which represents the first attempt in the related literature to discourse the combined roles and the close interaction between modulation and control strategies to achieve dc-offset-free and ultrafast closed-loop dynamics without having to sense the HF-link current. The findings reported in Chapter 3 reveal that, even in an SPS-modulated NR-DABC, there is still a significant room for improving its dynamics.

(3) The work presented in Chapter 4 focuses on studying the origin of HF transient oscillations in SR-DABC, and proposes a simple and cost-effective solution (i.e., TSM) to combat the oscillation problem arising from CTPSM.

Table 6.1 Comparisons of the proposed three transient modulation strategies.

Features & Capabilities	SS-OTPSM	TSM	GTSM
DC-offset Elimination	✓	×	✓
Oscillation Suppression	×	✓	✓
Compatibility with MPS Modulation	✓	×	✓
Topological Compatibility	NR-DABC	SR-DABC	DABC

By appropriately planning the transient state-plane trajectories, the TSM-modulated SR-DABC can converge into a new steady state within one switching cycle under open-loop conditions. Moreover, oscillation-free fast dynamic responses in SR-DABC are demonstrated by the combined use of TSM and MPC, which suggests that TSM is inherently compatible with high-gain controller for realizing high-quality closed-loop controlled dynamics.

(4) In Chapter 5, a powerful and generalized transient modulation approach, i.e., GTSM, is proposed for achieving fast, oscillation-free, and dc-offset-free dynamics in MPS-modulated SR-DABC/NR-DABC independent of operation modes and power-flow directions, which significantly enhances the trajectory control technique for DABC. Besides, the tolerances of resonant elements are considered when applying GTSM, and an automatic parameter identification method is presented to correct the modulation and control parameters used in PWM generator and controller.

Table 6.1 summarizes the main differences between the three proposed transient modulation methods, i.e., SS-OTPSM (Ch. 3 [141]), TSM (Ch. 4 [140]), and GTSM (Ch. 5 [145]). Although they present different ranges of applications and unique properties, all of them contribute to the development of OTPSM strategies for NR-DABC or SR-DABC with the objective to realize their fast and smooth transitions from the old to the new steady state. They also contributes to improving an understanding of the different roles of PWM generator (i.e., transient modulation) and controller in the closed-loop design of DABC.

6.2 Suggestions for Future Research

Some potential limitations/issues have not been fully treated in this thesis and could be explored in future research work, which are listed as follows:

(1) A limitation of the current studies is that the proposed transient modulation strategies (i.e., SS-OTPSM, TSM, and GTSM) are only applicable to NR-DABC and/or SR-DABC. More research efforts are needed to generalize the proposed transient modulation methods to other modulation schemes and converter topologies. In spite of this limitation, the insights gained from this thesis will lay the foundation for the future development of more advanced transient modulation strategies. Thus, in the future, efforts can be made to extend the proposed approaches to asymmetric phase-shift modulation and variable frequency modulation schemes and other variants of resonant converters.

(2) Due to the inherent nature of SR-DABC, one major process for developing the proposed TSM and GTSM is to find the analytical solutions of a set of second-order differential equations. However, when this development method is applied to higher-order resonant converters, a number of high-order non-linear differential equations must be solved, which leads to challenging solution procedure, not to mention that analytical solutions are not always available. In addition, for ultra-high frequency power converters, the available execution times for TSM and GTSM implemented on DSP/FPGA become an important consideration. As a result, more research is required to further investigate the design approach of OTPSM for high-order and ultra-high frequency applications.

(3) In general, the dynamics of PWM generator are seldom modelled precisely

in the existing modelling techniques, and it still remains unclear how the transient modulation strategies can affect the selection of control parameters in the control loop design. Future research can focus on developing mathematical model for the phase-shift PWM-generation block to aid the design and performance optimization of the overall control loop.

Bibliography

[1] F. Urban, R. M. Benders, and H. C. Moll, "Renewable and low-carbon energies as mitigation options of climate change for china," *Climatic Change*, vol. 94, no. 1, pp. 169–188, 2009.

[2] International Renewable Energy Agency (IRENA), "Global renewables outlook: Energy transformation 2050 (2020 Edition)," IRENA Headquarters, Masdar City, PO Box 236, Abu Dhabi, United Arab Emirates, 2020. [Online]. Available: https://www.irena.org/-/media/Files/IRENA/Agency/Publication/2020/Apr/IRENA_Global_Renewables_Outlook_2020.pdf

[3] M. Hannan, M. H. Lipu, P. J. Ker, R. Begum, V. G. Agelidis, and F. Blaabjerg, "Power electronics contribution to renewable energy conversion addressing emission reduction: Applications, issues, and recommendations," *Applied Energy*, vol. 251, p. 113404, 2019.

[4] W. Chen, P. Rong, and Z. Lu, "Snubberless bidirectional dc–dc converter with new cllc resonant tank featuring minimized switching loss," *IEEE Transactions on Industrial Electronics*, vol. 57, no. 9, pp. 3075–3086, 2010.

[5] D. Sha and G. Xu, *High-Frequency Isolated Bidirectional Dual Active Bridge DC–DC Converters with Wide Voltage Gain*. Singapore: Springer, 2019.

[6] M. Stecca, L. R. Elizondo, T. B. Soeiro, P. Bauer, and P. Palensky, "A comprehensive review of the integration of battery energy storage systems into

distribution networks," *IEEE Open Journal of the Industrial Electronics Society*, vol. 1, pp. 46–65, 2020.

[7] F. R. Badal, P. Das, S. K. Sarker, and S. K. Das, "A survey on control issues in renewable energy integration and microgrid," *Protection and Control of Modern Power Systems*, vol. 4, no. 1, pp. 1–27, 2019.

[8] S. A. Gorji, H. G. Sahebi, M. Ektesabi, and A. B. Rad, "Topologies and control schemes of bidirectional dc–dc power converters: An overview," *IEEE Access*, vol. 7, pp. 117 997–118 019, 2019.

[9] L. Chen, S. Shao, Q. Xiao, L. Tarisciotti, P. W. Wheeler, and T. Dragičević, "Model predictive control for dual-active-bridge converters supplying pulsed power loads in naval dc micro-grids," *IEEE Transactions on Power Electronics*, vol. 35, no. 2, pp. 1957–1966, 2020.

[10] M. Farhadi and O. A. Mohammed, "Performance enhancement of actively controlled hybrid dc microgrid incorporating pulsed load," *IEEE Transactions on Industry Applications*, vol. 51, no. 5, pp. 3570–3578, 2015.

[11] F. Boattini, J.-P. Burnet, and G. Skawinski, "Pops: The 60mw power converter for the ps accelerator: Control strategy and performances," in *2015 17th European Conference on Power Electronics and Applications (EPE'15 ECCE-Europe)*, 2015, pp. 1–10.

[12] T. Chen, R. Yu, and A. Q. Huang, "Variable-switching-frequency single-stage bidirectional gan ac–dc converter for the grid-tied battery energy storage system," *IEEE Transactions on Industrial Electronics*, vol. 69, no. 11, pp. 10 776–10 786, 2022.

[13] B. Zhao, Q. Song, W. Liu, and Y. Sun, "A synthetic discrete design methodology of high-frequency isolated bidirectional dc/dc converter for grid-

connected battery energy storage system using advanced components," *IEEE Transactions on Industrial Electronics*, vol. 61, no. 10, pp. 5402–5410, 2014.

[14] Q. Wang and D. Liang, "Efficiency enhancement of the high-frequency isolated grid-connected converter for the battery energy storage system," *Journal of Renewable and Sustainable Energy*, vol. 9, no. 6, p. 064104, 2017.

[15] W. Shi, J. He, J. Song, and S. Yang, "Unified-phase-shift control method of dual active bridge dc-dc converter for data center application," in *2021 IEEE Sustainable Power and Energy Conference (iSPEC)*, 2021, pp. 3199–3203.

[16] S. Baba, S. Bachman, M. Jasinski, and H. Li, "Evaluation of Modular Power Converter Integrated with 5G Network," *Energies*, vol. 14, no. 21, pp. 1–17, November 2021.

[17] M. Porru, A. Serpi, A. Soldati, L. Tassi, and A. Damiano, "Design, control and prototyping of a bidirectional dual active bridge converter for integrating a sodium metal halide battery into a telecom station," in *2021 IEEE Energy Conversion Congress and Exposition (ECCE)*, 2021, pp. 160–167.

[18] M. Antivachis, M. Kasper, D. Bortis, and J. W. Kolar, "Analysis of capacitive power transfer gan isop multi-cell dc/dc converter systems for single-phase telecom power supply modules," in *IECON 2016 - 42nd Annual Conference of the IEEE Industrial Electronics Society*, 2016, pp. 1280–1287.

[19] K. Qing, Z. Xuan, X. Jie, L. Feng, and S. Haiping, "Multiport energy router for satellite based on high-frequency transformer," in *2019 European Space Power Conference (ESPC)*, 2019, pp. 1–4.

[20] J. Chen, M.-K. Nguyen, Z. Yao, C. Wang, L. Gao, and G. Hu, "Dc-dc converters for transportation electrification: Topologies, control, and future challenges," *IEEE Electrification Magazine*, vol. 9, no. 2, pp. 10–22, 2021.

[21] Z. U. Zahid, Z. M. Dalala, R. Chen, B. Chen, and J.-S. Lai, "Design of bidirectional dc–dc resonant converter for vehicle-to-grid (v2g) applications," *IEEE Transactions on Transportation Electrification*, vol. 1, no. 3, pp. 232–244, 2015.

[22] Y. Yan, H. Bai, A. Foote, and W. Wang, "Securing full-power-range zero-voltage switching in both steady-state and transient operations for a dual-active-bridge-based bidirectional electric vehicle charger," *IEEE Transactions on Power Electronics*, vol. 35, no. 7, pp. 7506–7519, 2020.

[23] T. M. Parreiras, A. P. Machado, F. V. Amaral, G. C. Lobato, J. A. S. Brito, and B. C. Filho, "Forward dual-active-bridge solid-state transformer for a sic-based cascaded multilevel converter cell in solar applications," *IEEE Transactions on Industry Applications*, vol. 54, no. 6, pp. 6353–6363, 2018.

[24] H.-J. Choi, H.-P. Park, and J.-H. Jung, "Design methodology of dual active bridge converter for solid state transformer application in smart grid," in *2015 9th International Conference on Power Electronics and ECCE Asia (ICPE-ECCE Asia)*, 2015, pp. 196–201.

[25] C. Nan and R. Ayyanar, "Dual active bridge converter with pwm control for solid state transformer application," in *2013 IEEE Energy Conversion Congress and Exposition*, 2013, pp. 4747–4753.

[26] C. Tu, F. Xiao, Z. Lan, Q. Guo, and Z. Shuai, "Analysis and control of a novel modular-based energy router for dc microgrid cluster," *IEEE Journal of Emerging and Selected Topics in Power Electronics*, vol. 7, no. 1, pp. 331–342, 2019.

[27] B. Liu, Y. Peng, J. Xu, C. Mao, D. Wang, and Q. Duan, "Design and implementation of multiport energy routers toward future energy internet," *IEEE Transactions on Industry Applications*, vol. 57, no. 3, pp. 1945–1957, 2021.

[28] Y. Chen, P. Wang, Y. Elasser, and M. Chen, "Multicell reconfigurable multi-input multi-output energy router architecture," *IEEE Transactions on Power Electronics*, vol. 35, no. 12, pp. 13 210–13 224, 2020.

[29] R. De Doncker, D. Divan, and M. Kheraluwala, "A three-phase soft-switched high-power-density dc/dc converter for high-power applications," *IEEE Transactions on Industry Applications*, vol. 27, no. 1, pp. 63–73, 1991.

[30] M. Kheraluwala, R. Gascoigne, D. Divan, and E. Baumann, "Performance characterization of a high-power dual active bridge dc-to-dc converter," *IEEE Transactions on Industry Applications*, vol. 28, no. 6, pp. 1294–1301, 1992.

[31] X. Li and A. K. S. Bhat, "Analysis and design of high-frequency isolated dual-bridge series resonant dc/dc converter," *IEEE Transactions on Power Electronics*, vol. 25, no. 4, pp. 850–862, 2010.

[32] R. Lenke, F. Mura, and R. W. De Doncker, "Comparison of non-resonant and super-resonant dual-active zvs-operated high-power dc-dc converters," in *2009 13th European Conference on Power Electronics and Applications*, 2009, pp. 1–10.

[33] R. P. Twiname, "Two resonant topologies for isolated bi-directional dc-dc conversion," Ph.D. dissertation, Auckland University of Technology, 2015.

[34] J. Wu, Y. Li, X. Sun, and F. Liu, "A new dual-bridge series resonant dc–dc converter with dual tank," *IEEE Transactions on Power Electronics*, vol. 33, no. 5, pp. 3884–3897, 2018.

[35] M. Yaqoob, "Advanced topologies and modulation schemes for high-efficiency operation of dual-active-bridge series-resonant dc-dc converter," Ph.D. dissertation, The Hong Kong Polytechnic University, 2018.

[36] F. Krismer, J. Biela, and J. Kolar, "A comparative evaluation of isolated bi-directional dc/dc converters with wide input and output voltage range," in *Fourtieth IAS Annual Meeting. Conference Record of the 2005 Industry Applications Conference*, 2005, pp. 599–606.

[37] G. Ortiz, J. Biela, D. Bortis, and J. W. Kolar, "1 megawatt, 20 khz, isolated, bidirectional 12kv to 1.2kv dc-dc converter for renewable energy applications," in *The 2010 International Power Electronics Conference - ECCE ASIA* -, 2010, pp. 3212–3219.

[38] S. S. Chakraborty and K. Hatua, "Modeling with beat frequency dynamics and phase-frequency control design for a dual-bridge series resonant converter," *IEEE Transactions on Industrial Electronics*, vol. 69, no. 8, pp. 7952–7962, 2022.

[39] S. Tian, F. C. Lee, and Q. Li, "A simplified equivalent circuit model of series resonant converter," *IEEE Transactions on Power Electronics*, vol. 31, no. 5, pp. 3922–3931, 2016.

[40] B. Zhang, S. Shao, L. Chen, X. Wu, and J. Zhang, "Steady-state and transient dc magnetic flux bias suppression methods for a dual active bridge converter," *IEEE Journal of Emerging and Selected Topics in Power Electronics*, vol. 9, no. 1, pp. 744–753, 2021.

[41] F. An, W. Song, K. Yang, N. Hou, and J. Ma, "Improved dynamic performance of dual active bridge dc–dc converters using mpc scheme," *IET Power Electronics*, vol. 11, no. 11, pp. 1756–1765, 2018.

[42] Z. Xiao, W. Lei, G. Gao, Y. Cui, Q. Kang, and M. Wang, "Transient current constraint of dab converter based on model predictive control," in *2020 IEEE 9th International Power Electronics and Motion Control Conference (IPEMC2020-ECCE Asia)*, 2020, pp. 203–207.

[43] F. An, W. Song, B. Yu, and K. Yang, "Model predictive control with power self-balancing of the output parallel dab dc–dc converters in power electronic traction transformer," *IEEE Journal of Emerging and Selected Topics in Power Electronics*, vol. 6, no. 4, pp. 1806–1818, 2018.

[44] W. Song, M. Zhong, S. Luo, and S. Yang, "Model predictive power control for bidirectional series-resonant isolated dc–dc converters with fast dynamic response in locomotive traction system," *IEEE Transactions on Transportation Electrification*, vol. 6, no. 3, pp. 1326–1337, 2020.

[45] W. Song, M. Zhong, Y. Deng, S. Yin, and B. Yu, "Model predictive power control for bidirectional series resonant isolated dc–dc converters with steady-state and dynamic performance optimization," *IEEE Journal of Emerging and Selected Topics in Industrial Electronics*, vol. 3, no. 3, pp. 604–615, 2022.

[46] G. G. Oggier, G. O. GarcÍa, and A. R. Oliva, "Switching control strategy to minimize dual active bridge converter losses," *IEEE Transactions on Power Electronics*, vol. 24, no. 7, pp. 1826–1838, 2009.

[47] G. Oggier, G. O. García, and A. R. Oliva, "Modulation strategy to operate the dual active bridge dc-dc converter under soft switching in the whole operating range," *IEEE Transactions on Power Electronics*, vol. 26, no. 4, pp. 1228–1236, 2011.

[48] H. Wen, W. Xiao, and B. Su, "Nonactive power loss minimization in a bidirectional isolated dc–dc converter for distributed power systems," *IEEE Transactions on Industrial Electronics*, vol. 61, no. 12, pp. 6822–6831, 2014.

[49] F. Krismer and J. W. Kolar, "Closed form solution for minimum conduction loss modulation of dab converters," *IEEE Transactions on Power Electronics*, vol. 27, no. 1, pp. 174–188, 2012.

[50] W. Choi, K.-M. Rho, and B.-H. Cho, “Fundamental duty modulation of dual-active-bridge converter for wide-range operation,” *IEEE Transactions on Power Electronics*, vol. 31, no. 6, pp. 4048–4064, 2016.

[51] J. Huang, Y. Wang, Z. Li, and W. Lei, “Unified triple-phase-shift control to minimize current stress and achieve full soft-switching of isolated bidirectional dc–dc converter,” *IEEE Transactions on Industrial Electronics*, vol. 63, no. 7, pp. 4169–4179, 2016.

[52] L. Corradini, D. Seltzer, D. Bloomquist, R. Zane, D. Maksimović, and B. Jacobson, “Minimum current operation of bidirectional dual-bridge series resonant dc/dc converters,” *IEEE Transactions on Power Electronics*, vol. 27, no. 7, pp. 3266–3276, 2012.

[53] G. Chen, X. Li, and S. Zhou, “Unified boundary control with phase shift compensation for dual bridge series resonant dc-dc converter,” *IEEE Access*, vol. 8, pp. 131 137–131 149, 2020.

[54] J. Wu, W. Zhang, X. Sun, and X. Su, “Research on reactive power optimization control of a series-resonant dual-active-bridge converter,” *Energies*, vol. 15, no. 11, 2022.

[55] B. Zhao, Q. Yu, and W. Sun, “Extended-phase-shift control of isolated bidirectional dc–dc converter for power distribution in microgrid,” *IEEE Transactions on Power Electronics*, vol. 27, no. 11, pp. 4667–4680, 2012.

[56] B. Zhao, Q. Song, W. Liu, and Y. Sun, “Overview of dual-active-bridge isolated bidirectional dc–dc converter for high-frequency-link power-conversion system,” *IEEE Transactions on Power Electronics*, vol. 29, no. 8, pp. 4091–4106, 2014.

[57] N. Hou, W. Song, and M. Wu, “Minimum-current-stress scheme of dual active bridge dc–dc converter with unified phase-shift control,” *IEEE Transactions on Power Electronics*, vol. 31, no. 12, pp. 8552–8561, 2016.

[58] A. Tong, L. Hang, G. Li, X. Jiang, and S. Gao, “Modeling and analysis of a dual-active-bridge-isolated bidirectional dc/dc converter to minimize rms current with whole operating range,” *IEEE Transactions on Power Electronics*, vol. 33, no. 6, pp. 5302–5316, 2018.

[59] S. Shao, M. Jiang, W. Ye, Y. Li, J. Zhang, and K. Sheng, “Optimal phase-shift control to minimize reactive power for a dual active bridge dc–dc converter,” *IEEE Transactions on Power Electronics*, vol. 34, no. 10, pp. 10 193–10 205, 2019.

[60] A. K. Bhattacharjee and I. Batarseh, “Optimum hybrid modulation for improvement of efficiency over wide operating range for triple-phase-shift dual-active-bridge converter,” *IEEE Transactions on Power Electronics*, vol. 35, no. 5, pp. 4804–4818, 2020.

[61] J. Tian, F. Wang, F. Zhuo, Y. Wang, H. Wang, and Y. Li, “A zero-backflow-power eps control scheme with multiobjective coupled-relationship optimization in dab-based converter,” *IEEE Journal of Emerging and Selected Topics in Power Electronics*, vol. 10, no. 4, pp. 4128–4145, 2022.

[62] H. Shi, H. Wen, Y. Hu, and L. Jiang, “Reactive power minimization in bidirectional dc–dc converters using a unified-phasor-based particle swarm optimization,” *IEEE Transactions on Power Electronics*, vol. 33, no. 12, pp. 10 990–11 006, 2018.

[63] O. M. Hebala, A. A. Aboushady, K. H. Ahmed, and I. Abdelsalam, “Generic closed-loop controller for power regulation in dual active bridge dc–dc con-

verter with current stress minimization," *IEEE Transactions on Industrial Electronics*, vol. 66, no. 6, pp. 4468–4478, 2019.

[64] Y. Wang, H. Wen, Y. Zhu, H. Shi, Q. Bu, Y. Hu, and Y. Yang, "Minimum-current-stress scheme of three-level dual-active-bridge dc–dc converters with the particle swarm optimization," *IEEE Transactions on Transportation Electrification*, vol. 7, no. 4, pp. 2067–2084, 2021.

[65] L. Zhou, Y. Gao, H. Ma, and P. T. Krein, "Wide-load range multiobjective efficiency optimization produces closed-form control solutions for dual active bridge converter," *IEEE Transactions on Power Electronics*, vol. 36, no. 8, pp. 8612–8616, 2021.

[66] Y. Tang, W. Hu, D. Cao, N. Hou, Y. Li, Z. Chen, and F. Blaabjerg, "Artificial intelligence-aided minimum reactive power control for the dab converter based on harmonic analysis method," *IEEE Transactions on Power Electronics*, vol. 36, no. 9, pp. 9704–9710, 2021.

[67] Y. Tang, W. Hu, J. Xiao, Z. Chen, Q. Huang, Z. Chen, and F. Blaabjerg, "Reinforcement learning based efficiency optimization scheme for the dab dc–dc converter with triple-phase-shift modulation," *IEEE Transactions on Industrial Electronics*, vol. 68, no. 8, pp. 7350–7361, 2021.

[68] Y. Tang, W. Hu, B. Zhang, D. Cao, N. Hou, Y. Li, Z. Chen, and F. Blaabjerg, "Deep reinforcement learning-aided efficiency optimized dual active bridge converter for the distributed generation system," *IEEE Transactions on Energy Conversion*, vol. 37, no. 2, pp. 1251–1262, 2022.

[69] M. Lu, S. Hu, Y. Tang, S.-Z. Zhou, and X. Li, "A novel control strategy based on modified gating scheme for a dual-active-bridge converter," in *2017 12th IEEE Conference on Industrial Electronics and Applications (ICIEA)*, 2017, pp. 1576–1581.

[70] D. Mou, Q. Luo, J. Li, Y. Wei, Z. Wang, P. Sun, X. Du, and H. A. Mantooth, "Hybrid duty modulation for dual active bridge converter to minimize rms current and extend soft-switching range using the frequency domain analysis," *IEEE Transactions on Power Electronics*, vol. 36, no. 4, pp. 4738–4751, 2021.

[71] D. Mou, Q. Luo, Z. Wang, J. Li, Y. Wei, H. Shi, and X. Du, "Optimal asymmetric duty modulation to minimize inductor peak-to-peak current for dual active bridge dc–dc converter," *IEEE Transactions on Power Electronics*, vol. 36, no. 4, pp. 4572–4584, 2021.

[72] D. Mou, Q. Luo, J. Li, Y. Wei, and P. Sun, "Five-degree-of-freedom modulation scheme for dual active bridge dc–dc converter," *IEEE Transactions on Power Electronics*, vol. 36, no. 9, pp. 10 584–10 601, 2021.

[73] J. Li, Q. Luo, D. Mou, Y. Wei, P. Sun, and X. Du, "A hybrid five-variable modulation scheme for dual-active-bridge converter with minimal rms current," *IEEE Transactions on Industrial Electronics*, vol. 69, no. 1, pp. 336–346, 2022.

[74] G. Chen, Z. Chen, Y. Chen, C. Feng, and X. Zhu, "Asymmetric phase-shift modulation strategy of dab converters for improved light-load efficiency," *IEEE Transactions on Power Electronics*, vol. 37, no. 8, pp. 9104–9113, 2022.

[75] S. Hu, X. Li, and A. K. S. Bhat, "Operation of a bidirectional series-resonant converter with minimized tank current and wide zvs range," *IEEE Transactions on Power Electronics*, vol. 34, no. 1, pp. 904–915, 2019.

[76] S. Hu, X. Li, and Q.-F. Zheng, "A dual-bridge dc–dc resonant converter using extended pwm and phase-shift control," *IEEE Transactions on Industry Applications*, vol. 57, no. 4, pp. 4009–4020, 2021.

[77] X.-F. He, Z. Zhang, Y.-Y. Cai, and Y.-F. Liu, “A variable switching frequency hybrid control for zvs dual active bridge converters to achieve high efficiency in wide load range,” in *2014 IEEE Applied Power Electronics Conference and Exposition - APEC 2014*, 2014, pp. 1095–1099.

[78] V. Verma and A. Gupta, “Performance enhancement of the dual active bridge with dual phase shift control and variable frequency modulation,” in *2016 IEEE International Conference on Power Electronics, Drives and Energy Systems (PEDES)*, 2016, pp. 1–6.

[79] X. Han, Y. Tan, and H. Ma, “The switching frequency optimization of dual phase shift control for dual active bridge dc-dc converter,” in *IECON 2017 - 43rd Annual Conference of the IEEE Industrial Electronics Society*, 2017, pp. 1610–1615.

[80] C. Sun, X. Zhang, and X. Cai, “Dual switching frequency operation of dual active bridge converter,” in *2019 IEEE Energy Conversion Congress and Exposition (ECCE)*, 2019, pp. 5217–5222.

[81] T. Mishima and Y. Koga, “Variable frequency phase-shift modulation symmetrical series-resonant bidirectional dc-dc converter-analysis and verification of zvs performance and reactive power minimization,” *IEEJ Journal of Industry Applications*, p. 21002082, 2021.

[82] M. Yaqoob, K. H. Loo, and Y. M. Lai, “A four-degrees-of-freedom modulation strategy for dual-active-bridge series-resonant converter designed for total loss minimization,” *IEEE Transactions on Power Electronics*, vol. 34, no. 2, pp. 1065–1081, 2019.

[83] ——, “Extension of soft-switching region of dual-active-bridge converter by a tunable resonant tank,” *IEEE Transactions on Power Electronics*, vol. 32, no. 12, pp. 9093–9104, 2017.

[84] M. Yaqoob, K.-H. Loo, and Y. M. Lai, "Fully soft-switched dual-active-bridge series-resonant converter with switched-impedance-based power control," *IEEE Transactions on Power Electronics*, vol. 33, no. 11, pp. 9267–9281, 2018.

[85] M. Yaqoob, K.-H. Loo, Y. P. Chan, and J. Jatskevich, "Optimal modulation for a fifth-order dual-active-bridge resonant immittance dc–dc converter," *IEEE Transactions on Power Electronics*, vol. 35, no. 1, pp. 70–82, 2020.

[86] Y. P. Chan, K. H. Loo, M. Yaqoob, and Y. M. Lai, "A structurally reconfigurable resonant dual-active-bridge converter and modulation method to achieve full-range soft-switching and enhanced light-load efficiency," *IEEE Transactions on Power Electronics*, vol. 34, no. 5, pp. 4195–4207, 2019.

[87] Y. P. Chan, C. S. Wong, and K. H. Loo, "Dual-mode modulation scheme with seamless transition for a tunable immittance-based dab converter featuring high-efficiency performance over whole output power range," *IEEE Transactions on Power Electronics*, vol. 35, no. 9, pp. 9184–9201, 2020.

[88] A. Z. Khan, K. H. Loo, and Y. M. Lai, "Design, analysis, and performance characterization of dual-active-bridge dc–dc converter utilizing three-phase resonant immittance network," *IEEE Transactions on Power Electronics*, vol. 34, no. 2, pp. 1159–1180, 2019.

[89] A. Z. Khan and K. H. Loo, "A three-phase dual-active-bridge dc–dc converter with reconfigurable resonant network for efficient wide voltage range operation," *IEEE Transactions on Power Electronics*, vol. 35, no. 2, pp. 1322–1339, 2020.

[90] X. Li and Y.-F. Li, "An optimized phase-shift modulation for fast transient response in a dual-active-bridge converter," *IEEE Transactions on Power Electronics*, vol. 29, no. 6, pp. 2661–2665, 2014.

[91] C. Sun and X. Li, "Instantaneous current balance modulation for fast transient response in a dual-active-bridge converter," in *2018 IEEE International Power Electronics and Application Conference and Exposition (PEAC)*, 2018, pp. 1–6.

[92] R. Chattopadhyay, U. Raheja, G. Gohil, V. Nair, and S. Bhattacharya, "Sensorless phase shift control for phase shifted dc-dc converters for eliminating dc transients from transformer winding currents," in *2018 IEEE Applied Power Electronics Conference and Exposition (APEC)*, 2018, pp. 1882–1889.

[93] J. Yin, J. Lu, Y. Liu, J. Peng, and H. Jiang, "Novel phase-shift method for fast power reversal with transient zero voltage switching in a bidirectional dual active bridge dc–dc converter," *IEEE Transactions on Industrial Electronics*, vol. 68, no. 9, pp. 8028–8038, 2021.

[94] Y. Tang, X. Li, S.-Z. Zhou, C. Sun, and G. Chen, "Comprehensive study of fast load modulation with volt-second balance in a dual-active-bridge converter," *IET Power Electronics*, vol. 12, no. 6, pp. 1357–1367, 2019.

[95] J. Hong, Y. Liu, and J. Yin, "Modulation strategy for optimized transient performance of dual active bridge converter under reverse of power flow direction," in *2019 IEEE International Conference on Industrial Technology (ICIT)*, 2019, pp. 510–514.

[96] J. Lu and J. Yin, "Unified phase shift control strategy to optimize transient current response in a dual active bridge dc-dc converter during unidirectional and bidirectional power flow changes," in *2020 IEEE 9th International Power Electronics and Motion Control Conference (IPEMC2020-ECCE Asia)*, 2020, pp. 2599–2604.

[97] B. Zhao, Q. Song, W. Liu, and Y. Zhao, “Transient dc bias and current impact effects of high-frequency-isolated bidirectional dc–dc converter in practice,” *IEEE Transactions on Power Electronics*, vol. 31, no. 4, pp. 3203–3216, 2016.

[98] P. Yao, X. Jiang, P. Xue, S. Ji, and F. Wang, “Flux balancing control of ungapped nanocrystalline core-based transformer in dual active bridge converters,” *IEEE Transactions on Power Electronics*, vol. 35, no. 11, pp. 11 463–11 474, 2020.

[99] A. K. Bhattacharjee, S. M. Tayebi, and I. Batarseh, “Fast response dual active bridge converter with elimination of transient dc offset by intermediate asymmetric modulation,” in *2018 IEEE Energy Conversion Congress and Exposition (ECCE)*, 2018, pp. 637–642.

[100] K. Takagi and H. Fujita, “Dynamic control and performance of a dual-active-bridge dc–dc converter,” *IEEE Transactions on Power Electronics*, vol. 33, no. 9, pp. 7858–7866, 2018.

[101] K. Li, Y. Wang, J. Xu, J. Wang, R. Li, and C. Lv, “A novel control method for eliminating dc bias in dual-active-bridge dc-dc converters,” in *2018 IEEE International Power Electronics and Application Conference and Exposition (PEAC)*, 2018, pp. 1–6.

[102] M. Wattenberg, U. Schwalbe, and M. Pfost, “Impact of dc-bias on dual active bridge control and how to avoid it,” in *2019 21st European Conference on Power Electronics and Applications (EPE ’19 ECCE Europe)*, 2019, pp. P.1–P.8.

[103] D.-D. Nguyen, K. Yukita, G. Fujita, and M. C. Ta, “A simple dc bias elimination technique for dual-active-bridge dc/dc converters,” in *2019 10th International Conference on Power Electronics and ECCE Asia (ICPE 2019 - ECCE Asia)*, 2019, pp. 1–6.

[104] C. Sun and X. Li, "Fast transient modulation for a step load change in a dual-active-bridge converter with extended-phase-shift control," *Energies*, vol. 11, no. 6, p. 1569, 2018.

[105] C. Sun, X. Li, and S.-Z. Zhou, "Transient current control for a step load change in a dual-active-bridge converter," *Electronics Letters*, vol. 54, no. 22, pp. 1290–1292, 2018.

[106] Q. Bu, H. Wen, J. Wen, Y. Hu, and Y. Du, "Transient dc bias elimination of dual-active-bridge dc–dc converter with improved triple-phase-shift control," *IEEE Transactions on Industrial Electronics*, vol. 67, no. 10, pp. 8587–8598, 2020.

[107] Q. Bu, H. Wen, H. Shi, Y. Hu, and Y. Yang, "Universal transient dc-bias current suppression strategy in dual-active-bridge converters for energy storage systems," *IEEE Transactions on Transportation Electrification*, vol. 7, no. 2, pp. 509–526, 2021.

[108] J. Hu, S. Cui, D. v. d. Hoff, and R. W. De Doncker, "Generic dynamic phase-shift control for bidirectional dual-active bridge converters," *IEEE Transactions on Power Electronics*, vol. 36, no. 6, pp. 6197–6202, 2021.

[109] R. Duan, L. Yuan, Q. Gu, J. Nie, and Z. Zhao, "Trajectory-prediction-based fast bidirectional power transient control for series resonant dual-active-bridge converter," in *2018 IEEE Energy Conversion Congress and Exposition (ECCE)*, 2018, pp. 1415–1422.

[110] H. Xu, S.-Z. Zhou, X. Li, H. Chen, and S. Hu, "Fast transient modulation of a dual-bridge series resonant converter," in *IECON 2021 – 47th Annual Conference of the IEEE Industrial Electronics Society*, 2021, pp. 1–6.

[111] R. W. T. Bonten, J. M. Schellekens, B. J. D. Vermulst, F. M. Clermonts, and H. Huisman, "Improved dynamic behavior for the series-resonant converter

using bidirectional charge control," *IEEE Transactions on Power Electronics*, vol. 37, no. 10, pp. 11 607–11 619, 2022.

[112] R. Oruganti and F. C. Lee, "Resonant power processors, part i—state plane analysis," *IEEE Transactions on Industry Applications*, vol. IA-21, no. 6, pp. 1453–1460, 1985.

[113] ——, "Resonant power processors, part ii-methods of control," *IEEE Transactions on Industry Applications*, vol. IA-21, no. 6, pp. 1461–1471, 1985.

[114] R. Oruganti, J. J. Yang, and F. C. Lee, "Implementation of optimal trajectory control of series resonant converter," *IEEE transactions on power electronics*, vol. 3, no. 3, pp. 318–327, 1988.

[115] W. Feng, F. C. Lee, and P. Mattavelli, "Simplified optimal trajectory control (sotc) for llc resonant converters," *IEEE Transactions on Power Electronics*, vol. 28, no. 5, pp. 2415–2426, 2013.

[116] L. Rossetto, "A simple control technique for series resonant converters," *IEEE Transactions on Power Electronics*, vol. 11, no. 4, pp. 554–560, 1996.

[117] G. G. Oggier, M. Ordonez, J. M. Galvez, and F. Luchino, "Fast transient boundary control and steady-state operation of the dual active bridge converter using the natural switching surface," *IEEE Transactions on Power Electronics*, vol. 29, no. 2, pp. 946–957, 2014.

[118] G. G. Koch, S. S. Queiroz, C. Rech, R. C. L. F. Oliveira, R. A. Borges, E. S. Tognetti, and V. F. Montagner, "Design of a robust pi controller for a dual active bridge converter," in *2016 12th IEEE International Conference on Industry Applications (INDUSCON)*, 2016, pp. 1–6.

[119] F. L. F. Marcelino, H. H. Sathler, T. R. de Oliveira, and P. F. Donoso-Garcia, "Modeling and control of a dual active bridge for energy storage in dc mi-

crogrid applications," in *2017 IEEE 8th International Symposium on Power Electronics for Distributed Generation Systems (PEDG)*, 2017, pp. 1–8.

[120] Y. Pan, Y. Yang, J. He, A. Sangwongwanich, C. Zhang, Y. Liu, and F. Blaabjerg, "A dual-loop control to ensure fast and stable fault-tolerant operation of series resonant dab converters," *IEEE Transactions on Power Electronics*, vol. 35, no. 10, pp. 10 994–11 012, 2020.

[121] Hua Bai, Chunting Mi, Chongwu Wang, and S. Gargies, "The dynamic model and hybrid phase-shift control of a dual-active-bridge converter," in *2008 34th Annual Conference of IEEE Industrial Electronics*, 2008, pp. 2840–2845.

[122] F. Krismer and J. W. Kolar, "Accurate small-signal model for the digital control of an automotive bidirectional dual active bridge," *IEEE Transactions on Power Electronics*, vol. 24, no. 12, pp. 2756–2768, 2009.

[123] D. Seltzer, L. Corradini, D. Bloomquist, R. Zane, and D. Maksimović, "Small signal phasor modeling of dual active bridge series resonant dc/dc converters with multi-angle phase shift modulation," in *2011 IEEE Energy Conversion Congress and Exposition*, 2011, pp. 2757–2764.

[124] D. Segaran, D. G. Holmes, and B. P. McGrath, "Enhanced load step response for a bidirectional dc–dc converter," *IEEE Transactions on Power Electronics*, vol. 28, no. 1, pp. 371–379, 2013.

[125] W. Song, N. Hou, and M. Wu, "Virtual direct power control scheme of dual active bridge dc–dc converters for fast dynamic response," *IEEE Transactions on Power Electronics*, vol. 33, no. 2, pp. 1750–1759, 2018.

[126] S. Dutta, S. Hazra, and S. Bhattacharya, "A digital predictive current-mode controller for a single-phase high-frequency transformer-isolated dual-active

bridge dc-to-dc converter," *IEEE Transactions on Industrial Electronics*, vol. 63, no. 9, pp. 5943–5952, 2016.

[127] N. Vazquez and M. Liserre, "Peak current control and feed-forward compensation of a dab converter," *IEEE Transactions on Industrial Electronics*, vol. 67, no. 10, pp. 8381–8391, 2020.

[128] Z. Shan, J. Jatskevich, H. H. Iu, and T. Fernando, "Simplified load-feedforward control design for dual-active-bridge converters with current-mode modulation," *IEEE Journal of Emerging and Selected Topics in Power Electronics*, vol. 6, no. 4, pp. 2073–2085, 2018.

[129] Z. Ji, Q. Wang, D. Li, and Y. Sun, "Fast dc-bias current control of dual active bridge converters with feedforward compensation," *IEEE Transactions on Circuits and Systems II: Express Briefs*, vol. 67, no. 11, pp. 2587–2591, 2020.

[130] G. G. Oggier, M. Ordonez, J. M. Galvez, and F. Luchino, "Fast transient boundary control and steady-state operation of the dual active bridge converter using the natural switching surface," *IEEE Transactions on Power Electronics*, vol. 29, no. 2, pp. 946–957, 2014.

[131] S. Wei, Z. Zhao, K. Li, L. Yuan, and W. Wen, "Deadbeat current controller for bidirectional dual-active-bridge converter using an enhanced sps modulation method," *IEEE Transactions on Power Electronics*, vol. 36, no. 2, pp. 1274–1279, 2021.

[132] M. Ali, M. Yaqoob, L. Cao, and K. H. Loo, "Disturbance-observer-based dc-bus voltage control for ripple mitigation and improved dynamic response in two-stage single-phase inverter system," *IEEE Transactions on Industrial Electronics*, vol. 66, no. 9, pp. 6836–6845, 2019.

[133] F. Xiong, J. Wu, Z. Liu, and L. Hao, "Current sensorless control for dual active bridge dc–dc converter with estimated load-current feedforward," *IEEE Transactions on Power Electronics*, vol. 33, no. 4, pp. 3552–3566, 2018.

[134] Y.-C. Jeung and D.-C. Lee, "Voltage and current regulations of bidirectional isolated dual-active-bridge dc–dc converters based on a double-integral sliding mode control," *IEEE Transactions on Power Electronics*, vol. 34, no. 7, pp. 6937–6946, 2019.

[135] N. Hou and Y. W. Li, "Overview and comparison of modulation and control strategies for a nonresonant single-phase dual-active-bridge dc–dc converter," *IEEE Transactions on Power Electronics*, vol. 35, no. 3, pp. 3148–3172, 2020.

[136] S. Shao, L. Chen, Z. Shan, F. Gao, H. Chen, D. Sha, and T. Dragičević, "Modeling and advanced control of dual-active-bridge dc–dc converters: A review," *IEEE Transactions on Power Electronics*, vol. 37, no. 2, pp. 1524–1547, 2022.

[137] Y. Xiao, Z. Zhang, X. Mao, K. T. Manez, and M. A. E. Andersen, "Power plateau and anti-power phenomenon of dual active bridge converter with phase-shift modulation," in *2018 IEEE Applied Power Electronics Conference and Exposition (APEC)*, 2018, pp. 1871–1875.

[138] K. Takagi and H. Fujita, "Dynamic control and dead-time compensation method of an isolated dual-active-bridge dc-dc converter," in *2015 17th European Conference on Power Electronics and Applications (EPE'15 ECCE-Europe)*, 2015, pp. 1–10.

[139] S. Buso and P. Mattavelli, *Digital Control in Power Electronics*, 2nd ed. Morgan & Claypool Publishers, 2015.

[140] C. Sun, X. Jiang, L. Cao, and K. H. Loo, “Total suppression of high-frequency transient oscillations in dual-active-bridge series-resonant converter by trajectory-switching modulation,” *IEEE Transactions on Power Electronics*, vol. 37, no. 6, pp. 6511–6529, 2022.

[141] C. Sun, X. Jiang, J. Liu, L. Cao, Y. Yang, and K. H. Loo, “A unified design approach of optimal transient single-phase-shift modulation for nonresonant dual-active-bridge converter with complete transient dc-offset elimination,” *IEEE Transactions on Power Electronics*, vol. 37, no. 11, pp. 13 217–13 237, 2022.

[142] J. Liu, G. Wang, G. Xu, J. Peng, and H. Jiang, “A parameter identification approach with primary-side measurement for dc–dc wireless-power-transfer converters with different resonant tank topologies,” *IEEE Transactions on Transportation Electrification*, vol. 7, no. 3, pp. 1219–1235, 2021.

[143] Y. Wei, Q. Luo, and H. A. Mantooth, “A resonant frequency tracking technique for llc converter-based dc transformers,” *IEEE Journal of Emerging and Selected Topics in Industrial Electronics*, vol. 2, no. 4, pp. 579–590, 2021.

[144] Z. Guo, Y. Luo, and K. Sun, “Parameter identification of the series inductance in dab converters,” *IEEE Transactions on Power Electronics*, vol. 36, no. 7, pp. 7395–7399, 2021.

[145] C. Sun, J. Liu, X. Jiang, L. Cao, Y.-C. Wang, J.-X. Shen, and K.-H. Loo, “Generalized multiphase-shift transient modulation for dual-active-bridge series-resonant converter,” *IEEE Transactions on Power Electronics*, vol. 38, no. 7, pp. 8291–8309, 2023.